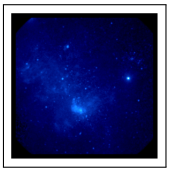

X-ray Telescopes in the Digital Lab: Instrument Performance Simulations

Röntgenteleskope im digitalen Labor: Simulationen der Instrumenten-Eigenschaften

Der Naturwissenschaftlichen Fakultät
der Friedrich-Alexander-Universität
Erlangen-Nürnberg
zur
Erlangung des Doktorgrades Dr. rer. nat.
vorgelegt von

Christian Schmid

aus Amberg

ERLANGEN CENTRE FOR ASTROPARTICLE PHYSICS

FRIEDRICH-ALEXANDER UNIVERSITÄT ERLANGEN-NÜRNBERG

ECAP-2012-013

Als Dissertation genehmigt
von der Naturwissenschaftlichen Fakultät
der Friedrich-Alexander-Universität Erlangen-Nürnberg

Tag der mündlichen Prüfung:	04. Juli 2012
Vorsitzender der Promotionskommission:	Prof. Dr. Rainer Fink
Erstberichterstatter:	Prof. Dr. Jörn Wilms
Zweitberichterstatter:	Dr. Randall Smith

The small image on the title page displays a simulated view of the Galactic Center region with the WFI on *ATHENA*.

Zusammenfassung

In dieser Arbeit stelle ich ein Softwarepaket vor, das ich zum Zweck von Monte-Carlo-Simulationen von Beobachtungen mit Röntgenteleskopen entwickelt habe. Ich gebe einen Überblick über die wichtigsten Technologien, die von derzeitigen und von künftigen Missionen verwendet werden. Insbesondere stelle ich die Prinzipien und die Herstellungsverfahren für verschiedene Röntgenoptiken und die zwei Hauptklassen von Halbleiterdetektoren und Kalorimetern vor. Des weiteren erkläre ich die wichtigsten Phänomene im Zusammenhang mit der Detektion von Röntgenphotonen.

Die Simulationssoftware verfolgt einen generischen Ansatz. Sie beinhaltet einen Satz an vordefinierten Teleskop- und Detektormodellen für bestehende Instrumente, aber sie kann auch mit geringem Aufwand auf weitere Missionen ausgedehnt werden. Ich stelle die Implementierung der physikalischen Eigenschaften der verschiedenen Arten von Detektoren vor, die in der Simulationssoftware enthalten sind. Der gewählte Ansatz basiert auf Dateien mit echten Kalibrationsdaten, um ein möglichst realistisches Setup der Modelle zu garantieren. Im Vergleich zu einer aufwändigen, physikalisch exakten Ray-Tracing-Simulation habe ich jedoch einige Vereinfachungen vorgenommen, um die numerische Effizienz der Simulation zu verbessern. Die Modelle für die verschiedenen Instrumente basieren auf diversen Kompromissen, um einerseits vertretbare Laufzeiten auf gegenwärtig üblichen Computersystemen und andererseits ausreichend physikalische Genauigkeit für die betrachteten Fragestellungen zu erreichen. Im Gegensatz zu zahlreichen bestehenden Simulations-Softwarepaketen kann das implementierte Teleskopmodell während einer laufenden Beobachtung eine beliebige Bewegung ausführen. Dies geschieht anhand der in einer sogenannten Attitudedatei vorgegebenen Daten. Für die Berechnung des Auftreffpunkts der Photonen auf dem Detektor wird die Energie einfallender Photonen und deren Position innerhalb des Gesichtsfelds berücksichtigt. Die Software beinhaltet sowohl ein allgemeines Detektormodell, das anhand einer speziellen XML-Beschreibung an die meisten gebräuchlichen Typen von Instrumenten angepasst werden kann, als auch einige spezielle Modelle für bestimmte Detektoren, die anhand des generischen Modells nicht mit der benötigten Genauigkeit beschrieben werden können. Die wichtigsten physikalischen Prozesse, die von den diversen Detektormodellen berücksichtigt werden, sind die Verteilung von Ladungswolken zwischen benachbarten Pixeln in Halbleiterdetektoren, Pile-up von Photonen, Totzeiten des Detektors, die Effizienz des Ladungstransports in Charge-Coupled Devices (CCDs) und eine realistische Energieauflösung mit einer detektorspezifischen Absorption von Photonen. Das generische Modell ist das wichtigste Element des Softwarepakets, da es einen flexiblen Rahmen mit anpassbaren Parametern darstellt und die Integration neuer Instrumententypen anhand von XML-Dateien erlaubt, ohne den eigentlichen Programmcode zu verändern. Es beinhaltet diverse Befehle, mit denen detektorspezifische Operationen zum Auslesen der Signale definiert werden können, die von absorbierten Photonen erzeugt werden.

Basierend auf der Simulationssoftware habe ich mehrere Studien für existierende und für die Zukunft geplante Röntgenteleskope durchgeführt, um deren spezifische Eigenschaften im Hinblick auf die wissenschaftliche Verwertbarkeit der Messdaten zu analysieren. In dieser Arbeit präsentiere ich mehrere Untersuchungen für das deutsche Projekt extended ROentgen Survey with an Imaging Telescope Array (eROSITA), das gerade gebaut wird, und das Konzept für die künftige Mission *International X-ray Observatory* (*IXO*)/*Advanced Telescope for High ENergy Astrophysics* (*ATHENA*), das im Hinblick auf einen Start im Jahr 2022 untersucht wird. Die Simulationssoftware wurde ursprünglich für diese beiden Missionen entwickelt, kann aber inzwischen auch für weitere Instrumente verwendet werden.

Für eROSITA stelle ich eine Studie über die Auswirkung der Bewegung des Teleskops während der geplanten Himmelsdurchmusterung auf die Punktbildfunktion vor. Außerdem zeige ich einige Ergebnisse für simulierte Beobachtungen verschiedener Arten von Röntgenquellen, wie z.B.

Galaxienhaufen, sowie eine Untersuchung des Pile-ups des Detektors. Das Verständnis des Pile-up-Verhaltens eines Instruments ist überaus wichtig für Spektralanalysen und zeitaufgelöste Studien gemessener Daten, insbesondere bei Beobachtungen von hellen Quellen, da es die gemessenen Energiespektren und andere wissenschaftliche Daten, wie z.B. die Statistik der gezählten Photonenereignisse verfälschen kann. Während eine genaue Beschreibung dieses Phänomens mit analytischen Modellen recht anspruchsvoll ist und meist auf Abschätzungen anhand von Wahrscheinlichkeitsrechnungen basiert, wird ein solcher Ansatz durch das Einbeziehen weiterer Detektoreffekte noch komplizierter. Im Gegensatz dazu sind Simulationen überaus geeignet für eine derartige Untersuchung.

Ein genaues Verständnis der Eigenschaften hinsichtlich Pile-up ist für den Wide Field Imager (WFI), das X-ray Microcalorimeter Spectrometer (XMS) und das High Time Resolution Spectrometer (HTRS) auf *IXO/ATHENA* noch weit wichtiger als für eROSITA, da die unterschiedlichen wissenschaftlichen Zielsetzungen dieser Mission genauere Spektralanalysen und zeitlich aufgelöste Beobachtungen heller Röntgenquellen erfordern. Ich habe daher derartige Beobachtungen mit diesen Instrumenten simuliert und zusätzlich einige weitere technische Analysen durchgeführt. Für den WFI auf *ATHENA* stelle ich in dieser Arbeit zudem einen Vergleich zum Advanced CCD Imaging Spectrometer (ACIS)-I Instrument auf *Chandra* vor, der den großen Fortschritt zwischen diesen beiden Instrumenten im Hinblick auf die damit möglichen Beobachtungen verdeutlicht. Obwohl sich die aufgeführten Beispiele auf eROSITA und *IXO/ATHENA* konzentrieren, zeige ich auch einige Ansätze für weitere Anwendungsgebiete der entwickelten Simulationssoftware im Zusammenhang mit anderen Projekten auf, um deren universelle Verwendbarkeit zu demonstrieren.

Abstract

In this thesis I present a software package, which I have developed for Monte Carlo simulations of observations with X-ray telescopes. I provide an overview of the most important technologies implemented in current and planned X-ray telescope missions. In particular I introduce the principles and the manufacturing techniques for different optical systems and give a short overview of the two main instrument classes of semiconductor-based detectors and calorimeters. In addition I explain the most important features related to the detection of X-ray photons.

The simulation software is designed in a generic way. It contains a set of predefined telescope and detector models for existing instruments, but it can be easily extended to other missions, as well. I present the implementation of the physical properties relevant for the different kinds of detector models, which are included in the simulation software. The selected approach relies on calibration files, which are commonly used for current instruments, in order to guarantee a realistic model setup. However, in comparison to a sophisticated ray-tracing simulation I have also implemented some simplifications in order to achieve numerical efficiency in the required computation processes. The assembly of the different instrument models deals with various trade-offs providing both a reasonable processing time on current standard computer systems and sufficient physical accuracy for the selected applications. In contrast to most existing simulation software the implemented telescope model is capable of modeling an arbitrary slewing motion during an observation. This motion is defined in a so-called attitude file. The model for the optical system of the telescope deals with the energy of the incident photons and their position within the Field Of View (FOV) in order to determine their impact position on the detector. There is a general detector model, which can be adjusted to most common instrument types using an XML description, but the software package also contains some specific models for particular detectors, which cannot be described by the generic model with the required fidelity. The most important features taken into account by the various detector models are charge cloud splitting between adjacent pixels in semiconductor devices, photon pile-up, dead time issues, Charge Transfer Efficiency (CTE) for Charge-Coupled Devices (CCDs), and a realistic energy resolution including detector-specific absorption features. The generic detector model is the most powerful item of the software package, since it provides a flexible framework with adjustable parameters and enables the setup of new instrument types based on XML files without any modifications of the program code. It provides several commands to define detector-specific operations for the read-out of the signals produced by the absorbed photons.

Based on this simulation software I have performed studies for different existing and future X-ray telescopes in order to analyze specific properties and their impact on the scientific output of the respective instruments. In this work I present several analyses for the German project extended ROentgen Survey with an Imaging Telescope Array (eROSITA), which is currently constructed, and the mission concept *International X-ray Observatory* (*IXO*)/*Advanced Telescope for High ENergy Astrophysics* (*ATHENA*), which is being studied for a launch around 2022. The simulation software has originally been developed for these two missions, although it can now also be applied to simulations of other instruments.

For eROSITA I introduce an investigation of the relation between the telescope motion during the planned all-sky survey and the Point Spread Function (PSF). I show some results of simulated observations of different kinds of X-ray sources, such as clusters of galaxies, and of a pile-up analysis of the detector. The understanding of the pile-up behavior of an instrument is essential for spectroscopic and timing analysis of the measured data in particular for observations of bright sources, since it may distort the measured energy spectra or affect other scientific data such as photon count statistics. While a detailed description of this phenomenon with analytical models is quite challenging and mainly relies on probabilistic estimates, it becomes even more

complicated if further detector effects are taken into account. Simulations, in contrast, are very well suited for such an analysis.

A detailed understanding of the pile-up properties is even more important for the instruments on *IXO/ATHENA* than for eROSITA, because different scientific objectives of this mission require more precise spectroscopic and timing analyses of bright X-ray sources. Therefore I have simulated such observations with these instruments in addition to some other technical investigations. In this thesis I also present a comparison of the Wide Field Imager (WFI) on *ATHENA* to the Advanced CCD Imaging Spectrometer (ACIS)-I instrument on *Chandra* illustrating the big advance in observational capabilities between these two instruments. Although the indicated examples focus on eROSITA and *IXO/ATHENA*, I also present some suggestions to further usage of the developed simulation software in other projects in order to demonstrate its universal applicability.

Contents

List of Figures

List of Tables

List of Acronyms

ABRIXAS	*A Broadband Imaging X-ray All-Sky Survey*
ACIS	Advanced CCD Imaging Spectrometer
AGN	Active Galactic Nuclei
APE	All-purpose Parameter Environment
APS	Active Pixel Sensor
ARF	Ancillary Response File
ART-XC	Astronomical Roentgen Telescope – X-ray Concentrator
ASCA	*Advanced Satellite for Cosmology and Astrophysics*
ASIC	Application-Specific Integrated Circuit
ASM	All-Sky Monitor
ASTEROID	Active current Switching TEchnique ReadOut In X-ray spectroscopy with DePFET
ATHENA	*Advanced Telescope for High ENergy Astrophysics*
BBXRT	Broad Band X-Ray Telescope
BH	Black Hole
BMWi	Bundesministerium für Wirtschaft und Technologie
BSC	Bright Source Catalog
BSDO	Bright Source Defocusing Optic
CAMEX	CMOS Analog MultiplEXer
CCD	Charge-Coupled Device
CDF-S	*Chandra* Deep Field–South
CESR	Centre d'Etude Spatiale des Rayonnements
CfA	Center for Astrophysics
CMB	Cosmic Microwave Background
CTE	Charge Transfer Efficiency
CTI	Charge Transfer Inefficiency
CXRB	Cosmic X-Ray Background
DePFET	Depleted P-channel Field Effect Transistor
DLR	Deutsches Zentrum für Luft- und Raumfahrt
DUO	*Dark Universe Observatory*
ECAP	Erlangen Centre for Astroparticle Physics
EPIC	European Photon Imaging Camera
eRASS	eROSITA All-Sky Survey
eROSITA	extended ROentgen Survey with an Imaging Telescope Array
ESA	European Space Agency
FET	Field Effect Transistor
FFT	Fast Fourier Transformation
FITS	Flexible Image Transport System
FOV	Field Of View
FSC	Faint Source Catalog
FWHM	Full Width at Half Maximum
GEANT4	GEometry ANd Tracking
Gen-X	*Generation-X*
GRB	Gamma-Ray Burst
GRAVITAS	*General Relativistic Astrophysics VIa Timing And Spectroscopy*
GRXE	Galactic Ridge X-ray Emission
GSL	GNU Scientific Library
HEALPix	Hierarchical Equal Area isoLatitude Pixelization
HEAO-1	*High Energy Astronomical Observatory 1*
HEAO-2	*High Energy Astronomical Observatory 2*
HDU	Header and Data Unit
HEAdas	High Energy Astronomy data analysis system
HEASARC	High Energy Astrophysics Science Archive Research Center
HEAsoft	High Energy Astronomy software
HEW	Half Energy Width
HIFI	HIgh Framerate Imager
HIFLUGCS	HIghest X-ray FLUx Galaxy Cluster Sample
HMXB	High-Mass X-ray Binary
HPD	Half Power Diameter
HTML	HyperText Markup

	Language
HTRS	High Time Resolution Spectrometer
HXI	Hard X-ray Imager
IAAT	Institute for Astronomy and Astrophysics Tübingen
ICM	Intra-Cluster Medium
`IDL`	Interactive Data Language
INTEGRAL	*INTErnational Gamma-Ray Astrophysics Laboratory*
ISCO	Innermost Stable Circular Orbit
`ISIS`	Interactive Spectral Interpretation System
ISM	Inter-Stellar Medium
ISS	*International Space Station*
IXO	*International X-ray Observatory*
JAXA	Japan Aerospace Exploration Agency
LAD	Large Area Detector
LMC	Large Magellanic Cloud
LMXB	Low-Mass X-ray Binary
LOFT	*Large Observatory For x-ray Timing*
MCP	Micro Channel Plate
Micro-X	*High-Resolution Microcalorimeter X-ray Imaging Rocket*
MIP	Moveable Instrument Platform
MIRAX	Monitor e Imageador de RAios-X
MIT	Massachusetts Institute of Technology
MOS	Metal Oxide Semiconductor
MOSFET	Metal Oxide Semiconductor Field Effect Transistor
MPE	Max-Planck-Institut für Extraterrestrische Physik
MPG	Max-Planck-Gesellschaft
NASA	National Aeronautics and Space Administration
NFI	Narrow Field Imager
NRTA	Near Real Time data Analysis
NS	Neutron Star
NuSTAR	*Nuclear Spectroscopic Telescope ARray*
OOT	Out Of Time
PHA	Pulse Height Amplitude
PIL	Parameter Interface Library
pn-CCD	p-n junction Charge-Coupled Device
PSD	Power Spectral Density
PSF	Point Spread Function
QCD	Quantum ChromoDynamics
QPO	Quasi-Periodic Oscillation
RASS	*ROSAT* All-Sky Survey
rms	root mean square
ROSAT	*ROentgen SATellite*
ROSITA	ROentgen Survey with an Imaging Telescope Array
RMF	Redistribution Matrix File
RXTE	*Rossi X-ray Timing Explorer*
SAO	Smithsonian Astrophysical Observatory
SAS	Scientific Analysis System
SASS	Science Analysis Software System
SDD	Silicon Drift Detector
SIMPUT	SIMulation inPUT
SIXTE	SImulation of X-ray TElescopes
SMC	Small Magellanic Cloud
SPO	Silicon Pore Optics
SQUID	Superconducting QUantum Interference Device
SRG	*Spektrum-Roentgen-Gamma*
SXI	Soft X-ray Imager
SXS	Soft X-ray Spectrometer
TES	Transition Edge Sensor
TRoPIC	Third Röntgen Photon Imaging Camera
USA	United States of America
VELA	VLSI ELectronics for Astronomy
WCS	World Coordinate System
WD	White Dwarf
WFI	Wide Field Imager
WFM	Wide Field Monitor
WHIM	Warm and Hot Intergalactic Medium
XEUS	*X-ray Evolving Universe Spectroscopy*
XGS	X-ray Grating Spectrometer
XIS	X-Ray Imaging

	Spectrometer
XLF	X-ray Luminosity Function
XML	eXtensible Markup Language
XMM-Newton	*X-ray Multi-Mirror Mission*
	Newton
XMS	X-ray Microcalorimeter Spectrometer
XPOL	X-ray POLarimeter
XRS	X-Ray Spectrometer

CHAPTER 1

INTRODUCTION

1.1 The X-ray Universe

Soft X-rays have about three orders of magnitude more energy than optical photons. In this thesis mainly the regime from approximately 0.1 to 10 keV is regarded. An estimate of the necessary conditions for the emission of such photons can be obtained from the spectrum of a black body, which is described by Planck's formula (Planck, 1901):

$$\rho(\nu, T)\,\mathrm{d}\nu = \frac{8\pi h\nu^3}{c^3}\,\frac{1}{e^{h\nu/(k_\mathrm{B}T)} - 1}\,\mathrm{d}\nu \tag{1.1}$$

The frequency and therefore the photon energy corresponding to the peak of the radiative emission can be calculated according to Wien's law (Wien, 1894; Meschede, 2002):

$$\nu_\mathrm{max} = \frac{2.82}{h}\,k_\mathrm{B}T \tag{1.2}$$

$$E_\mathrm{max} = h\,\nu_\mathrm{max} = 2.82\,k_\mathrm{B}T \tag{1.3}$$

with the Boltzmann constant $k_\mathrm{B} = 8.617386 \times 10^{-5}\,\mathrm{eV\,K^{-1}}$. For a peak emission of $E_\mathrm{max} = 1\,\mathrm{keV}$ the corresponding temperature is obtained as

$$T \approx 4.1 \times 10^6\,\mathrm{K} \tag{1.4}$$

Thus the emission of X-rays is usually related to extremely hot environments and the most energetic phenomena in the Universe. Typical conditions fulfilling this criterion are created by accretion of matter onto Neutron Stars (NSs) and Black Holes (BHs), which are the most compact objects in our Universe. Although BHs in principle are dark objects, since their gravitational field is so strong that no light can escape, their environment can be very luminous in a broad spectral range due to the violent physical processes taking place there.

While fusion of hydrogen and helium is the most important process that converts mass into energy, the accretion of matter onto compact objects is more efficient, due to the concentration of a high mass within a very small region. By the fusion of hydrogen to helium about 0.7 % of the involved mass is converted into energy (Frank et al., 1992). The energy released by accretion of a mass m from a quasi-infinite distance onto an orbit with radius R around a compact object with mass M can be obtained as

$$\Delta E = \underbrace{\frac{GmM}{R}}_{E_\mathrm{pot}} - \underbrace{\frac{GmM}{2R}}_{E_\mathrm{kin}} = \frac{GmM}{2R} \tag{1.5}$$

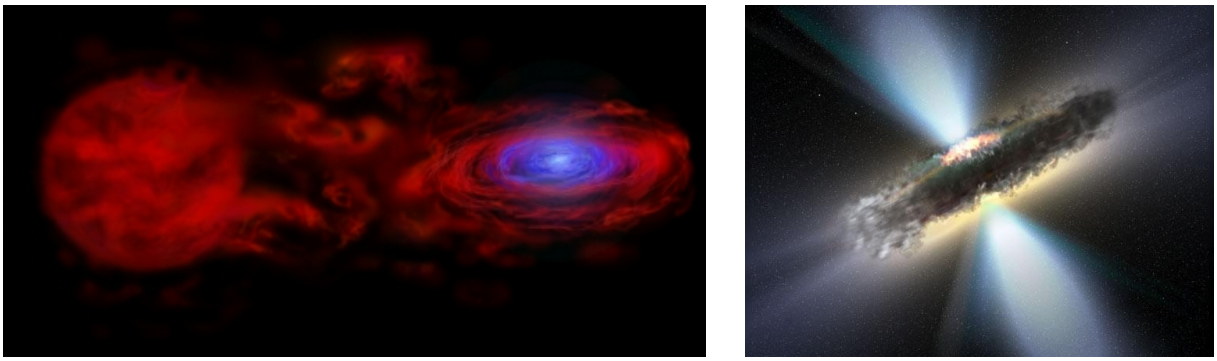

Figure 1.1: Schematic view of the accretion of matter onto BHs: binary system with a stellar-mass BH accreting matter from its companion star (left-hand side, `http://www.physics.uc.edu/`) and a super-massive BH in the center of an AGN (right-hand side, `http://integral.esac.esa.int/`). The accreted matter forms a disk around the BH due to conservation of angular momentum.

where $G = 6.673 \times 10^{-11}\,\mathrm{m^3\,kg^{-1}\,s^{-2}}$ is the gravitational constant. A fraction of the released potential energy E_{pot} is converted into kinetic energy, as indicated by the second term (E_{kin}) in Eq. (1.5).

For a BH the value of the radius R cannot be smaller than the event horizon, beyond which no light and therefore also no released energy can escape to its environment. All energy release contributing to the emission observed from a BH has to take place before the accreted matter reaches the event horizon. For a non-rotating BH the so-called Schwarzschild radius (Schwarzschild, 1916) corresponding to the event horizon can be determined as

$$R_{\mathrm{S}} = 2G \cdot \frac{M}{c^2} \tag{1.6}$$

According to Eqs. (1.5) and (1.6) the binding energy of matter at the Schwarzschild radius R_{S} can be estimated as $\sim$25 % of its rest energy mc^2. Although this value is a rough estimate for the energy released as electromagnetic radiation, it indicates that accretion onto a compact object is the most powerful process in the Universe (Salpeter, 1964; Pringle et al., 1973; Frank et al., 1992; Wilms, 2006). The efficiency η of the energy release in terms of electromagnetic radiation in an accretion process is defined by the relation

$$E_{\mathrm{rad}} = \eta mc^2 \tag{1.7}$$

with the radiated energy E_{rad}. Typically the efficiency is of the order of 0.1 (Hanke, 2011).

Due the conservation of angular momentum the accreted matter usually does not directly fall into a BH, but forms an accretion disk around it, as shown in Fig. 1.1 (Pringle & Rees, 1972). By the loss of angular momentum due to viscous dissipation and magnetic torque the matter slowly spirals inwards in the accretion disk towards the so-called Innermost Stable Circular Orbit (ISCO) close to the event horizon of the BH. The energy released thereby is mainly converted into thermal heating of the accretion disk and its surroundings.

The radius of the ISCO and therefore the fractional energy release into electromagnetic radiation depends on the spin of the BH (Bardeen et al., 1972; Dauser et al., 2010). For a non-rotating Schwarzschild BH the energy release is $\sim$6 % of the rest energy of the accreted matter, whereas for a maximum spinning Kerr BH this fraction can have a value of up to $\sim$43 % (Bardeen, 1970) or $\sim$30 % according to a closer analysis of the maximum spin of the BH (Thorne, 1974).

Due to its high efficiency, accretion onto compact objects can power heating to extreme temperatures. Such an environment provides multiple mechanisms to produce X-rays. Of course,

the existence of a BH or a NS itself is not sufficient for the emergence of X-rays. Actually these objects are very dark in any wavelength regime, if they are isolated in space without the possibility of accreting matter. In order to provide a sufficient supply of matter, there must be some other object in the direct neighborhood of the compact object. This condition is, e.g., realized in a binary system consisting of a compact object and a stellar companion (Fig. 1.1). In such a system matter can be transferred from the companion star to the NS or BH, e.g., by a stellar wind (Hoyle & Lyttleton, 1939; Bondi & Hoyle, 1944; Bondi, 1952; Hanke, 2011).

According to Hanke (2011) the following three major mechanisms contribute to the emitted X-ray spectrum: thermal emission from the accretion disk, inverse Compton scattering of the X-rays from the disk by a hot electron plasma in the corona of the accretion disk, and Compton reflection of the high energetic photons in the outer cool part of the accretion disk. In the usual form of Compton scattering (Compton, 1923) photons lose energy by interaction with electrons at rest. Inverse Compton scattering, however, takes place if the electrons form a hot plasma such that the photons gain energy by the scattering processes (Wilms, 2008). A more detailed description of the geometry in the vicinity of an accreting BH and the production of X-rays is given by Nowak et al. (2011).

Apart from BH binaries, similar accretion and radiation emission mechanisms also work on larger scales. The accretion of matter by super-massive BHs in the centers of Active Galactic Nuclei (AGN) operates according to the same principle (Fig. 1.1). In order to provide the observed amount of radiation, matter has to be accreted with a rate of several solar masses per year.

Due to the process of inverse Compton scattering with the electrons in the corona of the accretion disk which are distributed according to a power law, the typical X-ray spectrum observed for accreting BHs can often also be described by a power law. In addition to this continuum spectrum, fluorescence lines originate from the ionization of atoms in the accretion disk and the subsequent emission of X-ray photons with characteristic energies. Due to its large abundance in the Universe, the most prominent lines in the soft X-ray regime are the K shell transitions of Fe corresponding to a line energy of 6.4 keV (Fabian et al., 1989; Nandra et al., 1989).

For NSs the accretion process is slightly different than for BHs. On the one hand they do not have an event horizon behind which the accreted matter vanishes. On the other hand they usually exhibit strong magnetic fields[1] breaking up the inner parts of the accretion disk. Therefore the matter has to follow the magnetic field lines onto the surface of the NS, forming two accretion columns at the magnetic poles, as indicated in Fig. 1.2. Under the presence of such strong magnetic fields electrons can be confined to discrete Landau levels resulting in the emission of cyclotron radiation in the soft X-ray regime (Schönherr et al., 2007).

Another mechanism responsible for the production of X-rays is the thermal emission in hot plasmas with temperatures of ten to hundred million degrees as they can be found the Intra-Cluster Medium (ICM) of galaxy clusters (Böhringer, 2008). The images in Fig. 1.3 show the alignment of the X-ray emission with optically visible galaxies in the core of the Perseus cluster according to Fabian et al. (2011). The spectrum emitted by an optically thin, collisionally ionized plasma is described by different astrophysical models (Raymond & Smith, 1977; Mewe et al., 1986; Smith et al., 2001; Foster et al., 2010) including various components such as bremsstrahlung (free-free emission).

Due to their origin, observations of X-rays are ideal to investigate hot and violent processes taking place in our Universe (Lechner et al., 2003). They provide information about the environment of extreme objects such as BHs and NS, which are dominated by the effects of General Relativity, and allow us to study the physics of hot gases and plasmas (Giacconi, 2009).

[1] Typical magnetic fields range from 10^{12} G up to 10^{15} G for magnetars (Rosswog & Bruggen, 2007, Chapter 5).

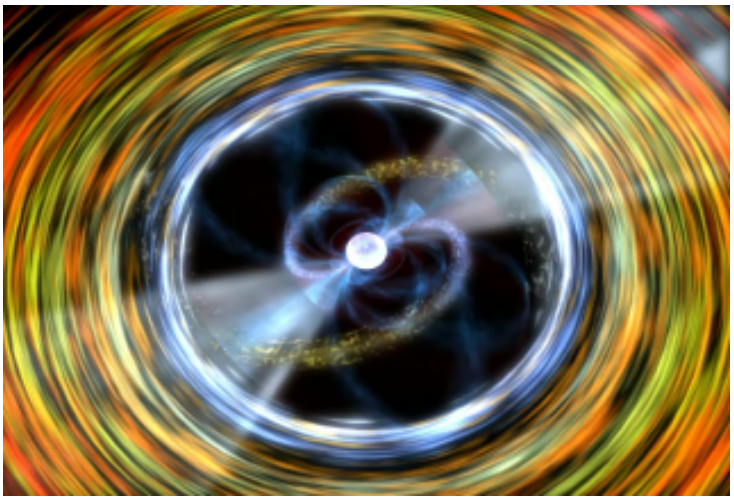

Figure 1.2: Schematic view of the accretion of matter onto a NS (`http://svs.gsfc.nasa.gov/`). The strong magnetic field of the NS is breaking up the inner parts of the accretion disk. The matter is falling onto its surface along the magnetic field lines forming accretion columns at the magnetic poles.

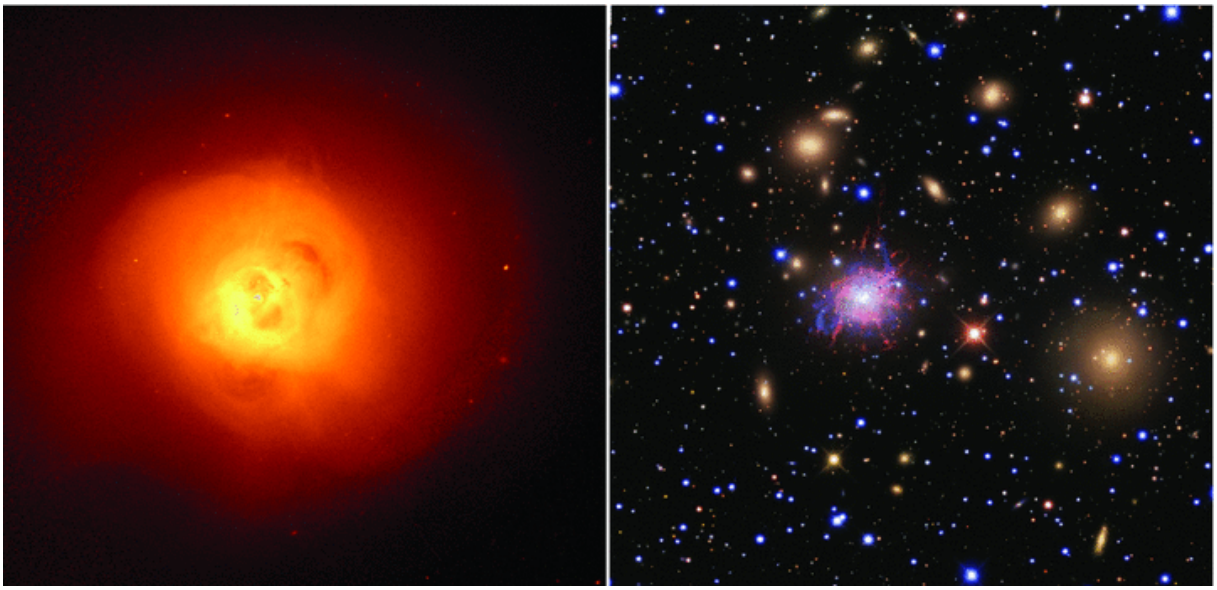

Figure 1.3: The Perseus cluster, as seen in the X-rays with *Chandra* (left-hand side), and in the optical (right-hand side). The hot ICM confined in the deep gravitational potential of the galaxy cluster has a temperature of some 10 million K and is therefore well visible in the X-rays (Fabian et al., 2011).

1.2 History of X-ray Astronomy

One of the main issues affecting observations of astronomical X-ray sources is the absorption of X-rays in the atmosphere of the Earth. Although it is almost completely transparent for optical light, X-ray photons cannot penetrate the atmosphere and therefore have to be observed from its outer layers or from space. This circumstance results in an enormous technical effort, since suitable instruments have to be installed on balloons, rockets, or satellites.

One of the first astronomical X-ray observations was the measurement of X-ray radiation from the Sun with a photon counter tube on a V-2 rocket in 1949 (Friedman et al., 1951). Another pioneering experiment was the attempt to detect fluorescence X-rays from the surface of the Moon caused by X-rays from the Sun with sounding rockets in 1962, which resulted in the discovery of Sco X-1 as the first known X-ray source outside the solar system and the isotropic Cosmic X-Ray Background (CXRB) radiation (Giacconi et al., 1962).

The observing time available during a single rocket flight is limited to a very short duration.

In order to obtain the possibility of longer observation intervals, it is necessary to mount the X-ray instruments on a spacecraft such as a satellite. The particular orbit of a satellite still imposes a large number of restrictions on the fraction of the sky that is accessible at a particular point of time. However, it is possible to perform continuous observations with typical durations of several hours. By composition of multiple observations total exposure times of several days can be obtained on individual targets. The total operation times of X-ray satellites are typically several years.

The first X-ray satellite, *Uhuru*, was launched in 1970 (Giacconi et al., 1971). It was equipped with collimated large-area proportional counters providing an angular resolution of ∼30 arcmin. As a big advance in comparison to rocket-based measurements *Uhuru* detected ∼300 X-ray sources. Further advancements in X-ray astronomy could be achieved with the *High Energy Astronomical Observatory 1* (*HEAO-1*) launched in 1979. One of its most important achievements was the observation of the spectrum of the Cosmic X-Ray Background (CXRB, Marshall et al., 1980).

The next step providing higher sensitivities was the introduction of X-ray telescopes with imaging techniques based on Wolter optics (Wolter, 1952a). The *High Energy Astronomical Observatory 2* (*HEAO-2*), also called *Einstein* (Giacconi et al., 1979b), was the first X-ray satellite equipped with a Wolter type I telescope. It was launched in 1978 and provided a gain in sensitivity by a factor of ∼100 in comparison to previous collimating instruments (Giacconi et al., 1979a). The first all-sky survey with an imaging telescope was performed by the *ROentgen SATellite* (*ROSAT*) launched in 1990 (Trümper, 1982, 1992). In comparison to the ∼300 X-ray sources detected by *Uhuru*, the *ROSAT* All-Sky Survey (RASS) source catalogs (Bright Source Catalog and Faint Source Catalog) comprise in total ∼125 000 sources (Voges et al., 1999, 2000a,b).

The most important currently operating missions are the *X-ray Multi-Mirror Mission Newton* (*XMM-Newton*, Jansen et al., 2001), the *Chandra* X-ray observatory (Weisskopf et al., 2002), both launched in 1999, and *Suzaku* (Mitsuda et al., 2007), which was launched in 2005. As with almost any modern X-ray telescope for the low energetic X-ray regime $\lesssim 10\,\mathrm{keV}$ they are equipped with Wolter type I optics. These three major X-ray telescopes, shown in Fig. 1.4, and several smaller instruments on other satellites currently form the basis for investigations of a large variety of scientific aspects with different observational means.

However, collimating techniques based on a blocking aperture that absorbs photons originating from other sources than the target are still applicable for observations of X-ray radiation $\gtrsim 10\,\mathrm{keV}$. Imaging optics suitable for this energy regime require currently hardly manageable long focal lengths. Especially the technology of coded mask telescopes (Fenimore & Cannon, 1978) is therefore a popular alternative for the high energetic X-ray domain. The *INTErnational Gamma-Ray Astrophysics Laboratory* (*INTEGRAL*, Winkler et al., 2003, 2011, Fig. 1.4d), which was launched in 2002, is based on this technique.

1.3 Future Investigations

With the advance of technological means there are also plans to extend the observational capabilities of current telescopes further using recently developed detector types. One of these future missions is the German X-ray telescope extended ROentgen Survey with an Imaging Telescope Array (eROSITA, Predehl et al., 2006, 2007, 2010a,b, 2011), which can be regarded as the successor of the previous *ROSAT* mission. The telescope has a large Field Of View (FOV) with a diameter of ∼1 deg and will perform an all-sky survey with an increased energy range and a 30 times improved sensitivity with respect to *ROSAT* (Figs. 1.5 and 1.6). In comparison to the ∼125 000 sources contained in the RASS catalogs, eROSITA will discover several million

(a) *XMM-Newton* (`http://xmm.esa.int/`)

(b) *Chandra* (`http://chandra.harvard.edu/`)

(c) *Suzaku* (`http://www.jaxa.jp/`)

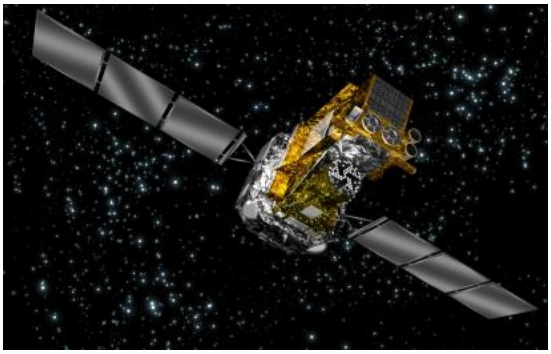

(d) *INTEGRAL* (`http://integral.esa.int/`)

Figure 1.4: Artists' impressions of the currently three major telescopes for the soft X-ray regime $\lesssim 10\,\mathrm{keV}$ (**(a)**–**(c)**) and *INTEGRAL* for the hard energy range $\gtrsim 10\,\mathrm{keV}$ (**(d)**).

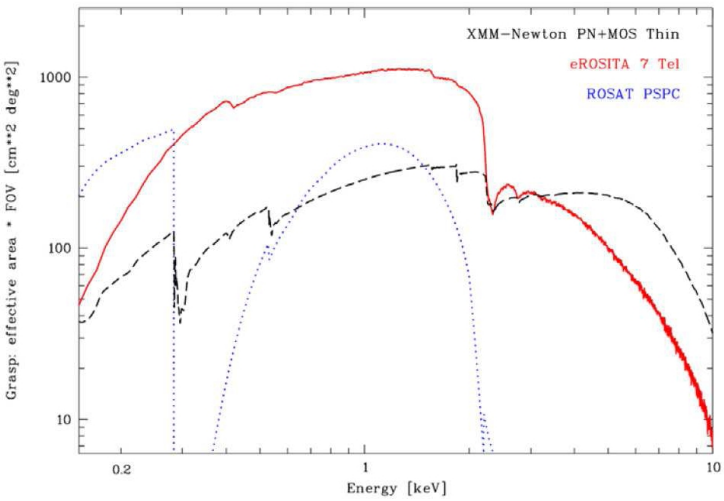

Figure 1.5: Grasp of the eROSITA telescope (Predehl et al., 2010b). The grasp is the product of the effective area of an instrument, i.e., its capability to collect photons (Chapter 2), and its FOV. For a survey covering a wide area on the sky a large grasp is essential. In the energy range 0.5–2 keV, which is in particular relevant for the detection of galaxy clusters, the grasp of eROSITA clearly outranges the values for *ROSAT* and *XMM-Newton*.

X-ray sources.

As a successor of *XMM-Newton* and *Chandra* a large international collaboration is currently studying a mission called *Advanced Telescope for High ENergy Astrophysics* (*ATHENA*, Barcons et al., 2011b), which provides two X-ray telescopes with an unprecedented collecting area and modern detector types. The mission concept of *ATHENA* is partly based on former studies for the *X-ray Evolving Universe Spectroscopy* (*XEUS*, Arnaud et al., 2008), *Constellation-X* (Bookbinder et al., 2008), and the *International X-ray Observatory* (*IXO*, Bookbinder, 2010; Bookbinder et al., 2010; Barcons et al., 2011a). It comprises two instruments. The Wide Field Imager (WFI) is a Si-based Active Pixel Sensor (APS) device with a large FOV and moderate energy resolution. The X-ray Microcalorimeter Spectrometer (XMS) consists of an array of

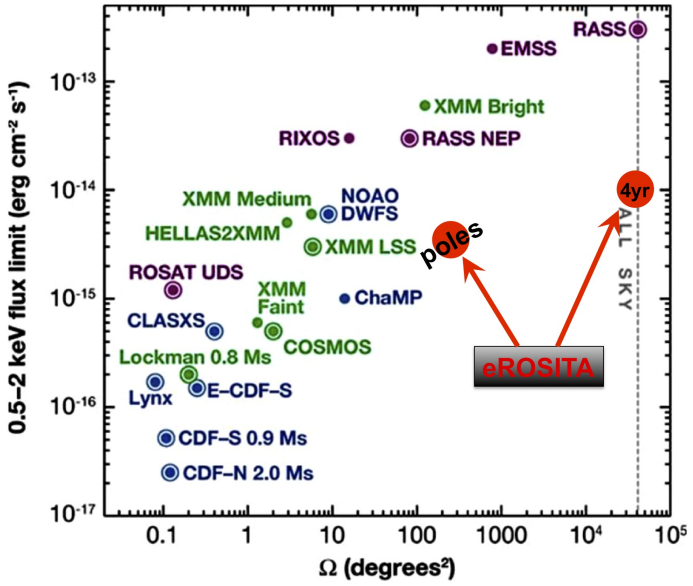

Figure 1.6: Sensitivity of the eROSITA survey in comparison to existing surveys (`http://www.mpe.mpg.de/erosita/`). Similar to the *ROSAT* All-Sky Survey (RASS) the eROSITA All-Sky Survey (eRASS) will cover the whole sky, but with a 30 times higher sensitivity. The polar survey is part of the four-year eRASS, but has a lower sensitivity limit than the rest of the survey because of a higher total exposure time according to the particular survey geometry.

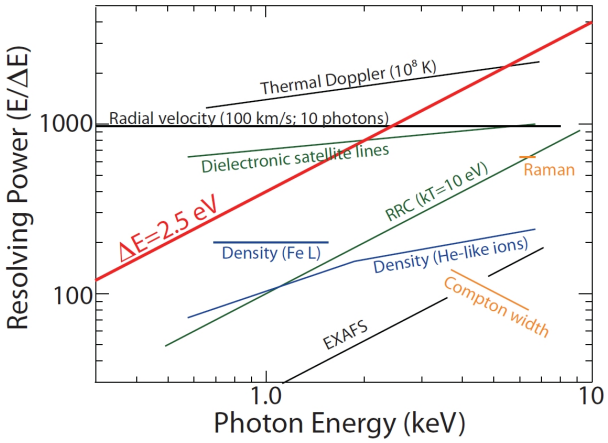

Figure 1.7: Illustration of the scientific issues accessible with the spectral resolution provided by microcalorimeters (Barcons et al., 2011a, according to a figure by Paerels, 2010). Such an instrument enables, e.g., Raman spectroscopy and density measurements based on the Fe K- and L-shell transition lines respectively. The red line represents the energy resolution of 2.5 eV of the XMS on *IXO*. The resolution of the XMS on *ATHENA* is only slightly worse with a value of 3 eV.

Transition Edge Sensor (TES) microcalorimeters, which are quite new in X-ray astronomy and provide an unprecedented energy resolution of a few eV. The range of scientific issues accessible with such an instrument is illustrated in Fig. 1.7. The graphs in Fig. 1.8 provide an overview of the performance of both instruments on *ATHENA* in comparison to current missions.

A closer description of the instrumentation of eROSITA and *ATHENA* is given in Chapters 4 and 5. In the following I provide an overview of the most prominent scientific objectives of both telescopes, since the work presented in this thesis is focused on these two missions. The overview is a summary of the more detailed description of the scientific targets of eROSITA, which is given by Merloni et al. (2011), and the objectives of *ATHENA*, which are described by Barcons et al. (2011b).

Apart from these two telescopes, there is also a big variety of smaller missions mainly developed by individual countries. The entity of all these instruments are the basis for the continuation of X-ray astronomy in the next decade.

1.3.1 Accretion Physics

As shown in Sec. 1.1, accretion of matter onto compact objects is a very powerful mechanism, which can give rise to the emission of X-rays as observed from Galactic as well as very distant sources such as AGN. The observation of the X-ray emission from these objects allows to

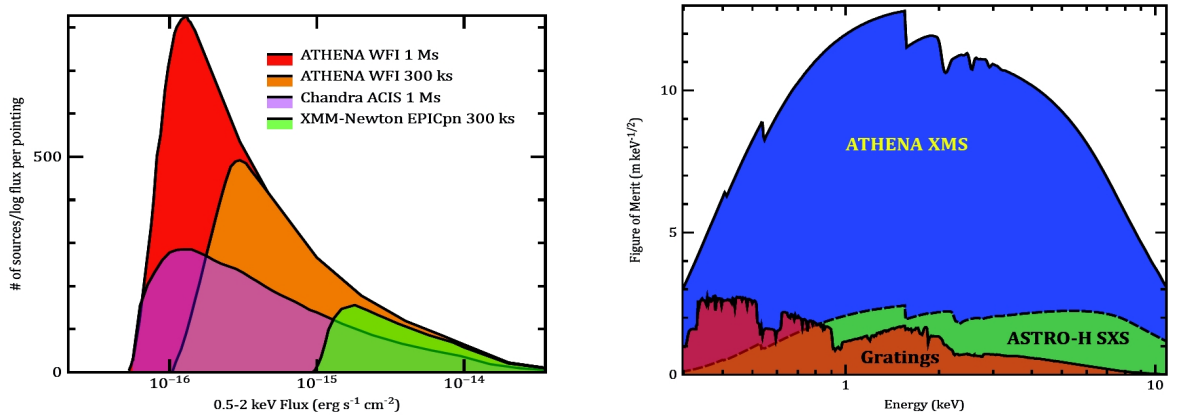

(a) Number of detected sources for observations with different instruments. The WFI on *ATHENA* has a large effective area and a wide FOV. For comparable exposure times the number of detected sources is therefore higher than for *XMM-Newton* or *Chandra*.

(b) Figure of merit for the XMS on *ATHENA* representing the square root of the fraction of the effective area of the instrument and the energy resolution. The XMS significantly outranges the spectral capabilities of *Astro-H* and the gratings on *XMM-Newton* and *Chandra*.

Figure 1.8: Performance of the two instruments on *ATHENA* (Barcons et al., 2011b).

investigate the conditions of strong gravity in their direct environment.

The data from the eRASS will result in the discovery of many new accretion-powered X-ray sources at Galactic and cosmological distances. Our own galaxy is populated by a large variety of different compact objects, such as White Dwarfs (WDs), NSs, or stellar-mass BHs (Merloni et al., 2011). They can be either located isolated in space or be part of X-ray binary systems, in which accretion of mass transferred from a companion star onto the compact object can power the emission of X-rays[2]. With eROSITA yet unknown X-ray binaries will be found in our galaxy and in its two companions, the Large Magellanic Cloud (LMC) and the Small Magellanic Cloud (SMC). In addition a large number of AGN will be discovered below the sensitivity limit of previous surveys.

Apart from stellar-mass compact objects and super-massive BHs there is also evidence for the existence of intermediate mass BHs, as shown by Farrell et al. (2009). These sources could be detected with eROSITA in close-by galaxies if they undergo some outburst such that follow-up observations with other instruments can be triggered.

The particular observing strategy of the eRASS with approximately one full-sky coverage each half year enables the monitoring of the X-ray sky in order to study time-variable objects and transient phenomena. Especially sources located close to one of the two survey poles will be monitored quite frequently, whereas objects at less convenient locations in the area around the survey equator will only be visible during a few subsequent short observations each half year. Examples for possible detections of transient phenomena are type I X-ray bursts (Galloway et al., 2008) or flares caused by the tidal disruption of a star in the vicinity of a super-massive BH (Frank, 1978) in a neighboring galaxy.

Black Holes

BHs are some of the most extreme systems in our Universe. According to the "no hair" theorem (Carter, 1971) they are characterized only by their mass and spin (Hanke, 2011). The concentration

[2]Catalogs of HMXBs and LMXBs, classified according to the mass of the companion star, are provided by Liu et al. (2006, 2007).

of mass in a BH gives rise to a strong gravitational field such that its environment is ideal to probe the laws of General Relativity. Their spin has a significant impact on the measurable observables and is subject to various investigations trying to confirm theoretical models about their formation history. BHs are found as Galactic objects in X-ray binaries and as super-massive objects in the cores of AGN and the centers of other galaxies such as our Milky Way (Wilms, 2006, 2008, and references therein). Also intermediate mass BHs are supposed to exist in galaxies (Farrell et al., 2009).

As mentioned in Sec. 1.1, the typical photon spectrum observed from the environment of a BH is strongly dominated by the accretion disk and its surrounding hot corona. Since the inner parts of the accretion disk can reach into an area very close to the event horizon, they are subject to very strong gravitational fields. Therefore the emission observed from these regions is influenced by effects of General Relativity. For instance, emission lines originating from the innermost part of the accretion disk are redshifted, as the observed photons had to escape from the deep gravitational potential in order to reach the observer.

Apart from the gravitational redshift, emission lines are strongly broadened due to the relativistic Doppler shift, because the emitting matter in the accretion disk is orbiting at high velocities around the central BH. Lines emerging from the receding side of the disk are redshifted, whereas the emission from the opposite approaching side is blueshifted. This broadening in combination with relativistic boosting effects and a dependence on the spin of the BH results in characteristic line profiles, as described, e.g., by Fabian et al. (1989), Laor (1991), and Dauser et al. (2010).

Some of the most prominent lines in the X-ray regime result from the Fe K-shell transitions at 6.4 keV. Measuring the exact shape of the line profiles and the maximum redshift provides information about the inner radius of the accretion disk, the typical velocities and temperatures of the material, and the spin of the BH. The required effective area in the energy range around 6 keV is provided by the *ATHENA* telescope. The necessary spectral resolution can be achieved in particular with the XMS. The high time resolution and throughput of the WFI enable the tracking of variations of the line profile caused by inhomogeneities in the accretion disk. Hints for such hot spots circulating around the BH have been seen in data from *XMM-Newton* (Iwasawa et al., 2004; de Marco et al., 2009). However, for a detailed analysis an instrument with a high throughput around 6 keV is required in order to allow for time-resolved spectroscopy with high spectral quality.

The WFI also allows to measure the frequency of Quasi-Periodic Oscillations (QPOs) caused by matter orbiting in the inner regions of the accretion disk around a BH under conditions described by General Relativity. In addition to the measurement of the shape of relativistically broadened Fe lines, these observations provide information about the mass, spin, and dimensions of the innermost region close to the event horizon. Another method to put constraints on the spin of a BH is the measurement of the thermal continuum emission of the innermost part of the accretion disk, since the spin determines the radius of the ISCO for the accreted matter and therefore the temperature profile of the disk. Spin measurements are especially interesting, because they can give hints about the formation of a BH (Berti & Volonteri, 2008) as well as its relation to the powering of relativistic jets emitting synchrotron radiation. Jets have been observed for Galactic BHs as well as for super-massive BHs in AGN (Rees et al., 1982; Wilms, 2008).

Another possibility to gain information about the geometry of the accretion disk and its corona is the measurement of time lags between the continuum emission from the corona and the spectrum reflected from the disk. This method of so-called "reverberation mapping" requires good time resolution and a large collecting area of the telescope. It allows distance measurements according to the light travel time. Observed time lags are of the order of 30 s, as discovered by

Fabian et al. (2009) in a Narrow Line Seyfert 1 galaxy. With their large effective area the WFI and the XMS on *ATHENA* collect sufficient photons for an appropriate analysis on these short time scales, even for weak sources, such as AGN.

Apart from the broad Fe lines emerging from the inner parts of an accretion disk, with *ATHENA* it is also possible to measure the width of narrow lines observed in the spectra of AGN (Nandra et al., 2007). Such observations allow to study the distribution of gas around the central part of an AGN including the Broad-Line Region and the Narrow-Line Region, which are key components of the unified model of AGN (Antonucci, 1993; Urry & Padovani, 1995).

Neutron Stars

The accretion physics of NSs are slightly different from those of BHs. Apart from general relativistic effects due to their strong gravitational fields, the surroundings of many NSs are influenced by the strong magnetic fields breaking up an accretion disk at a particular radius. Following the magnetic field lines towards the surface of the NS, the accreted matter forms two accretion columns. Measurements of the mass and the radius of NSs give hints to their equation of state and are therefore of great interest to probe theoretical models of Quantum ChromoDynamics (QCD).

The equation of state of a NS can be expressed as a relation between its mass and its radius (Lattimer & Prakash, 2001). So far various different models have been proposed by QCD (Lattimer & Prakash, 2007). However, the observational data do not allow to decide on a particular model due to large uncertainties for simultaneous measurements of mass and radius. *ATHENA* will provide the necessary accuracy to strongly constrain the mass-radius relationship by different independent measurement methods.

Similar to BHs, the emission lines of NSs are affected by the Doppler effect and General Relativity. *ATHENA* provides the count rate capabilities to measure broadened Fe line profiles in luminous NS X-ray binaries. Its high time resolution enables the detection of kHz QPOs (Barret et al., 2006), which are related to the orbital frequency of the innermost disk radius and therefore represent an upper limit for the radius of a NS. Its mass can be directly determined by combining the frequency of a kHz QPO with measurements of emission lines (Miller et al., 1998; Piraino et al., 2000; Cackett et al., 2008, 2010).

In addition to that, gravitationally redshifted absorption lines can be detected in the spectrum of type I X-ray bursts (Chang et al., 2005) providing information about the mass-radius relationship. Another method is the observation of thermal emission from transiently accreting NSs in their quiescent state. This technique allows to model the atmosphere of the NS.

1.3.2 Cosmic Feedback

Especially *ATHENA* allows to study the relation between super-massive BHs and their host galaxies. With current observatories evidence for various links has been found, but the underlying physical processes are not fully understood. Super-massive BHs can power strong jets and galactic winds ejecting gas from the galaxy. Similar to supernovae these phenomena are expected to have an influence on the star formation rate in the galaxy as well as metal enrichment. The XMS is an ideal instrument to measure the metal composition of gas outflows in the intergalactic medium by spatially resolved spectroscopy. Observations with *ATHENA* will therefore provide information about the formation and the evolution of galaxies and the super-massive BHs themselves.

AGN Feedback on Gas

It is assumed that interactions of AGN with the ICM are responsible for cavities, which can be observed in nearby galaxy clusters (Fabian et al., 2003). So far there are different models

proposing radiative interaction with gas and dust or the formation of winds and jets, which are not fully understood. The composition of relativistic outflows of ionized particles from AGN can be investigated with spatially resolved spectroscopy and compared to the measured radiative output. The observed radiative cooling of intra-cluster gas is lower than expected, which is explained by yet unknown powering mechanisms from supernovae and super-massive BHs. The physics of this heating process can be studied by high-precision spatially resolved spectroscopy of galaxy clusters.

These questions can be approached with *ATHENA* by detecting a large sample of galaxies containing super-massive BHs. Spatially resolved spectroscopy of the discovered sources with the XMS allows to determine bulk motions of gas inside the cluster with high precision based on line broadening.

AGN Evolution

AGN are visible in a large number of galaxies. Although they comprise a wide range of different observational source types characterized by a variety of spectral properties such as weak or strong radio emission, they can be explained by a unified physical model consisting of an accreting super-massive BH in the center of the galaxy surrounded by gas clouds, which are responsible for characteristic emission features, and an obscuring dust torus (Antonucci, 1993; Urry & Padovani, 1995). For instance, observations of such a system from the top or from the bottom provide direct insight onto the accretion disk and the emission region close to the BH, whereas for a view from the side most of the emitted radiation is absorbed by the obscuring dust torus.

According to current observations the distribution of AGN with respect to their number-flux relationship can be described by a power law (Hasinger et al., 2001; Brandt & Hasinger, 2005; Cappelluti et al., 2007; Comastri & Brusa, 2008; Cappelluti et al., 2009, and references therein). It is usually graphically illustrated in a double-logarithmic diagram and commonly called log$N$-log$S$ distribution. For eROSITA AGN will comprise the majority of the detected extra-Galactic X-ray sources (Predehl et al., 2010a; Merloni et al., 2011). During the eRASS $\sim$3 million AGN will be discovered with some of them located at very high redshifts (Predehl et al., 2006). This sample will provide accurate information about the evolution of the X-ray Luminosity Function (XLF) over different redshifts (Brandt & Hasinger, 2005; Aird et al., 2010), which is strongly related to the evolution of the Universe. In the eRASS even some of the very luminous AGN will be detected, although these sources are very rare. The telescope will map the space density of AGN and solve the question, whether its evolution over various redshifts exhibits a luminosity-dependency or not (Ueda et al., 2003; Silverman et al., 2008; Aird et al., 2010).

The entity of all AGN in the sky is thought to be responsible for the observed CXRB. This diffuse radiation in the X-ray regime has been discovered by Giacconi et al. (1962) during a rocket-based experiment. Similar to the commonly known Cosmic Microwave Background (CMB, Dicke et al., 1965), it can be uniformly observed from all (extra-Galactic) directions of the sky. After its discovery Marshall et al. (1980) proposed free-free emission in an optically thin plasma as an explanation for their broad band observation of the CXRB in the range of 3–50 keV with the *HEAO-1*. Using more advanced telescopes with better resolution such as *ROSAT* (Trümper, 1982, 1992), *Chandra* (Weisskopf et al., 2000), and *XMM-Newton* (Jansen et al., 2001) the low energy band of the CXRB radiation up to about 2 keV has almost completely been resolved to individual point-like sources (Giacconi et al., 2002; Worsley et al., 2005). Most of these sources are super-massive BHs in the centers of AGN (Hasinger et al., 2001; Brandt & Hasinger, 2005; Predehl et al., 2006, 2007). However, observations with current telescopes are mainly restricted to the low energy range. It is therefore assumed that there is an additional large number of yet undiscovered AGN, which are highly obscured at low energies due to absorption by thick gas and dust clouds in their host galaxies (Hasinger et al., 2001; Comastri & Brusa, 2008). The existence

of these sources is necessary to explain the overall observed spectrum of the CXRB emission with its maximum at about 30 keV (Gruber et al., 1999; Türler et al., 2010) by a composition of AGN spectra, which are affected by different absorption columns (Ueda et al., 2003; Gilli et al., 2007).

The high sensitivity of eROSITA in the energy range between 2 and 10 keV is suitable to investigate a large fraction of the yet unresolved CXRB in this intermediate energy regime. It will still be difficult to detect heavily obscured AGN, which are mainly visible at energies above 10 keV, but due to its high sensitivity and large survey area the telescope will still discover some of these interesting sources (Merloni et al., 2011).

The combination of the large effective area of *ATHENA* at higher energies and its good angular resolution enable observations in the energy range above 2 keV with a very low sensitivity limit for reasonable exposure times, without being affected by source confusion. *ATHENA* is therefore even better suited for the detection of the faint X-ray emission from obscured AGN than eROSITA. Thanks to the large FOV of the WFI, a large sample of such objects will be discovered even at very high redshifts in deep surveys covering a wide area. The measured data will provide information about the evolution of AGN and their super-massive BHs going back till the formation of the first galaxies. This analysis allows to probe synthesis models for the composition of the CXRB, as proposed by Gilli et al. (2007).

With *ATHENA* the relation between the mass of the central BH and characteristic properties of the host galaxies, such as the bulge mass, can be studied. Simultaneous observations at different wavelengths with optical and radio telescopes will offer additional information about redshifts, stellar and gas masses, and star formation rates. In comparison to *Chandra* the large effective area of *ATHENA* will enable detailed spectroscopy of AGN instead of only determining hardness ratios.

1.3.3 Large-scale Structure of the Universe

Galaxy clusters are some of the largest structures in the Universe. About 80–90 % of their mass is dark matter. Of the remaining baryonic mass about 85 % is contained as hot gas in the ICM emitting in the X-ray regime (Böhringer, 2011). Due to the high gas temperatures of the order of 10^7 K in the cores of galaxy clusters, they are very well detectable with X-ray telescopes. However, in order to observe the fainter outer parts an instrument with a high effective area such as *ATHENA* is required. The XMS provides the energy resolution necessary for the study of weak emission and absorption lines, and the large FOV of the WFI is suitable for the detection of large-scale structures.

Galaxy Cluster Formation

So far it is unknown how the energy released by accretion during the formation of the galaxy clusters has caused the heating of the ICM. Many of the observed clusters are not relaxed, but contain shock fronts (Markevitch & Vikhlinin, 2007), which is an evidence for ongoing interactions. Spatially resolved spectroscopy allows to study gas motion in the ICM in order to provide information about the responsible heating processes.

The chemical composition of the ICM is another key for the investigation of the formation mechanisms. The heavy elements are mainly formed by nuclear fusion in stars and are distributed in the ICM by supernova explosions. Abundance measurements in the ICM of clusters at different redshifts provide information about the feedback from the stellar population and its evolution over cosmic time.

Galaxy Cluster Cosmology

Due to their large-scale structure, galaxy clusters are common objectives for current cosmological investigations. The biggest fraction of the mass of galaxy clusters consists of Dark Matter, of which the exact physical nature is yet unknown (Böhringer, 2011). As large-scale objects galaxy clusters are tightly connected to the evolution of the Universe and the growth of structure. Their mass function and baryon fraction are relevant to probe different cosmological models.

Whereas its is quite challenging to identify galaxy clusters from optical observations based on the distribution of the individual galaxies, they are very well detectable in the X-ray regime due to the thermal emission of the ICM, a hot, highly ionized thermal plasma with a temperature of ten to hundred million degrees (Böhringer, 2008). In contrast to the visible galaxies, which contribute only about 2 % of the total mass of a galaxy cluster, the ICM makes up about 11 % of its mass (Böhringer, 2011). It is concentrated in the cores of the clusters according to the gravitational potential caused by the Dark Matter distribution. X-ray surveys covering a wide solid angle, such as eROSITA, are ideal to detect a large number of galaxy clusters by their emission in the soft X-ray regime.

The X-ray luminosity of a galaxy cluster is correlated with its gravitational mass M (Reiprich & Böhringer, 2002; Pratt et al., 2009). Therefore the observational data from a cluster census in the X-ray regime over different redshifts z can be used to determine the cluster mass function $f(M, z)$. The shape of the mass function and its evolution over time can be compared to the predictions of cosmological models based on assumptions about Dark Matter and Dark Energy (Borgani & Guzzo, 2001; Tinker et al., 2008; Vikhlinin et al., 2009a,b). Especially the high-mass end of the cluster mass function is very sensitive to the parameters of the regarded cosmological model (Böhringer, 2011). Besides the determination of the mass function, another method to probe cosmological models is the investigation of the spatial distribution of galaxy clusters and in particular the corresponding power spectrum.

For this kind of cosmological analysis a sufficiently large sample of galaxy clusters is required in order to limit the arising uncertainties. The key science driver for eROSITA is the detection of 50 000 to 100 000 galaxy clusters during the four years of the eRASS (Predehl et al., 2006, 2007, 2010a; Merloni et al., 2011). With the data provided by this large number of clusters it will be possible to constrain cosmological parameters such as Ω_m (matter density parameter), Ω_{DE} (Dark Energy density parameter), the equation of state of Dark Energy, and σ_8 (amplitude of the primordial power spectrum) with high accuracy (Predehl et al., 2010a; Böhringer, 2011; Merloni et al., 2011). The mirror quality of the eROSITA telescopes is essential for this goal, because a high angular resolution is required in order to be able to distinguish between galaxy clusters and point-like sources such as AGN even at redshifts of $z \approx 1$ (Predehl et al., 2006, 2007).

While eROSITA mainly focuses on the mere detection of the clusters and the mass determination according to their X-ray luminosity, *ATHENA* provides the sensitivity to measure various parameters such as the ICM temperature and gas mass even at high redshifts. In deep surveys *ATHENA* can detect galaxy clusters and groups up to redshifts of $z \sim 2.5$ and therefore allows to extend the mass function determined by eROSITA into this regime.

Missing Baryons

With current X-ray telescopes the observation of galaxy clusters is mainly limited to their hot and bright core regions. According to hydrodynamical cosmological simulations it is expected that a significant part of the yet undetected baryonic mass is contained in the so-called Warm and Hot Intergalactic Medium (WHIM) aligned in filaments connecting different galaxy clusters. These filaments form the so-called cosmic web following the Dark Matter distribution. The contained gas can be either detected by emission or by absorption lines against bright background objects

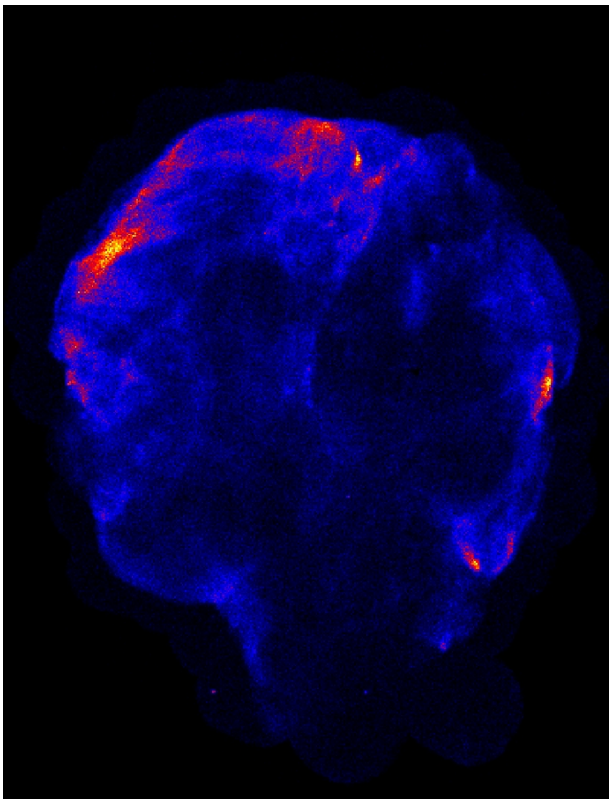

Figure 1.9: eROSITA view of the Cygnus loop supernova remnant. The image displays composite data from a simulation of a half-year period of the eRASS. Despite the limited FOV of the telescope with a diameter of 1 deg, the full extension of the supernova remnant with roughly 3 deg × 3 deg is visible because of the superposition of multiple survey revolutions to a composite image. The simulation has been performed with the software presented in this thesis and is based on an input model provided by M. Sasaki (priv. comm.).

such as Gamma-Ray Burst (GRB) afterglows. In order to be able to observe the WHIM, a very high sensitivity is required, as provided by *ATHENA*.

1.3.4 Our Galactic Environment

Apart from the detection and monitoring of Galactic X-ray binaries, which are listed above as key science drivers, eROSITA will also increase our knowledge about the X-ray emission from stars. Young stellar populations are a popular goal for X-ray surveys (Stelzer et al., 2005). In addition to the mere detection of new stellar X-ray sources, eROSITA will enable spectroscopy of stars with adequate energy resolution. Similar to the monitoring of compact objects, the eRASS will provide information about the time variability of many stellar sources.

In addition to the mostly point-like objects mentioned so far, galaxies contain lots of hot gas, the Inter-Stellar Medium (ISM), apparent in spatially extended thermal emission of X-rays. Due to its large FOV, eROSITA is a suitable instrument for the observation of supernova remnants, bubbles, and super-bubbles in the Milky Way, the SMC and the LMC (Merloni et al., 2011). Even objects larger than the FOV can be observed in composite images obtained from the superposition of multiple survey revolutions, as shown in Fig. 1.9. The telescope can be used to study the so-called Galactic Ridge X-ray Emission (GRXE), which is aligned along the Galactic bulge and disk. The origin of the GRXE is still discussed. For instance, Revnivtsev et al. (2006) assume that most of the GRXE arises from cataclysmic variables, whereas (Ebisawa et al., 2008) support the idea of a collisional ionization equilibrium plasma. Observational data from eROSITA with its high sensitivity will hopefully bring more light into this question.

Even in our direct neighborhood, within the Solar system, eROSITA can detect X-ray emission from planets and comets, which originates, e.g., from charge exchange processes (Dennerl, 2010).

1.4 Outline of this Thesis

The development of a new X-ray telescope is a technically challenging and expensive process. In order to achieve a major advance in the investigation of scientific questions, it is often necessary to implement new detector types promising more powerful capabilities than current instrumentation. However, these devices also must be suitable for the operation on a spacecraft, i.e., they have to cope with strongly limited resources and the exposure to extreme thermal and radiative conditions. In addition to these technical issues, the observational capabilities of new instruments have to be analyzed in order predict the achieved improvement in comparison to current instruments. Not all of the investigations necessary to ensure these demanding requirements can be performed with real hardware. Experiments in a laboratory are expensive and the manufacturing of hardware often requires a lot of time.

It is therefore essential to perform computer simulations of the developed devices, because software is much more flexible than hardware and can be adjusted with much lower effort. Although, of course, simulated data cannot fully replace calibration measurements, for many purposes they can provide sufficiently accurate information. There are even some instrumental processes that can be much better understood with simulations than with experiments because the setup of a simulation is well defined and arbitrarily repeatable in contrast to an experiment. With the power of current computer systems many simulations of a particular setup can be run in parallel in order to minimize statistical uncertainties, whereas it might be impossible with an experiment to obtain the same amount of data.

Due to these reasons, simulations play a key role in the technical development of new X-ray telescopes and the advance of scientific capabilities. In addition to that, they are also useful for the understanding of already existing instruments and can help scientists to reproduce particular effects in their observations. Simulations can provide an estimate of the observed data even before the launch of a mission such that the scientific analysis process can be prepared and optimized in order to guarantee a quick processing of the later measurements. It is therefore important to provide simulations for future as well as for existing telescopes based on realistic models of the implemented instrumentation. In this thesis I present a generic simulation software package, which I have developed during the last years at the Dr. Remeis-Sternwarte Bamberg. In contrast to most existing simulation software in the field, the implemented models are very flexible and can be easily adjusted to different observation scenarios and telescopes.

As an introduction I present the most common technologies used for the fabrication of current and future X-ray telescopes in Chapter 2, including an overview of the specific features related to the different detector types. In Chapter 3 I introduce the simulation software package, which I have developed and used for the simulations presented in this thesis. I explain the implementation of the various features and the interaction between the different components of the software package. In Chapter 4 the German X-ray telescope eROSITA is introduced and I present several simulations performed in order to investigate the properties of this instrument. In Chapter 5 the mission concepts of *IXO* and its successor *ATHENA* are presented, followed by simulation results for some of their instruments. A summary of the thesis and an outlook to additional projects is given in Chapter 6. In the appendix I explain the setup and the usage of the simulation software and the SIMulation inPUT (SIMPUT) file format required for the definition of input data.

CHAPTER 2

X-RAY TELESCOPES

2.1 Overview

In order to avoid the limitation imposed by the absorption of X-rays by the Earth's atmosphere, X-ray telescopes are usually mounted on satellites or spacecraft and operated in space. There is a big variety of different technologies implemented or planned in past, current, and future missions. Depending on the particular instrument design, an X-ray telescope can provide imaging, spectroscopic, and timing capabilities. There are two main categories, the collimating and the imaging telescopes, which differ with respect to their photon collection method. Whereas the first instruments in the history of X-ray astronomy relied on collimating techniques and large detector cross sections, most modern telescopes for the energy range up to 10 keV are designed as imaging instruments. In comparison to collimating instruments, imaging telescopes provide a higher sensitivity due to the focusing of photons from the target of the observation and a lower background fraction (Staubert & Trümper, 2008).

This chapter provides a short overview of some of the most commonly used optics and detector types for current and next generation imaging X-ray telescopes. Of course, this is not a comprehensive discussion, but introduces the technologies implemented in the instruments that are analyzed in the context of this work. The focus is put on imaging telescopes, although simple collimating instruments as well as coded mask telescopes (Fenimore & Cannon, 1978) with a partly blocking aperture are still in use, especially for the high energy range above 10 keV.

An imaging instrument basically consists of an optical system responsible for the focusing of the incident X-rays, and a detector converting the photons into electronic signals. In contrast to optical light, the energy of X-ray photons is usually large enough to detect single photons. However, suitable instrument technologies must provide a combination of high sensitivity and low background.

2.2 Optics

The development of precisely shaped optics is a key requirement for an imaging X-ray telescope. In this section I provide an overview of the most relevant characteristics and the most common types of X-ray optics.

2.2.1 Characteristics

The imaging of X-rays is problematic, since their index of refraction is slightly less than unity in most materials. Therefore conventional techniques developed for optical telescopes are not applicable. Instead one has to rely on the total reflection of X-ray photons incident on a metal

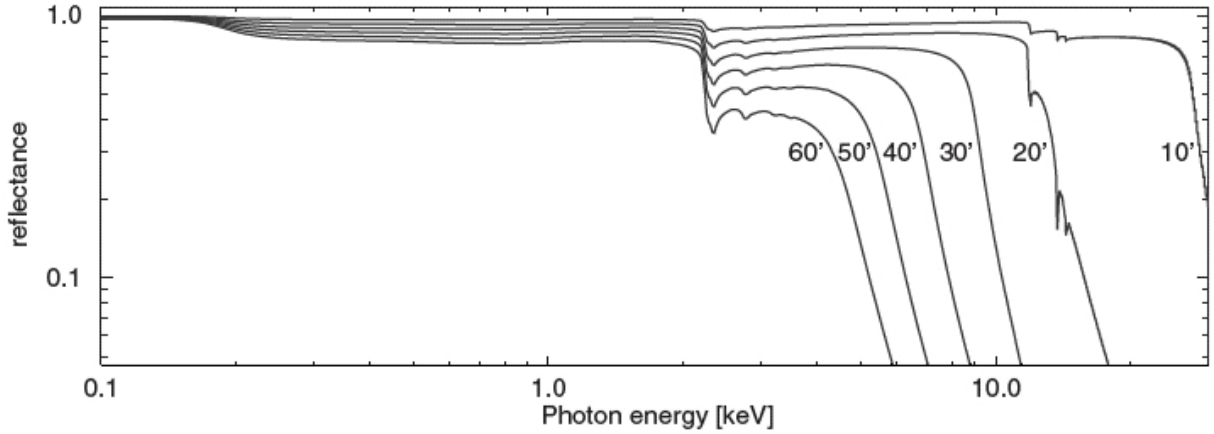

Figure 2.1: Reflectivity of a gold surface as a function of the photon energy for different angles of incidence given in arcmin (Friedrich, 2008). The sudden decrease of reflectivity at energies around 2.2 keV corresponds to the absorption edges of gold (Fraser et al., 1994). Photons above this threshold can excite electrons from the M-shell of gold atoms. Due to this possible interaction, they have a higher absorption cross section than photons below the threshold and the reflectivity therefore decreases.

surface of a heavy high-Z element under a grazing angle (Aschenbach, 1985, 2009; Friedrich, 2008). Typical reflection surfaces are made from nickel, gold, iridium, or some multilayer coatings. In Fig. 2.1 the reflectivity of gold as a function of the photon energy is displayed for different angles of incidence.

For a target at an infinite distance Abbe's sine condition for the principal surface of an optical system can be formulated as

$$\frac{h}{\sin \rho} = f \tag{2.1}$$

where h denotes the distance of the target from the optical axis, ρ the angle between the diffracted beam and the optical axis, and f the focal length of the system (Friedrich, 2008). The condition defined by Eq. (2.1) is fulfilled by a sphere with a radius f. However, due to the requirement of grazing incidence, a spherical reflection surface is not applicable for the imaging of X-rays.

Several alternative geometries have been proposed by Kirkpatrick & Baez (1948) and Wolter (1952a,b) to construct imaging X-ray optics fulfilling Abbe's condition based on the reflection of photons on multiple surfaces. Most of the current imaging X-ray telescopes are designed according to the Wolter type I, which consists of a combination of a paraboloidal and a hyperboloidal surface, as shown in Fig. 2.2 (Wolter, 1952a; Aschenbach, 1981, 1985, 2009; Giacconi, 2009). The presented technique is based on the double-reflection of photons on several nested paraboloidal and hyperboloidal mirror shells. However, it is also possible that photons from outside the FOV reach the detector plane by single-reflection on only one of the two mirror surfaces. These photons corrupt the image quality of the optical system. They can mostly be avoided by collimating baffles in front of the mirror shells.

Apart from the size of its FOV, an X-ray mirror system is usually characterized by its effective area, its vignetting function, and its Point Spread Function (PSF). The effective area translates into the ability of collecting photons, which is important, e.g., for observations of faint sources. The PSF represents the imaging quality of the telescope and accounts for image aberrations. The vignetting function is mainly relevant for telescopes developed for wide-field surveys, as it describes the decrease of the effective area for off-axis targets.

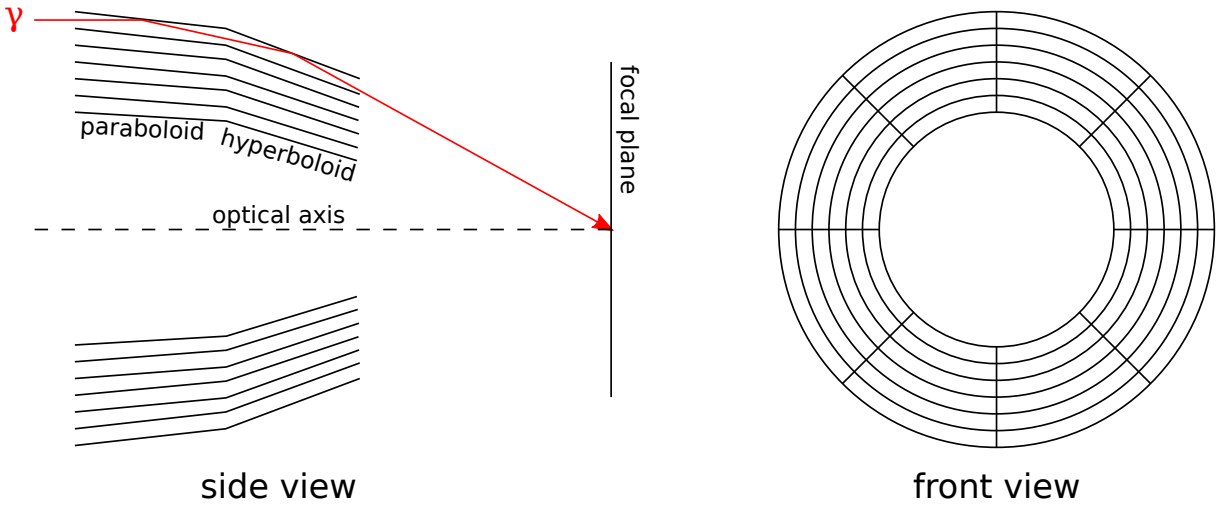

Figure 2.2: Schematic drawing of a Wolter type I X-ray telescope (Wolter, 1952a). On the left-hand side the path of an incident photon through the mirror system is shown. Via double-reflection under grazing angles on the paraboloidal and the hyperboloidal surface photons from a parallel incident beam are focused to a single spot in the focal plane. The sketch on the right-hand side displays the front view of the system. Several mirror shells are nested inside of each other, aligned by a spider wheel, in order to obtain a sufficiently large projected mirror surface despite of the grazing angle condition.

Effective Area

For the collection of photons the projected area as seen from the front of the telescope has to be considered. Due to the condition of grazing angle incidence, this quantity is quite small in comparison to the total reflecting surface. In order to obtain a significant value, usually many mirror shells are nested inside of each other and aligned in a spider wheel, as shown in Fig. 2.2 (Predehl et al., 2007; Friedrich et al., 2008; Friedrich, 2008; Burwitz et al., 2011).

The product of the projected area with the reflectivity of the mirrors is denoted as the effective area of the telescope. Since for increasing photon energies the critical angle of total reflection decreases according to Fig. 2.1 (Friedrich, 2008), the outer shells of telescopes with a short focal length hardly contribute to the effective area at high photon energies. Therefore the construction of telescopes suitable for the regime around 10 keV requires long focal length.

For astronomical X-ray instruments the effective area of the mirrors is often combined with instrumental effects, such as the filling factor (accounting for gaps in the detector surface) and the quantum efficiency of the respective detector[1]. The product of the effective area provided by the optics with this instrumental efficiency is commonly stored in a so-called Ancillary Response File (ARF, George et al., 1998, 2007)[2]. In Fig. 2.3 the ARFs of eROSITA and of the two instruments on *ATHENA* are displayed. Especially for the detection of very faint sources and in order to guarantee a high photon throughput for time-resolved spectroscopy a large effective area is an essential requirement for an X-ray mission.

Vignetting Function

The vignetting function represents the fraction of incident photons reaching the focal plane as a function of the off-axis angle, the azimuthal angle, and the photon energy. Especially telescopes

[1]The quantum efficiency is defined as the probability that a photon hitting the surface of the detector is really detected (Edgar, 2011).

[2]For some X-ray instruments the ARF only contains the effective area of the mirrors without detector contributions such as the quantum efficiency.

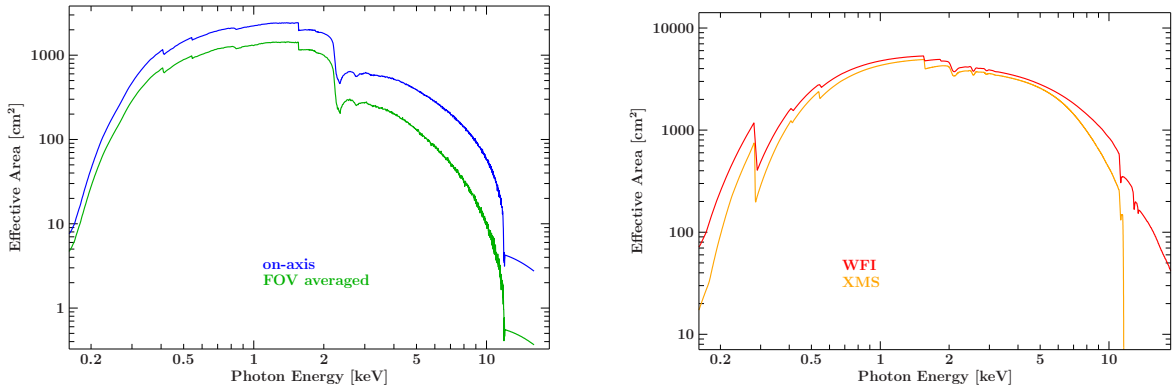

(a) eROSITA **(b)** *ATHENA*

Figure 2.3: The ARF of an X-ray instrument usually is the product of the effective area provided by the telescope and the detector efficiency. **(a)**: ARF of eROSITA. The blue curve is valid for an observation with the target source on the optical axis. The green curve is the average value over the entire FOV (for off-axis angles $\theta > 0$ the effective area is lower than on-axis). **(b)**: ARFs of the two instruments on *ATHENA*. Both instruments together provide an unprecedented effective area of $\sim 1\,\mathrm{m}^2$ at 1 keV.

performing a wide-angle survey, such as eROSITA, require adequate vignetting properties. Ideally the vignetting function has a value of 1 over the entire FOV. However, at high off-axis angles the vignetting function of Wolter type I telescopes decreases (Friedrich et al., 2008). This decrease is, e.g., indicated by the difference between the on-axis and the FOV averaged ARF in Fig. 2.3. It is only partly caused by the lower projected cross section of the telescope aperture, which is proportional to the cosine of the off-axis angle. This effect is negligible for the typically small off-axis angles (Mühlegger, 2010). The main reasons for the loss of photons are the lower fraction of reflecting area fulfilling the condition of a grazing angle of incidence and occultation effects by the tightly nested mirror shells (or pores for Silicon Pore Optics) and potential baffles. The vignetting functions of the eROSITA mirrors and the *ATHENA* Silicon Pore Optics (SPO) are shown in Fig. 2.4.

Point Spread Function

The imaging capabilities of an X-ray telescope are mostly described by its Point Spread Function (PSF). According to its definition it represents the image of an observed on-axis, point-like source on the detector, which is normally located in the focal plane.

In general the spatial intensity distribution of the incident radiation from an observed source within the FOV can be described as the source function $i(\theta, \varphi)$, with the off-axis angle θ and the azimuthal angle φ, which are indicated in Fig. 2.5. Both angles are directly related to the 2-dimensional Cartesian coordinates x and y in the focal plane corresponding to the image position assuming an ideal optical system:

$$\begin{aligned} x &= f \cdot \tan(\theta) \cos(\varphi) \\ y &= f \cdot \tan(\theta) \sin(\varphi) \end{aligned} \tag{2.2}$$

where f denotes the focal length of the telescope. According to Eq. (2.2) the function $i(\theta, \varphi)$ can also be expressed in terms of x and y:

$$i(\theta, \varphi) \rightarrow I(x, y) = i\left(\tan^{-1}\left(\sqrt{\frac{x^2 + y^2}{f^2}}\right), \tan^{-1}\left(\frac{y}{x}\right)\right) \tag{2.3}$$

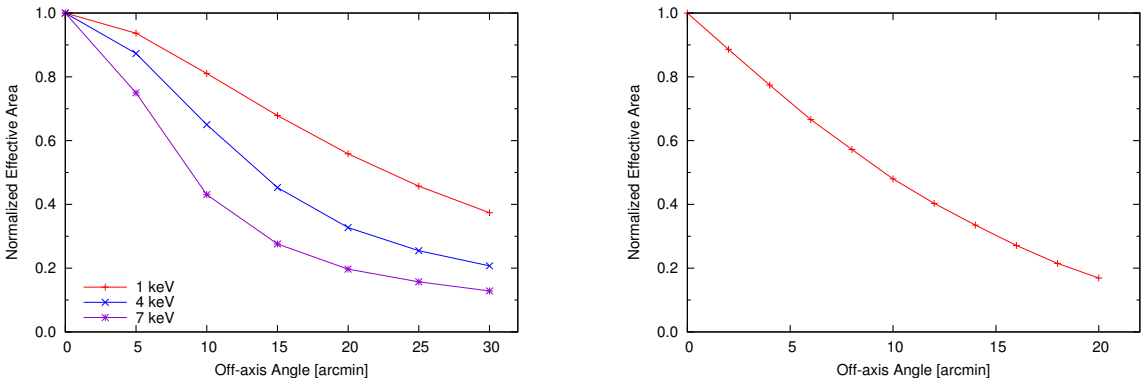

(a) eROSITA **(b)** *ATHENA*

Figure 2.4: The vignetting function of an instrument describes the dependence of the effective area on the off-axis angle and the photon energy. For large values of both quantities it can decrease significantly. **(a)**: The eROSITA vignetting function for different photon energies. The plot is based on ray-tracing data provided by P. Friedrich (priv. comm.). The ray-tracing simulation does not take into account the baffles preventing single-reflected photons. Therefore the obtained vignetting function has larger values at large off-axis angles than the one presented by Friedrich et al. (2008). With the baffles the decrease towards the edge of the FOV would be more significant. **(b)**: The vignetting function of the *ATHENA* SPO.

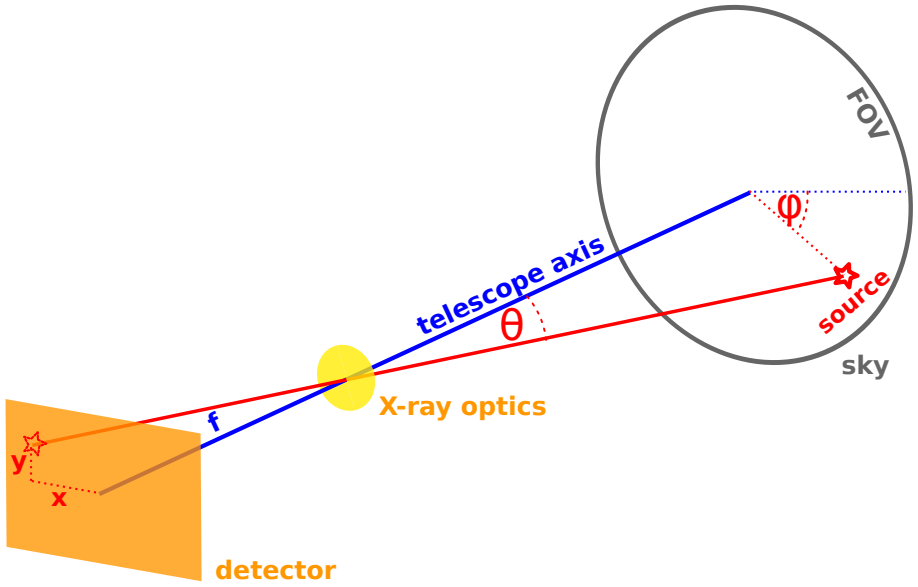

Figure 2.5: The position of an X-ray source within the FOV can be described by the off-axis angle θ and the azimuthal angle φ. The corresponding image position on the detector assuming an ideal optical system is denoted by the Cartesian coordinates x and y.

Note that the function $\tan^{-1}(y/x)$ constituting the second argument of $i(\theta, \varphi)$ in Eq. (2.3) is assumed to deliever angles $\varphi \in [0, 360)\,\mathrm{deg}$, instead of $\varphi \in [0, 180)\,\mathrm{deg}$ according to the usual definition of $\tan^{-1}()$. This corresponds to the `atan2()` function common in computer applications.

For a point-like source at the position (x_0, y_0) inside of the FOV, corresponding to a particular (θ_0, φ_0), the source function $I(x, y)$ can be written as

$$I(x, y) = \delta_{\mathrm{D}}(x - x_0)\delta_{\mathrm{D}}(y - y_0) \tag{2.4}$$

with the Dirac δ-function

$$\delta_{\mathrm{D}}(x) = \begin{cases} \infty & , \ x = 0 \\ 0 & , \ \text{elsewhere} \end{cases} \tag{2.5}$$

$$\int_{-\infty}^{\infty} \delta_{\mathrm{D}}(x)\,\mathrm{d}x = 1 \tag{2.6}$$

The intensity distribution on the detector $D(x', y')$ can be calculated by convolving the source function $I(x, y)$ with the PSF[3] (Davis, 2001b; Arnaud & Smith, 2011):

$$D(x', y') = \int_{-\infty}^{\infty}\int_{-\infty}^{\infty} I(x, y) \cdot \mathrm{PSF}(x' - x, y' - y)\,\mathrm{d}x\,\mathrm{d}y \tag{2.8}$$

The PSF has to be normalized, because any inefficiencies in the imaging process are contained in the effective area and the vignetting function:

$$\int_{-\infty}^{\infty}\int_{-\infty}^{\infty} \mathrm{PSF}(x, y)\,\mathrm{d}x\,\mathrm{d}y = 1 \tag{2.9}$$

For the case of a point-like source according to Eq. (2.4) the detector image is obtained as

$$D(x', y') = \int_{-\infty}^{\infty}\int_{-\infty}^{\infty} \delta_{\mathrm{D}}(x - x_0)\delta_{\mathrm{D}}(y - y_0) \cdot \mathrm{PSF}(x' - x, y' - y)\,\mathrm{d}x\,\mathrm{d}y = \mathrm{PSF}(x' - x_0, y' - y_0) \tag{2.10}$$

I.e., according the definition of the PSF, the image of a point-like source at an arbitrary location in the FOV is given by the PSF centered around the corresponding position on the detector. For an extended source the source function $I(x, y)$ is different than in Eq. (2.4), but the image can still be determined by convolution of $I(x, y)$ with the PSF according to Eq. (2.8).[4]

In the previous calculations a constant shape of the PSF has been assumed for source positions inside the FOV. In reality the particular shape of the Wolter type I X-ray mirrors has a significant impact on the shape of the PSF for different off-axis angles. Different conditions for the grazing angle reflection at different photon energies cause an energy-dependence, and due to asymmetries of the mirrors and the mounting there is an azimuthal variation. Therefore in general the PSF has to be written as

$$\mathrm{PSF}(x', y', x, y, E) \tag{2.11}$$

[3] For simplicity vignetting effects are neglected here, i.e., the vignetting function is defined as unity. If vignetting effects are included, Eq. (2.8) contains an extra term:

$$D(x', y') = \int_{-\infty}^{\infty}\int_{-\infty}^{\infty} I(x, y) \cdot \mathrm{vignetting}(x, y) \cdot \mathrm{PSF}(x' - x, y' - y)\,\mathrm{d}x\,\mathrm{d}y \tag{2.7}$$

[4] In order to determine the image of a source on the detector according to Eq. (2.8), it is convenient to have the source function and the PSF as functions of the focal plane coordinates (x, y): $I(x, y)$ and $\mathrm{PSF}(x, y)$. However, sometimes the source function is defined via the FOV coordinates instead: $i(\theta, \varphi)$. In this case the calculation of the integral in Eq. (2.4) can also be performed on the FOV coordinates, but it has to take into account the Jacobian determinant of the coordinate transformation given by Eq. (2.2):

$$D(x', y') = \int_{0}^{\theta_{\mathrm{FOV}}/2}\int_{0}^{2\pi} i(\theta, \varphi) \cdot \mathrm{PSF}\left(x' - f \cdot \tan(\theta)\cos(\varphi), y' - f \cdot \tan(\theta)\sin(\varphi)\right) \cdot \frac{f^2\,\tan\theta}{\cos^2\theta}\,\mathrm{d}\varphi\,\mathrm{d}\theta$$

where θ_{FOV} is the angular diameter of the FOV.

with x' and y' the image coordinates on the detector, as in the previous formulae. The values x and y correspond to the off-axis angle θ and the azimuthal angle φ of the source position according to Eq. (2.2). The energy of the photon is given by E. Introducing an energy-dependent source function $I(x, y, E)\,\mathrm{d}E$, which denotes the source intensity in an infinitesimal energy range $\mathrm{d}E$, the detector image in an energy band from E_1 to E_2 can be obtained as

$$D_{E_1,E_2}(x', y') = \int_{-\infty}^{\infty}\int_{-\infty}^{\infty}\int_{E_1}^{E_2} I(x, y, E) \cdot \mathrm{PSF}(x' - x, y' - y, x, y, E)\,\mathrm{d}E\,\mathrm{d}x\,\mathrm{d}y \tag{2.12}$$

In X-ray astronomy one usually deals with individual photons instead of intensity distributions as defined by the continuous source function $I(x, y, E)$. Especially in the context of simulations it is therefore convenient to regard $\mathrm{PSF}(x' - x, y' - y, \theta, \varphi, E)$ as the probability density for the impact position (x', y') of an individual photon on the detector.

For telescopes such as *XMM-Newton*, *Chandra*, or *ATHENA*, which are mainly designed for pointed observations, the observed target usually resides in the center of the FOV. In this region the deviations of the PSF from a rotationally symmetric shape can be neglected for many applications. The assumption of a 2-dimensional Gaussian or a rotationally symmetric King profile[5] are common approximations for the PSF if no accurate model is required. However, for a mission such as eROSITA, which is scanning over the sky in a slew mode, the dependence on the off-axis angle has to be taken into account. As shown in Fig. 2.6, the shape of the PSF at large off-axis angles is quite complicated and can only be approximated with sophisticated analytical models.

Angular Resolution The PSF of a particular telescope is usually characterized by its Half Energy Width (HEW) or Half Power Diameter (HPD), which is the diameter d_{HEW} of a circle containing 50 % of the incident radiation in the focal plane:

$$\int_0^{d_{\mathrm{HEW}}/2}\int_0^{2\pi} \mathrm{PSF}\,(r, \rho)\; r\,\mathrm{d}\rho\,\mathrm{d}r = \frac{1}{2} \tag{2.13}$$

where r and ρ are polar coordinates in the detector plane. The point $(r = 0, \rho = 0)$ corresponds to the center of the PSF.

Another common quantity for the characterization of the resolution of a telescope is the Full Width at Half Maximum (FWHM). It is defined as twice the radius at which the PSF has decreased to the half of its peak value in the center[6]:

$$\mathrm{PSF}\left(r = \frac{d_{\mathrm{FWHM}}}{2}, \rho\right) = \frac{1}{2} \cdot \mathrm{PSF}\,(0, 0) \tag{2.14}$$

As previously mentioned, in simple models the PSF is often approximated by a 2-dimensional Gaussian:

$$\mathrm{PSF}\,(r, \rho) = \mathrm{PSF}\,(r) = \frac{1}{2\pi\sigma^2} \cdot \mathrm{e}^{-\frac{r^2}{2\sigma^2}} \tag{2.15}$$

For this particular case the HEW and the FWHM coincide:

$$\frac{1}{2} \overset{!}{=} \int_0^{d_{\mathrm{HEW}}/2}\int_0^{2\pi} \mathrm{PSF}\,(r, \rho)\; r\,\mathrm{d}\rho\,\mathrm{d}r = \int_0^{d_{\mathrm{HEW}}/2} \frac{r}{\sigma^2} \cdot \mathrm{e}^{-\frac{r^2}{2\sigma^2}}\,\mathrm{d}r = 1 - \mathrm{e}^{-\frac{(d_{\mathrm{HEW}}/2)^2}{2\sigma^2}}$$
$$\Rightarrow d_{\mathrm{HEW}} = \sigma \cdot 2\sqrt{2\ln 2} \tag{2.16}$$

[5] $\mathrm{PSF}(r) \sim \left(1 + \left(\frac{r}{r_c}\right)^2\right)^{-\beta}$ with the core radius r_c (King, 1962)

[6] Note that in general the shape of the PSF can be asymmetric such that the FWHM can have different values for different directions.

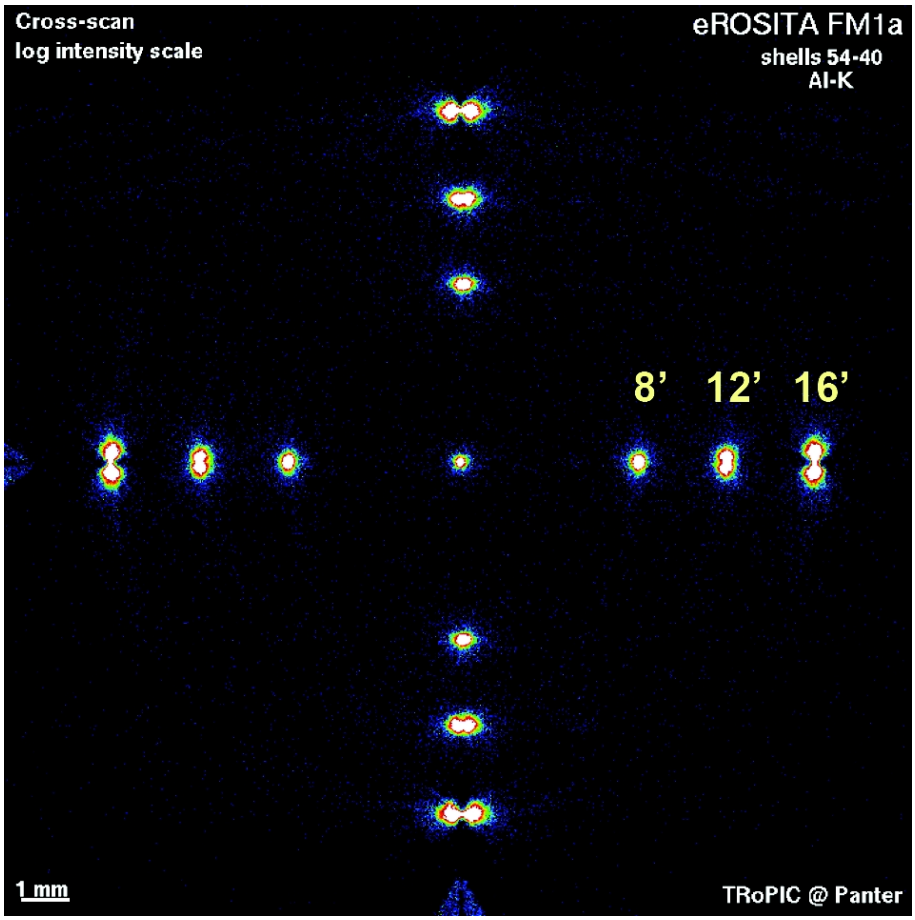

Figure 2.6: PSF of the mirror shells 54–40 of one eROSITA telescope according to measurements at the PANTER X-ray test facility of the MPE (Friedrich, 2011). For a source on the optical axis the PSF is quite symmetric. However, for larger off-axis angles its shape becomes more complicated (“butterfly”).

and

$$\frac{1}{2} \stackrel{!}{=} \frac{\mathrm{PSF}\left(d_{\mathrm{FWHM}}/2\right)}{\mathrm{PSF}\left(0\right)} = \mathrm{e}^{-\frac{\left(d_{\mathrm{FWHM}}/2\right)^2}{2\sigma^2}} \quad \Rightarrow d_{\mathrm{FWHM}} = \sigma \cdot 2\sqrt{2\ln 2} \tag{2.17}$$

However, in general the HEW and the FWHM have different values. For practical reasons both quantities are often expressed in terms of the opening angle α of the corresponding light cone:

$$\tan\frac{\alpha_{\mathrm{HEW}}}{2} = \frac{d_{\mathrm{HEW}}}{2 \cdot f} \tag{2.18}$$

$$\tan\frac{\alpha_{\mathrm{FWHM}}}{2} = \frac{d_{\mathrm{FWHM}}}{2 \cdot f} \tag{2.19}$$

The specification of α_{HEW} or α_{FWHM} allows a quick comparison of the spatial resolution of different telescopes independently of the focal length f.

2.2.2 Mirror Manufacturing

For the manufacturing of Wolter type I optics different technologies are used (Friedrich, 2008). Each technology has its advantages and disadvantages. For a particular mission concept the most appropriate option has to be selected. Usually the relevant criteria are the specific mass of the mirrors and the angular resolution. The specific mass, i.e., the mass per unit effective area,

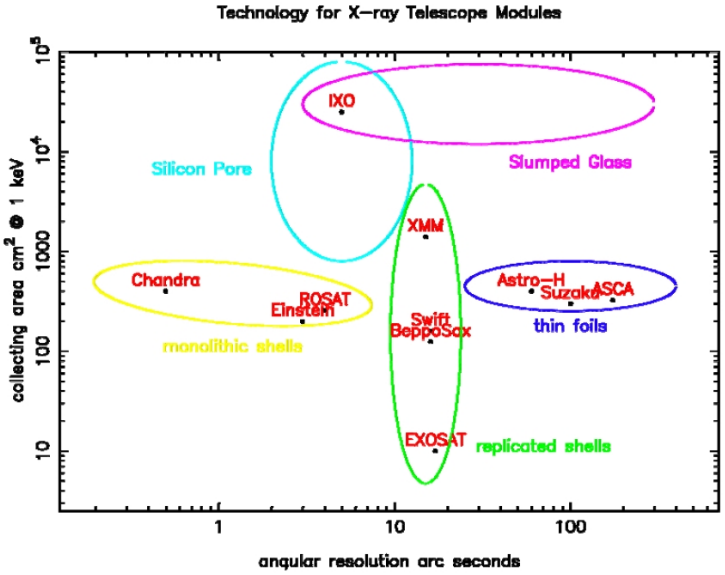

Figure 2.7: Telescope performance for different mirror fabrication technologies (Willingale, 2011b). The assembly of a particular telescope is usually a trade-off between the maximum achievable effective area, which is mainly determined by the specific mass of the mirrors, and the angular resolution (Schwartz, 2011).

determines the maximum achievable effective area on a spacecraft with limited mass budget. An overview of these two performance parameters is provided in Fig. 2.7 for different X-ray telescopes.

Super-Polished Glass

The mirrors of the *Chandra* telescope are made from iridium-coated Zerodur glass providing a high angular resolution of about 0.5 arcsec (Weisskopf et al., 2000, 2002). Due to their high specific mass, the telescope is assembled by only four mirror shells with the consequence of a low effective area.

Electroforming

The mirror shells of the X-ray telescopes on *XMM-Newton* (Gondoin et al., 1994), *ABRIXAS* (Predehl, 1999), and eROSITA (Friedrich et al., 2008) are produced by a nickel electroforming technique from super-polished mandrels (Citterio et al., 1988). The reflective surface is coated with gold. Replicated nickel shell mirrors provide angular resolutions with a HEW of about 15 arcsec, but are still quite heavy in comparison to the alternatives presented in the following.

Thin Foils

The X-ray optics of the Broad Band X-Ray Telescope (BBXRT), the *Advanced Satellite for Cosmology and Astrophysics* (*ASCA*, Serlemitsos & Soong, 1996), and *Suzaku* (Kunieda et al., 2001; Serlemitsos et al., 2007) are based on the light-weight thin-foil technique using thin aluminum sheets with a few 100 μm thickness as mirror substrate, coated with a reflection layer of gold or platinum. These mirrors have quite low weight per effective area, but they are usually produced under a conical assumption and provide low angular resolution with a HEW of the order of a few arcmin.

Silicon Pore Optics

One of the key requirements for the next generation of X-ray missions such as *ATHENA* and its predecessor concepts *IXO*, *XEUS*, and *Constellation-X* is a large effective area. Therefore two alternative techniques have been investigated for these telescopes. One possible option to

manufacture mirrors providing an effective area of the order of $3\,\mathrm{m}^2$ are Silicon Pore Optics (SPO). They are based on the focusing of X-rays through coated microchannels in stacked Si wafers (Beijersbergen et al., 2004a,b; Collon et al., 2006a,b). Both *ATHENA* mirror systems will consist of SPO. The angular resolution of such a telescope is mainly determined by the alignment of the wafer petals to a large mirror assembly (Collon et al., 2007, 2008, 2009, 2010) and by the selected approximation of the Wolter type I shape (Willingale & Spaan, 2010). The telescopes of *ATHENA* will achieve a HEW of 10 arcsec or better. In addition to their low specific mass, a big advantage of SPO are their relatively low costs due to the processing of commercially available Si wavers manufactured in mass production by the semiconductor industries (Wille et al., 2011).

Slumped Glass

The other option with a low specific mass taken into account, e.g., for the *IXO* mirror system are slumped glass sheets (Friedrich et al., 2005a, 2006; Zhang et al., 2005). They are produced by heating flat glass panes to high temperatures, until they adapt the shape of a suitable mirror mold. In order to gain an appropriate reflectivity at X-ray energies, the glass is coated with a high-Z material such as gold or nickel.

2.3 Detectors

Apart from the focusing of the collected X-ray photons by the optical system, an appropriate detector has to be implemented providing the measurement capabilities that are required by the respective scientific objectives of an instrument. This section contains a summary of some common detector technologies and an introduction to the most important properties related to X-ray measurements, which are relevant for the investigations presented in Chapters 4 and 5. A comprehensive overview of these topics is provided by various textbooks, such as Lutz (1999) or Knoll (2010).

2.3.1 Technology

In optical astronomy usually many photons have to be collected in a typical device in order to obtain a reasonable signal. In X-ray astronomy photon energies are high enough and photon rates are usually low enough to detect individual photons (Lumb et al., 1991; Kraft et al., 1995). With detectors providing spatial resolution it is therefore possible to perform imaging and spectroscopy at the same time. If the detector in addition has a suitable time resolution, light curves with time-resolved photon number counts can be obtained. Some of the available instruments provide all these three capabilities of good spatial, spectroscopic, and time resolution, whereas others focus on a particular one of these properties.

In order to be able to detect X-rays and to measure their energy, the photons have to interact with some absorbing material. Apart from the usually neglected coherent scattering, the three main types of interaction between photons and matter producing a measurable signal are photoelectric absorption, Compton scattering, and pair production (Knoll, 2010, Chapter 2; Lauf, 2011). Pair production is only possible for photon energies $E_\mathrm{ph} \geq 2m_\mathrm{e}c^2$, with the rest mass of the electron m_e and the speed of light c, and for most detector materials Compton scattering is mainly relevant in the regime between a few 100 keV and a few MeV (Knoll, 2010). Therefore the dominant interaction mechanism for X-ray detection in the energy range below 50 keV is photoelectric absorption (Martin, 2009). The excitation of an electron by the absorption of a photon results in a cascade of subsequent processes, such as the emission of fluorescence photons or Auger electrons, which can excite further electrons (Popp, 2000). The electrons can be detected, e.g., in proportional counters. In scintillation counters the light produced by

fluorescent emission from excited atoms can be measured (Knoll, 2010, Chapter 10). However, this technique will not be described here, since it is not relevant for the regarded detector types. In a semiconductor detector the electron-hole pairs generated by the absorption process are separated by an applied electric field in order to avoid recombinations, and the corresponding electric signal can be measured. In calorimeter devices the energy of the absorbed photon completely thermalizes by the excitation of phonons resulting in a temperature increase of the absorbing material. Both the electric as well as the thermal detection mechanism are used for detectors in X-ray astronomy and are discussed in the following.

The technology of Si-based detectors such as Charge-Coupled Devices (CCDs, Boyle & Smith, 1970; Amelio et al., 1970) is well established in X-ray astronomy. Some examples are the EPIC-MOS (Turner et al., 2001) and the EPIC-pn (Strüder et al., 2001) on *XMM-Newton*, the Advanced CCD Imaging Spectrometer (ACIS) instruments on *Chandra* (Weisskopf et al., 2002), the X-Ray Imaging Spectrometer (XIS, Koyama et al., 2007) on *Suzaku*, the p-n junction Charge-Coupled Device (pn-CCD, Meidinger et al., 2009) on eROSITA, the Soft X-ray Imager (SXI, Tsunemi et al., 2010) on *Astro-H*, the Wide Field Imager (WFI, Lechner et al., 2010b; Strüder et al., 2010) on *IXO*/*ATHENA*, and the High Time Resolution Spectrometer (HTRS, Barret et al., 2010; Lechner et al., 2010a) on *IXO*. In this section I explain the technologies of CCDs, Silicon Drift Detectors (SDDs), and APSs. Although there are also other Si-based instrument types such as strip detectors, they are not relevant for the simulations presented in this thesis.

Further common detector types are, e.g., CdTe detectors (Takahashi et al., 2005) or proportional gas counters (Bradt et al., 1993) suitable for the measurement of higher energetic photons. Like the Si-based detectors these instrument types rely on the detection of charge signals produced by the absorption of incident photons. The interested reader might refer to Kendziorra (2008), Pfeffermann (2008b,a), Knoll (2010), and Edgar (2011).

The class of microcalorimeters is based on the detection of the thermal heating produced by the absorption of an X-ray photon in the detector material. Its application in X-ray astronomy is quite new (Kelley et al., 2007). Despite of a challenging technical implementation, they promise a big advance in high resolution spectroscopy. This section contains a short introduction to this interesting technology, since microcalorimeters are part of the *IXO* and *ATHENA* mission concepts.

Charge-Coupled Devices

CCDs are among the most popular representatives of semiconductor detectors in X-ray astronomy. They can provide good spatial resolution in combination with non-dispersive spectroscopy (Kraft et al., 1995). In order to understand the functionality of semiconductor detectors such as Si-based CCDs, I will provide a short summary of the relevant physical properties. More detailed introductions can, e.g., be found in the previously listed textbooks about detectors.

The crystal structure of a semiconductor is usually formed either by atoms of a single chemical element of the fourth group of the periodic table of elements, such as Si or Ge, or by an alternating combination of elements of the third and the fifth group, such as Ga and As, or the second and the sixth group, such as Cd and Te. Therefore there are on average four valence electrons per atom.

The electron orbitals of the individual atoms in the crystal lattice overlap forming different energy bands. The uppermost band completely filled with electrons in the ground state at zero temperature is called the valence band. The next higher band, which in the ground state is completely empty, is called the conduction band. As long as the valence band is completely filled and the conduction band is completely empty, no current can flow through the semiconductor. The electrons in the valence band can only move if they exchange their place with another

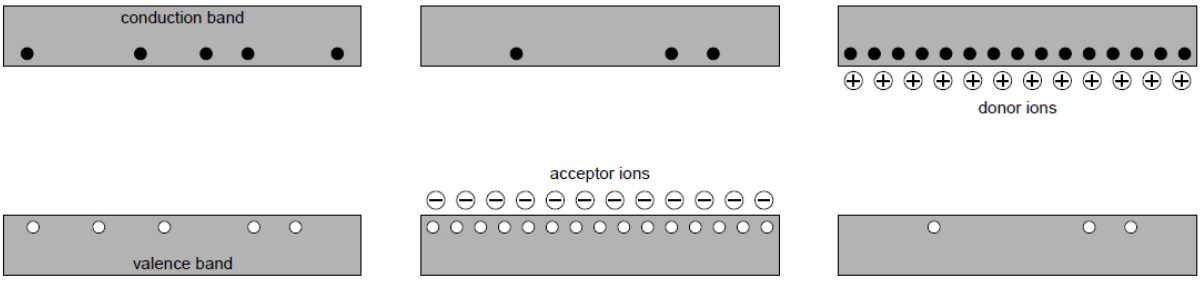

Figure 2.8: Population of the valence and the conduction band in semiconductors (Lauf, 2011). In an intrinsic semiconductor (left-hand) the number of electrons (black circles) in the conduction band is equal to the number of holes (white circles) in the valence band. In a p-doped semiconductor (middle) additional holes are generated in the valence band due to the capture of electrons by the acceptor atoms. In an n-doped semiconductor (right-hand) electrons are inserted into the conduction band from the donor atoms.

electron such that the effective current is zero. However, if electrons are excited from the valence band into the conduction band, e.g., by thermal excitation or photon absorption, they leave behind a hole in the valence band. Both the electron in the conduction band and the hole in the valence band, which can be regarded as a positive charge carrier, can move freely within the semiconductor. If an electric field is applied, a current can flow.

The population of electrons in the valence and conduction band is described by a Fermi distribution (Martin, 2009). For a so-called intrinsic semiconductor without any impurities as described above, the Fermi level is located in the middle between the valence and the conduction band. The number of electrons in the conduction band therefore equals the number of holes in the valence band.

However, the population of electrons in the conduction band and the population of holes in the valence band can be strongly influenced by impurities in the regular structure of the semiconductor material. For these so-called doped semiconductors either atoms of the third group, i.e. with three valence electrons, or atoms of the fifth group, i.e. with five valence electrons, are implanted in the crystal lattice. Regarding the band structure of the energy bands additional levels are thereby introduced, which are located between the valence and the conduction band.

Atoms of the third group form energy levels closely above the valence band and are called acceptors, because an electron from the valence band can be easily excited to an acceptor level leaving behind a hole in the valence band. Therefore holes are the so-called majority charge carriers in a semiconductor with acceptor impurities. These conditions are also designated as p-doping.

Atoms of the fifth group, in contrast, form energy levels slightly below the conduction band and are called donors. As they have five valence electrons, one of them can easily be excited into the conduction band such that electrons are the majority charge carriers in these so-called n-doped semiconductors. The population of the valence and conduction band is shown in Fig. 2.8 for different doping conditions.

The Fermi level, which for intrinsic semiconductors is located in the middle between the valence and the conduction band, is shifted by the implantation of donor and acceptor atoms. If regions with n- and p-doping are in direct contact, which can, e.g., be achieved by a spatial variation of the doping conditions, the majority charge carriers from both regions can drift into the respectively other region and recombine with each other. By this diffusion process a depletion region without mobile charge carriers is formed. From the diffusion and recombination of the electrons and holes a voltage arises opposite to the diffusion current resulting in an equilibrium state, as show in Fig. 2.9 (Martin, 2009; Lauf, 2011).

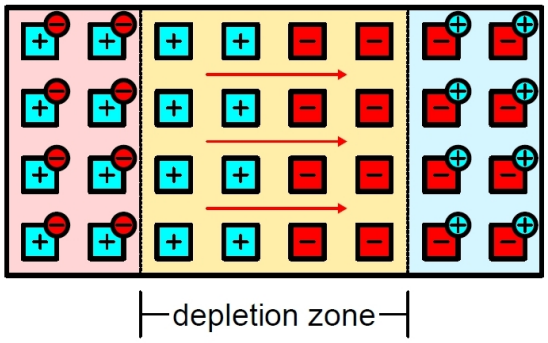

(a) In the depletion zone at the contact of the different doping regions the electrons from the n-doped region (left-hand) have recombined with the holes from the p-doped region (right-hand). The arising electric field (red arrows) prevents further diffusion such that an equilibrium state is achieved.

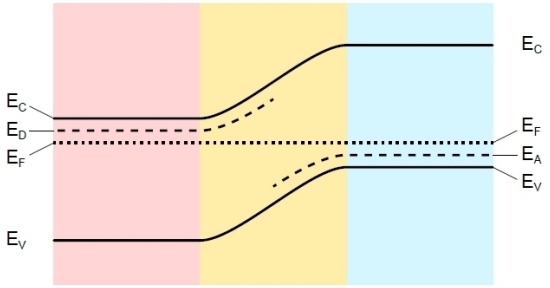

(b) The energy levels of the valence band E_V and the conduction band E_C are deformed across the p-n junction, whereas the Fermi level E_F remains constant. The donor level E_D and the acceptor level E_A are indicated for the n- and the p-doped regions respectively.

Figure 2.9: Schematic view of a p-n junction (adapted from Lauf, 2011).

The spatial extension of the depletion region can be modified by applying an additional external voltage to this so-called p-n junction. Its width is proportional to the square root of the applied voltage (Martin, 2009; Lauf, 2011)[7]. Electron-hole pairs produced in the depletion region, e.g., by thermal excitation or by interaction with a photon are separated by the electric field and therefore prevented from recombination. The arising electric signal can be measured with suitable electronic circuits in order to detect the photon interaction.

The first CCD detectors used in X-ray astronomy are based on the Metal Oxide Semiconductor (MOS) technology developed for applications with optical light (Lutz, 1999, Chapter 6). The thickness of the depletion layer in the semiconductor substrate can be increased up to about 50 μm in order to improve the sensitivity for X-rays (Short et al., 1998; Strüder et al., 1987; Strüder & Meidinger, 2008). In order to obtain good quantum efficiency and energy resolution over a wide range of photon energies up to 30 keV, a depletion thickness of the order of 1 mm is required (Strüder & Meidinger, 2008). This can be achieved using the principle of sideward depletion as proposed by Gatti & Rehak (1984). In pn-CCDs (Strüder et al., 2001), which are based on this principle, the fully depleted Si substrate guarantees a high absorption probability for X-rays with energies up to the order of 10 keV (Lechner et al., 2003).

Incident X-ray photons generate a major number of electron-hole pairs by photoelectric absorption in the substrate. Although the band gap of Si is 1.1 eV, on average 3.68 eV are necessary to create an electron-hole pair (Lumb et al., 1991; Kraft et al., 1995), since part of the photon energy has to be transferred to lattice vibrations, i.e. phonons, in order to conserve the momentum (Janesick, 2007). The electrons and holes are separated by an electric field in the depleted detector volume in order to avoid recombinations. The electrons are usually collected in a potential maximum about 10 μm below the front surface of the Si (Strüder & Meidinger, 2008), whereas the holes drift to the backside of the detector. The electric field can have a horizontal component applied by electrodes on the Si surface such that the electron cloud, produced by the absorption of an individual photon, is collected within particular regions defining a pixel structure.

[7] In order to increase the width of the depletion zone, the p-n junction has to be reverse biased, i.e., a negative voltage is applied to the p-doped side and a positive voltage to the n-doped side. For forward biasing with the opposite polarity a significant current can flow through the junction.

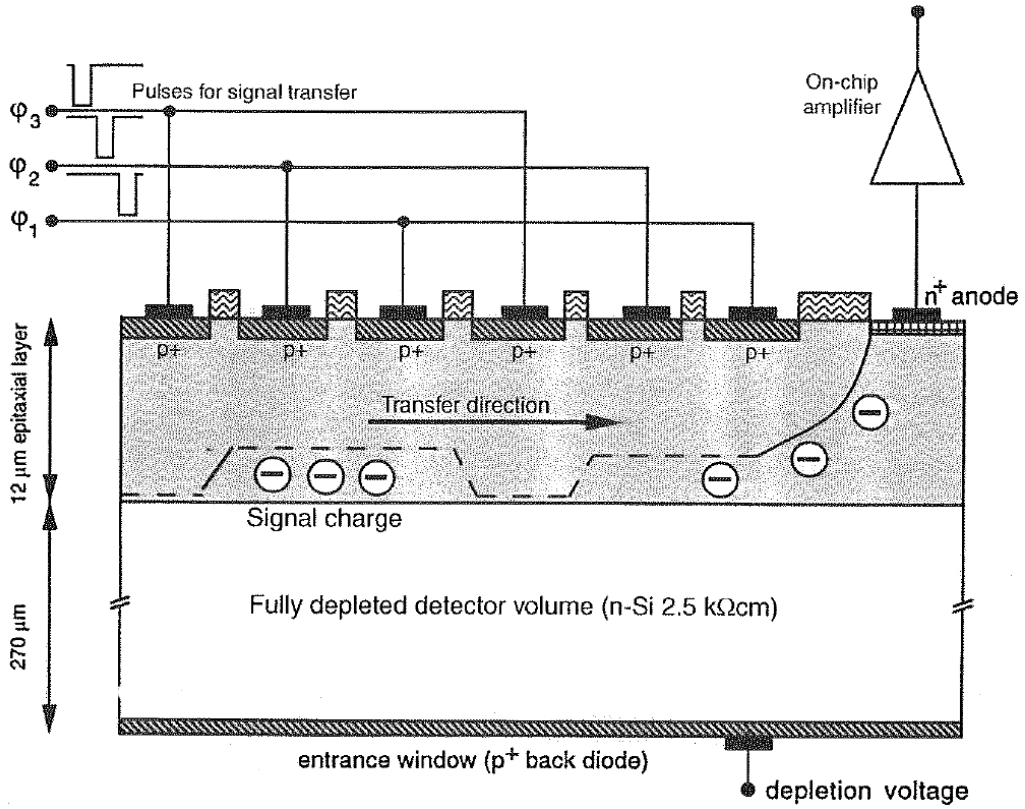

Figure 2.10: Schematic cross section of a CCD (Soltau et al., 1996). The electrons produced by the absorption of photons in the depletion region drift to the potential maximum closely below the detector surface. In this buried channel the electrons are transferred towards the readout anodes at the edge of the detector by periodically clocking the voltage applied to the electrodes on the surface.

In order to measure the collected charge, the electrons confined in the potential maximum below the detector surface have to be shifted towards the readout anodes at the edge of the detector, as indicated in Fig. 2.10 (Lumb et al., 1991). This shift is performed by periodically clocking the voltage of the transfer register electrodes on the detector surface. A detailed description of this process is provided by Strüder & Meidinger (2008).

Charge Transfer Efficiency Due to the trapping of electrons by defects in the crystal structure of the Si material, the efficiency of the shift process, which is denoted as Charge Transfer Efficiency (CTE), is usually less than 100 %. For common detectors the Charge Transfer Inefficiency (CTI) representing the loss of electrons per pixel shift (Popp, 2000), $\mathrm{CTI} = 1 - \mathrm{CTE}$, is of the order of 10^{-5} (Lumb et al., 1991; Hopkinson, 1992; Strüder & Meidinger, 2008). The exact value depends on the defects in the buried transfer channel for the charges below the detector surface and can deteriorate due to radiation damage in orbit (Turner et al., 2001). The CTE can also depend on the observed count rate, since electron traps in the detector causing the CTI might be saturated for observations with a high photon flux (Popp, 2000; Duro et al., 2011).

Out Of Time Events As the cameras used in X-ray telescopes usually have no shutter (Lumb et al., 1991; Grant, 2011), further photons can hit the detector during the shift of signal charges to the readout anodes. These photons result in so-called Out Of Time (OOT) events, which are assigned to a wrong pixel along the shift direction. This effect is explained in Fig. 2.11 and the impact on a typical CCD detector image is displayed in Fig. 2.12. The proper position of OOT

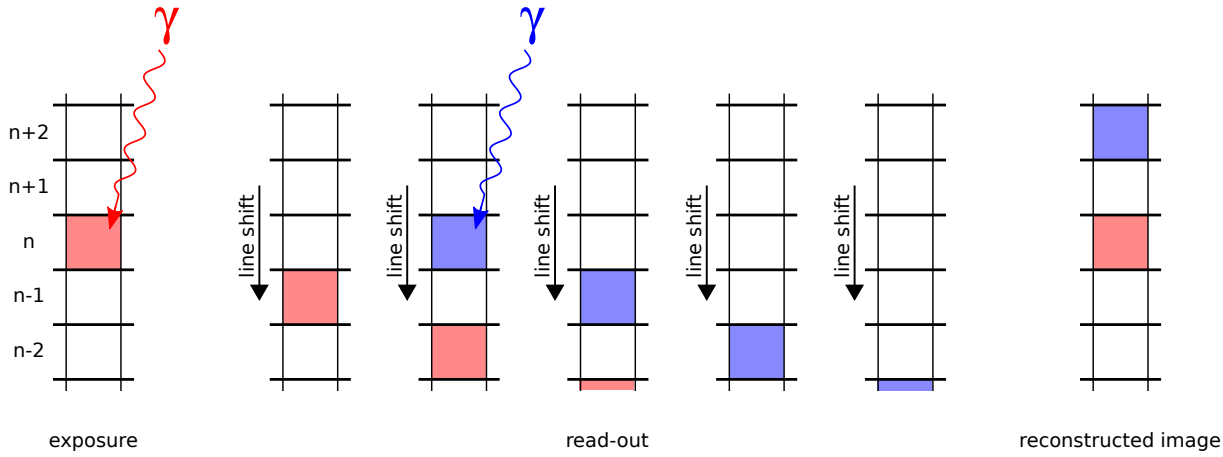

Figure 2.11: Since the cameras used in X-ray astronomy are usually not equipped with a shutter, photons incident on the detector during the line shifts for charge readout can create a signal, which is then assigned to a wrong position by the readout electronics. In the displayed example the blue photon hitting the pixel in row n after the second line shift is assigned to the pixel in row $n+2$. The red photon is assigned to the correct row.

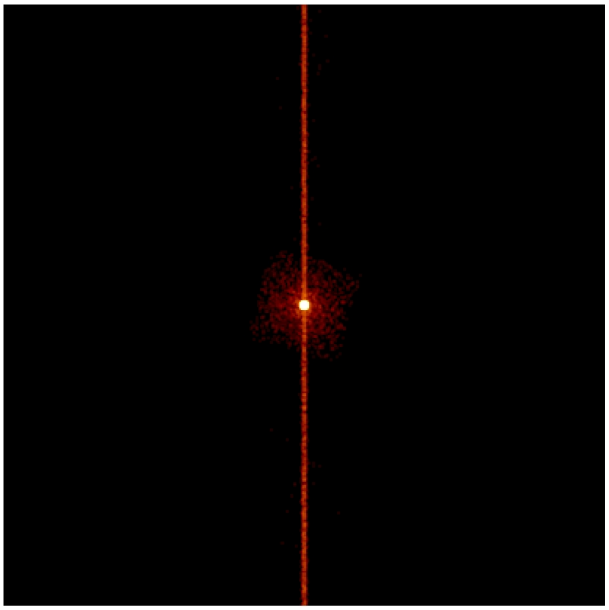

Figure 2.12: The image displays a simulated illumination of a typical CCD detector (with logarithmic color scale). The observed source is located above the center of the CCD. The vertical strip consists of OOT events hitting the CCD during the line shift process. The fraction of OOT events can be estimated from the readout time and the exposure time as $\frac{t_{\text{readout}}}{t_{\text{readout}}+t_{\text{exposure}}} \approx 2.3\,\%$ for the simulated device.

events can be reconstructed if the observed image is not confused by other sources along the smeared column on the detector, since the actual source position can be determined from the main spot in the image.

In addition to wrong positional information, OOT events can also distort the measured spectrum, when position-dependent algorithms like a CTE correction are applied. For CCD cameras with a significant ratio of shifting time versus total exposure, the effect of OOT events has to be taken into account for an accurate spectral analysis.

As described by Kendziorra et al. (1998) and Kuster et al. (1999), the fraction of OOT events in the full-frame mode of the European Photon Imaging Camera (EPIC)-pn CCD on *XMM-Newton* is about 7 %. In some different operating modes such as the burst mode (Kendziorra et al., 1997; Kirsch et al., 2006) of the EPIC-pn camera all incident photons are on purpose detected as OOT events. In this mode the positional information in the direction of the charge shift is sacrificed in favor of a higher count rate capability.

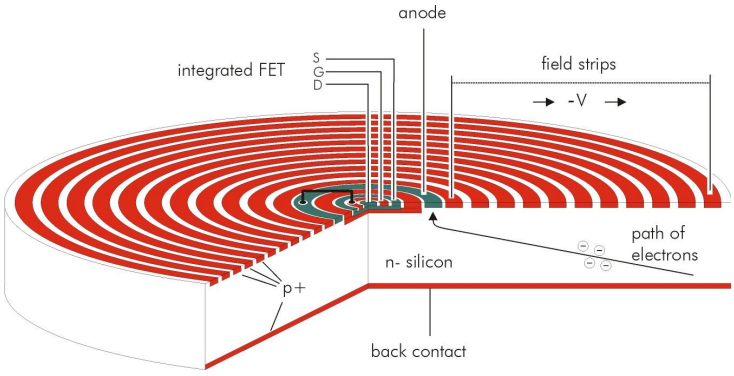

Figure 2.13: SDD (Barret et al., 2004). The electrons generated by a photon impact drift along the electric field induced by the applied external voltage towards the integrated FET in the center of the macro-pixel.

In framestore CCDs such as the eROSITA pn-CCD (Meidinger et al., 2009) the fraction of OOT events is significantly reduced with respect to conventional CCDs. Framestore devices have a sensitive area exposed to the incident photons and an additional area with the same number of pixels, which is ideally shielded against X-rays or at least contains no bright X-ray sources in its FOV (Lumb et al., 1991). After each exposure interval the electrons collected in the sensitive area are rapidly transferred to the framestore area, from where they can be read out with a lower speed. Since the transfer time to the framestore area is much shorter than the readout of individual lines, the fraction of the interval during which OOT events can occur is significantly reduced.

Silicon Drift Detectors

For instruments that do not require a high spatial resolution it is possible to build devices with a large detection area. The detection volume is fully depleted by sideward depletion (Gatti & Rehak, 1984) and an electrical field is induced in the volume by applying an external voltage on the surface of the detector. The electrons produced by a photon impact are drifting along the electric field lines towards the readout anodes, which can, e.g., be located at the edge of the detector (Lutz, 1999, Chapter 6). In such a linear SDD spatial information about the location of the photon absorption point can be estimated based on the dependence of the charge cloud spread on the drift length to the anodes (Campana et al., 2011).

It is also possible to construct a macro-pixel by the combination of a circular SDD with a Field Effect Transistor (FET) in its center for the readout of the collected charges. The electrons generated by a photon impact somewhere in the macro-pixel drift towards the center due to the voltage applied to the field rings on the detector surface, which are shown in Fig. 2.13 (Barret et al., 2004; Lutz et al., 2007; Lechner et al., 2008). The drift time of the charge cloud usually is much less than 1 μs (Barret et al., 2008). Once collected in the center of the pixel, the charge results in a change of the voltage of the integrated FET, which is measured by the subsequent electronics. Due to the low capacitance of the anode, which is of the order of a few 100 fF (Lechner et al., 2001, 2010a), even small amounts of charge produce a measurable signal. Such SDDs are especially suitable for high count rate applications, since they can be operated with short signal shaping times.

Active Pixel Sensors

An APS detector (Kemmer & Lutz, 1987; Kemmer et al., 1990) consists of several pixels each having an integrated amplifier on top of the fully depleted Si substrate. In contrast to a CCD, the pixels can be addressed individually without having to shift the collected charge towards the edge of the detector. This technology guarantees low-noise signal processing by avoiding long electric connections between the detector and the readout electronics with the first amplification stage,

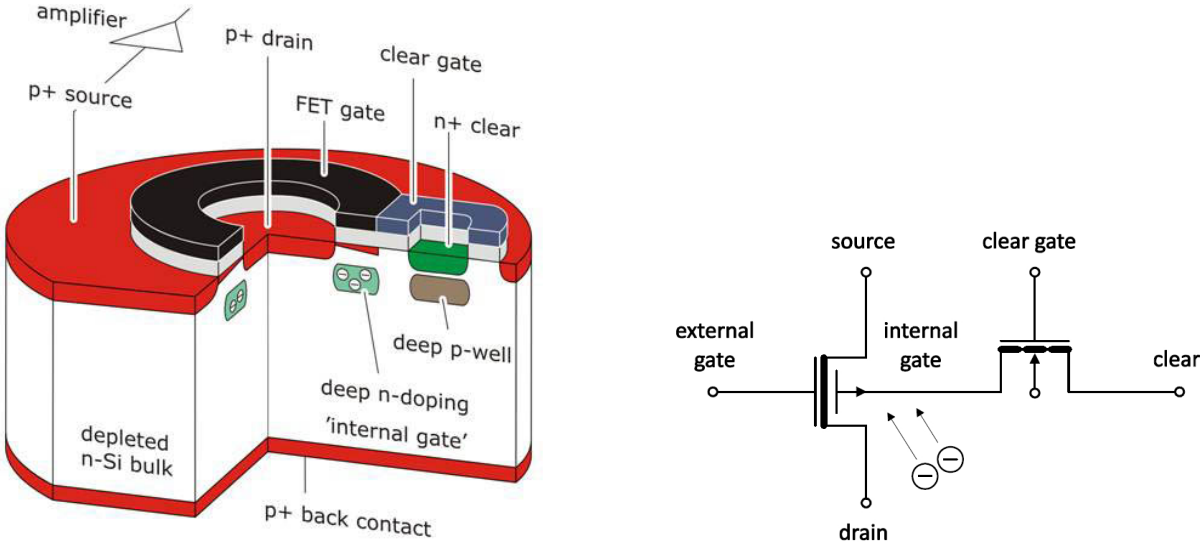

Figure 2.14: Cutaway and electronic circuit of a DePFET pixel (Treis et al., 2005a). The electrons produced by the absorption of an X-ray photon in the Si bulk are collected in the potential maximum of the internal gate. The amount of collected charge is determined by measuring the transistor current. The electrons are removed from the internal gate via the clear gate and the clear contact.

and it circumvents many calibration issues of CCDs, such as CTE corrections or OOT events (Lutz, 2005). The possibility of a non-destructive readout of the collected charge additionally allows the reduction of electronic noise by repeated signal samplings.

APS instruments proposed for current mission designs such as *Simbol-X* (Ferrando et al., 2006, 2009), *IXO*, or *ATHENA* consist of Depleted P-channel Field Effect Transistors (DePFETs) invented by Kemmer & Lutz (1987). A DePFET is based on a fully depleted Si bulk and an electronic structure on its front surface forming a FET (Lechner et al., 2003; Lutz et al., 2007). The FET usually is a Metal Oxide Semiconductor Field Effect Transistor (MOSFET, Martin, 2009). A schematic overview of a DePFET device is given in Fig. 2.14. The electrons generated by absorbed photons in the depleted Si bulk drift to a potential maximum close to the surface and are collected there. This region is denoted as internal gate, since the accumulated electrons regulate the current in the FET on the detector surface. The amount of collected charge can be determined by measuring the transistor current and comparing it to the base value, which is obtained for an empty internal gate (Lechner et al., 2003). In order to determine the latter value, the collected electrons have to be removed from the internal gate by applying appropriate voltages to the clear gate and the clear contact, after the current with the accumulated charge has been sampled.

A large number of DePFET pixels can be combined to a 2-dimensional array in order to construct a detector with spatial resolution. Accessing individual pixels in such a large array would require an unreasonable number of circuit tracks between the integrated FETs and the subsequent electronics. This problem is usually avoided by a line-wise readout strategy, as explained, e.g., by Strüder et al. (2010) or Stefanescu et al. (2010). In a single step all pixels in the currently active row of the detector are read out in parallel. By repeating this step over all rows of the array all pixels can be read out.

Due to the direct readout of individual pixels, a shifting of signal charges is not required. In contrast to CCD detectors, the energy resolution of APSs is therefore not deteriorated by OOT events or a bad CTE. With pixel sizes of 100 μm and an energy resolution of about 130 eV FWHM at 5.9 keV the present detectors provide good imaging and Fano-limited (see below)

spectroscopic capabilities. The operation time of arrays of APSs with about 1 ms per frame is much faster than for CCD cameras. If the central DePFET structure is surrounded by several drift rings with an externally applied voltage gradient, macro-pixels according to the principle of SDDs can be constructed. Further advantages of DePFET APSs in comparison to CCDs are listed by Lauf (2011).

A detailed description of the functionality of DePFET APS devices is given by Treis et al. (2005a,b), Lechner et al. (2008, 2010b), Martin (2009), Strüder et al. (2010), and Lauf (2011).

Microcalorimeters

In contrast to the previously presented detectors that measure the charge created by the interaction of a photon with a semiconductor material, cryogenic microcalorimeters determine the thermalization energy of a photon deposited in an absorber material (Moseley et al., 1984). Whereas the energy resolution of devices based on the measurement of electric charge is restricted by statistical fluctuations of the electron excitation process within the Fano limit (see below), in a microcalorimeter the energy of a photon is completely thermalized enabling a higher energy resolution. For charge-based semiconductor detectors a resolution comparable to that of microcalorimeters is only achievable with dispersive spectrometers such as the grating spectrometers on *Chandra* (Weisskopf et al., 2002) and *XMM-Newton* (den Herder et al., 2001). For low photon energies up to about 1–2 keV dispersive spectrometers outreach microcalorimeters in terms of resolving power. For higher photon energies the resolution of microcalorimeters is better (Kelley et al., 2007; Mitsuda et al., 2010). Apart from that, dispersive instruments are disadvantageous for observations of spatially extended sources (Stahle et al., 1999).

Microcalorimeters are operated at very low temperatures (below 1 K). When a photon hits the device or an attached absorber with a low heat capacity, the temperature increases accompanied by a change of the electrical resistance, which can be measured in order to determine the energy of the absorbed photon. Via a weak thermal link to a heat sink the device is cooled and returns to its base temperature (Stahle et al., 1999; Enss, 2001; Knoll, 2010, Chapter 19). In order to improve the quantum efficiency of the photon absorption, microcalorimeters usually have an absorber with a suitable heat capacity and a high thermal conductivity on top (de Korte et al., 2004; Kilbourne et al., 2007). A schematic drawing of a microcalorimeter is displayed in Fig. 2.15.

By combining a major number of individual microcalorimeter elements in an array of pixels non-dispersive imaging spectrometers can be built (Irwin, 2002; Irwin et al., 2004; de Korte et al., 2004; Porter et al., 2006; Kelley et al., 2007; Kilbourne et al., 2007, 2008; Smith et al., 2008; Bandler et al., 2010). However, the cooling to the necessary low temperatures of about 0.05–0.1 K is challenging with the limited resources available on a spacecraft platform. Nevertheless microcalorimeters on future X-ray missions promise the measurement of spectra with unprecedented resolution.

In comparison to charge-based semiconductor detectors the implementation of microcalorimeters in astronomical X-ray missions is quite new. After the unsuccessful launch of *Astro-E* (Kunieda et al., 2001) the first microcalorimeter on an X-ray mission, the X-Ray Spectrometer (XRS, Porter et al., 2004, 2006; Kelley et al., 2007) aboard *Suzaku* (*Astro-E2*) was only usable for a very short period due to a thermal short between the helium and the neon tanks required for cooling (Mitsuda et al., 2007). Despite of technical issues, the technology of microcalorimeters is very promising especially with respect to the achievable energy resolution. The X-ray Microcalorimeter Spectrometer (XMS, den Herder et al., 2010) aboard *IXO/ATHENA* and the Soft X-ray Spectrometer (SXS, Mitsuda et al., 2010) on *Astro-H* are current approaches to implement such devices on future X-ray missions.

There are different technologies implemented for microcalorimeters. The detectors of the XRS on *Suzaku* and the SXS on *Astro-H* are based on highly doped Si just below the metal-insulator transition (Zhang et al., 1998; Kelley et al., 2007), whereas the XMS aboard *IXO/ATHENA* uses

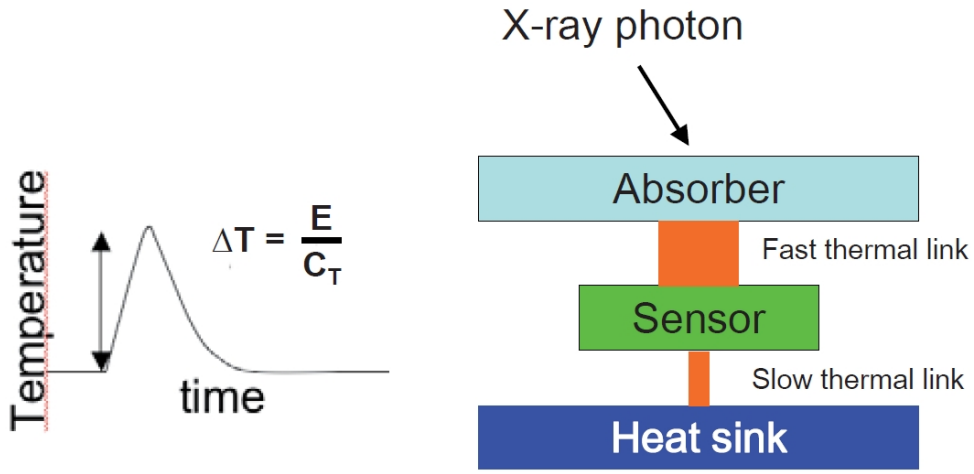

Figure 2.15: Schematic view of a microcalorimeter (Barcons et al., 2011a). The energy released by the absorption of an X-ray photon increases the temperature of the absorber and the attached sensor. This heating ΔT is directly related to the energy of the photon and can be measured by the corresponding change in electrical resistance. The sensor is connected to the heat sink via a weak thermal link for temperature stabilization.

the technology of TESs (Irwin, 1995; Irwin et al., 1996, 1998).

TESs are operated at the transition edge from the superconducting to the normal phase such that a small temperature change caused by an absorbed X-ray photon results in a significant change of the electrical resistance. The temperature change and therefore the energy of a photon is determined via electro-thermal feedback. The TES is voltage biased by an external electrical power supply and coupled to a heat sink via a weak thermal link (Knoll, 2010, Chapter 19). In equilibrium the heat flow into the heat sink equals the Joule heating by the electrical current. Due to the increase of temperature and electrical resistance at the absorption of an X-ray photon, the current through the device decreases, as the voltage remains constant. The TES is then exposed to less Joule heating such that the heat flow to the heat sink reduces the temperature again to its initial value. The current flowing through the TES is measured with a Superconducting QUantum Interference Device (SQUID) such that the energy of the absorbed photon can be determined by integrating the signal over the time (Irwin, 1995; Enss, 2001):

$$E_{\text{photon}} = \int_{\text{pulse}} \Delta P_{\text{Joule}}\,\mathrm{d}t = V_{\text{bias}} \int_{\text{pulse}} \Delta I_{\text{SQUID}}\,\mathrm{d}t \tag{2.20}$$

The transition temperature of the device can by adjusted using the proximity effect of a superconductor-metal multilayer. A typical value of the transition temperature is 0.05–0.1 K and the transition width is about 100 μK (Irwin, 1995; Irwin et al., 1996, 1998; Kilbourne et al., 2007; den Herder et al., 2010). The described measurement procedure via electro-thermal feedback guarantees short response times and high energy resolution (Knoll, 2010, Chapter 19).

2.3.2 Characteristics

In the following some effects typical for the presented detector types are introduced. They have to be considered for the development of a realistic simulation software.

Energy Resolution

In a Si-based semiconductor the average number of electron-hole pairs generated by the absorption of photons with energy E_{ph} in the Si substrate is obtained as

$$\bar{N} = \frac{E_{\mathrm{ph}}}{E_{\mathrm{e-h}}} \tag{2.21}$$

with $E_{\mathrm{e-h}} = 3.68\,\mathrm{eV}$ (Popp, 2000). The derived photon energy measured by the instrument is determined from the actually detected number of electron-hole pairs:

$$E = N \cdot E_{\mathrm{e-h}} \tag{2.22}$$

In general N and $\bar{N}$ are not identical, since $\bar{N}$ is just an expectation value and the actual number of electron-hole pairs generated by a single photon impact is subject to statistical fluctuations, denoted as shot noise (Janesick, 2007). Since the absorption process of a photon in the Si material is not purely statistical, the corresponding fluctuations are lower than for a common Poisson process, as determined by Fano (1947) for gas detectors. The standard deviation of N is obtained as

$$\sigma_N = \sqrt{F \cdot \bar{N}} \tag{2.23}$$

with the so-called Fano factor F, which has a value of about 0.115 for Si (Alig et al., 1980)[8]. The standard deviation of the measured energy is therefore obtained as

$$\sigma_{E,\mathrm{Fano}} = \sigma_N \cdot E_{\mathrm{e-h}} = \sqrt{F \cdot E_{\mathrm{ph}} \cdot E_{\mathrm{e-h}}} \tag{2.24}$$

The FWHM of the maximum achievable energy resolution is

$$\Delta E_{\mathrm{FWHM,Fano}} = 2.35 \cdot \sigma_{E,\mathrm{Fano}} \tag{2.25}$$

In case of a Si-based detector the energy resolution for a 1 keV photon therefore cannot be better than about 50 eV. An instrument approaching this value is usually called Fano-limited.

Considering Eqs. (2.24) and (2.25), the energy resolution can be improved by selecting a material with a low value of $E_{\mathrm{e-h}}$. The energy required for the ionization of the gas contained in a proportional counter is at least one order of magnitude larger than the corresponding value in a semiconductor (Knoll, 2010) such that the accuracy of the energy measurement is subject to relatively large Fano noise. In a semiconductor device a single X-ray photon can generate hundreds or thousands of electron-hole pairs, which can be detected with appropriate amplification. The therefore better energy resolution is one of the main advantages of semiconductor devices in comparison to traditional proportional counters.

In microcalorimeters the energy of an absorbed photon is not converted in the separation of electrical charges but thermalizes completely. The energy resolution of these instruments is therefore not determined by the Fano noise of the electron-hole pair production, but by the statistics of the excited phonons, which have a significantly lower average excitation energy (Moseley et al., 1984; Knoll, 2010, Chapter 19). The limiting energy resolution can be calculated as

$$\Delta E_{\mathrm{FWHM,phon}} \approx 2.35 \cdot \sigma_{E,\mathrm{phon}} = 2.35\xi \sqrt{k_{\mathrm{B}} T^2 C} \tag{2.26}$$

[8] There are indications that the Fano factor is not a material-specific constant, but depends on several conditions, such as the energy of the observed photon (Perotti & Fiorini, 1999). However, these variations are of minor importance for the regarded energy range and therefore neglected in the current context.

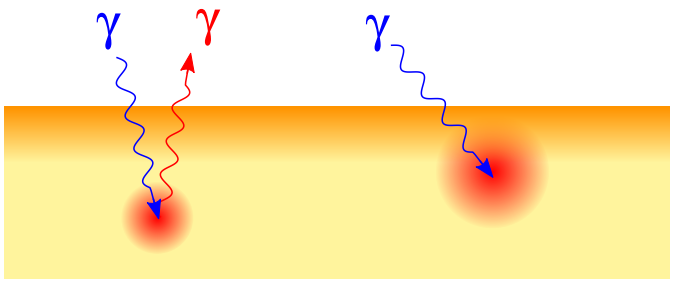

Figure 2.16: Escape peak (left-hand side) and partial absorption (right-hand side). After absorption of an incident photon a fluorescence photon can be emitted and escape from the detector such that its energy is missing in the measured signal budget. If the absorption takes place close to the surface of the detector, a part of produced charge cloud can be lost in the dead layer.

with the Boltzmann constant $k_\mathrm{B} = 8.617 \times 10^{-5}\,\mathrm{eV\,K^{-1}}$, the absolute temperature T, the heat capacity of the device C, and ξ a factor between 1 and 2.[9] Since the phonons are uncorrelated, Eq. (2.26) does not contain a Fano factor (Knoll, 2010, Chapter 19). In contrast to Eq. (2.24), the absolute limiting resolution of a microcalorimeter given by Eq. (2.26) is independent of the energy of the absorbed photon. For operating temperatures of $T \approx 0.1\,\mathrm{K}$ and a heat capacity of $C \approx 10\,\mathrm{pJ\,K^{-1}}$ the achievable energy resolution is of the order of 1 eV. An overview of the noise contributions to the signal measured with microcalorimeters is given by Galeazzi (2004, 2006, 2011).

Signal Readout

In semiconductor devices the accuracy of the signal determination is limited by the shot or Fano noise of the electron-hole pair production and by some electronic noise due to dark or leakage current and the readout process (Popp, 2000; Berry & Burnell, 2005; Knoll, 2010; Grant, 2011). For modern detectors the contribution of the dark current is often negligible or can be corrected. The readout noise usually only accounts for a few electrons (Lechner et al., 2003; Lutz, 2005; Treis et al., 2005a). The total energy resolution of the device is determined by the noise budget containing the shot noise and the electronic noise:

$$\sigma_E = \sqrt{{\sigma_N}^2 + {\sigma_\mathrm{el}}^2} \cdot E_\mathrm{e-h} \tag{2.27}$$

$$\Delta E_\mathrm{FWHM} = 2.35 \cdot \sigma_E \tag{2.28}$$

The energy resolution of a CCD as a function of the photon energy is shown, e.g., by Lumb et al. (1991) or Grant (2011) for different readout noise contributions.

The energy resolution of microcalorimeters is determined by the intrinsic noise, e.g., due to phonon fluctuations, and by the electronic noise of the readout process:

$$\sigma_E = \sqrt{{\sigma_\mathrm{phon}}^2 + {\sigma_\mathrm{read}}^2} \tag{2.29}$$

$$\Delta E_\mathrm{FWHM} = 2.35 \cdot \sigma_E \tag{2.30}$$

Escape Peak and Partial Absorption

In addition to the described energy resolution, effects with significant impact on the energy determination with a detector are the partial absorption of photons close to the detector surface and the so-called escape peak (Popp, 2000). A schematic drawing of both effects is displayed in Fig. 2.16.

The escape peak is caused by photons that ionize a Si atom by exciting a K- or higher shell electron. The photon emerging from de-excitation of the ion may escape from the detector

[9] The mechanism of electro-thermal feedback applied in TES microcalorimeters further improves the achievable energy resolution by a factor of $\frac{2}{\sqrt{\alpha}}$, where $\alpha = \frac{\partial T}{\partial R}\left(\frac{R}{T}\right)$ is the thermal response with the electrical resistance R (Knoll, 2010, Chapter 19).

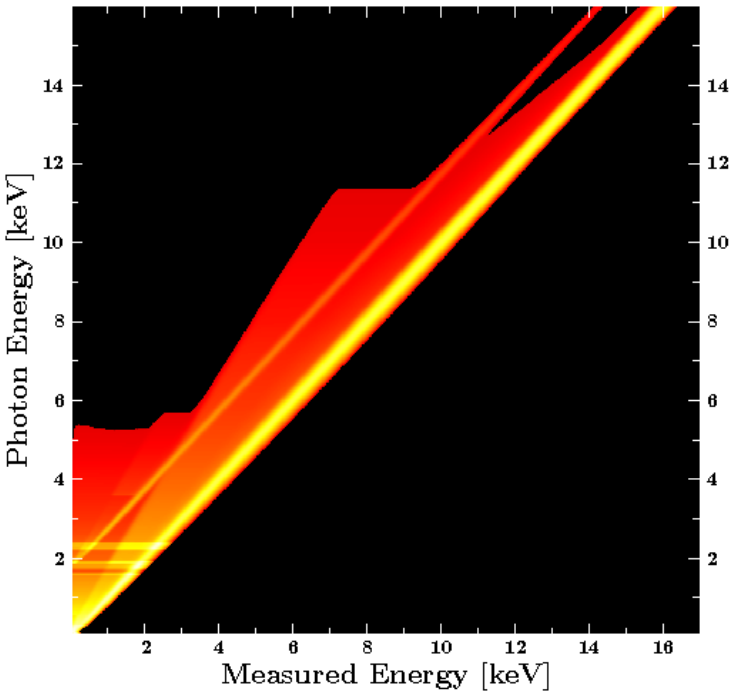

Figure 2.17: Redistribution matrix for the EPIC-pn camera on *XMM-Newton*. Each incident photon with a particular energy can be detected within a certain range of different energies due to noise and other detector features. Apart from the width of the main diagonal resembling the resolution of the detector, a parallel line with a lower intensity is visible. This line accounts for the escape peak of Si and is shifted by 1.7 keV with respect to the main diagonal. At low energies the absorption depth of photons is very low. Therefore the probability for partial absorption and signal loss at the detector surface is higher than at high photon energies. This effect is visible on the lower left-hand side. The image has a logarithmic color scale in order to emphasize side features, such as partial absorption.

such that its energy is not detected and therefore missing in the measured energy budget. As a consequence the incident photon is wrongly assumed to have a lower energy.

Partial absorption is caused in charge-based detectors if part of the ionization energy is lost in the dead layer at the surface of the detector material. This effect is mainly relevant for photons with a low energy, because they have a low penetration depth (Lutz, 1999, Chapter 6). It can be avoided by making the entrance window of the detector as thin as possible.

Detector Response

Due to the presented issues, the energy measured by a detector in general does not exactly agree with the energy of the absorbed photon, but is subject to fluctuations and systematic effects. For particular detectors these effects are usually modeled in a so-called Redistribution Matrix File (RMF, George et al., 1998, 2007). It summarizes the most important features in order to enable fast spectral analysis. Formally the RMF defines the probability density for the detection of an incident photon with a particular energy in a set of detector-specific energy channels. For a particular observation with an exposure time T_{exp} the number of observed counts $C(h)$ in a certain detector channel h can be obtained as

$$C(h) = T_{\mathrm{exp}} \int \mathrm{RMF}(h, E)\, \mathrm{ARF}(E)\, P(E)\, \mathrm{d}E \tag{2.31}$$

with the instrument-specific RMF and ARF (Sec. 2.2.1), and the spectrum of the observed source $P(E)$ (Davis, 2001b; Arnaud & Smith, 2011).

For an ideal detector the RMF would be the identity matrix, mapping each photon energy to the corresponding channel. In reality the energy determination process includes uncertainties and systematic effects such as partial absorption. Therefore the RMF usually consists of a broad main diagonal with a minor parallel and some additional features, as shown in Fig. 2.17. An overview of the characteristic features of semiconductor detectors is given by Popp (2000) for the special case of the EPIC-pn camera on *XMM-Newton*.

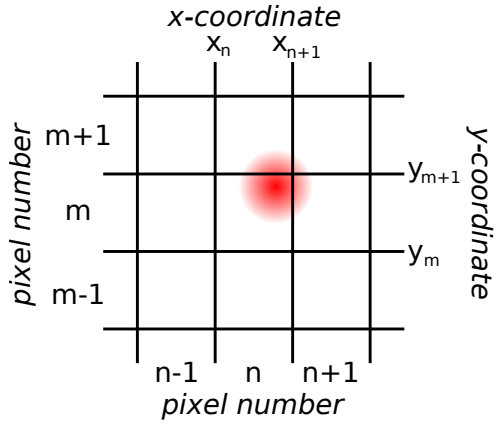

Figure 2.18: Due to diffusion and the electrostatic repulsion of the charges, the charge cloud generated by a photon has a finite extension and may be distributed among several neighboring pixels causing split events.

Charge Cloud Splitting

In semiconductor devices consisting of an array of adjacent pixels the electron cloud generated by the absorption of a single photon is ideally collected in the potential maximum of a single pixel. However, due to diffusion and electrostatic repulsion, the cloud has a finite extension, which can be of the same order as the pixel size, as indicated in Fig. 2.18. The actual size of the charge cloud is mainly determined by the strength and the shape of the electric drift field in the depleted Si, and by the energy of the absorbed photon (Kimmel et al., 2006a,c). If the photon impact position is located close to the boundary of a pixel, the generated charges are distributed among several neighboring pixels. In order to determine the energy of the initial photon, the signal in all these pixels has to be taken into account (Lumb et al., 1991; Martin, 2009; Lauf, 2011).

For common pixel and charge cloud sizes the main types of charge distribution patterns are displayed in Fig. 2.19. Since a split event implies a photon absorption close to the edge of a pixel, the distribution of split patterns provides additional spatial information beyond the resolution defined by the pixel structure (Kimmel et al., 2006a,c). An analysis of this sub-pixel resolution and applications to the spatial resolution of an X-ray telescope is provided, e.g., by Li et al. (2003, 2004) and Mühlegger (2010).

Pile-up

Although the general assumption that the pattern types presented in Fig. 2.19a are generated by a single photon impact is usually true for low rates of incident photons per pixel, for higher rates a significant part of them could also originate from multiple photon impacts during the same detector readout cycle. This phenomenon is denoted as pile-up and is particularly important for observations of bright X-ray sources corresponding to high photon rates (Popp, 2000; Martin, 2009).

For devices which are read out with a particular frame rate there is a certain probability that a single pixel is hit by multiple photons during one integration period. In that case the generated charges will be summed up, and the readout electronics, assuming that the entire signal has been generated by one individual photon, will determine a wrong energy value. This feature is denoted as **energy pile-up** and is visualized in Fig. 2.20. It has to be taken into account for the analysis of observations with high photon rates.

A similar effect is possible for devices with a continuous monitoring of the output signal of the detector. If the time difference between two subsequent photons is so short that the signal-processing electronics cannot discriminate the two photons, they are wrongly detected as a single photon, as indicated in Fig. 2.21. This phenomenon is denoted as **pulse pile-up**. In

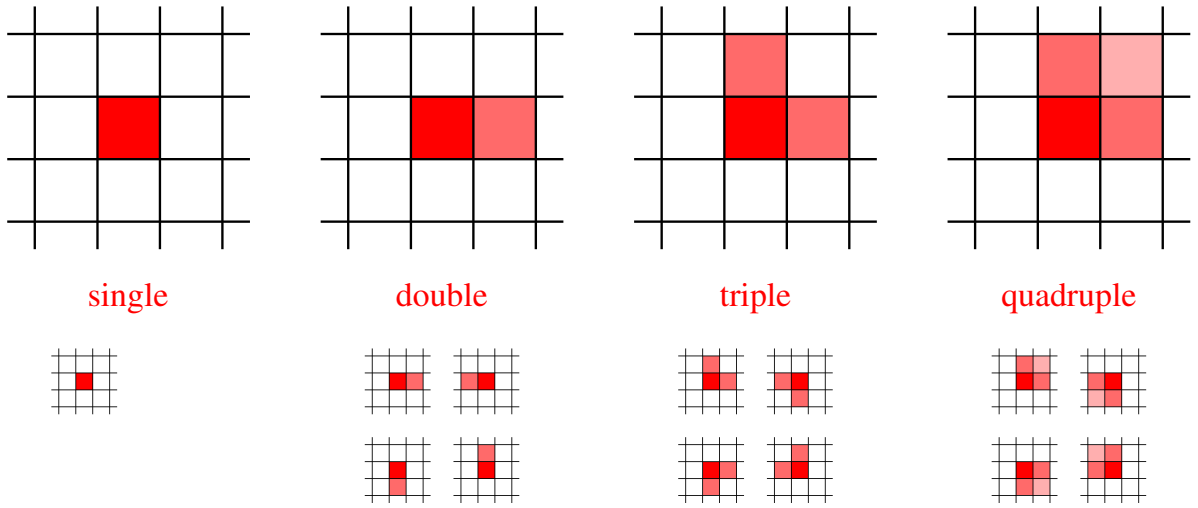

(a) The four main types of valid patterns that can be generated by a single photon impact due to charge cloud splitting. The dark-red pixels contain the major fraction of the produced charge signal, whereas the light-red colors indicate a minor charge fraction. Sub-types can be obtained by rotation, as indicated by the small images. Any pattern types different from the displayed ones are regarded as invalid throughout this thesis, since for the regarded detectors they can only be generated by more than one photon (Popp, 2000; Martin, 2009; Lauf, 2011).

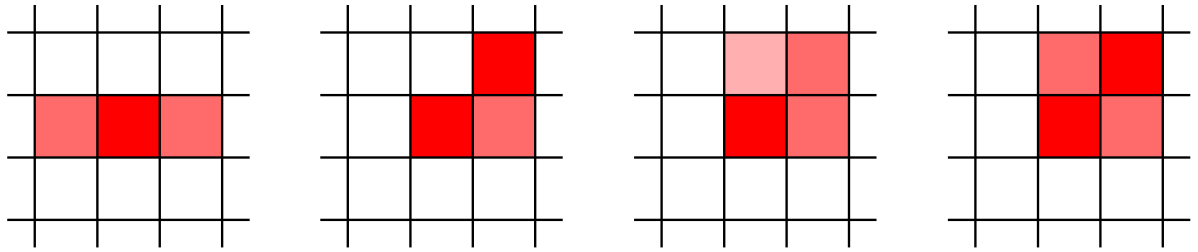

(b) Some examples for invalid pattern types, which are very unlikely to be generated by a single photon impact. In general all patterns affecting more than 2×2 pixels are denoted as invalid (Popp, 2000; Martin, 2009; Lauf, 2011). (This approach only holds for the detector types regarded in this work, for which the extension of the charge cloud is significantly smaller than the pixel size. For some other detectors valid patterns covering more than 2×2 pixels are possible due to smaller pixel sizes or trailing charges caused by imperfect charge shifts.) But also for those fulfilling this condition an analysis of the particular charge distribution is required, as shown in the three figures from the right.

Figure 2.19: Pattern types produced by charge cloud splitting in a detector with pixels larger than the extension of the charge cloud. An overview of the different pattern types generated by X-ray photons is given, e.g., by Ballet (1999). Kimmel et al. (2006b) present experimental data on the charge cloud splitting.

modern devices several techniques are applied to reject this kind of pile-up. They are usually based on an additional fast pulse trigger, which only discriminates subsequent signal pulses without measuring their exact shape. The actual energy determination is performed in parallel by sampling the amplitude and shape of the signal pulse produced by the detector. This process requires a longer time than the event discrimination by the fast trigger. In case the fast pulse trigger detects pile-up, the measured signal is discarded. The observed data have to be corrected in order to avoid corruption by the rejection mechanism (Pommé et al., 1999; Pommé, 1999).

Energy and pulse pile-up are possible for both charge detecting devices and microcalorimeters. Another kind of pile-up originates from the recombination of split events and is therefore mainly relevant for instruments measuring electric signals. In real measurements split events cannot be distinguished from events generated by two or more individual photons, as indicated by

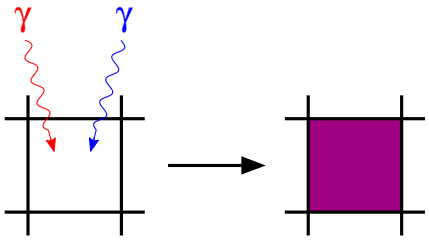

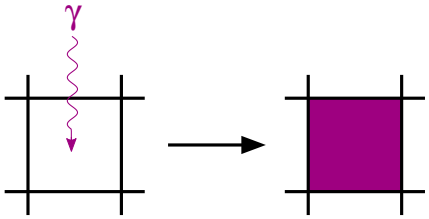

Figure 2.20: In reality it is impossible to distinguish whether the signal in a single pixel has been generated by one individual photon or by multiple photons hitting the same pixel during one integration period. The latter case is denoted as energy pile-up and results in wrong energy and photon rate measurements, as for the scientific analysis it is usually assumed that the event originates from a single photon.

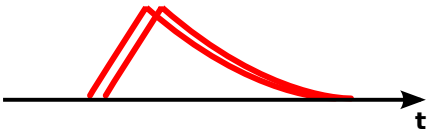

Figure 2.21: The time difference between the two subsequent photons is so short that the displayed pulses cannot be discriminated by the readout electronics. Therefore they are wrongly identified as a single event. This phenomenon is denoted as pulse pile-up.

the sketch in Fig. 2.22. The probability of having a split event mainly depends on the pixel dimensions and the charge cloud size, but not on the rate of incident photons. In contrast to that, the probability of having two or more photon impacts in neighboring pixels during the same readout cycle is directly correlated with the photon rate. At low photon rates this probability is usually much lower than the probability of a split event. For observations of faint sources one can therefore assume that charges in neighboring pixels forming one of the valid patterns displayed in Fig. 2.19a arise from a single photon, and the energy of this photon can be reconstructed by combining all the signals[10].

For higher rates this assumption is not applicable, because a significant part of the valid patterns may be created by multiple photons. In this case the energy information about the individual photons cannot be reconstructed. If the default assumption that all valid split patterns originate from a single photon is applied, there might be a significant fraction of wrong energy recombinations. This feature is denoted as **pattern pile-up** or grade migration (Davis, 2001a). In Fig. 2.23 the fraction of pile-up is shown for a distribution of pure single-pixel events, which, however, also contains other pattern types due to pattern pile-up.

In real observations events affected by pile-up in general cannot be identified. Therefore

[10]Invalid pattern types shown in Fig. 2.19b are known to originate from multiple photons and are therefore generally neglected in the event analysis.

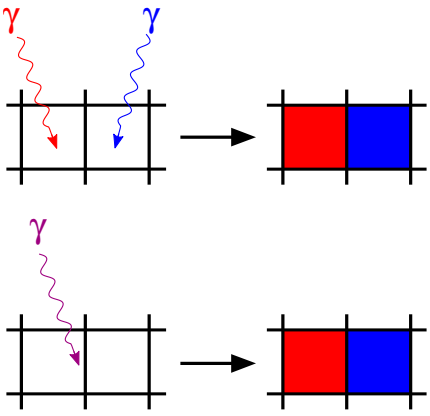

Figure 2.22: From the information about the read out signals it is not possible to distinguish, whether the two events have been generated by an individual photon impact resulting in a split event or by two photons hitting the neighboring pixels during the same readout cycle. The latter case is denoted as pattern pile-up. For the scientific analysis it is usually assumed that the pattern originates from a single photon.

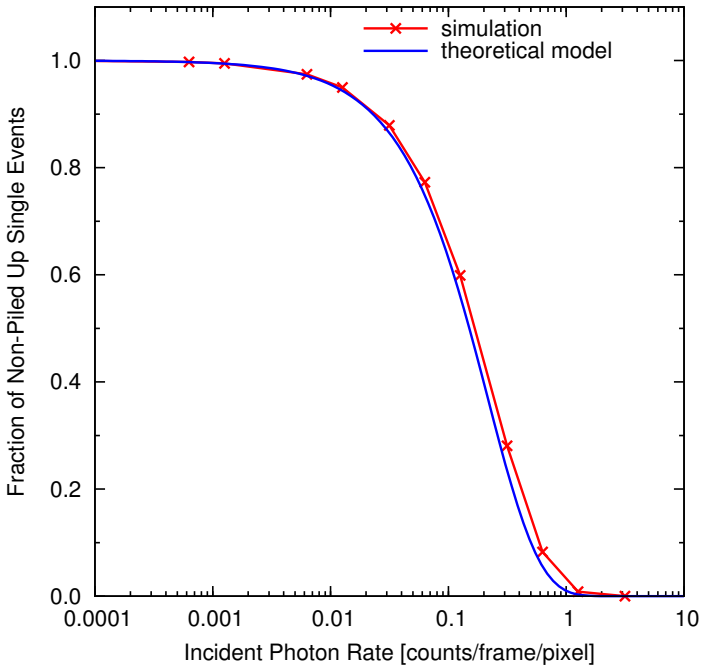

Figure 2.23: Pile-up effects for a distribution of pure single-pixel events, i.e., without charge cloud splitting[a]. Other pattern types than singles are only produced by pattern pile-up. The plot displays the fraction of single-pixel events, which are produced by single photons, i.e., not affected by pile-up, over the total number of incident photons. For high incident photon rates the fraction of good single-pixel events with correct energy information vanishes. The red curve represents data from my simulation and the blue curve a theoretical estimate according to a pile-up model adapted from Ballet (1999).

[a]This condition can be easily realized within a simulation, whereas for a real experiment it is hardly feasible.

such data can significantly corrupt the scientific output of the instrument. In the case of pile-up the observed photon count rates are too low and the measured spectra seem to have more high energetic photons due to the wrong identification of signals arising from multiple photons (Davis, 2001a; Arnaud & Smith, 2011; Grant, 2011). In contrast to observations in the regime of optical light, where a measurable signal is only produced by pile-up of a large number of individual photons, in X-ray astronomy pile-up usually is very undesirable.

Dead Time

A phenomenon closely related to pile-up for continuously read out detectors is the so-called dead time. It denotes the fraction of time during which the detector is insensitive to incident radiation. For some detector types this happens after the absorption of a photon. In this case additional photons that hit the same pixel directly after the absorption of the first photon are simply neglected. In contrast to pile-up, the signal of the additional photons is not combined with the contribution of the first photon, but is completely discarded. Dead time can also be caused if the charge produced in the pixel first has to be cleared before detecting further photons. Another common reason for dead time periods during the detector operation are background events triggered by an anti-coincidence device.

In general one has to distinguish between **paralyzable** and **non-paralyzable** dead time (also termed "extended" and "non-extended", Müller, 1973; Zhang et al., 1995; Knoll, 2010, Chapter 4). In the former case the dead time interval after a photon impact is extended by any further photon impact during this interval, although the additional photon is not detected. As described, e.g., by Knoll (2010), the fraction of undetected events can be determined in the case of paralyzable dead time as

$$f_{\mathrm{p}} = 1 - \mathrm{e}^{-r\tau} \tag{2.32}$$

where r is the average rate of incident photons per pixel and τ is the dead time interval after a single photon impact.

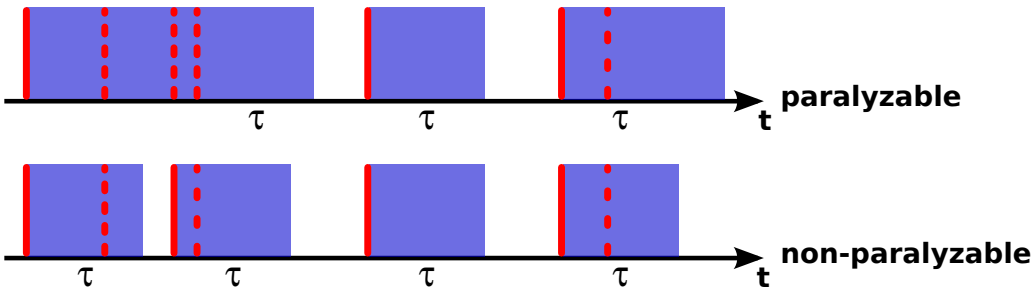

Figure 2.24: Difference between paralyzable and non-paralyzable dead time. The red bars represent photon events and the blue shaded boxes the corresponding dead time intervals. The straight red bar are properly detected photon events, whereas the dashed ones represent undetected photons, which are lost due to dead time. In the paralyzable case the detector is insensitive for an interval τ after each photon impact, i.e., the dead time interval can be extended by further impacts during the period of insensitivity. In the non-paralyzable case the dead time period of length τ starts at the impact of a properly detected photon and is not extended by further impacts during the subsequent period of insensitivity.

For non-paralyzable dead time the period during which the detector is insensitive to radiation is only determined by the last properly detected photon impact. Any further impacts during the subsequent dead time interval have no effect on its total length. Therefore the fraction of undetected events can be obtained according to Knoll (2010) as

$$f_{\mathrm{np}} = \frac{r\tau}{1 + r\tau} \tag{2.33}$$

The difference between paralyzable and non-paralyzable dead time is illustrated in Fig. 2.24. The two phenomena of pile-up and dead time are very closely related to each other such that their definition is sometimes confused. In this thesis I use the term pile-up if the signals caused by multiple photons are wrongly assigned to a single photon. The term dead time is used for intervals during which the detector is insensitive to incident radiation such that photons absorbed during this period are neglected.

Particle-induced Background

An X-ray detector is subject to different kinds of background. Apart from electronic noise and X-ray background, there is also a non-X-ray component caused by the interactions of γ-rays and charged particles with the detector material or its surroundings, which can result in fluorescence effects (Lumb et al., 2002; Read & Ponman, 2003; Carter & Read, 2007; Tawa et al., 2008; Kuntz, 2011). In Si-based devices so-called minimum ionizing particles[11] deposit on average 80 electron-hole pairs per μm along their track in the Si substrate (Lumb et al., 1991; Strüder et al., 2001). With regard to typical depletion depths of several 100 μm this corresponds to several tens of keV such that these particles can be distinguished easily from absorbed X-ray photons according to the measured signal (Lumb et al., 2002). Apart from its high signal, a minimum ionizing particle on average affects ten adjacent pixels in a typical detector (Strüder et al., 2000, 2001), in contrast to a maximum of four for an X-ray photon. In Fig. 2.25 an image of the EPIC-pn camera on *XMM-Newton* is shown, which comprises several tracks of charged particles.

The discrimination of events caused by minimum ionizing particles is usually performed by the on-board electronics with an efficiency of approximately 100 % by applying an upper threshold

[11] For charged particles of different kinds the specific energy loss, i.e., the energy loss per penetration depth, in a certain medium approaches a common minimum value for velocities close to the velocity of light (Knoll, 2010, p. 31f.; Lauf, 2011). However, for the typical thickness of an X-ray detector the deposited energy is still significantly higher than the signal from X-rays.

to the detected charge (Kendziorra et al., 1999) and a filter for invalid split pattern types. The discrimination of events caused by soft protons is much more challenging, since they mainly produce single-pixel events (Strüder et al., 2001). Another possibility of background rejection, which is often implemented in microcalorimeters or proportional counters, is an anti-coincidence detector surrounding the actual measurement device.

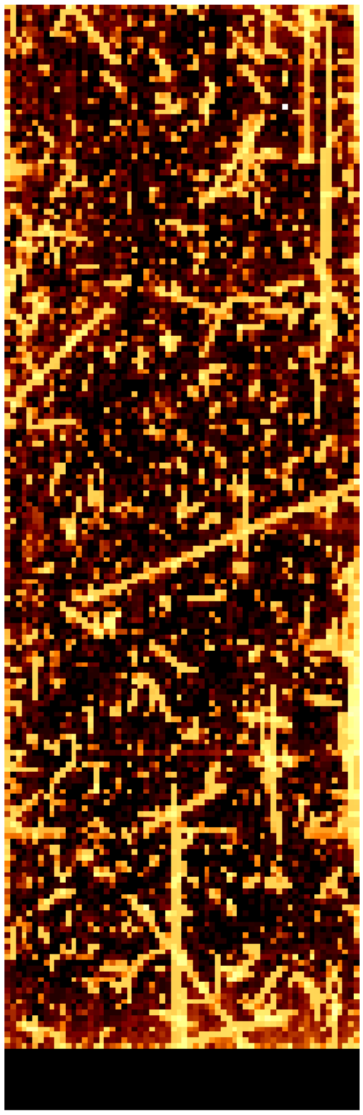

Figure 2.25: Image taken with the EPIC-pn camera on *XMM-Newton* (Wille, 2011). The image displays all events accumulated during an entire observation. It does not contain any bright X-ray sources and is therefore dominated by background events. Several cosmic rays crossing the detector quasi-parallel to its surface can be seen as long bright streaks.

Detector Defects

Due to defects in the crystal lattice, a semiconductor detector can contain electron traps or pixels with increased dark current. These so-called cold or hot pixels either give rise to a loss of signal charge or produce charge despite the absence of photon absorption. In contrast to hot pixels with a steady increased dark current, flickering pixels exhibit random temporal variations in their dark current (Hopkinson, 1992; Grant, 2011).

Such defects can be caused by interactions of cosmic particles or micrometeorites with the Si substrate. They can be detected with appropriate algorithms monitoring the measured signal in individual pixels over a large number of exposure frames (Wille, 2011). The fully depletion of the Si substrate allows illumination of detectors from the backside. This method on the one hand improves the sensitivity for low energetic photons and on the other hand protects the electronic structure on the front side of the detector from the incident radiation, especially from soft protons imaged through the X-ray optics. They have to penetrate the whole Si bulk before they can damage the transfer channel for the signal charge (Castelli et al., 1991; Nartallo et al., 2000; Strüder et al., 2001; Grant, 2011). However, the fraction of split events slightly increases for backside illuminated devices since the charge cloud can further disperse before the electrons are confined by the electrical potential of the pixel structure.

In microcalorimeter devices the quality of individual sensors can fluctuate from pixel to pixel, including some pixels with better and worse energy resolution. This effect has to be taken into account in the calibration and the analysis of the measured data.

Optical Photons

Apart from X-rays, also optical photons can be absorbed in the detector substrate. In semiconductor devices they can usually only excite single electron-hole pairs because of their low energy. However, for observations of optically bright sources a large number of optical photons can produce a significant contributing to the measured signal and therefore distort the observed spectrum. Analogously to pile-up the generated signal is added to the signal produced by X-rays (Turner et al., 2001). The effect of this so-called optical loading can be reduced by appropriate filters for optical light and by calculating and subtracting offset maps from the measured data (Kendziorra et al., 1999).

CHAPTER 3

SIMULATION SOFTWARE

3.1 Motivation

Most modern X-ray telescopes are mounted on satellites or other spacecrafts and are therefore quite expensive. It is difficult or even impossible to access them for maintenance after the launch. Due to these circumstances, it is necessary to fully understand and test a new telescope even before its construction, in order to make sure that it meets the scientific requirements. In this analysis simulations play an important part.

Apart from the development of a new instrument, simulations of existing detectors are very useful to support the scientific analysis of measurements. For instance, particular detector effects can be investigated in order to understand the impact of the instrument design on the scientific data. Simulations can also help to check, e.g., the completeness of a survey performed with an existing telescope.

The importance of simulations for the technical development as well as the scientific analysis is supported by the large number of different existing simulation tools. Since most of the available software is either specialized for particular telescopes and detectors, it can hardly be used for a different analysis than originally intended. For instance, Martin (2009) describes a simulation tool for the WFI and the HTRS on *IXO* based on the Interactive Data Language (`IDL`)[1]. This software implements detector-specific features in a very realistic way, which enables a detailed comparison between simulated data and measurements with detector prototypes. But this approach also complicates the implementation of different instrument concepts with the same software.

A commonly used simulation software, which is applicable for a large variety of future X-ray telescopes such as *IXO/ATHENA*, *Astro-H* (Takahashi et al., 2010), *Generation-X* (*Gen-X*, Cameron et al., 2004), *Nuclear Spectroscopic Telescope ARray* (*NuSTAR*, Harrison et al., 2010), and *High-Resolution Microcalorimeter X-ray Imaging Rocket* (*Micro-X*, Wikus et al., 2010), is `simx`[2]. It is developed by R. Smith and comprises various detector models. With its intuitively usable interface `simx` provides quick access to simulations of observations with the implemented telescope models. The selected approach allows to obtain an estimate on the scientific output of observations with various X-ray instruments. However, some technical investigations require a more advanced description of particular instrument-specific features, such as the readout mode, pile-up effects, or the attitude of the telescope in order to simulate a slew motion, such as in the eRASS.

The main goal of the work performed in the course of my thesis was the development of

[1] `http://www.ittvis.com/`

[2] `http://hea-www.harvard.edu/simx/`

a generic Monte Carlo simulation software that is suitable to model different imaging X-ray instruments, but also provides more sophisticated models of detector-specific features than most common analysis tools. This software package is called SImulation of X-ray TElescopes (SIXTE). It is implemented as a toolbox providing generic telescope and detector models to investigate technical and scientific issues for existing and future instruments with a focus on imaging telescopes. However, in addition to a model for Wolter optics, it also comprises some tools to construct numerical mock-ups of collimating instruments, for some particular mission designs. Some of the functionality of the simulation is provided in the separate SIMPUT library, which is used by the SIXTE package. As a simplification I often only use the name of the actual simulation software package SIXTE, neglecting the fact that SIXTE in many points relies on routines provided by the SIMPUT library. This chapter provides an overview of both SIXTE and SIMPUT and the implemented features and introduces the individual tools required for a simulation run.

The software is based on an eROSITA simulation developed in the course of my diploma thesis (Schmid, 2008) and has been extended to other X-ray instruments (Schmid et al., 2010). Starting with eROSITA, I have introduced additional flexibility in order to be able to define numerical mock-ups for various instruments. With the developed software I have performed different studies for eROSITA, *IXO*, and *ATHENA*. Examples for applications of SIXTE to these missions are displayed in Chaps. 4 and 5.

In Chapter 2 different instrument categories have been introduced. The mirrors of most current imaging telescopes are based on the Wolter type I geometry (Wolter, 1952a). However, the parameters for the individual missions can be very different. The variety among the implemented detector concepts is even larger. Nevertheless the SIXTE software package provides a generic model, which can be adjusted to most of the common types.

The setup of the instrument configuration in the software package relies on some common properties of the popular detector types. The generic model can be specialized to a particular mission by defining characteristic parameters in an XML format such that individual properties can be easily adjusted without modifying the program code itself. This property is especially useful during the study phase of an instrument, when different parameter constellations have to be investigated.

In addition to the generic approach of using XML files for the instrument configuration, the software is developed according to a modular concept such that individual components can be exchanged easily. This is sometimes necessary if a special instrument cannot be described with the required accuracy using the generic model. In that case a specialized module for the respective instrument can be inserted.

Apart from flexibility, another important objective of SIXTE is to provide a framework for simulations with affordable computational effort, which is still physically accurate enough to study instrumental effects. In contrast to an elaborate ray-tracing code, the implemented algorithms are able to run on a standard computer in approximately real time or even faster. For instance, a simulation of the eRASS is required to be performed in significantly less than the four years of the real survey.

The design of SIXTE follows a trade-off between physical accuracy and computational efficiency. On the one hand, some simplifications are required, which, however, have only a minor impact on the accuracy of the implemented instrument models. For instance, the processes which contribute to the energy resolution of a detector are replaced by a randomization based on the particular RMF. On the other hand, a detailed description of the readout process is required for the analysis of pile-up and similar detector-related effects. For the eRASS the dependence of the PSF on the energy and off-axis angle of individual photons and the attitude of the telescope play an important role. With these features SIXTE provides a suitable framework

for the investigations presented in this work.

3.2 Functionality

The basic requirement for the development of the presented simulation software package was to provide a generic tool to perform fast and accurate simulations of astronomical X-ray observations with different satellite-based telescopes. The main purposes of the simulation are the investigation of the influence of instrument-specific properties on the quality of the scientific data and the generation of realistic test data, which can be used for the development and the verification of scientific analysis software.

Therefore the software must provide a sufficiently accurate model of the respective X-ray instrument. In addition a high flexibility is required to fulfill the generic approach and to be able to simulate all possible observation scenarios. The presented software combines these two requirements.

The simulation is based on individual photons characterized by their energy, arrival time at the instrument, and their direction of origin. During the simulation process the photons are manipulated by different instruments models, which can be summarized as the telescope and the detector model. The main output of the simulation is an event file, as it is available for most real X-ray telescopes. It contains individual detected photon events characterized by the measured signal, the time of the detection, and the indices of the affected pixel. The event file can be further processed with standard analysis tools in order to obtain images, energy spectra, or light curves for the simulated observations.

In order to achieve numerical efficiency, the models in the simulation do not follow a physically exact ray-tracing implementation but are based on some simplifying assumptions, which, nevertheless, still guarantee the required accuracy. For instance, the imaging process is implemented via a randomization process based on the PSF of the telescope, but not on the detailed alignment of the individual mirror shells. The PSF itself can be obtained either from measurements or from elaborate ray-tracing simulations providing the physical basis for this approach.

Due to this concept, complicated physical processes such as the imaging of an X-ray photon on a particular surface or the absorption of a photon in a solid state detector are hidden in the respective calibration data. Therefore the numerical effort required for a detailed ray-tracing of such phenomena is avoided. This simplification allows to investigate scientific issues with large numbers of photons in a reasonable time frame and with an accuracy which is still sufficient for the desired analysis. The simulated photon events still can be assumed to match the data from the real telescope with negligible deviations. The justification of this assumption is shown in this work by comparing simulated data with measurements.

The demand of flexibility also plays a key role in the presented simulation software, since there is a large variety of currently planned and future X-ray missions, which have to be investigated via simulations. Therefore the implemented models should be adjustable to different telescope concepts. This issue is solved by a modular structure of the software package with separate tools for the individual tasks. For instance, the algorithms responsible for the generation of a photon sample, the imaging by the X-ray telescope, and the detection of the photons are implemented separately.

In order to set up a full simulation for an instrument, a pipeline is compiled from the individual tools. If a particular instrument cannot be described with the available means, the respective tool in the pipeline can be easily replaced. For instance, the telescope model for Wolter type I telescopes can be replaced in order to construct a numerical mock-up of a collimating instrument, while the algorithm for producing X-ray photons from a catalog of sources remains the same. In

addition, the instrument models use calibration data provided according to common file formats, which are used by the different instruments and can be exchanged easily.

For a simulation of an observation of an astronomical X-ray source based on individual photons, the following three steps have to be addressed:

- generate a photon sample
- model the imaging process of the photons by the optical components of the telescope
- model the detection process of the photons

The issues related to these steps and the implemented solutions are discussed in the following.

3.2.1 Photon Sample

Since the SIXTE software works with individual photons, it requires a sample of X-ray photons which can be processed by the subsequent mirror and detector models. Depending on the specific application, this sample needs to have realistic properties such as a proper energy spectrum and arrival times following a Poisson distribution. This section provides an overview of the issues related to these requirements.

In order to be able to generate a realistic sample of X-ray photons, a suitable description of the observed sources has to be provided. The SIXTE software relies on the SIMPUT format (Schmid et al., 2011a), which is described in Sec. 3.3.1 and provides various models to define simple as well as sophisticated X-ray sources. A SIMPUT file contains a catalog with either a single or multiple source definitions, providing all required data to construct a proper photon sample.

The input catalog can cover a much larger area on the sky than the FOV of the telescope such that the same catalog can be used for different simulations. The photon generation algorithm produces a list of X-ray photons for all sources which are inside or close to the FOV of the telescope. Sources far away from the FOV are neglected, since their photons are usually blocked by the telescope structure. The photon sample resembles the energy spectra of the particular sources, their brightness, and their positions. It is stored in a list ordered by the arrival time of the photons at the telescope. An overview of the photon generation process is given in Fig. 3.1. Basically the following tasks have to be performed:

- select all visible sources
- determine the number and arrival times of the photons
- determine the energies of the photons
- determine the directions of origin of the photons

The detailed implementation of the individual steps are described in the following.

Source Selection

The catalogs of input sources provided to the simulation might contain many more sources than required for a particular observation. For instance, for a pointed observation only a minor fraction of the sources contained in a source catalog covering the whole sky will be observable. And even in an all-sky slew survey such as the eRASS not all sources are visible at the same time. Therefore computation time can be saved if the simulation only generates photons which are visible inside the FOV of the respective instrument at their arrival time at the telescope.

For that purpose the simulated time interval is split up into minor chunks with a duration of about 1 s, and the responsible algorithm selects all sources which are inside or close to the FOV during this interval. In fact photons are generated for all sources which are separated from the telescope axis by less than 120 % of the radius of the FOV. The margin of 20 % on the FOV radius has been implemented in order to account for close-by sources, since they might enter the

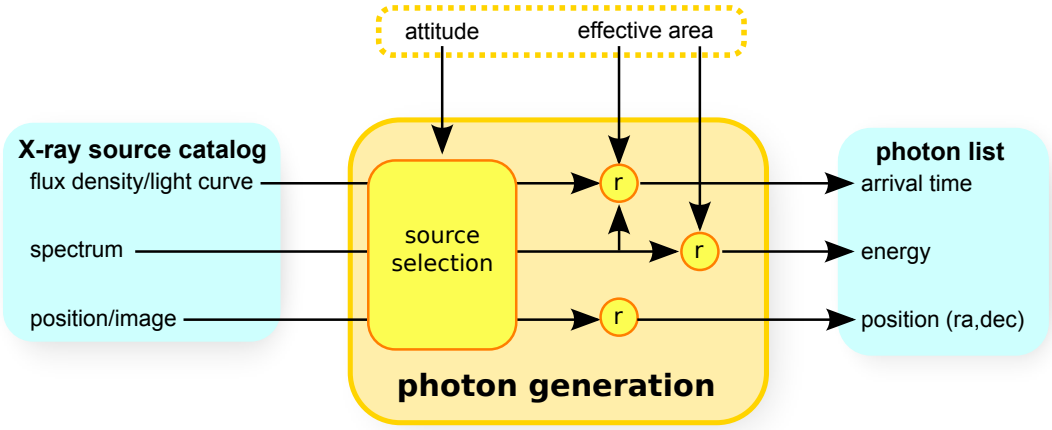

Figure 3.1: Schematic layout of the photon generation process. The small circles with an "r" represent a randomization process. Based on the telescope attitude, only X-ray sources inside or close to the FOV are selected from the catalog. For these sources photons are generated and stored in a list. For each individual source the photon arrival times are obtained from a Poisson randomization process with an average rate determined by the flux density in a particular range of the energy spectrum and the ARF of the instrument. The photon energies are randomly distributed according to the overall shape of the input spectrum. For point-like sources the direction of origin of each photon is equivalent to the source position. For extended sources the direction is obtained from a randomization process based on the spatial distribution of the source flux defined by the respective image.

FOV due to a telescope motion during the regarded time interval of 1 s.[3]

For source catalogs containing a large number of X-ray sources the selection of all sources close to the FOV might be computationally challenging. In order to simulate the eRASS, for instance, an AGN catalog with several million sources is required. Due to the homogeneously distributed positions of these sources on the unit sphere, a simple linear sorting scheme, which would make the search easier, is not applicable.

One possible approach providing a fast search for sources in a particular region of the sky would be the sorting of the source position according to a pixelization scheme such as the Hierarchical Equal Area isoLatitude Pixelization (HEALPix, Górski et al., 2005). It allows to address the individual pixels covered by the FOV via appropriate indices. However, in order to avoid overheads, a suitable grid with a pixel size of the same order as the FOV of the telescope has to be selected.

An alternative sorting scheme providing a comparably fast access to the individual sources are k-d trees (Bentley, 1975; Friedman et al., 1977), where k is the dimension of the regarded space. In contrast to HEALPix, they do not rely on a discretization of the positions of the sources by a pixel scheme with a fixed size. Therefore the sorting of the sources is independent of the size of the FOV of the particular instrument. For optimized k-d trees the computational effort to search for sources inside a certain radius around a particular location scales logarithmically with the total number of sources N in the sample (Friedman et al., 1977; Preparata & Shamos, 1985). The numerically challenging task of building up an optimized k-d tree from the source catalog scales as $N \log N$. This operation has to be performed only once at the beginning of a simulation run.

The construction of a k-d tree is described, e.g., by Moore (1991). For a 2-dimensional scenario

[3]Photons from X-ray sources outside but close to the FOV actually can reach the detector by single-reflections in the mirror system if they are not prevented by suitable baffles. However, this effect is neglected in the presented simulations.

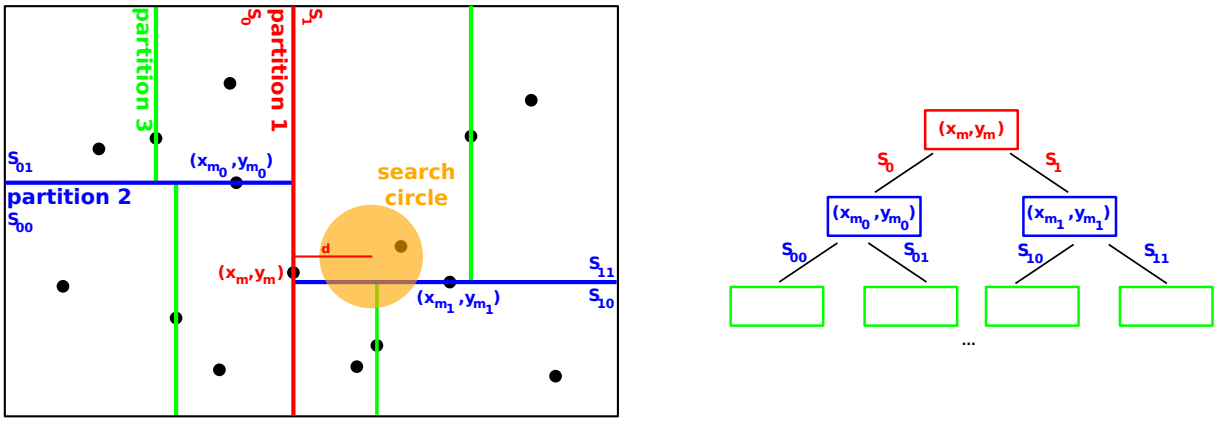

Figure 3.2: Structure of a 2-d tree. The total search volume containing the source positions (black dots) is iteratively divided in sub-volumes. Each partition of a volume is performed at the median of the subset of points with respect to either the x or y coordinate in an alternating sequence. The orange circle denotes the search circle, which can be identical to the FOV or a slightly larger radius around the telescope pointing direction, in order to include also sources close to the FOV. Since the distance of the telescope pointing direction to the "partition 1" line corresponding to $x = x_m$ is larger than the search radius, the left part of the tree corresponding to S_0 can be neglected in the range search.

the process is illustrated in Fig. 3.2: Starting from a sample of N points characterized by their coordinates $S = \{(x_i, y_i), i \in (0, ..., N-1)\}$, the sample is sorted according to the x coordinates of the individual points x_i. Then the median element m of this ordered list is selected and the remaining elements are split into two sub-samples according to $S_0 = \{x_i | x_i \leq x_m\}$ and $S_1 = \{x_i | x_i > x_m\}$. The median element m itself is neither included in S_0 nor in S_1 but handled separately. Both sub-samples are then ordered according to their y coordinate and again split with respect to their median elements m_0 and m_1, resulting in the four sub-samples $S_{0,0}, S_{0,1}, S_{1,0}, S_{1,1}$. Those sub-samples are again sorted with respect to their x coordinate and split into eight smaller sub-samples. This split process with alternate use of the x and y coordinate is repeated recursively, until the sub-samples contain at most one element. The median elements, which are not included in the sub-samples produced by the splitting processes, are inserted as elements of a tree structure, as indicated in Fig. 3.2. Each element can have up to two child elements, which correspond to the median elements of the subsequent splitting process of the sub-samples. Leaf elements at the end of a branch do not have any children, since the corresponding sub-samples are empty.

Although the source positions can be given by only two coordinates (e.g. right ascension and declination), I am using their Cartesian coordinates on the unit sphere of 3-dimensional space for the construction of a k-d tree, i.e., $k = 3$, in order to allow a fast distance calculation between two arbitrary locations. The construction of the corresponding 3-d tree is performed analogously to the case $k = 2$, using alternating x, y, and z coordinates for the splitting of the source positions into sub-samples. I am applying the quick sort algorithm (Hoare, 1962) for the sorting of the samples of source positions.

In order to identify all sources located within or close to the FOV of the telescope, a range search with an appropriate search radius is performed. The search is started at the root of the tree, corresponding to the median element m in Fig. 3.2, and descends iteratively down into the branches of the tree, excluding all branches which only contain sources far from the FOV. For instance, in Fig. 3.2 the left branch corresponding to S_0 can be excluded, since the distance from the telescope pointing direction to the delimiting border of the sub-sample corresponding to $x = x_m$ is larger than the search radius. The algorithm based on the simple exclusion of

irrelevant branches enables a fast search for sources within the requested radius, scaling as $\log N$.

Energy Spectrum

The energies of the generated photons are distributed according to the spectra defined for the sources in the SIMPUT catalog and the effective area of the respective instrument. Although the SIMPUT format provides different ways to specify the spectrum of a source, in the presented simulations spectra are usually defined by the observed distribution of the photon flux density $P(E)$ given in the units photons $\mathrm{s}^{-1}\,\mathrm{cm}^{-2}\,\mathrm{keV}^{-1}$.

In order to obtain the photon energy spectrum for a particular instrument $p(E)$, the flux density distribution has to be multiplied with the respective energy-dependent on-axis ARF:

$$p(E) = P(E) \cdot \mathrm{ARF}(E) \tag{3.1}$$

In general the spectrum is not given as an analytic function, but is defined on a particular energy grid $P(E_i)$ in order to be stored in the SIMPUT file. The ARF in the typical format specified by George et al. (1998, 2007) is given for discrete energy bins $\mathrm{ARF}(E'_{j,\mathrm{low}}$ to $E'_{j,\mathrm{high}})$. In the simulation the responsible algorithm calculating the product in Eq. (3.1) is dealing with this discrete energy grids by applying interpolations of the spectrum $P(E_i)$ to the energy bins of the ARF. The resulting photon flux distribution $p(E'_{j,\mathrm{low}}$ to $E'_{j,\mathrm{high}})$ is given for the energy bins of the ARF. In order to enable the determination of random energy values, it is converted to a normalized photon flux distribution function:

$$p'_k = \frac{1}{\sum_{j=0}^{N-1} p(E'_{j,\mathrm{low}} \text{ to } E'_{j,\mathrm{high}})} \sum_{j=0}^{k} p(E'_{j,\mathrm{low}} \text{ to } E'_{j,\mathrm{high}}) \tag{3.2}$$

where N is the total number of energy bins of the ARF. Using p'_k the determination of random photon energies according to the specified distribution can be achieved by applying the inversion method (e.g., Deák, 1990, p. 68ff.; Gould et al., 2006, Chapter 11). For each photon a uniformly distributed random number $r \in [0, 1)$ is selected. Using a binary search algorithm, the corresponding energy is obtained as:

$$l = \min\{k | p'_k > r\} \tag{3.3}$$

where l is the index of the respective energy bin of the ARF[4].

The spectra for the source definition in the SIMPUT catalog can be easily generated from appropriate spectral models using standard data analysis software for X-ray astronomy, such as the Interactive Spectral Interpretation System (`ISIS`[5], Houck & Denicola, 2000, 2002) or `Xspec`[6] (Arnaud, 1996). It is important to note that the absolute values of the spectra are neglected by the randomization algorithm due to the normalization applied in Eq. (3.2). Only the spectral shape is taken into account such that the same spectrum can be used for different sources with different brightness but the same spectral type. The absolute count rate for a particular source is calculated from the reference flux of each individual source given in the source catalog, as shown in the following.

[4] The simulation uniformly distributes the corresponding photon energy between $E'_{l,\mathrm{low}}$ and $E'_{l,\mathrm{high}}$.

[5] `http://space.mit.edu/cxc/isis/`

[6] `http://heasarc.nasa.gov/xanadu/xspec/`

Arrival Times

Since the simulation produces time-resolved data, the sample of generated X-ray photons also has to comprise the arrival time of each photon at the telescope, in addition to its energy and its direction of origin. The average photon rate R for a particular source is determined from the energy flux density F_X specified in the SIMPUT catalog for a particular reference energy band, the respective spectrum, and the on-axis ARF of the instrument according to the following formula:

$$R = \frac{F_\mathrm{X}}{\int\limits_{E_\mathrm{min}}^{E_\mathrm{max}} P(E)\, E\, \mathrm{d}E} \cdot \int\limits_0^\infty P(E)\, \mathrm{ARF}(E)\, \mathrm{d}E \tag{3.4}$$

where E_min and E_max are the limits of the reference energy band. The number N of photons generated within a certain time interval T is determined by Poisson statistics:

$$P_\lambda(N) = \frac{\lambda^N}{N!}\, \mathrm{e}^{-\lambda} \tag{3.5}$$

with

$$\lambda = R \cdot T \tag{3.6}$$

The probability density of the time intervals between subsequent photons, as required by the simulation, can be determined easily according to Knoll (2010), p. 99f. The probability of the next event to take place within $\mathrm{d}t$ after an interval of Δt is the product of the probability to have no event during the interval Δt according to the Poisson distribution and the probability to have a photon during the interval $R\,\mathrm{d}(\Delta t)$:

$$k(\Delta t)\,\mathrm{d}(\Delta t) = \frac{(R \cdot \Delta t)^0\ \mathrm{e}^{-R\cdot\Delta t}}{0!} \cdot R\,\mathrm{d}(\Delta t) = R \cdot \mathrm{e}^{-R\cdot\Delta t}\,\mathrm{d}(\Delta t) \tag{3.7}$$

The corresponding probability distribution $K\,(\Delta t)$ is obtained by integration:

$$k\,(\Delta t) = R\mathrm{e}^{-R\Delta t} \tag{3.8}$$

$$K\,(\Delta t) = \int\limits_0^\infty k\,(\Delta t)\ \mathrm{d}(\Delta t) = 1 - \mathrm{e}^{-R\Delta t} \tag{3.9}$$

with the average photon rate R. Such a distribution can be easily generated by selecting the time intervals $(\Delta t)_i$ between subsequent photons according to the inversion method (e.g., Deák, 1990, p. 68ff.; Gould et al., 2006, Chapter 11):

$$(\Delta t)_i = -\frac{1}{R} \ln\,(1 - u_i) \tag{3.10}$$

where u_i are uniformly distributed random numbers in the interval from $[0, 1)$. Because of the uniform distribution of the u_i, the following formula can be used instead:

$$(\Delta t)_i = -\frac{1}{R} \ln\,(u_i) \tag{3.11}$$

In Fig. 3.3 the distribution of time intervals between subsequent photons and the number of photons within a time interval of $T = 10\,\mathrm{s}$ are shown for a photon rate of $R = 1\,\mathrm{photon}\,s^{-1}$. The data from the simulated photon sample agree very well with the theoretical values.

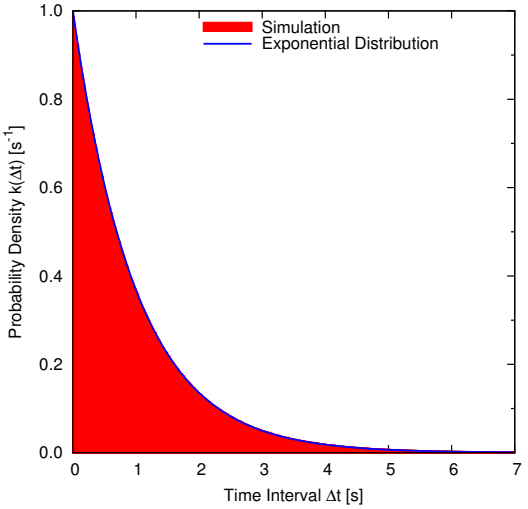

(a) Probability density for the time intervals between subsequent photons. The theoretical exponential distribution is calculated according to Eq. (3.9) with $R = 1\,\text{photon}\,\text{s}^{-1}$.

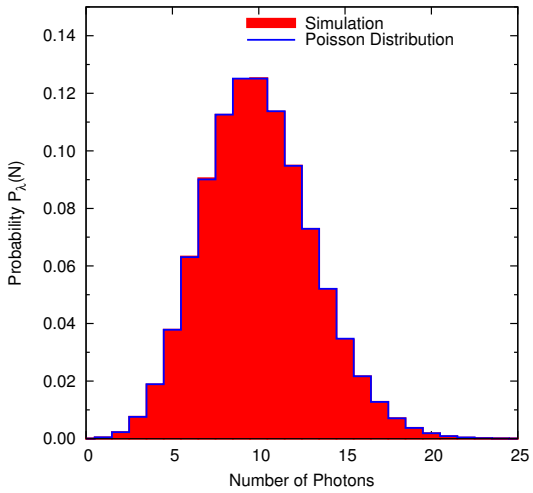

(b) Distribution of the number of photons within a time interval of 10 s. The theoretical Poisson distribution is calculated according to Eqs. (3.5) and (3.6) with R=1 photon s^{-1} and T=10 s.

Figure 3.3: Comparison of the photon arrival times for a simulated sample and the theoretical models.

The presented approach works quite well for sources with a constant brightness. However, if the source brightness is a function of time described, e.g., by a light curve or a Power Spectral Density (PSD), the formula given by Eq. (3.11) might cause problems. Although the photon rate R can be determined as a function of time, a fixed value of R is used for each evaluation of Eq. (3.11). In other words, the calculation of the arrival time $t_i = t_{i-1} + (\Delta t)_i$ of the ith photon, requires the assumption of a particular value for R, which can, e.g., be chosen as $R = r\,(t_{i-1})$. Since the application of Eq. (3.11) assumes that R is constant in the interval from t_{i-1} to t_i, it does not account for any variations of the average photon rate $r(t)$ within this interval. Especially if $r(t)$ changes rapidly from small to large values, the application of Eq. (3.11) can result in a strange behavior. For instance, the transition from a low to a high photon rate can be delayed.

This problem is described by Martin (2009) and is illustrated in Fig. 3.4. In SIXTE it is avoided by calculating the photon arrival times with the Poisson arrival process generator presented by Klein & Roberts (1984), which is basically an extension of Eq. (3.11) for piecewise linear rate functions $r(t)$. For a time-variable rate function the relation given by Eq. (3.9) has to be modified:

$$K\,(\Delta t) = 1 - \exp\left[-\int\limits_{t_{i-1}}^{t_{i-1}+\Delta t} r(t)\,\mathrm{d}t\right] \tag{3.12}$$

If we again apply the inversion method as for Eq. (3.10), we obtain:

$$u_i = 1 - \exp\left[-\int\limits_{t_{i-1}}^{t_i} r(t)\,\mathrm{d}t\right] \quad \text{with} \quad t_i = t_{i-1} + (\Delta t)_i \tag{3.13}$$

$$\ln\,(1 - u_i) = -\int\limits_{t_{i-1}}^{t_i} r(t)\,\mathrm{d}t \tag{3.14}$$

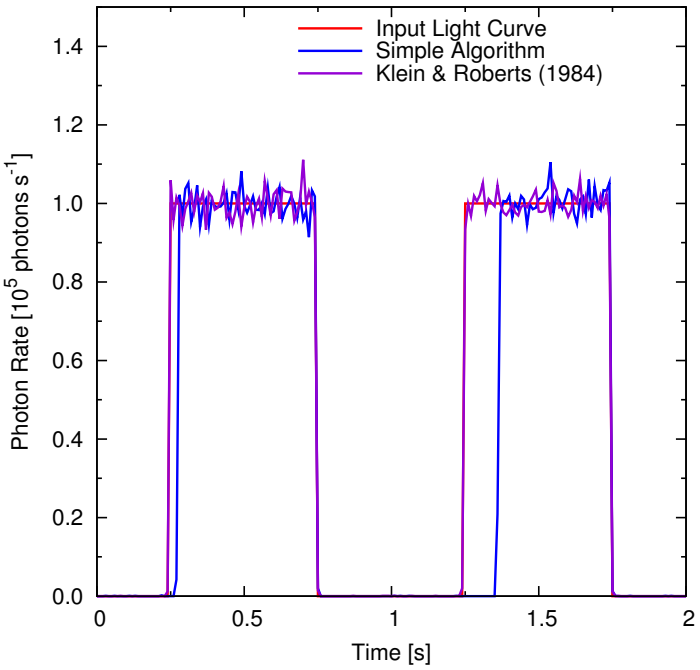

Figure 3.4: Light curve generation with different Poisson arrival process generators. The red curve displays the input light curve. The blue curve is the simulated photon rate using a simple algorithm based on Eq. (3.11) with $R = r(t_{i-1})$. This algorithm is not suitable for rapidly increasing photon rates. As shown in the plot, the rising edge can be significantly delayed. The algorithm presented by Klein & Roberts (1984) does not have this problem, but properly reproduces the shape of the input light curve, apart from some statistical fluctuations.

In the SIMPUT format the time-dependence of the rate function $r(t)$ is determined by the product of the light curve $l(t)$ of the respective source, representing the time-dependence of the relative flux variations, and the reference photon rate R, which is obtained according to Eq. (3.4) as for a constant source:

$$r(t) = R \cdot l(t) \tag{3.15}$$

If $r(t)$ is a piecewise linear function, it can be written as

$$r(t) = a_n t + b_n \quad \text{for} \quad s_n \leq t \leq s_{n+1} \tag{3.16}$$

with the supporting points s_n. Inserting Eq. (3.16) in Eqs. (3.13) and (3.14) one obtains

$$u_i = 1 - \exp\left[-\frac{a_n}{2}\left(t_i^2 - t_{i-1}^2\right) - b_n\left(t_i - t_{i-1}\right)\right] \tag{3.17}$$

$$\ln\left(1 - u_i\right) = -\left[\frac{a_n}{2}\left(t_i^2 - t_{i-1}^2\right) + b_n\left(t_i - t_{i-1}\right)\right] \tag{3.18}$$

under the assumption that $s_n \leq t_{i-1} \leq s_{n+1}$ and $t_i \leq s_{n+1}$. Equation (3.18) yields

$$t_i = \begin{cases} t_{i-1} - \frac{1}{b_n}\ln\left(1 - u_i\right) & , \; a_n = 0 \\ \frac{-b_n + \sqrt{b_n^2 + a_n^2 t_{i-1}^2 + 2a_n b_n t_{i-1} - 2a_n \ln(1-u_i)}}{a_n} & , \; a_n \neq 0 \end{cases} \tag{3.19}$$

The case $a_n = 0$ is analogous to Eq. (3.10). However, Eq. (3.19) only holds for $t_i \leq s_{n+1}$. But t_i exceeds the interval between the two supporting points s_n and s_{n+1} if $u_i > w_{n+1}$ with

$$w_{n+1} = 1 - \exp\left[-\frac{a_n}{2}\left(s_{n+1}^2 - t_{i-1}^2\right) - b_n\left(s_{n+1} - t_{i-1}\right)\right] \tag{3.20}$$

Therefore it has to be considered that

$$\int_{t_{i-1}}^{t_i} r(t)\,\mathrm{d}t = \int_{t_{i-1}}^{s_{n+1}} r(t)\,\mathrm{d}t + \int_{s_{n+1}}^{t_i} r(t)\,\mathrm{d}t \tag{3.21}$$

According to Eq. (3.14) this can be written as

$$-\ln(1-u_i) = -\ln(1-w_{n+1}) - \ln(1-u'_i) \tag{3.22}$$

Therefore one obtains

$$u'_i = \frac{u_i - w_{n+1}}{1-w_{n+1}} \tag{3.23}$$

and

$$t_i = \begin{cases} s_{n+1} - \frac{1}{b_{n+1}} \ln(1-u'_i) & , \; a_{n+1} = 0 \\ \frac{-b_{n+1} + \sqrt{b_{n+1}^2 + a_{n+1}^2 s_{n+1}^2 + 2a_{n+1}b_{n+1}s_{n+1} - 2a_{n+1}\ln(1-u'_i)}}{a_{n+1}} & , \; a_{n+1} \neq 0 \end{cases} \tag{3.24}$$

If t_i also exceeds s_{n+2}, the steps defined by Eqs. (3.23) and (3.24) have to be applied iteratively, by inserting u'_i instead of u_i in Eq. (3.23) in order to obtain the next value for u'_i. The step defined by Eq. (3.23) avoids the problem of the delayed count rate increases shown in Fig. 3.4 for the simple algorithm based on Eq. (3.11).

The numerical implementation of the algorithm for piecewise linear rate functions is explicitly described by Klein & Roberts (1984), including a sample application of the arrival rate of customers at a lunch wagon.

Power Spectral Density

For time-variable sources the time-dependence of the photon rate can be given explicitly in the SIMPUT file by a light curve $l(t)$. Although this method is quite suitable to model, e.g., phenomena with a typical time-evolution such as type-I X-ray bursts or the periodic oscillations of X-ray pulsars with a fixed time offset, a PSD is more convenient to describe random variations such as noise.

A single PSD can be used for different sources to model statistically-independent brightness variations. In order to be usable for the photon generation process, the PSD has to converted to a light curve by the simulation software. An appropriate algorithm for this task is presented by Timmer & König (1995). It is implemented in the SIMPUT library. The therefore necessary Gaussian distributed random numbers are obtained via the Box-Muller method (Box & Muller, 1958; Gould et al., 2006, Chapter 11), and the Fast Fourier Transformation (FFT) is performed with the appropriate routines of the `fftw`[7] library. For a PSD included in a SIMPUT file the normalization proposed by Miyamoto et al. (1992) is obligatory such that the fractional root mean square (rms) can be directly determined as

$$\int_0^\infty \mathrm{PSD}(f)\,\mathrm{d}f = \left(\frac{\mathrm{rms}}{\langle l \rangle}\right)^2 \tag{3.25}$$

The rms is normalized to the mean value $\langle l \rangle$ of the light curve with length T:

$$\langle l \rangle = \frac{1}{T}\int_0^T l(t)\,\mathrm{d}t \tag{3.26}$$

An introduction to the application of PSDs in the context of BH X-ray binaries is given by Pottschmidt (2002).

[7] `http://www.fftw.org/`

Extended Sources

For point-like sources such as AGN the direction of origin of the generated photons is identical to the source coordinates. For extended sources such as galaxy clusters this approach is, of course, not sufficient, in particular for a simulation with imaging capabilities. Since extended sources can have different and complicated shapes, it is difficult to find a suitable analytical description for all possible types. Therefore extended sources in SIMPUT files are described by specifying an image of the spatial distribution of the observed flux. Such an image can, e.g., be obtained from an observation or from another simulation.

The image must be a standard Flexible Image Transport System (FITS)[8] image (Wells et al., 1981; Ponz et al., 1994; Hanisch et al., 2001; Pence et al., 2010). The values of the individual pixels of the image are regarded as a probability density for the spatial distribution of the generated photons:

$$P(k,l) = \sum_{i=0}^{k-1} \sum_{j=0}^{M-1} p_{i,j} + \sum_{j=0}^{l} p_{k,j} \quad \text{with} \quad 0 \leq k < N \wedge 0 \leq l < M \tag{3.27}$$

where N and M are the width and the height of the image, and $p_{i,j}$ is the normalized value of the pixel i,j in the image such that $P(N-1, M-1) = 1$. For each photon a uniformly distributed random number $r \in [0,1)$ is selected, and the corresponding pixel indices k,l are determined in a 2-dimensional binary search according to the following relations:

$$\begin{aligned} k &= \min\{k' | 0 \leq k' < N \wedge P(k', M-1) > r\} \\ l &= \min\{l' | 0 \leq l' < M \wedge P(k, l') > r\} \end{aligned} \tag{3.28}$$

For a sufficiently large number of simulated photons the input spatial flux distribution is reproduced with this method even for complicated source shapes.

The relation between the image pixels k,l and the corresponding coordinates in the equatorial system used by the simulation is defined by the World Coordinate System (WCS) header keywords (Greisen & Calabretta, 2002; Calabretta & Greisen, 2002) contained the respective FITS Header and Data Unit (HDU). The coordinate conversion itself is performed using the appropriate functions of the `WCSLIB`[9] library.

3.2.2 Mirror Model

After generating a sample of X-ray photons for the observed sources, the imaging process of these photons in the mirror system of the telescope has to be properly simulated. The simulation does not follow an exact ray-tracing approach of the reflections in a Wolter telescope, but uses a simplified but still sufficiently accurate model of the X-ray telescope. The most important input data are the PSF and the vignetting function provided by the corresponding calibration files (George & Yusaf, 1994, 1995). The latter can be obtained from accurate ray-tracing simulations or from laboratory measurements based on prototypes of the mirror modules in order to guarantee a realistic mirror model.

The imaging algorithm implemented in SIXTE basically consists of three steps, which are applied to each simulated photon:

- application of the vignetting function
- calculation of the ideal impact position
- PSF randomization

An overview of the process is presented in Fig. 3.5. The imaging algorithm produces a list of impact positions on the detector surface for the reflected photons.

[8] `http://fits.gsfc.nasa.gov/`

[9] `http://www.atnf.csiro.au/people/mcalabre/WCS/wcslib/`

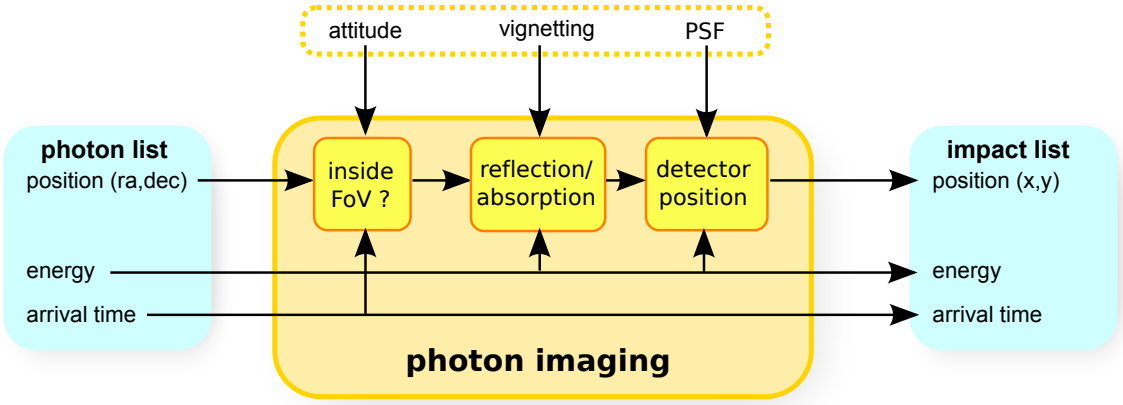

Figure 3.5: Schematic layout of the photon imaging process. For each photon its position inside the FOV is determined according to the attitude of the telescope at the arrival time of the photon[a]. Photons outside the FOV are discarded. Photons inside the FOV can either be reflected or also be discarded, according to a randomization process based on the vignetting function. The final impact position of each photon on the detector is calculated from its position inside the FOV, the focal length of the telescope, and a superimposed smearing according to the PSF.

[a]Taking into account the time-dependency of the telescope's attitude is one of the major advantages of SIXTE in comparison to many other simulation tools for X-ray telescopes. They are mostly designed for pointed observations and are therefore not suitable to simulate a slew survey with a constantly changing viewing direction, such as the eRASS.

Vignetting Correction

Based on the attitude of the telescope and the direction of origin of a photon its off-axis and azimuthal angle with respected to the coordinate system of the telescope are determined. In case the photon lies outside the FOV it is simply discarded. For photons inside the FOV the vignetting function, which depends on the energy E, off-axis angle θ, and azimuthal angle φ of the photon, defines the probability that the photon is properly reflected by the mirror system. This is implemented as a discrete randomization process, i.e., each photon is either reflected if $\text{vignetting}(E, \theta, \varphi) < r$ with a uniformly distributed random number $r \in [0, 1)$, or discarded otherwise.

The particular vignetting function is selected according to the simulated telescope. For eROSITA and *ATHENA* the data presented in Fig. 2.4 are used[10].

Ideal Impact Position

Depending on the off-axis angle θ and the azimuthal angle φ of a reflected photon, its ideal impact position on the detector assuming a perfect optical system can be determined according to Eq. (2.2) by taking into account the focal length f of the telescope.

[10]As explained in Sec. 2.2, the ray-tracing simulation by P. Friedrich, which the optical model for eROSITA is based on, does not implement the baffles in front of the telescope. Therefore the currently applied vignetting function also includes some photons that will be mostly absorbed by the baffles in the real telescope. Unfortunately these photons cannot be disentangled from the output of the ray-tracing simulation such that the obtained values of the vignetting function are larger than expected for large off-axis angles.

PSF Randomization

In general the real impact position of the photon on the detector deviates from its ideal value determined by Eq. (2.2). In the simulation this is accounted for by adding a deviation $(\Delta x, \Delta y)$ to the ideal impact position in order to obtain a realistic value:

$$\begin{aligned} x' &= x + \Delta x \\ y' &= y + \Delta y \end{aligned} \tag{3.29}$$

The deviation terms Δx and Δy are obtained by a 2-dimensional randomization process modeling the PSF of the telescope. According to its definition in Sec. 2.2.1, the PSF defines the image of a point source as seen by the telescope. In general it depends on the photon energy, the off-axis angle, and the azimuthal angle.

In the current implementation the photon imaging module only takes into account the energy and off-axis angle-dependence. The dependence on the azimuthal angle is neglected, since this information is not contained in the available models for eROSITA and *IXO*/*ATHENA*. For particular X-ray telescopes several PSF images are provided on a 2-dimensional parameter grid for different photon energies E_i and off-axis angles θ_j. All images are centered on the ideal impact position corresponding to a certain off-axis angle $\theta = \theta_i$ and the azimuthal angle $\varphi = 0$ according to Eq. (2.2). In order to achieve short processing times, each PSF image is converted to a 2-dimensional probability distribution analogous to the flux maps of extended sources according to Eq. (3.27). For each incident photon having an energy E with $E_i \leq E < E_{i+1}$ and an off-axis angle θ with $\theta_j \leq \theta < \theta_{j+1}$ two indices are selected according to

$$k = \begin{cases} i & , \; r < \frac{E - E_i}{E_{i+1} - E_i} \\ i+1 & , \; \text{else} \end{cases} \tag{3.30}$$

$$l = \begin{cases} j & , \; s < \frac{\theta - \theta_j}{\theta_{j+1} - \theta_i} \\ j+1 & , \; \text{else} \end{cases} \tag{3.31}$$

where r and s are uniformly distributed random numbers in the interval $[0, 1)$. The indices k and l identify a particular PSF image for a certain energy and off-axis angle within the available set. From the probability distribution defined by this PSF image with the indices k and l, the deviation $(\Delta x, \Delta y)$ from the ideal impact position determined by Eq. (2.2) is obtained in a 2-dimensional randomization process analogous to the selection of a random pixel from a flux map according to Eq. (3.28).

For most simulations of *IXO* and *ATHENA* presented in Chapter 5 I have used a simple 2-dimensional Gaussian model for the PSF according to Eq. (2.15). At the current early stage of the mission study elaborate models of the PSF have not been available. For the analysis performed on eROSITA I have used a numerical model for the PSF, which is based on a ray-tracing simulation performed by P. Friedrich (priv. comm.). It comprises 21 PSF images for 7 different off-axis angles ($\theta \in \{0, 5, 10, 15, 20, 25, 30\}$ arcmin), and 3 different photon energies ($E \in \{1, 4, 7\}$ keV). A selection of nine of the PSF images is displayed in Fig. 3.6. The simulated data obtained with this model are much more realistic than for a simple Gaussian PSF. An even more advanced approach would be to use measured instead of simulated data, but at the time of writing no sufficient dataset was available.

3.2.3 Detector Model

The SIXTE software package contains a generic detector model that can be used for most of the common X-ray detectors consisting of an array of rectangular pixels. The specific properties of each detector are provided in an XML description file following a particular format, as described

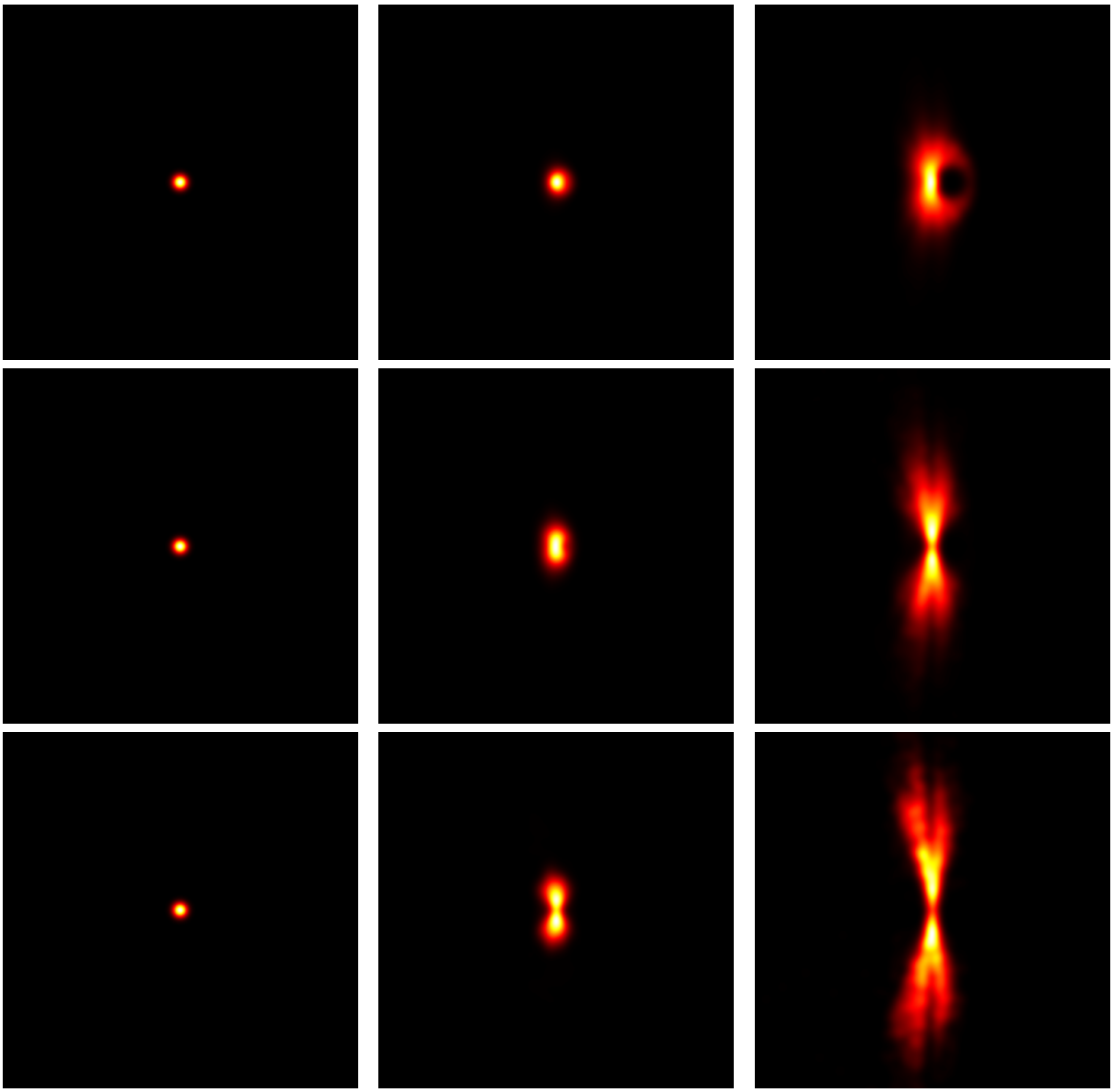

Figure 3.6: Shape of the PSF of eROSITA for different off-axis angles (θ = 0, 15, and 30 arcmin, horizontal direction) and photon energies (1, 4, and 7 keV, vertical direction) according to ray-tracing simulations performed by P. Friedrich (priv. comm.). The currently implemented model takes into account the dependence of the PSF on the off-axis angle and on the photon energy. In general the PSF also depends on the azimuthal angle due to asymmetries in the optical system, but this dependency has been neglected in the presented model.

in Appendix A.2. Apart from the generic detector model, the software package contains a separate model for the HTRS on *IXO*, since the geometry of this detector is too specific for the generic approach.

All detector models process the list of photon impacts generated by the imaging algorithm and produce a list of events measured by the detector. For each photon the affected detector pixel is determined according to the impact position, and the photon energy is converted into a measured Pulse Height Amplitude (PHA) value. The time assigned to each event is the readout time determined by the instrument operation mode. In general this value is different from the arrival time of the photon at the telescope, which is used in the photon list and in the impact list.

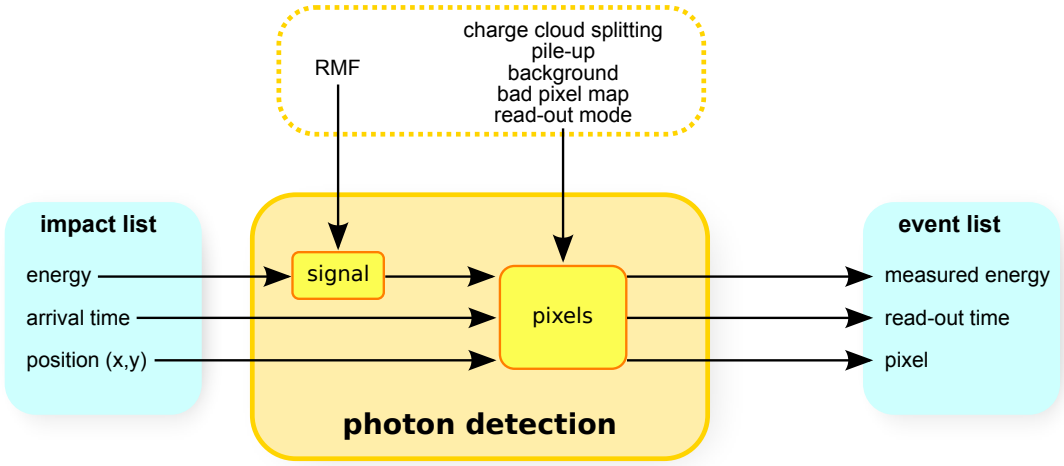

Figure 3.7: Schematic layout of the photon detection process. For each photon impact the signal produced by the absorption process is determined from the RMF. The generated charge is distributed according to the selected model among the affected pixels around the impact position. Additional background events are added. Detector effects such as bad pixels are taken into account. The signal charges collected in the detector pixels are read out according to the instrument-specific readout scheme resulting in the final event list with the measured energy, the time of the readout, and the pixel coordinates.

A single photon might result in multiple events due to charge cloud splitting between adjacent pixels. The other way round is also possible: a single event might originate from several photons hitting the same pixel during one readout cycle and therefore causing pile-up.

The detector model comprises the following functionality:

- array of pixels
- RMF randomization
- charge cloud splitting
- detector background
- detector defects
- readout scheme
- charge transfer
- thresholds

From these elements numerical mock-ups for different instruments can be assembled. The final output of the detector module is a list of individual events characterized by the time, at which they were read out, their signal, and their pixel coordinates. An overview of the detection process is presented in Fig. 3.7. A more detailed description of the implementation of the various features in the simulation software is provided in the following.

Pixel Array

All detector models consist of an array of pixels. For the generic detector model this array is rectangular and the number of pixels in x- and y-direction as well as the physical dimensions of a pixel are defined in the XML file describing the instrument.

For the HTRS on *IXO* the circular pixel geometry presented in Sec. 5.1.1 is implemented. In an early design the HTRS consisted of hexagonal pixels arranged in a honeycomb structure (Barret et al., 2004). I have originally implemented a corresponding detector model in SIXTE, but discarded it later, when the circular design was adopted.

For all detector models the layout and dimensions of the pixels are essential to determine the

pixel coordinates corresponding to the impact position of a photon.

RMF

The energy measured by a detector can be different from the energy of the incident photon. The main reason for such a deviation is the imperfection of the measurement process itself. Due to different noise components or an incomplete conversion of photon energy to electric charge in the detector, the measured signal is not a well-defined function of the photon energy (Popp, 2000; Edgar, 2011). Though, for each photon energy a probability distribution for the measured energy channels can be defined.

For astronomical X-ray instruments such detector-specific effects are usually accounted for in the RMF (George et al., 1998, 2007). At different incident photon energies the RMF provides the corresponding probability distribution of the measured energy channels. For instance, a photon with an energy of 6 keV might be detected in one out of many different channels between 5.5 and 6.5 keV according to the probability distribution described by the RMF[11].

In the simulation the detector noise and absorption features are implemented by assigning a signal equivalent to each absorbed photon, which is determined from its energy in a randomization process with a probability distribution defined by the RMF. A random energy channel is determined using the routine `ReturnChannel()`[12] in the HEAsoft software package. This routine is basically a 1-dimensional version of the algorithm applied for the randomization of the photon direction for extended sources (Sec. 3.2.1) or the impact position on the detector based on the PSF (Sec. 3.2.2). First a probability distribution function is calculated from the probability per detector channel, which is given by the RMF. Then the channel corresponding to a uniformly distributed random number $r \in [0, 1)$ is determined in a binary search according to the inversion method (e.g., Deák, 1990, p. 68ff.; Gould et al., 2006, Chapter 11).

The channel obtained from `ReturnChannel()` is converted back to the corresponding signal equivalent according to the channel-to-energy mapping defined by the `EBOUNDS` extension of the RMF (George et al., 2007), because for the subsequent simulation steps it is necessary to deal with floating point numbers instead of integer channel numbers. For instance, the splitting of the signal charge cloud among several pixels requires floating point numbers in order to avoid inaccuracies caused by rounding effects, non-zero channel offsets, or inhomogeneous bin widths.

Charge Cloud Splitting

If a photon impact takes place close to the edge of a pixel, the generated signal charge might partly drift to the adjacent pixels (Sec. 2.3.2). The simulation software contains two different models for these split events. The more generic approach assumes a 2-dimensional Gaussian charge cloud (Kimmel et al., 2006a; Martin, 2009), whereas for eROSITA a specific model developed by K. Dennerl (priv. comm.) is implemented.

Gaussian Charge Cloud Model The Gaussian charge cloud model assumes that a particular photon impact produces a 2-dimensional rotationally symmetric charge cloud. The charge distribution around the impact position $(x_\mathrm{i}, y_\mathrm{i})$ on the detector is obtained as (Popp, 2000):

$$c(x, y) = \frac{1}{2\pi\sigma^2} \cdot \mathrm{e}^{-\frac{(x-x_\mathrm{i})^2+(y-y_\mathrm{i})^2}{2\sigma^2}} \tag{3.32}$$

[11] The product of the RMF with the ARF is usually called the detector response (George et al., 1998, 2007) and is commonly used in spectral analysis of X-ray data.

[12] In the High Energy Astronomy software (HEAsoft) version `6.11.1` and previous the routine `ReturnChannel()` contains a bug affecting RMF files, in which the channel numbering does not start at zero. I discovered this error in the course of my work, reported it to the developers of HEAsoft, and applied a suitable correction in my simulation software in order to provide compatibility with older versions of HEAsoft.

The charge fraction contained in the detector pixel (n, m) defined by the corners (x_n, y_m), (x_{n+1}, y_m), (x_{n+1}, y_{m+1}), and (x_n, y_{m+1}) can be determined as:

$$c_{n,m} = \frac{1}{2\pi\sigma^2} \cdot \int_{x_n}^{x_{n+1}} \mathrm{e}^{-\frac{(x-x_\mathrm{i})^2}{2\sigma^2}} \,\mathrm{d}x \int_{y_m}^{y_{m+1}} \mathrm{e}^{-\frac{(y-y_\mathrm{i})^2}{2\sigma^2}} \,\mathrm{d}y \tag{3.33}$$

Since the typical charge cloud size ($\sigma \sim 10\,\mu$m) is smaller than the typical size of the detector pixels for the instruments analyzed in this work ($d \sim 50$–$100\,\mu$m), it can be assumed that nearly all created charge is collected in the four pixels directly surrounding the impact position. For the impact shown in Fig. 2.18 it is therefore sufficient to calculate the charge fractions in the pixels (n, m), $(n+1, m)$, $(n, m+1)$, and $(n+1, m+1)$, with the indices n, m satisfying the following relations:

$$|x_\mathrm{i} - x_{n+1}| \leq \frac{d_x}{2} \tag{3.34}$$

$$|y_\mathrm{i} - y_{m+1}| \leq \frac{d_y}{2} \tag{3.35}$$

with the pixel edge lengths $d_x = x_{n+1} - x_n$ and $d_y = y_{m+1} - y_m$. Any other pixels are assumed to be not affected by the impact. In the case of equality of Eq. (3.34) or Eq. (3.35) the indices n or m respectively are set to the values of the pixel containing the impact position of the photon. For the scenario shown in Fig. 2.18 the charge fractions in the four pixels are therefore obtained as[13]:

$$Q_x = \frac{1}{\sqrt{2\pi}\sigma} \cdot \int_{-\infty}^{x_{n+1}} \mathrm{e}^{-\frac{(x-x_\mathrm{i})^2}{2\sigma^2}} \,\mathrm{d}x \tag{3.36}$$

$$Q_y = \frac{1}{\sqrt{2\pi}\sigma} \cdot \int_{-\infty}^{y_{m+1}} \mathrm{e}^{-\frac{(y-y_\mathrm{i})^2}{2\sigma^2}} \,\mathrm{d}y \tag{3.37}$$

$$c_{n,m} = Q_x \cdot Q_y \tag{3.38}$$

$$c_{n+1,m} = (1 - Q_x) \cdot Q_y \tag{3.39}$$

$$c_{n,m+1} = Q_x \cdot (1 - Q_y) \tag{3.40}$$

$$c_{n+1,m+1} = (1 - Q_x) \cdot (1 - Q_y) \tag{3.41}$$

In the simulation Eqs. (3.36) and (3.37) are evaluated using the function `gsl_sf_erf_Q()` of the GNU Scientific Library (GSL)[14].

The determination of the charge cloud size σ is a quite challenging task, since it depends on the particular detector-specific electrical potential and on the energy of the absorbed photon. It is influenced by the drift length from the point of absorption into the potential wells of the pixel structure. The charge cloud size can be defined in the XML file of a particular instrument as an energy-dependent quantity via two parameters a and b:

$$\sigma = a + b \cdot \sqrt{E} \tag{3.42}$$

where E is the photon energy in keV. By adjusting the parameters a and b, and the lower threshold for split events, the simulated pattern distribution can be adjusted to fit measurements with real detectors, as shown below. For most applications the thereby obtained accuracy is sufficient.

[13] Note that the lower boundary in the integrals has been replaced by $-\infty$ corresponding to the assumption that all charge is distributed among the regarded 2×2 pixels.

[14] `http://www.gnu.org/software/gsl/`

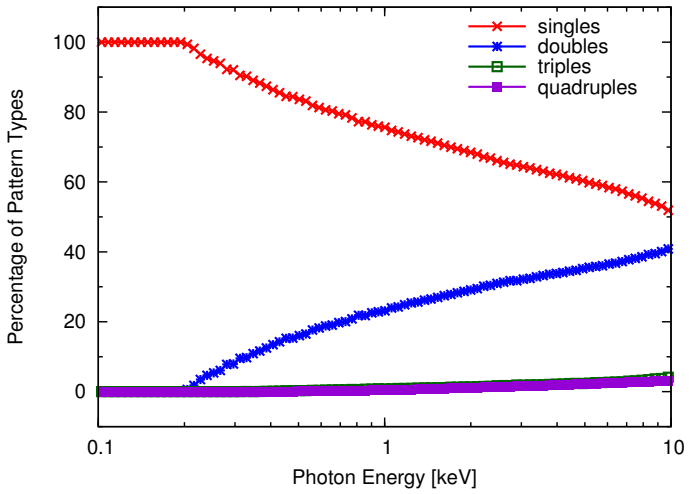

Figure 3.8: Energy-dependent ratio of the four main split pattern types for a simulation of the EPIC-pn camera on *XMM-Newton* in full-frame mode with a count rate of $\sim$14 counts s^{-1}. The Gaussian charge cloud model has been used. For a photon energy of 1 keV the fraction of single events is roughly 75 %, the fraction of double events is roughly 25 %, and the fractions of triple and quadruple events are negligible.

Split Model for eROSITA In the charge split model developed by K. Dennerl (priv. comm.) for eROSITA the relative charge distribution among the four surrounding pixels (indices defined as above) is obtained as:

$$c^{\star}_{k,l} = \exp\left[-\left(\frac{r_{k,l}}{0.355}\right)^2\right] \tag{3.43}$$

with

$$r_{k,l} = \sqrt{\left(x_\mathrm{i} - x_k - \frac{d_x}{2}\right)^2 + \left(y_\mathrm{i} - y_l - \frac{d_y}{2}\right)^2} \tag{3.44}$$

for $k = n, n+1$ and $l = m, m+1$ with n, m as in Eqs. (3.34) and (3.35). This is a relative distribution and has to be normalized:

$$c_{k,l} = \frac{c^{\star}_{k,l}}{\sum_{i=n}^{n+1}\sum_{j=m}^{m+1} c^{\star}_{i,j}} \tag{3.45}$$

Note that the presented model is independent of the photon energy. In order to obtain a proper distribution of split events matching the measured data a suitable selection of the lower signal thresholds is required.

Implementation For the Gaussian charge cloud model as well as for the eROSITA split model the detector module determines the charge fraction $c_{k,l}$ for each pixel in the 2×2 array around the impact position and distributes the signal equivalent according to these fractions.

In order to verify the proper implementation of the Gaussian charge cloud model, I have tried to reproduce the energy-dependent pattern distribution of the EPIC-pn camera on *XMM-Newton*. The theoretical data can be obtained using the tool `epatplot` of the *XMM-Newton* Scientific Analysis System (SAS)[15]. The *XMM-Newton* Users Handbook (Ness et al., 2010), e.g., contains a plot for the full-frame mode with an observed count rate of $\sim$14 counts s^{-1}. The graph in Fig. 3.8 represents the corresponding pattern distribution obtained with the Gaussian charge cloud model of SIXTE. The overall shape and the quantitative values agree quite well with the respective plot in the *XMM-Newton* Users Handbook (Ness et al., 2010).

In cooperation with M. Martin at the Institute for Astronomy and Astrophysics Tübingen (IAAT) I have performed a comparison of simulated data using the Gaussian charge cloud model

[15] `http://xmm.esa.int/sas/`

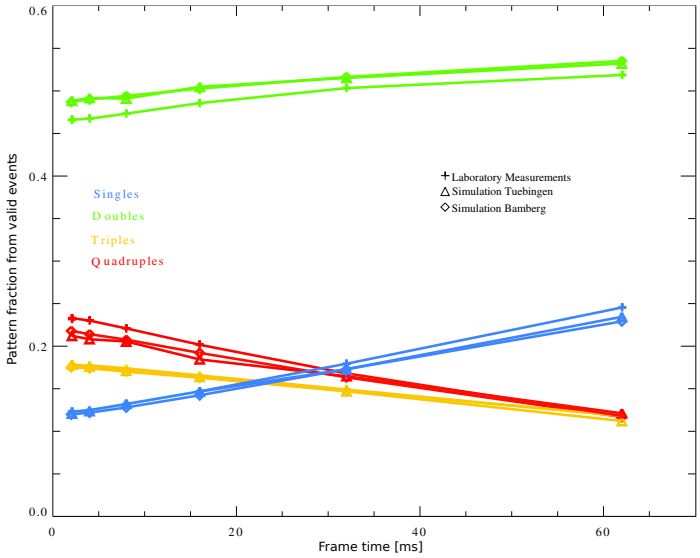

Figure 3.9: Simulated and measured ratio of split pattern types for a prototype of the WFI on *IXO*. The data obtained from SIXTE ("Simulation Bamberg") agree very well with the data from an independent simulation and the corresponding measurements performed by Martin (2009). With increasing frame time the lower threshold had to be increased due to a higher noise component in the measurements. Therefore the fraction of single events is increasing with increasing frame time, while the fraction of triple and quadruple events decreases. The systematic constant difference between the simulated and the measured fraction of double events is well-understood and is caused by an asymmetry feature of the particular detector prototype. The simulated data are based on a charge cloud size of $\sigma = 11\,\mu$m. The energy-dependence of the charge cloud size is not considered, since the measurements have been performed only for a particular X-ray photon energy. However the data still prove that the model is sufficient to describe the real data with high accuracy. The figure is adapted from M. Martin (priv. comm.).

with real measurements using a prototype of the WFI. For the proper configuration of the charge cloud size and the applied thresholds the simulated and measured data agree very well, as shown in Fig. 3.9.

In order to verify the proper implementation of the eROSITA split model, I have tried to reproduce the fractional distribution of the simulated event pattern types, as determined by K. Dennerl (priv. comm.). The result is shown in Fig. 3.10 for simulations with low source flux, i.e., with negligible pile-up. Although there are some slight deviations, the overall shape agrees very well with the data provided by K. Dennerl.

Detector Background

For eROSITA the detector internal background induced by interactions of cosmic ray protons with the camera housing can be simulated based on a dataset of such events obtained from a simulation with GEometry ANd Tracking (GEANT4, Geant4 Collaboration, 2003; Allison et al., 2006) performed by Tenzer et al. (2010). For a certain time interval a Poisson distributed number of these background events is selected by SIXTE from the GEANT4 dataset and the corresponding signal is added to the detector pixel array. The module responsible for this background generation in SIXTE has been developed by Wille (2011).

Electronic noise is not included in the simulation, because this would be the topic of a more sophisticated detector simulation beyond the purpose of the SIXTE framework. The detector background is treated separately from the CXRB, which is modeled by a large catalog of AGN (Chapter 4). This AGN catalog is included in the simulation already during the photon generation process (Sec. 3.2.1).

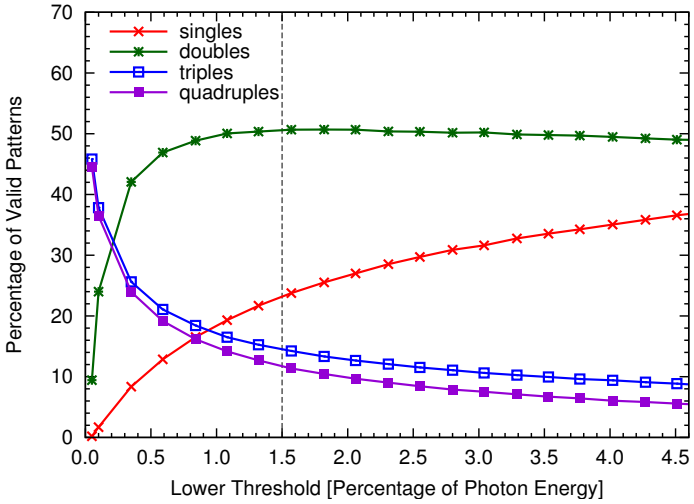

Figure 3.10: Simulated ratio of the four main split pattern types using the split model developed for eROSITA by K. Dennerl (priv. comm.) with different lower split thresholds. For eROSITA an appropriate value for the fractional split threshold would be about 1.5 %, as indicated by the vertical line. For this configuration the presented distribution agrees with the data of K. Dennerl within a few percentage points.

Detector Defects

In order to account for defects in real detectors, a bad pixel map can be specified in the XML definition of the instrument. This map is basically an image declaring individual pixels either as cold or hot. In SIXTE cold pixels cannot store any signal charge such that signals produced in these pixels or shifted into them are lost assuming a recombination of the electrons and holes[16]. Hot pixels produce signal even without interaction with a photon corresponding to an increased leakage current.

Readout

In principle there are two different readout techniques supported by the generic detector model. In the time-triggered mode the signals generated by incident photons are stored in the affected detector pixel, until after a specific exposure time the signal is read out and converted to an event with the current time. This method is used, e.g., for CCD-type detectors. It is especially important in order to simulate the energy pile-up (Sec. 2.3.2) for observations of bright sources, when the signal charges from multiple photons hitting the same pixel during the exposure time are collected and summed up.

The event-triggered readout mode, which is also implemented for the HTRS detector model, directly converts each incident photon into an event. This mode is suitable for instruments monitoring the output signal of the detector with a high sampling frequency[17]. In the simulation the readout time for these instruments is assumed to be equivalent to the photon arrival time. Apart from the HTRS detector model, the event-triggered readout mode is also used in the generic detector model, e.g., for simulations of the XMS on *IXO* or *ATHENA*. It also allows the simulation of pile-up and dead time effects by regarding the time intervals between subsequent events in the same pixel.

The selection of either a time- or event-triggered readout mode is part of the instrument definition in the XML file.

[16] In real detectors the electrons are often only trapped by some defects in the crystal lattice and released again after a while. However, this is currently not implemented in SIXTE.

[17] For instance, the output voltage of the individual SDDs of the HTRS is monitored by the subsequent electronics with a high frequency in order to detect steps arising from the charge produced by newly absorbed photons. In contrast to devices with a certain exposure time, such as CCDs, the time difference between the photon interaction and the detection is therefore negligible.

Charge Transfer

The signal generated in a particular pixel of a detector is either directly read out from this pixel or has to be shifted towards an anode at the edge of the pixel array. A typical example for the direct readout are the APS detectors, which have the first amplifier integrated in the pixel and sufficient wiring to address individual pixels. Charge shifting is mainly used in CCD detectors.

In the simulation the shift of a pixel row requires a specific time interval as in a real detector. Therefore OOT events (Sec. 2.3.1) are simulated properly. In addition the loss of signal charges during the shifting process is accounted for by applying a CTE factor (Sec. 2.3.1) to each shifted line of pixels.

The developed XML description format provides the required commands to define either a direct pixel readout or a shift of the collected signal.

Thresholds

In the detector model several thresholds are applied to the read out signals:

- As in a real instrument certain lower and upper **readout thresholds** for the signal of the detected events can be defined by the appropriate XML tags. If the signal contained in a pixel is less than the lower threshold or higher than the upper threshold, no output event is generated, but the signal is discarded. For each pixel containing a signal within the range defined by the lower and upper thresholds a separate event is produced.
- On the list of detected events a split pattern analysis is performed. The respective algorithm first searches for individual pixels with a signal above the specified **event threshold**.
- If such an event is found, its neighborhood is analyzed with a **split threshold**, which is usually lower than the event threshold. All neighboring pixels above this split threshold are taken into account for the recombination of the total event signal. The split threshold can be either specified as a fixed value or as a fraction of the maximum signal in the central pixel of a pattern. The latter option is applied in particular for the eROSITA model based on an algorithm proposed by K. Dennerl (priv. comm.).

3.2.4 Auxiliary Tools

Apart from the main functionality implemented in the previously described models, the SIXTE package contains several auxiliary tools addressing different tasks. In the following a short summary of the most important tools is given.

Sky Projection

The output of the detector simulation is a list of events read out from the detector model. Apart from the associated signal and time, each event is characterized by the indices of the affected pixel. Since the telescope in general can be moving during an observation, the image obtained from these pixel coordinates represents the traces of the observed sources through the FOV, as shown in Figs. 3.11 and 3.12, but not a direct image of the observed region of the sky. Therefore it is necessary to project the pixel coordinates back to the sky based on the attitude information of the telescope as a function of time. This reconstruction is possible, as the exposure time for individual detector images, and therefore the uncertainty of the photon arrival time is usually significantly shorter than the time scale of the slewing motion[18].

[18] Uncertainties in the attitude determination could be accounted for by randomizing the projected sky positions of individual events according to the respective uncertainties. However, this method is currently only applied for the uncertainty arising from the finite size of the detector pixels, but not for uncertainties in the knowledge of the attitude. For a more sophisticated analysis it would therefore be necessary to extend the current algorithm or to

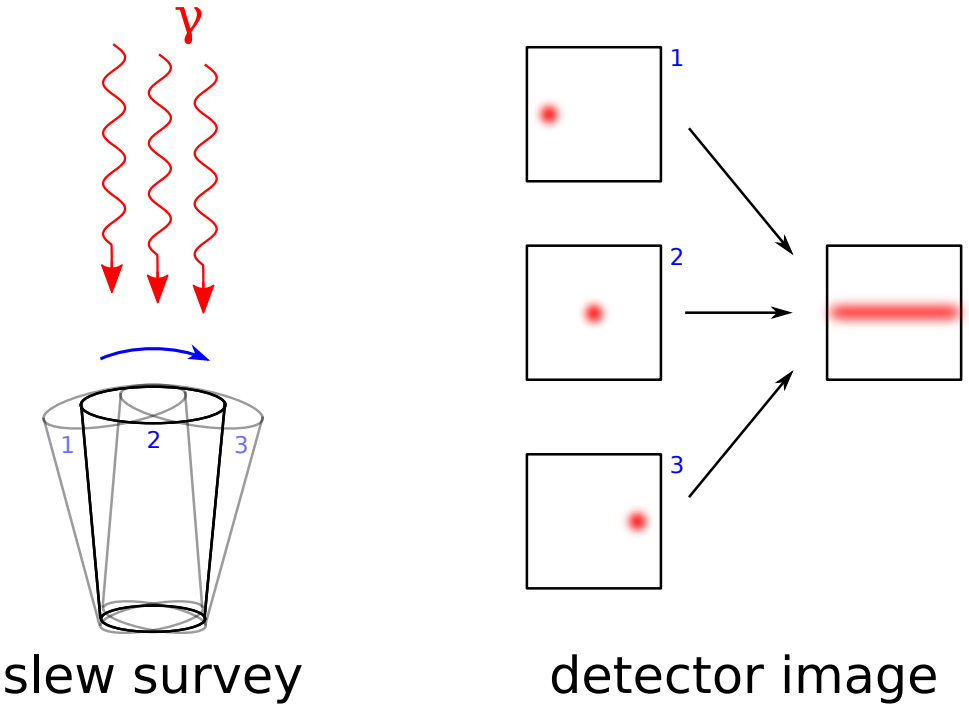

Figure 3.11: Sketch of the imaging process during a slew survey. As the telescope viewing direction is slewing over the sky, individual sources are moving through the FOV. Their images on the detector form elongated traces. In order to reconstruct the source positions on the sky, the timing information of the observed events has to be combined with the attitude of the telescope.

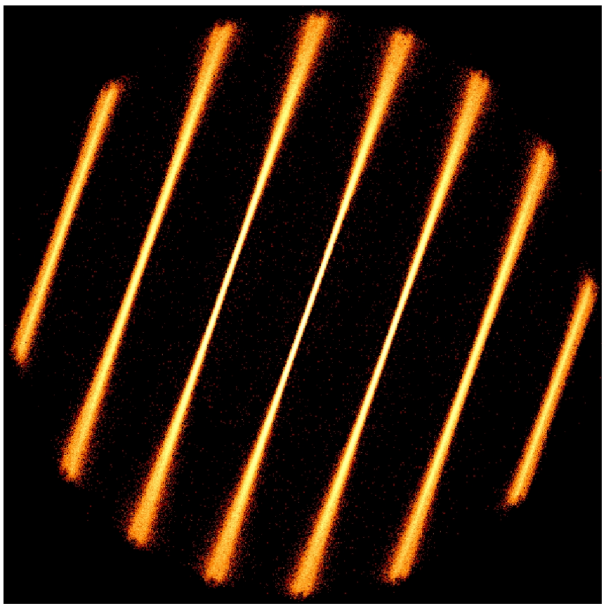

Figure 3.12: Trace of an X-ray source on one of the eROSITA pn-CCD chips caused by the continuous slewing motion of the telescope axis during the eRASS. The source is visible seven times within the simulated period. In order to get a sufficient number of photons for this illustrative purpose, the flux of the source has been set to a very bright value of $3.5 \cdot 10^{-8}\,\mathrm{erg\,s^{-1}\,cm^{-2}}$. (In X-ray astronomy the observed flux is often given in units of $\mathrm{erg\,s^{-1}\,cm^{-2}}$, with $1\,\mathrm{erg} = 10^{-7}\,\mathrm{J} \approx 6.24 \cdot 10^{8}\,\mathrm{keV}$.) At the edges of the FOV the stripes are wider than in the center due to the degradation of the PSF for large off-axis angles.

The projection is implemented in a particular algorithm, which uses the `WCSLIB`[19] library in order to obtain sky images for different projection types. For instance, all-sky images for eROSITA require a global projection type such as the Hammer-Aitoff projection, whereas for local pointed observations, e.g., the Gnomonic projection might be appropriate. For an overview

use other software, such as respective tools developed, e.g., in the framework of the eROSITA Science Analysis Software System (SASS).

[19] `http://www.atnf.csiro.au/people/mcalabre/WCS/wcslib/`

of the different projection types supported by `WCSLIB` see Calabretta & Greisen (2002).

Pattern Recombination

Due to charge cloud splitting between adjacent detector pixels a single photon, as in a real detector, can cause several events in the output event list. For data from real instruments usually a pattern analysis is performed in order to identify common split patterns. Such algorithms mainly search for the valid pattern types that can be created by a single photon impact and reconstruct the photon energy from the combination of the individual event signals.

The pattern recombination algorithm implemented in SIXTE assumes that all patterns of the four main types displayed in Fig. 2.19 are caused by a single photon. Of course, some of these patterns might originate from multiple photons, but usually the assumption holds for observations of weak sources with low photon rates. The energy of the associated photon is determined by the combination of the event signals contributing to the pattern. Any other pattern types, apart from the ones presented in Fig. 2.19, cannot be created by a single photon impact and are therefore discarded as invalid patterns.

The pattern recombination relies on particular assumptions about the valid pattern types and is therefore not as flexible as most other algorithms in SIXTE. The four main types displayed in Fig. 2.19 are usually applied for missions such as *XMM-Newton*, eROSITA, and *IXO/ATHENA*, whereas other telescopes such as *Advanced Satellite for Cosmology and Astrophysics* (*ASCA*) or *Chandra* have another event grading policy. In order to perform a split pattern analysis for a mission with different typical pattern types, the respective task has to be replaced by an appropriate algorithm, which, however, is possible due to the modularity of SIXTE.

Data Stream Conversion

As the simulated events shall be used for the verification of scientific analysis software such as the SASS or the Near Real Time data Analysis (NRTA, Kreykenbohm et al., 2009) for eROSITA, it is necessary to convert the output data of the simulation into the instrument-specific data format. The direct output of the actual simulation program are event files with either single-pixel events or recombined split patterns in FITS table format (Cotton et al., 1995), whereas the real instrument produces binary data. For eROSITA the SIXTE software package comprises a particular tool that converts FITS event files into a format compliant with the binary data stream of the telescope[20]. These binary data can be used as input for the SASS or the NRTA.

3.3 Implementation

The functionality of the Monte Carlo simulation presented in this work actually is implemented in two separate software packages:

- The task of handling the input catalogs with the X-ray sources and generating photons for them is mainly fulfilled by the SIMPUT library. This library has been developed parallel to the SIMPUT format description document (Schmid et al., 2011a) and is provided to the public community in order to enable access to SIMPUT files. Its functions can also be used for other simulations than the one presented in this work.
- The rest of the functionality, i.e., the imaging and detector models, and the auxiliary tools are combined in the SIXTE software package. This package consists of a library containing

[20] Currently the data format of the Third Röntgen Photon Imaging Camera (operated at the PANTER X-ray test facility of the MPE, TRoPIC) is used, since so far the format for eROSITA has not been defined. It will, however, be similar to the TRoPIC format.

the actual functionality and a set of tools providing an interface between the user and the library.

The SIXTE software package uses functions provided by the SIMPUT library for the generation of photon samples for the Monte Carlo simulation.

Both software packages, SIMPUT and SIXTE, are developed in `C`. Their source code is managed with the version control system `git`[21]. It can be compiled and installed using the `GNU Autotools` `autoconf`[22] and `automake`[23].

Since most data in X-ray astronomy are stored in files according to the FITS standard (Wells et al., 1981; Hanisch et al., 2001; Pence et al., 2010), both software packages use the `cfitsio` library (Pence, 1999) to access FITS files. The instrument calibration data are stored according to the standards of the High Energy Astrophysics Science Archive Research Center (HEASARC)[24]. The SIMPUT and SIXTE packages rely in particular on the following standard file formats, which can be found on the web[25]:

- effective area (George & Zellar, 1995)
- vignetting (George & Yusaf, 1994)
- PSF (George & Yusaf, 1995)
- ARF and RMF (George et al., 1998, 2007)

Physical units in the FITS files are specified according to George & Angelini (1995).

For conversions between pixel coordinates of FITS images and one of the WCS types presented by Calabretta & Greisen (2002) the library `WCSLIB` is required. For different mathematical operations such as the evaluation of the Gaussian probability function the appropriate routines from the GSL are used. For FFTs the `fftw` library is used.

In the following an short overview of the SIMPUT and the SIXTE software packages is given.

3.3.1 SIMPUT

The SIMPUT library is based on a particular file format developed for the definition of input data for a telescope simulation. Before describing the library itself I will shortly introduce the SIMPUT format. A detailed description is given in the respective format definition document (Appendix B, Schmid et al., 2011a).

Apart from the instrument model, the most important issue in the development of a telescope simulation is the description of the observed X-ray sources. Depending on their particular purpose different simulation software packages follow different approaches. For instance, an AGN simulation can be based on simple point-like sources represented by their position in the sky and their brightness. For extended sources usually an image-based model is most suitable. If the simulation, apart from spatial resolution, also implements spectral or time resolution, energy spectra or light curves are required as additional information. It is obvious that there are many different ways to combine these elements to a digital form stored on a computer disk.

A big disadvantage of this big variety of source models is the lack of compatibility between different software packages. Usually a lot of effort is invested in finding an appropriate interface between scientists providing input data for a simulation and its developers or users. In addition it is mostly not possible to use the same input also for another simulation of another telescope.

Therefore I and my colleagues R. Smith and J. Wilms have started an attempt to solve this problem by defining a standard file format providing means to describe any possibly interesting X-ray source in the sky. Actually the format is even more powerful, since it can also be applied

[21] `http://git-scm.com/`
[22] `http://www.gnu.org/software/autoconf/`
[23] `http://www.gnu.org/software/automake/`
[24] `http://heasarc.gsfc.nasa.gov/`
[25] `http://heasarc.gsfc.nasa.gov/docs/heasarc/caldb/caldb_doc.html`

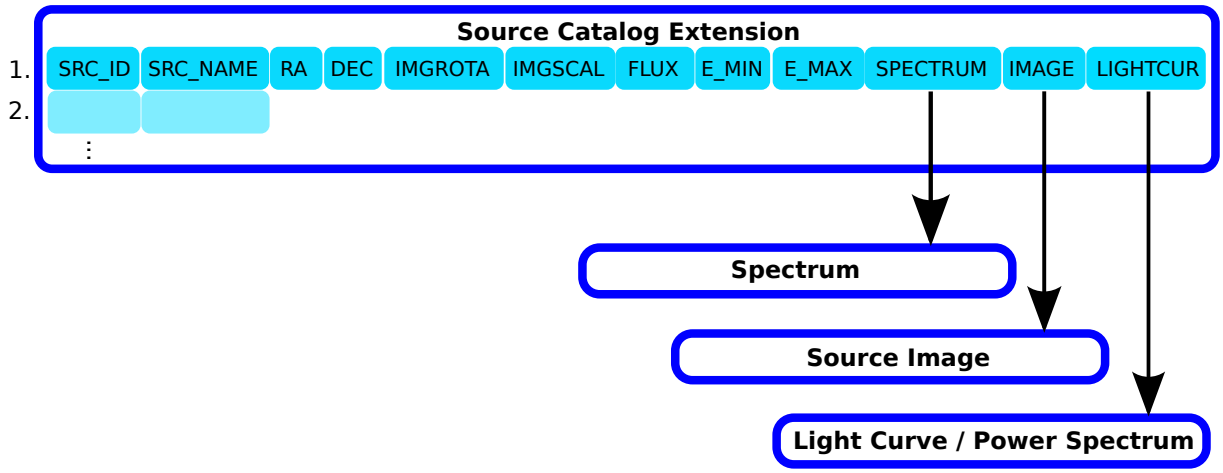

Figure 3.13: Layout of a SIMPUT source catalog extension. Apart from basic source properties such as the position or flux density, each source refers to a spectrum stored in a separate extension. The specification of a light curve or PSD and a source image is optional.

for other wavelength regimes, but in the context of this work I will only focus on its capabilities concerning X-ray sources, which are shortly summarized in the following.

The file format with the name SIMPUT is described in a formal document (Schmid et al., 2011a). It is based on the FITS file format (Wells et al., 1981; Hanisch et al., 2001; Pence et al., 2010), which is very common in X-ray astronomy, and implements different HDU types containing the particular data. The core of a SIMPUT file is a source catalog containing one or multiple X-ray sources with their basic properties such as their position, observed flux density, energy spectrum, and possible references to further data. The layout of the source catalog is outlined in Fig. 3.13.

There are different approaches to define the energy spectra of the sources in a SIMPUT file. The preferred method is a mission independent way. In that case the spectrum is defined via the distribution of its photon flux density at different energies without including the effective area of a particular instrument. According to the SIMPUT format only the shape of a spectrum and not its absolute values are taken into account. The brightness and therefore the normalization of the spectrum of an individual source is defined in the catalog such that a single spectrum can be used for multiple sources of a particular type, minimizing the amount of required disk space.

The time variability of a source can be described either by a light curve representing the temporal evolution of the observed brightness or by a PSD[26], which is especially useful to implement noise fluctuations. Spatially extended sources are characterized by an image representing the observed flux distribution on the sky. Similar to spectra, individual light curves, PSDs, or images can be used for multiple sources of the same type with appropriate scaling factors.

By combining multiple spectra, light curves, and source images, complicated phenomena like periodic spectral variations or extended sources with different emission regions can be modeled. Examples are contained in the format description document (Schmid et al., 2011a).

For the access to SIMPUT files I have developed a `C` library. It contains routines to write source catalogs and the required extensions containing spectra, light curves, PSDs, and source images. It also provides an interface to read these data from a given SIMPUT file as well as additional algorithms such as the Poisson arrival time generator according to Klein & Roberts (1984), which is described in Sec. 3.2.1, or the algorithm introduced by Timmer & König (1995)

[26] The functionality for the access to PSDs has partly been implemented by my colleague M. Wille.

to convert a PSD into a light curve.

For the photon generation in particular the following high-level functions are useful:

- `getSimputPhotonEnergy()`
- `getSimputPhotonTime()`
- `getSimputPhotonCoord()`

These routines provide the basic characteristics of a photon as required by a telescope simulation.

Software developers who want to use the SIMPUT library in order to access input catalogs can either use the low-level routines to just extract the data from the file and implement the photon generation according to their particular needs, or they can rely on the high-level interface, which encapsulates the treatment of the particular source properties and delivers photons based on the algorithms presented in this chapter.

The SIMPUT library cannot only be used by SIXTE, but is also accessible for other simulations, that want to make use of the powerful means of the SIMPUT file format to describe astronomical sources.

3.3.2 SIXTE

The SIXTE software package provides the generic framework for Monte Carlo simulations of imaging X-ray telescopes that I have used for the studies presented in this work. The installation of SIXTE and a sample simulation run are described in Appendix A.

Interface

In order to provide the user with a familiar interface, the tools contained in the SIXTE package follow the High Energy Astronomy data analysis system (HEAdas) programming guidelines (Arnaud, 2008). They rely on routines of the HEAsoft package, which is commonly used in X-ray astronomy and provided by HEASARC. It comprises small tools called `ftools`[27] for specific tasks. The usage of the tools contained in SIXTE is designed similar to the interface of the `ftools`. For instance, they also use the Parameter Interface Library (PIL) or All-purpose Parameter Environment (APE) to read program parameters.

The configuration of a numerical instrument mock-up is done via a particular file with XML format (Appendix A). Apart from links to the required calibration files and other instrument-specific parameters such as the focal length of the telescope, this configuration file provides the possibility to describe the detector operation mode by a set of some elementary commands.

Structure of the Software Package

The SIXTE software package consists of a library containing the main functionality of the simulation and different tools providing an interface between the library and the user. The tools themselves are mainly wrappers around the library functions, which provide the more complex functionality.

In order to to open and read in a source catalog specified by the user, the basic routines of the SIMPUT library are used. The storage of the catalog in the computer memory using a k-d tree and the selection of the sources close to the FOV is implemented in SIXTE itself, since this requires some information about the telescope and its attitude. However, the photon generation is completely performed by the corresponding high-level routines of the SIMPUT library.

Apart from the wrapper around the photon generation procedure, the central constituents of the SIXTE package are the imaging module, responsible for the modeling of the X-ray optics, and the detector module, which can be adjusted for different instrument designs. Also many

[27] `http://heasarc.nasa.gov/docs/software/ftools/`

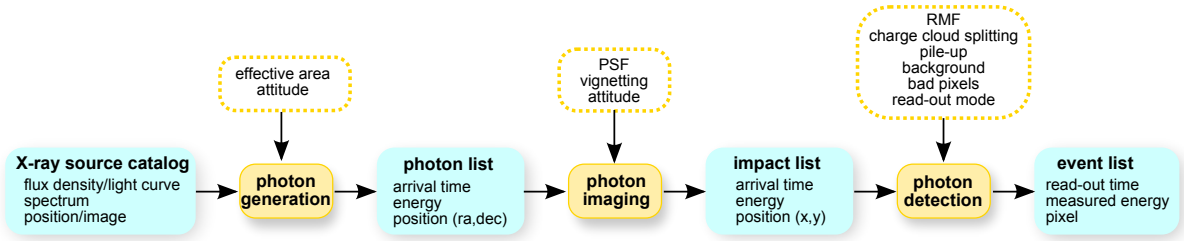

Figure 3.14: Schematic layout of a simulation pipeline built from several modules contained in SIXTE. For the X-ray sources in the SIMPUT catalog a sample of photons is generated taking into account the effective area and the attitude of the telescope. The mirror module determines the distribution of the generated photons on the detector surface according to their position in the FOV, the PSF, and the vignetting function. Finally the detector module implements the selected detector model and produces an output event list.

additional auxiliary tools are contained in the software package. The following will provide a short overview of the most important ones.

In order to set up a simulation for a particular telescope, the required modules are usually combined in a pipeline, as shown in Fig. 3.14. In addition to the presented core pipeline setup, additional tools mainly for particular instruments can be inserted or appended at the end.

Library

The library `libsixt` contains almost all the functionality of the SIXTE software package, whereas the individual tools are basically wrappers around the library routines. The main constituents of the library are the mirror and the detector models. It implements the algorithms presented in this chapter, unless they are part of the SIMPUT library.

Tools

The following tools are the most important ones required to set up a simulation for a particular instrument.

phogen This tool is a wrapper around the generation of a photon sample from a particular SIMPUT source catalog. Its output is a list of individual photons characterized by their energy, arrival time at the telescope, and direction of origin. Additional information appended to each photon are two identifiers referring to the original X-ray source and to the photon itself. These numbers are useful to track the photons in the simulation pipeline from their generation via the imaging up to the detection process.

phoimg This tools is a wrapper around the telescope mirror module modeling the photon imaging process. It processes the photon list produced by `phogen` and generates a list of photon impacts on the detector surface. Each impact is characterized by the energy of the corresponding photon, its arrival time at the instrument, and its impact position on the detector in physical coordinates. The photon identifiers produced by `phogen` are transferred from the photon list to the impact list.

gendetsim This tool is a wrapper around the generic detector model, which has to be customized by a specific XML file. It processes the impact list produced by `phoimg` and generates a

list of events, characterized by the measured signal, the detection time, and the respective pixel indices. The photon identifiers are transferred from the impact list to the event list.

evpat This tool is a wrapper around the routines used for the identification of event patterns produced by charge cloud splitting. It searches for valid pattern types in an event file produced by `gendetsim` and combines the corresponding events in order to reconstruct the energy of the original photon.

projev The spatial information of the events contained in the output files of the detector module and the pattern analysis tool `evpat` is provided in the detector coordinate system, i.e., each event is characterized by its pixel indices. In order to obtain an image of the simulated section of the sky, the pixel coordinates have to be converted to a WCS taking into account the attitude of the telescope. This particular task is carried out by the `projev` tool, which assigns WCS coordinates to each event pattern.

runsixt This tool provides no additional functionality, but is only a wrapper around the main tasks `phogen`, `phoimg`, and `gendetsim` of the core simulation pipeline, and the subsequent tasks `evpat` and `projev`. Instead of calling these tools subsequently, one can simply run `runsixt`.

htrssim The HTRS detector on *IXO* cannot be implemented with the generic detector model due to its particular pixel geometry (Sec. 5.1.1). The tool `htrssim` therefore can replace `gendetsim` providing the pixel geometry of the HTRS. Apart from the geometry, it uses the same functionality for X-ray detectors implemented in the SIXTE library as the generic detector model. Like `gendetsim` it processes an impact list produced by `phoimg` and generates a list of events.

CHAPTER 4

eROSITA

4.1 Mission Profile

The eROSITA project is a German X-ray telescope, which will perform an all-sky survey in the soft X-ray regime of 0.5–10 keV (Predehl et al., 2006, 2007, 2010a,b, 2011). It is developed by the MPE in cooperation with several other institutes, amongst them the Erlangen Centre for Astroparticle Physics (ECAP) represented by the Dr. Remeis Observatory Bamberg. The telescope will be launched together with the instrument Astronomical Roentgen Telescope – X-ray Concentrator (ART-XC, Pavlinsky et al., 2007, 2011) on the Russian spacecraft *Spektrum-Roentgen-Gamma* (*SRG*, Pavlinsky et al., 2006, 2008, 2009) from Baikonur in 2013. The spacecraft, which is displayed in Fig. 4.1, will be transferred into a halo orbit (Farquhar, 1968; Howell, 1984) around the second Lagrange point L_2 of the Sun-Earth system (Fig. 4.2).

During the first four years of the mission the two co-aligned telescopes on *SRG* will perform a quasi-continuous all-sky survey. Therefore their viewing direction will rotate approximately on a great circle perpendicular to the solar panels, which are pointing towards the Sun[1], as shown in Fig. 4.3. The revolution time for one great circle is about four hours (Predehl et al., 2011). As the spacecraft travels around the Sun once a year together with the L_2, the scan axis is slowly precessing in the ecliptic plane. Due to this precession, the whole sky will be scanned by both telescopes within a half-year period (Fürmetz et al., 2010)[2], i.e., the first four years of the mission constitute eight complete scans of the whole sky. Due to the intersection of the great circles around the ecliptic poles, regions at high ecliptic latitudes will be covered with a higher total exposure time than other fields around the survey equator. After the four years of the all-sky survey the spacecraft will perform pointed observations of particular targets during another three years of operation.

From the historical point of view eROSITA will be the successor of the very successful *ROSAT* mission, which has performed the first all-sky survey in X-rays with an imaging telescope (Trümper, 1982, 1992). The first attempt to extend the *ROSAT* survey to a wider energy range of 0.5–12 keV was *A Broadband Imaging X-ray All-Sky Survey* (*ABRIXAS*). Unfortunately the mission failed shortly after its launch in 1999 due to a battery problem (Predehl, 1999). The next concept for an imaging telescope in the X-ray regime up to 10 keV was to install the ROentgen Survey with an Imaging Telescope Array (ROSITA) on the *International Space Station* (*ISS*, Predehl et al., 2003). Although ROSITA was technically verified after several design studies, the project had to be abandoned, since the *ISS* turned out to be not suitable for the telescope

[1] Currently slight off-Sun pointings are considered in order to modify the distribution of the overall exposure time on the sky.

[2] The statement in this paper that the scan axis is pointing towards the Earth instead of the Sun corresponds to a previous approach. According to the current planning the axis will point towards the Sun.

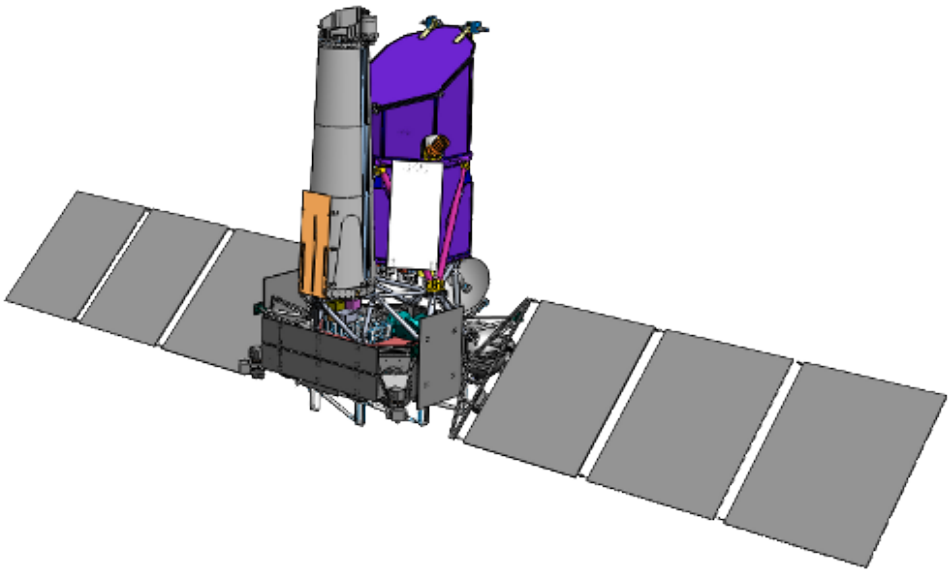

Figure 4.1: The spacecraft *SRG* with the two instruments ART-XC (front left) and eROSITA (back right) with closed front cover (Predehl et al., 2010a).

(Friedrich et al., 2005b; Predehl et al., 2007). The *Dark Universe Observatory* (*DUO*, Griffiths et al., 2004; Friedrich et al., 2004) proposed to NASA was not supported after its phase A study and was therefore not implemented.

Whereas all previous attempts to build a successor of *ROSAT* failed, eROSITA is in a very promising shape. It is fully approved and funded by the German Space Agency Deutsches Zentrum für Luft- und Raumfahrt (DLR) and the Max-Planck-Gesellschaft (MPG, Predehl et al., 2010a). The project is currently in phase C/D and the fabrication of the components is ongoing. The launch is scheduled for September 2013 (Merloni et al., 2011). The sensitivity limit of the eROSITA All-Sky Survey (eRASS) will be about 30 times lower than that of the *ROSAT* All-Sky Survey (RASS, see Fig. 1.6), while the energy range is extended to 0.5–10 keV (Predehl et al., 2010a). The first four years of the mission are dedicated to the all-sky survey. In the subsequent time the telescope will be used for pointed observations, partly dedicated to a follow-up analysis of objects detected in the eRASS. Nevertheless most of the telescope parameters such as the FOV, the PSF, and the detector operation are optimized for the survey phase, since the eRASS and the corresponding science are the key drivers for eROSITA.

A detailed explanation of the technical implementation of eROSITA is given by Predehl et al. (2006, 2007, 2010a,b, 2011), Cappelluti et al. (2011), and references therein. Nevertheless I provide a short summary of the most characteristic properties, since the instrumental configuration is important for the understanding of the presented simulations. An overview of the most important properties is given in Table 4.1.

Similar to *ABRIXAS* eROSITA consists of seven separate Wolter type I (Wolter, 1952a) mirror systems, but in contrast to *ABRIXAS* each sub-telescope has its own detector such that they can be operated independently. Each mirror module consists of 54 gold-coated, electroformed nickel mirror shells. The outer diameter of each mirror module is 360 mm and the telescope has a focal length of 1600 mm resulting in a quite low f-ration[3] in comparison to, e.g., *XMM-Newton* or *ATHENA*. As shown in Fig. 2.3a, the maximum sensitivity of the telescope lies in the regime

[3]In order to provide a large effective area at high photon energies, the ratio of focal length vs. aperture has to be maximized (Sec. 2.2.1).

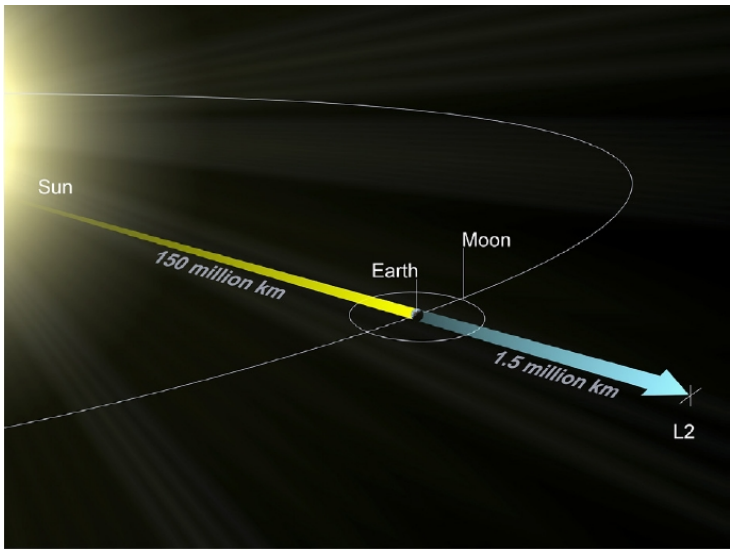

Figure 4.2: The Lagrange points define locations of zero gravity in a two-body gravitational potential. The L_2 is located on the extended Sun-Earth connection line at a distance of about 1.5 million km behind the Earth in the anti-Sun direction. At this point the centrifugal force caused by the rotation around the Sun compensates the gravitational attraction by both the Earth and the Sun. This equilibrium is unstable such that a spacecraft located in the L_2 requires occasional correction maneuvers in order to keep its position. However, eROSITA will not be located directly in the L_2, but will be put into a halo orbit (Farquhar, 1968; Howell, 1984)[a] around this point (`http://www.stsci.edu/jwst/overview/design/orbit`).

[a]Due to the instability of the equilibrium in the L_2, the question might arise, how a spacecraft can be put into an orbit around a point that does not exhibit any attractive force without the need for continuous propulsion. In fact the existence of halo orbits originates from the combination of the two-body gravitational potential and the Coriolis force due to the motion of the spacecraft in the rotating reference frame defined by the motion of the Earth around the Sun.

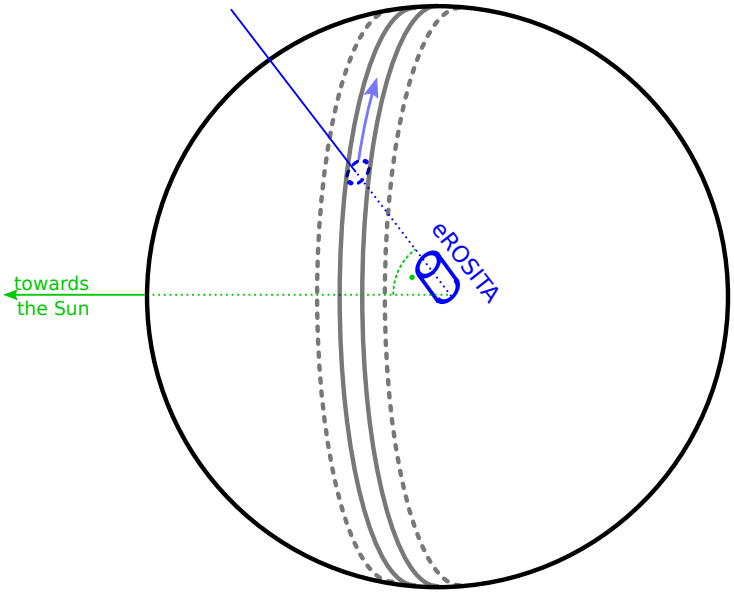

Figure 4.3: During the eRASS the telescope is scanning over the sky on approximate great circles. The revolution time for one great circle is about four hours. The scan axis is pointing towards the Sun such that the scanning great circle is precessing due the motion of the spacecraft around the Sun. Approximately once every half-year period the full sky is covered. Since the great circles intersect at the ecliptic poles, these regions are observed with the highest total exposure time.

below 2 keV (Predehl et al., 2010a), since the contribution of the outer 27 mirror shells to the effective area at higher energies is negligible. In order to prevent single-reflected photons from passing the optical system and reaching the focal plane, the mirrors are equipped with baffles.

According to the goal of the mission to perform an all-sky survey the telescopes have a wide

Table 4.1: Characteristic properties of the eROSITA telescope.

telescope type	7 independent Wolter type I mirror systems
on-axis resolution	15 arcsec HEW
detector type	framestore pn-CCD with 384×384 pixels
FOV	61 arcmin
pixel size	75 μm ($\sim$9.7 arcsec)
time resolution	50 ms
energy resolution	138 eV at 6 keV
energy range	0.5–10 keV

FOV with a diameter of 61 arcmin. The angular resolution for sources on the optical axis is 15 arcsec HEW. The average value over the entire FOV is slightly worse at about 26–30 arcsec. The design of the telescope mirrors is described by Friedrich et al. (2008), Burwitz et al. (2011), and Vernani et al. (2011).

Inside of each sub-telescope incident photons are focused onto a pn-CCD detector (Meidinger et al., 2006, 2007, 2008, 2009, 2010, 2011), which is basically an extension of the EPIC-pn camera on *XMM-Newton* (Strüder et al., 2001). It provides a near Fano-limited energy resolution of 138 eV at 6 keV (Predehl et al., 2011). Each pn-CCD consists of a sensitive imaging array with 384×384 pixels covering an area of $28.8 \times 28.8\,\mathrm{mm}^2$. In addition to the sensitive area each eROSITA pn-CCD has another 384×384 pixels forming a so-called framestore area, which shielded against incident radiation (Fig. 4.4). During an observation the imaging array is exposed to the incident photons. Each 50 ms the charges collected in the pixels are shifted into the framestore area, from where they are read out without confusion by further incident photons. Since X-ray cameras usually have no shutter, detectors without a framestore area, such as the EPIC-pn camera on *XMM-Newton*, suffer from so-called OOT events (Sec. 2.3.1). Due to the framestore technology, for eROSITA the fraction of OOT events is negligible.

4.2 Simulations

In this section I present some of the simulations that I have carried out for studies of the eROSITA telescope. The investigated scenarios illustrate the power of the SIXTE simulation software by showing several possible applications.

4.2.1 Survey PSF

The number of photons detected from faint sources during the eRASS will be strongly limited. Under this condition an accurate understanding of the survey PSF is essential in order to distinguish between point-like AGN and extended galaxy clusters even on the basis of a few photons. As shown in the following, simulations can be used to study the shape of the PSF for different locations on the sky.

According to Figs. 3.6 and 2.4a the shape of the eROSITA PSF and the mirror reflectivity described by the vignetting function strongly depend on the off-axis angle of the observed X-ray source with respect to the telescope axis. During the eRASS the FOV of the telescope is continuously moving over the sky such that an individual source at a particular position will be observed under a changing off-axis angle (Figs. 3.11 and 3.12). Therefore the image of the source as seen by the detector will be influenced by different components of the angle-dependent PSF. The particular composition of different PSF contributions is determined by the respective survey geometry with respect to the source position. Therefore, the shape of the average PSF can be different for a source at the survey equator than for a source close to a survey pole, due to the

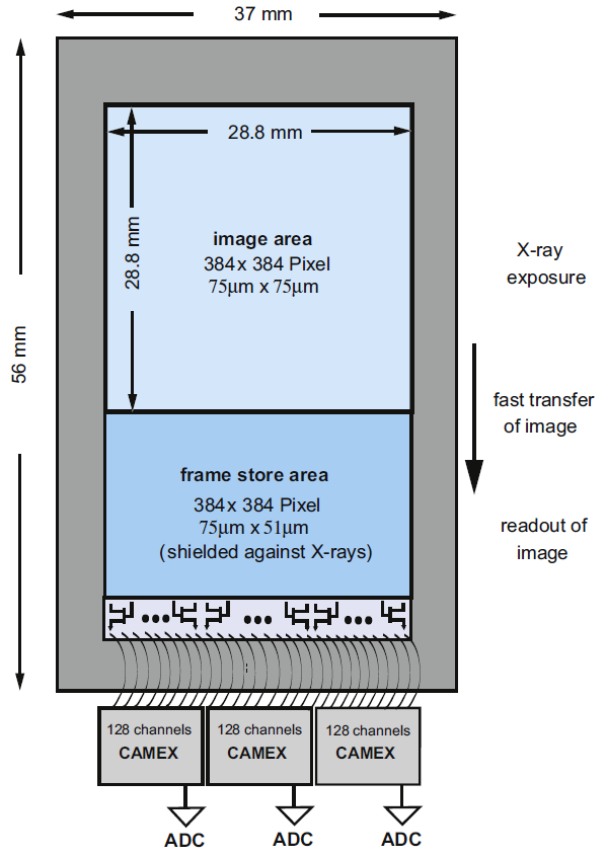

Figure 4.4: The concept of the eROSITA frame-store pn-CCDs (Meidinger et al., 2010). Incident photons produce signal charges in the pixels of the sensitive imaging area. After an integration time of 50 ms the collected electrons are transferred to the framestore area in a fast shifting process lasting about 115 μs. From the framestore area, which is protected against incident radiation, they are slowly read out by the CAMEX devices.

different superposition of various slew scans. This dependence can be analyzed with simulated observations.

Setup

In order to investigate the survey PSF at a particular location on the sky I, have used a SIMPUT file with a single point-like source at the respective position. In order to avoid a distortion of the observed PSF shape by pile-up (Sec. 4.2.2), the source is set up with a low brightness of $1 \times 10^{-11}\,\mathrm{erg\,s^{-1}\,cm^{-2}}$ corresponding to $\sim$0.03 counts frame^{-1} detector^{-1}.

For the scenario presented in the following the source is located on the survey equator. As indicated in Fig. 4.5a, during the observation the telescope axis is moving in vertical direction perpendicular to the survey equator. The individual slew scans are aligned parallel to each other with a distance of 10 arcmin. Due to the 61 arcmin diameter of the FOV, the overall image of the source is obtained from a composition of seven overlapping scans. The exposure map for an approximately 1 deg $\times$ 1 deg field around the source location is displayed in Fig. 4.5b.

The simulations have been performed without any background and without charge cloud splitting between the detector pixels in order to obtain an undisturbed image of the PSF. I have only simulated one of the seven sub-telescopes, since the currently available PSF obtained from ray-tracing simulations is identical for all sub-telescopes.

Results

The images in Fig. 4.6 display the survey PSF for the individual scans, which are numbered from 1 to 7 according to Fig. 4.5a. For each scan data from 10 000 independent simulation runs have

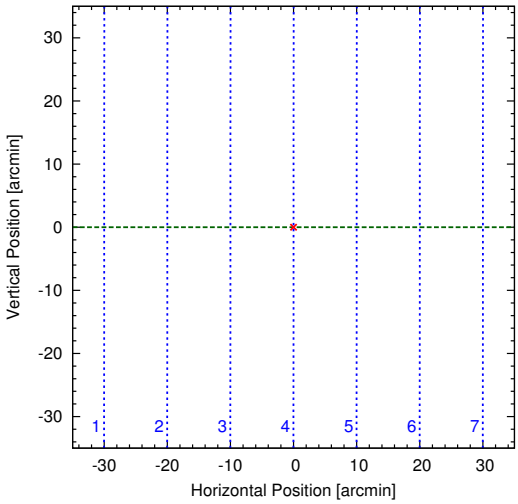

(a) Slew motion of the telescope pointing direction in the neighborhood of the source. The position of the source in the center of the image is marked with a red cross. The horizontal dashed green line represents the survey equator. The telescope axis is moving along the vertical dotted blue lines, which are numbered for later identification.

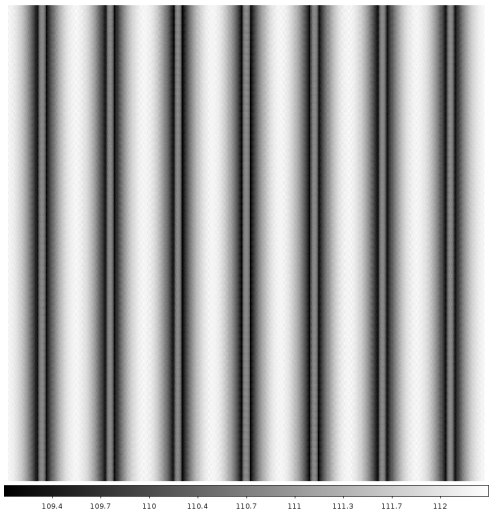

(b) Vignetting corrected exposure time for the field shown in **(a)**. The exposure is distributed quite homogeneously with an average value of ∼111 s. Note that not only the seven displayed scans but also the previous and subsequent scans with a pointing direction slightly outside of the displayed field have been considered for the calculation of the exposure map.

Figure 4.5: I have investigated the effective PSF for a source located on the survey equator based on simulated observations. Around the source position the individual scan stripes corresponding to the survey strategy of the eRASS are aligned quasi-parallel. The images of the individual scans overlap due to the 61 arcmin diameter of the FOV. The overall image of the source is obtained from the superposition of the data from the individual scans.

been superimposed in order to obtain a sufficient number of photons to neglect statistical effects. The composite image of all individual scans is displayed in Fig. 4.7.

The HEW of the composite PSF is 35 arcsec and therefore worse than, e.g., the 28 arcsec mentioned by Predehl et al. (2011). This difference is partly caused by the fact that the simulations also account for the discrete pixel size of 75 μm of the detector. I have repeated the simulation with a pixel size of 7.5 μm corresponding to a 10 times better spatial resolution. For this configuration the HEW of the average simulated PSF has a value of 33 arcsec. The remaining discrepancy can be attributed to the finite exposure time of the pn-CCD and to the particular implementation of the PSF model in the simulation:

- During the survey the telescope axis is slewing in vertical direction with a speed of $\sim$90 deg hour^{-1}. With regard to a frame time of 50 ms, this motion accounts for an additional uncertainty of 4.5 arcsec along the slew motion.
- The ray-tracing simulation of P. Friedrich, which the implemented mirror model is based on, does not include the baffles in front of the telescope that prevent single-reflected photons from reaching the focal plane. Therefore the assumed PSF at large off-axis angles is worse than the real optics will probably be.
- The on-axis PSF obtained from a simulation of a pointed observation has a value of 15 arcsec in agreement with the expected data. But since the PSF images from the ray-tracing simulation of P. Friedrich are only provided on an off-axis angle grid with a step width of $\Delta\theta = 5$ arcmin, the applied interpolation might result in a further contribution to the

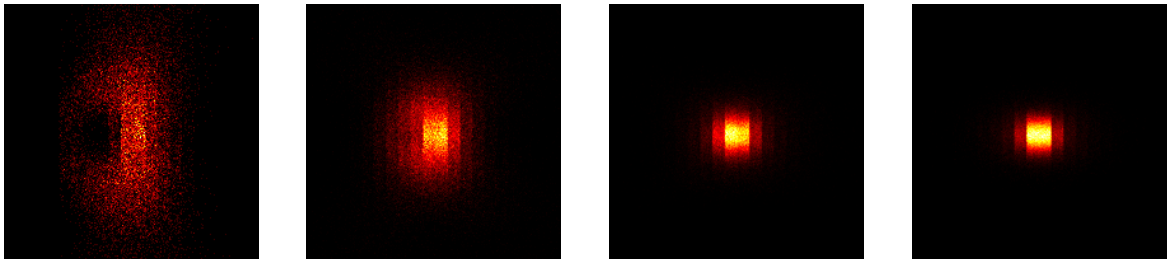

(a) Slew 1. **(b)** Slew 2. **(c)** Slew 3. **(d)** Slew 4.

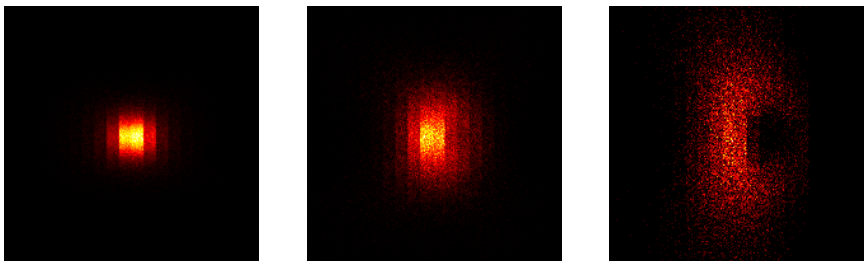

(e) Slew 5. **(f)** Slew 6. **(g)** Slew 7.

Figure 4.6: Survey PSF for individual slew scans over the observed X-ray source[a]. The slews can be identified by the numbering given in Fig. 4.5a.

[a]Actually each image is composed of a superposition of 10 000 independent simulation runs for the particular slew motion. Otherwise the number of observed photons would be too low to produce a reasonable image.

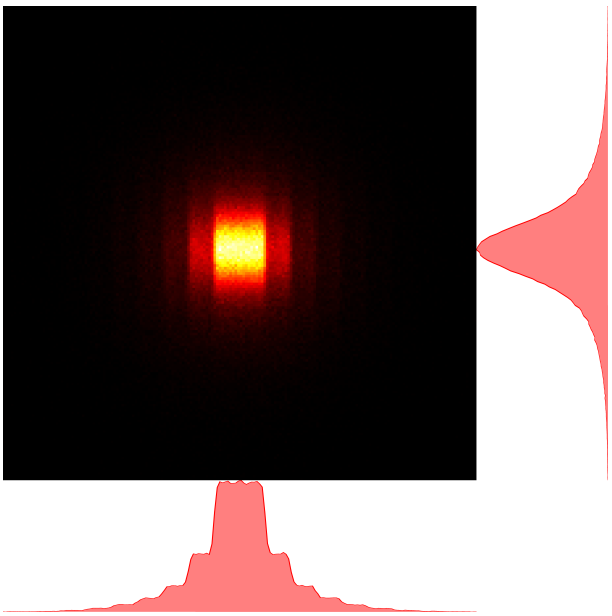

Figure 4.7: Composite survey PSF. The image is obtained from the superposition of the simulated individual slews presented in Fig. 4.6. The graphs on the right and on the bottom display sections through the center of the PSF. In horizontal direction the pixel structure of the detector is clearly visible, whereas in vertical direction the pixels are smeared due to the slew motion.

discrepancy between the survey PSF simulated with SIXTE and the analysis of P. Friedrich. In order to obtain more accurate data, it would be necessary to re-run the simulations again using a better model for the PSF with a finer off-axis angle grid and excluding single-reflected photons. The smearing of the PSF along the scan direction due to the slew motion and the positional uncertainty due to the finite size of the detector pixels, however, are no effects caused by the implemented model, but also affect the real observations. They therefore cannot be avoided.

4.2.2 Bright Source Performance

The primary intention of the eRASS is the detection of yet unknown sources, which are outside the covered area or below the sensitivity threshold of previous surveys. During the first four years of the telescope operation the impact of pile-up is therefore only relevant for the few occasions, when the telescope slews over a bright source. But even for these occasions accurate spectral information usually is only of secondary importance.

However, after the completion of the eRASS the telescope will also be used for pointed observations of interesting objects, including bright Galactic sources. Due to the large collecting area of its mirrors and the relatively long integration time of its pn-CCD detectors, the data measured by eROSITA in such a case might be corrupted by pile-up effects. Therefore it is necessary to investigate the performance of the telescope with regard to observations of bright sources in order to be able to correct for these effects.

Apart from calibration measurements in an X-ray facility, simulations provide an estimate of the impact of pile-up. In contrast to real measurements, the history of individual photons can be tracked and the fraction of events affected by pile-up can be analyzed. In SIXTE the photons contributing to an event can be identified individually. It is well-known whether an event measured by the detector model originates from a single or from multiple photons. Based on this information I have analyzed the effect of pile-up on observations with eROSITA.

Setup

For this investigation I have simulated pointed observations of individual point-like X-ray sources with different brightness values. Then I have analyzed the simulated data in order to determine the fraction of events affected by pile-up in dependence of the brightness of the respective source and investigated the impact on the quality of the spectral data.

The simulated X-ray sources were equipped with the spectrum of the Crab nebula, since this source is commonly used as a standard candle for in-flight calibration of X-ray instruments (Toor & Seward, 1974). Its spectrum has been investigated with many telescopes (Kirsch et al., 2005), and even measured fluxes of other X-ray sources are often given as a fraction of the corresponding Crab flux. Following Kirsch et al. (2005, 2006), I have used an absorbed power law (`ISIS` model *powerlaw*phabs*) with the spectral parameters displayed in Table 4.2 assuming the chemical abundances given by Wilms et al. (2000) and the cross sections given by Balucinska-Church & McCammon (1992). With these spectral parameters and the response file `erosita_iv_7telonaxis_ff.rsp`[4] for the eROSITA telescope an observation of the Crab nebula corresponds a photon rate[5] of 13 500 photons s^{-1}. I have used this number as a reference value for the subsequent analysis. The energy flux of the sources, i.e., the normalization of their spectra, has been adjusted in order to obtain different brightness values for the individual simulation runs and therefore different pile-up contributions to the measured data. However, the overall shape of the spectrum remained constant for all observations.

For a realistic simulation of pattern pile-up (Sec. 2.3.2) the model developed by K. Dennerl (priv. comm.) has been used to describe the charge cloud splitting between adjacent pixels in the eROSITA pn-CCD detector. Events distributed over several pixels are recombined by applying the pattern recombination algorithm described in Sec. 3.2.4. In contrast to the 1.5 % introduced in Sec. 3.2.3 I have selected a fractional lower split threshold of 0.3 %. This value avoids the loss of split partners with a low signal-fraction and therefore allows a more precise determination of the parameters of the simulated spectra. For the real instrument a higher value of about 1.5 % is more reasonable in order to suppress electronic noise contributions. Though, this aspect is not

[4] The response matrix is available at the eROSITA web site: `http://www.mpe.mpg.de/erosita/`.

[5] Due to pile-up effects the actually measured count rate will be lower.

photon index Γ	2.1	
normalization	9.5	photons $\mathrm{keV}^{-1}\,\mathrm{cm}^{-2}\,\mathrm{s}^{-1}$ at 1 keV
absorption column N_H	0.4×10^{22}	cm^{-2}

Table 4.2: Parameters of the spectrum of the Crab nebula following Kirsch et al. (2005, 2006). The Crab spectrum is used as a standard input for the presented pile-up simulations.

relevant for the presented simulations due to the absence of any background, including electronic noise. Neglecting background is justified in this case, because it has only a minor contribution in comparison to the simulated bright sources. The events affected by pile-up are identified by a particular column in the event file containing a unique number for each contributing photon. If an event originates from several photons with different identifiers, it is marked to be affected pile-up.

In addition to this analysis based on simulations, I have tried to estimate the pile-up fraction with a simple analytical model. As the observed flux is homogeneously distributed among all seven sub-telescopes, the count rate per telescope for an observation of a source with a brightness B_Crab given as a fraction of 1 Crab can be determined as

$$R_\mathrm{telescope} = B_\mathrm{Crab} \cdot \frac{13\,500\,\mathrm{photons\,s^{-1}}}{7} \approx B_\mathrm{Crab} \cdot 1930\,\mathrm{photons\,s^{-1}} \tag{4.1}$$

For moderate count rates pile-up mainly occurs in the innermost part of the PSF. If the observed source is located directly on the optical axis, one can assume that about 75 % of the incident photons are distributed among the inner 2×2 detector pixels, since the on-axis HEW of the eROSITA telescope is 15 arcsec corresponding to 116 μm or 1.6 detector pixels. The count rate in this 2×2 array is therefore given as

$$R_{2\times2} \approx B_\mathrm{Crab} \cdot 1450\,\mathrm{photons\,s^{-1}} \tag{4.2}$$

The eROSITA pn-CCD has an integration time of 50 ms such that the average number of photons per detector frame in the innermost 2×2 pixels of the PSF can be obtained as

$$N = R_{2\times2} \cdot 0.05\,\mathrm{s} \approx B_\mathrm{Crab} \cdot 72\,\mathrm{photons} \tag{4.3}$$

Under the assumption that the number of incident photons obeys Poisson statistics, the probability to have more than one photon in the inner 2×2 pixels during one readout cycle can be determined as

$$P_N(k > 1) = 1 - (P_N(0) + P_N(1)) = 1 - e^{-N} - N \cdot e^{-N} \tag{4.4}$$

with $P_N(k)$ the Poisson probability of having k photons for an expectation value of N photons. One can therefore roughly estimate the pile-up fraction among the detected events, with the following formula:

$$\frac{P_N(k > 1)}{P_N(k > 0)} = \frac{1 - e^{-N} - N \cdot e^{-N}}{1 - e^{-N}} \tag{4.5}$$

Note that this approach is only valid for low and moderate source brightness. It only takes into account the innermost 2×2 pixels of the detector and neglects the production of invalid pattern types for strong pile-up.

Apart from the determination of the fraction of events affected by pile-up, I have performed an analysis of their impact on the quality of the scientific data. Therefore I have fitted the spectra obtained from the simulations with the original model using the data analysis tool `ISIS`. This procedure allows to determine, how well the input spectrum can be reconstructed for different pile-up fractions, and how much the spectral parameters are distorted by corrupted events with a wrong energy information.

Results

In Fig. 4.8 the fraction of events affected by pile-up is displayed vs. the rate of incident photons. The presented data are obtained from simulated observations with different source brightness. In addition the analytical estimate described by Eq. (4.5) is plotted. However, due to the implemented simplifications, it represents only a rough approximation of the actual pile-up behavior. For the presented observation scenario the development of an accurate analytical model is more challenging than in the simple case shown in Sec. 2.3.2, because the incident photons are not homogeneously distributed on the detector but follow the spatial distribution represented by the PSF. It is also difficult to apply analytical pile-up models with a spatial variation of the count rate on the detector, as presented by Ballet (1999), because the HEW of the telescope is of the same order as the pixel size of the detector. This fact significantly complicates the analytical calculation.

The plots in Figs. 4.9 and 4.10 illustrate the impact of pile-up on the quality of the measured data. For pile-up fractions bigger than $\sim$2 % spectral parameters, such as the photon index Γ of a power law model or the absorption column, obtained from a fit to the simulated data significantly deviate from the actual values of the input source, as presented in Table 4.2. Therefore a value of 2 % represents a reasonable threshold for the pile-up fraction beyond which the quality of the spectral data might not be trustworthy.

For data analysis only valid split pattern types are taken into account, since invalid pattern types can only be produced by photon pile-up. In addition valid pattern types affected by strong energy pile-up can exceed the upper readout threshold and might therefore be neglected as well, and, of course, also multiple piled up photons below the upper threshold are only counted as one event. Due to these selection criteria, the count rate of the detector decreases in the case of strong pile-up. Since the region in the core of the PSF is mostly illuminated, this decrease in the data rate can be significant there, as shown by Ballet (1999), Popp (2000), and Martin (2009). This effect is evident in the simulated detector images displayed in Fig. 4.11.

As the presented simulations demonstrate, for eROSITA observations of X-ray sources with a brightness above a few mCrab can be significantly affected by pile-up. Data of such observations therefore have to be treated carefully. Apart from the possibility to use only single-pixel events, which are less affected by pile-up (Fig. 4.8, Ballet, 1999), another option to minimize the corruption of the spectral quality is to take into account only events from the less illuminated pixels in the wings of the PSF. Though, both methods require neglecting a significant number of the measured events.

4.2.3 Galaxy Clusters

The key science driver for eROSITA is the discovery of 50 000 to 100 000 clusters of galaxies in order to study the large scale structure of the Universe and to probe cosmological models (Predehl et al., 2010a). In order to distinguish between galaxy clusters and point-like sources based on typically a few X-ray photons detected during the eRASS, a narrow PSF is required as well as well-calibrated source detection algorithms. Simulated event data are used to develop and test these algorithms before the launch of the spacecraft *SRG*.

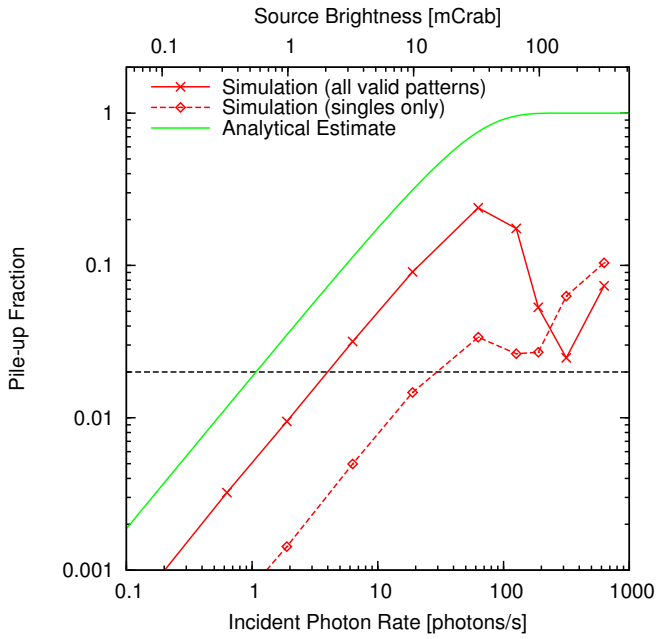

Figure 4.8: The fraction of valid events affected by pile-up according to simulated observations with eROSITA. The horizontal axis represents the rate of incident photons on a single eROSITA sub-telescope. Events forming an invalid split pattern are not considered in this analysis. As expected by Ballet (1999), the pile-up fraction among the single-pixel events is significantly lower than for all four valid pattern types. However, using only single-pixel events for the data analysis results in a noticeable loss of events, since singles make up only a minor fraction of all events, as shown in Fig. 3.10. The horizontal dashed line denotes a pile-up fraction of 2 %, above which the impact of pile-up becomes significant. The dip of the pile-up fraction at high photon rates is due to the discrete size of the pixels of the detector[a]. The displayed analytical estimate is only a rough approximation of the actual pile-up behavior due to the necessary simplifications.

[a]For very high incident photon rates the pixels in the core of the PSF only contain invalid pattern types, which are discarded anyway, whereas the outer parts in the wings still contain valid pattern types, which are only slightly affected by pile-up. Therefore the overall fraction of pile-up among all valid events decreases. If the photon rate further increases, the outer pixels are also affected by pile-up and the overall pile-up fraction increases again.

Mühlegger (2010) has developed an image-based simulation designed in particular for this purpose, which convolves images of 3.78 deg × 3.78 deg fields populated with galaxy clusters and background AGN with an average survey PSF in order to obtain an image of this section of the sky as it would look like with eROSITA. The input images are obtained from cosmological hydrodynamical simulations (Borgani et al., 2004; Roncarelli et al., 2006). The background AGN are randomly distributed with a brightness distribution according to the empirical values presented by Cappelluti et al. (2007).

The output of this simulation is an image of the observed region of the sky, whereas SIXTE produces an event list similar to the output of the real telescope[6]. The event lists can be directly used as input for the SASS of eROSITA and can be processed with common data analysis tools. While the software of Mühlegger (2010) is very convenient to obtain a quick estimate on how an image of a particular field might look like with eROSITA, a detailed investigation including time-resolved or detector-specific effects requires the use of the event-based SIXTE software.

The convolution of an input image with the average survey PSF by the software of Mühlegger

[6]This event list can be converted into an image with standard software or the appropriate tools contained in the SIXTE software package.

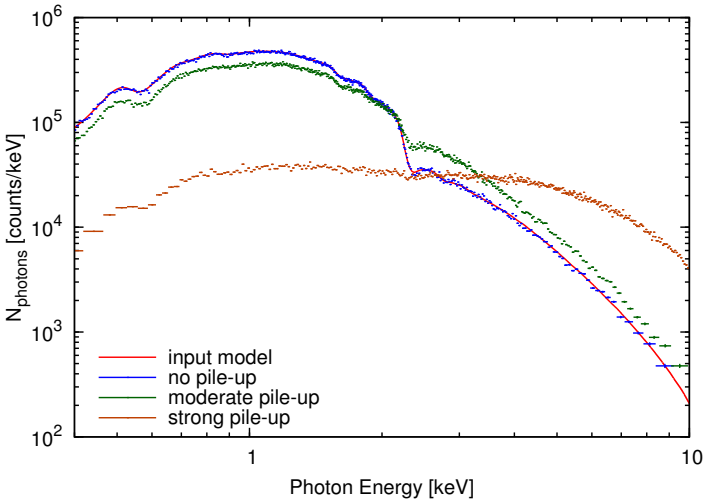

Figure 4.9: Distortion of the observed spectrum (absorbed power law) due to pile-up. For low count rates, i.e., no pile-up, the measured spectral shape agrees with the input model, whereas for increasing illumination rates the measurement is more and more influenced by pile-up. In the case of moderate and strong pile-up the signal of multiple soft photons is wrongly recombined and identified with single photons at higher energies such that there is a lack of soft photons and an excess of hard photons. This effect is also described, e.g., by Arnaud & Smith (2011).

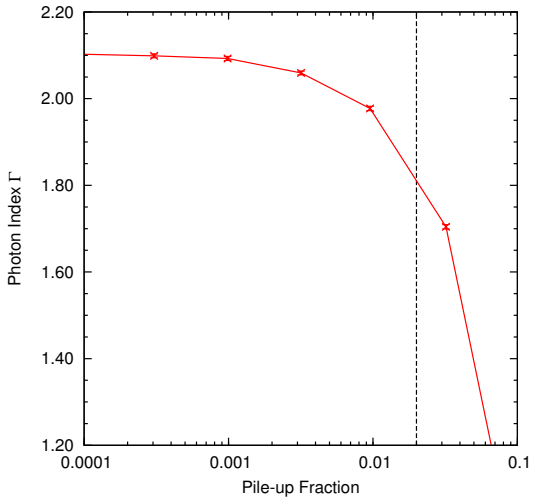

(a) For high pile-up fractions the photon index of the fitted power law seems to be lower than its actual value, as shown in Fig. 4.9. The apparent excess of hard photons results in a spectral hardening, i.e., a lower photon index. (During the fitting of the simulated data a fixed value was assumed for the absorption column.)

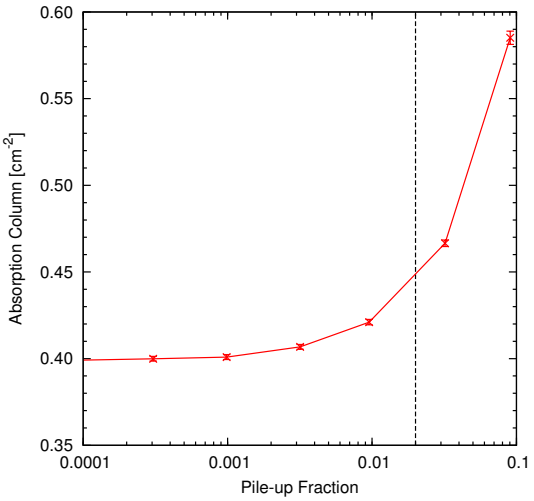

(b) For high pile-up fractions in the simulated data the absorption column seems to be thicker than its actual value, because the observed lack of soft photons, which is shown in Fig. 4.9, can be interpreted by a higher absorption column. (During the fitting of the simulated data a fixed value was assumed for the photon index.)

Figure 4.10: Impact of pile-up on the quality of the spectral data. I have fitted the simulated spectrum for different pile-up fractions in order to recover the parameters of the spectral model of the input source (Table 4.2). The influence of pile-up can result in a false identification of either spectral hardening or a denser absorption column. Spectra obtained from data with a pile-up fraction above 2 % (indicated by the vertical dashed line) are significantly distorted.

(2010) requires less computational effort than the more elaborate modeling of the imaging and detection process that is implemented in SIXTE. But it is also based on some simplifications such as the assumption of a constant average survey PSF. As shown in Sec. 4.2.1, in reality the composite PSF for a particular X-ray source is a superposition of multiple PSF contributions from different off-axis angles depending on the location of the source with respect to the telescope axis. Therefore the actually observed image is very sensitive to the particular survey strategy.

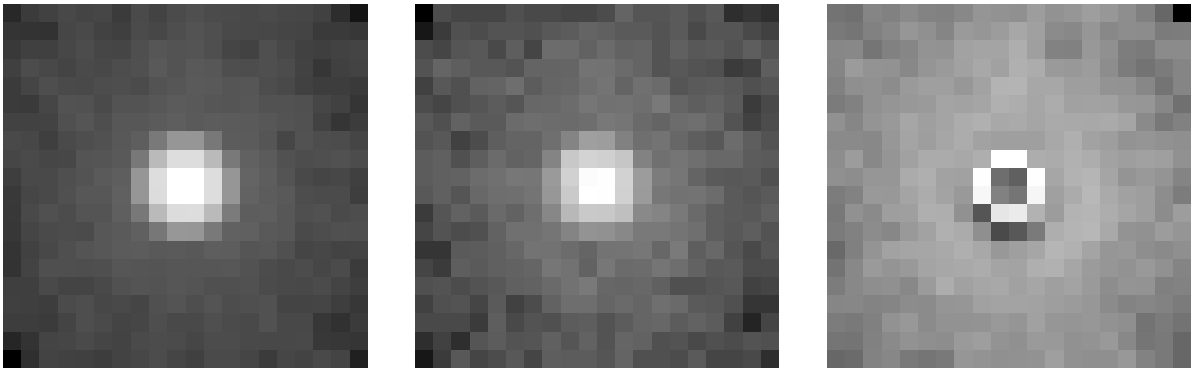

(a) No pile-up.

(b) Moderate pile–up at about 66 mCrab.

(c) Heavy pile–up at about 330 mCrab.

Figure 4.11: Pile-up affects mainly the core region of the PSF, because there the photon rate per pixel is higher than in the less illuminated pixels in the wings of the PSF. For high photon rates the core of the PSF contains hardly any valid event patterns. The displayed images are obtained from simulated observations of sources with different photon rates and have a logarithmic brightness scale.

The PSF for a source at the survey equator in general has a different shape than for a source located around one of the survey poles. This dependence of the average PSF on the regarded location is not provided by the simulation of Mühlegger (2010), but should be taken into account in simulations that are producing data for the development of sophisticated source detection algorithms.

Setup

In the following I present some sample data for simulated observations of the above-mentioned light cones populated with galaxy clusters, which are provided by Roncarelli et al. (2006). For the same setup similar data from the simulation of Mühlegger (2010) are available. The input images of the light cones represent the 2-dimensional X-ray surface brightness originating from the ICM of galaxy clusters in the regarded 3.78 deg × 3.78 deg-wide section of the sky. The observed radiation from a particular direction is integrated over galaxy clusters at different redshifts in the line of sight.

The first simulation runs have been based on two images per light cone representing the surface brightness in the two energy bands 0.5–2 keV and 2–10 keV. In order to have a more realistic spectrum than just these two wide energy bins, I have used the model introduced by Raymond & Smith (1977) to define an overall input spectrum for the generated photons. Of course, this approach is only a rough approximation of the actually emitted spectrum. Actually the individual spectra of the clusters in the light cones have different temperatures and redshifts, whereas the overall spectrum has one particular set of parameters. A more realistic approach was not possible, since the light cone images do not contain any information about the cluster parameters, such as temperatures.

In order to approach this issue, F. Pace and M. Roncarelli have produced a new data set providing the 2-dimensional surface brightness of 3.6 deg × 3.6 deg light cones in 146 energy bins. The covered energy range is 0.2–10 keV with a resolution of 50 eV below 5 keV and 100 eV above 5 keV. The 2-dimensional energy-resolved maps are arranged in a 3-dimensional data cube stored as a FITS image. For the second iteration of the presented simulations I have used this data cube converted into a SIMPUT catalog.

The provided maps of the light cones only contain galaxy clusters from the cosmological

simulation, but no other X-ray sources. In order to obtain a realistic observation scenario, additional source types have to be included. For the presented setup I have assumed that the observed light cone is located at a high Galactic latitude, i.e., there are neither bright Galactic sources nor absorption due to gas and dust within the Milky Way. For this scenario the emission from the clusters in the light cone is completed by a sample of randomly produced AGN according to observed log$N$-log$S$ distributions with a lower flux limit of $1 \times 10^{-17}\,\mathrm{erg\,s^{-1}\,cm^{-2}}$, as described in Sec. 4.2.4. The overall spectrum of these AGN accounts for the CXRB. The particle-induced instrument background is included by the cosmic ray background model introduced in Sec. 3.2.3.

By changing the WCS reference point of the light cone maps, their location on the sky and therefore their relative position within the eRASS can be modified. For instance, it is possible to simulate observations at the survey equator and at the survey poles and to compare the results. Different locations are primarily related to different exposure times, but also the shape of the average PSF can be different, as explained in Sec. 4.2.1. For a realistic approach the background model and the absorption by Galactic gas and dust have to be adapted to the respective position on the sky. For instance, locations within the Galactic plane are affected by a background component from the GRXE and by high absorption columns[7].

Results

In this work I only present data from the second simulation run with the energy-resolved surface brightness maps. During a more detailed analysis of the data provided by F. Pace and M. Roncarelli it was discovered by G. Lamer (priv. comm.) that the brightness distribution of the galaxy clusters extracted from the maps does not agree with empirical values. Actually the clusters in the light cones are approximately by a factor of 10 brighter than in observed distributions. Unfortunately the reason for this discrepancy has not been discovered at the time of writing this thesis. Therefore in the image and the spectrum presented below the cluster contributions are too bright. The simulations will be re-run once the problem in the generation of the surface brightness maps has been solved.

In Fig. 4.12 one of the regarded light cones is displayed. Its location is set on the survey equator, i.e., the individual slews over the field are aligned quasi-parallel, resulting in the exposure map shown in Fig. 4.13. The overall spectrum of the galaxy clusters in the light cone is presented in Fig. 4.14. The displayed spectral shape, which is obtained from the simulated photon impacts, agrees quite well with the estimated values obtained from the input distribution of the X-ray flux among the different energy bands according to the 3-dimensional data cube, the average vignetting-corrected exposure of approximately 111 s, and the effective area of the eROSITA telescope.

The event lists produced by the simulation are equipped with the specific FITS header keywords foreseen for eROSITA and are used to test new software tools such as source detection algorithms during the development of the SASS.

4.2.4 All-Sky Survey

The primary goals of the eRASS, which will be performed during the first four years of the mission, are the detection of 50 000 to 100 000 galaxy clusters and of 3 to 10 million AGN (Predehl et al., 2010a). Due to the particular survey strategy introduced in Sec. 4.1, the effective exposure time and therefore the sensitivity will be much larger at the survey poles than at the survey equator. The discovery of new X-ray sources will be strongly influenced by the calibration of the instrument, mainly the PSF and the detector background.

[7] A software tool is currently developed by my colleagues T. Brand and J. Wilms to apply Galactic absorption effects to existing SIMPUT files.

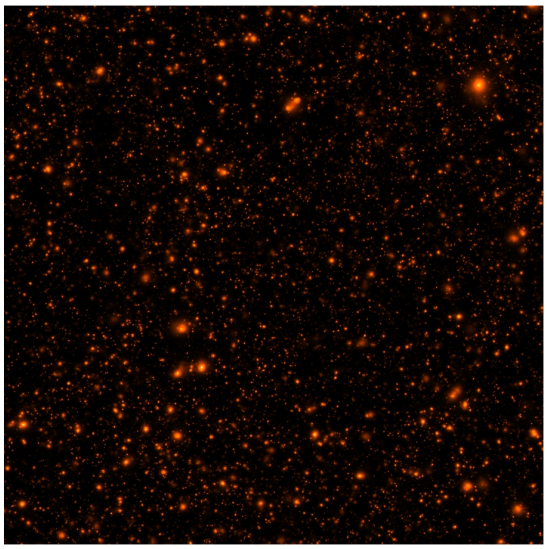

(a) Input image for the survey simulation with SIXTE obtained from the cosmological hydrodynamical simulations. The image is a weighted sum of the sub-images for the different energy bins according to their relative surface brightness contribution.

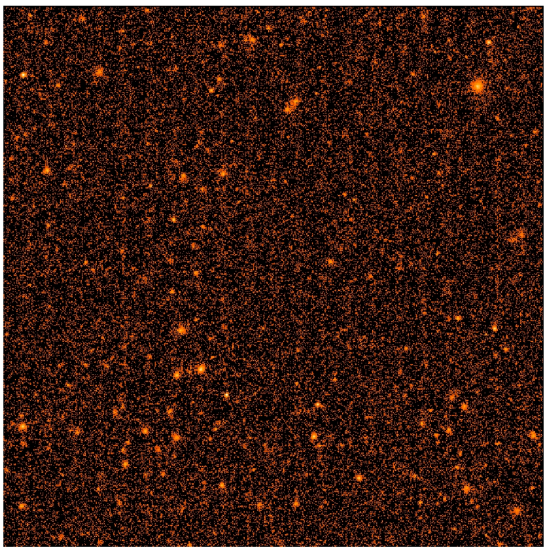

(b) Simulated observation with eROSITA using the light cone with galaxy clusters and a catalog of randomly distributed AGN as input data.

Figure 4.12: Simulated observations of a 3.6 deg × 3.6 deg light cone. The average vignetting-corrected exposure time is 111 s. Both images have a logarithmic color scale.

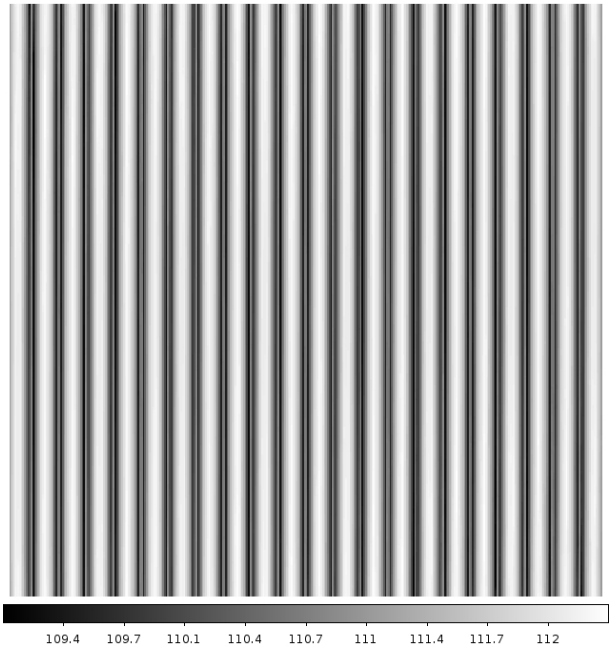

Figure 4.13: Exposure map of the 3.6 deg × 3.6 deg field covered by a light cone for a location on the survey equator. The individual slews over the field are performed in vertical direction and parallel to each other with a distance of 10 arcmin. The average vignetting-corrected exposure time is 111 s. Despite the impression caused by the offset of the color scale the variation of the exposure time over the field is relatively low with about ±2 s.

Simulations can be used to predict the expected number of source detections and to determine the completeness of the survey. Detection algorithms and other tools of the data analysis software can be developed, tested, and improved based on simulated data. Observables like the cluster mass function or the cluster power spectrum depend on the applied cosmological model. Variations of these quantities in the input data for the simulation will result in different simulation output. Therefore these modifications can be used to study the sensitivity of the

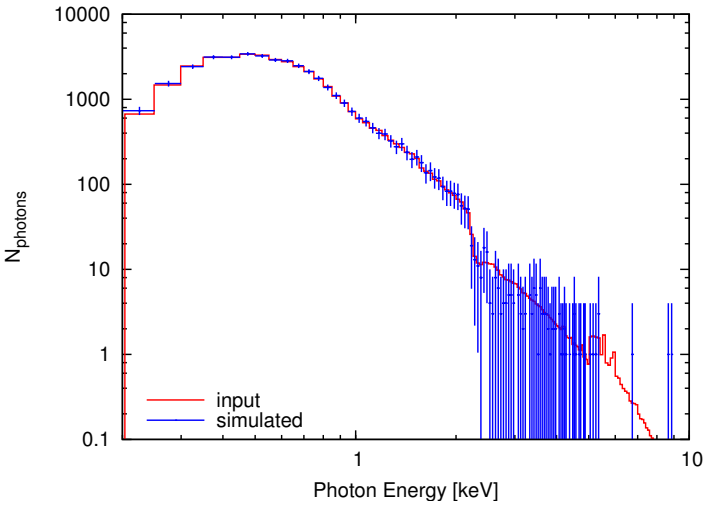

Figure 4.14: Composite spectrum of the observed X-ray emission from all clusters in the field for an exposure time of 111 s. The red line represents the estimated spectrum obtained from the spectral distribution of the flux in the input data cube and the effective area of the eROSITA telescope. The blue data points display the spectrum of the simulated photons.

measurements on cosmological parameters.

Setup

A simulation of the eRASS requires a comprehensive catalog of the most important types of X-ray sources in the sky. In part known sources from existing surveys such as the RASS can be used, in part new sources have to be generated that are below the sensitivity limit of previous missions, as the main task of eROSITA is the discovery of yet unknown sources. For simulations of the eRASS there is a selection of several catalogs comprising the following source types:

- the sources from the RASS Bright Source Catalog (BSC) and Faint Source Catalog (FSC)
- a catalog of time-variable sources obtained from measurements with the All-Sky Monitor (ASM) on the *Rossi X-ray Timing Explorer* (*RXTE*)
- a sample of randomly generated AGN
- a sample of randomly generated galaxy clusters
- diffuse GRXE

All these catalogs of X-ray sources are available in individual SIMPUT files and can be combined with respect to the particular objective of a simulation. A more detailed description of the different catalogs is given in the following.

RASS The RASS BSC (Voges et al., 1999) consists of 18 806 X-ray sources and the FSC (Voges et al., 2000a,b) of 105 924 X-ray sources. Both catalogs amongst other data provide the positional information of the detected sources. Spectral information is given in terms of the measured count rate with *ROSAT* and two hardness ratios. Based on these data a SIMPUT version of both catalogs has been produced as input for simulations with SIXTE. In principle a particular spectral model could be constructed for each individual source in the catalog based on the given hardness ratios. However, in the current version an overall spectrum, which is represented by an absorbed power law, is assigned to all entries in the SIMPUT catalog.

This approximation is justified by the fact that for the first analysis of the eRASS the focus is put on the positional information of the X-ray sources, whereas detailed spectral studies are hardly possible due to the usually low number of photons detected from an individual source during the all-sky survey. The total exposure time for an individual object at the survey equator is of the order of 1 ks. So for the majority of the sources only a small number of photons will be observed.

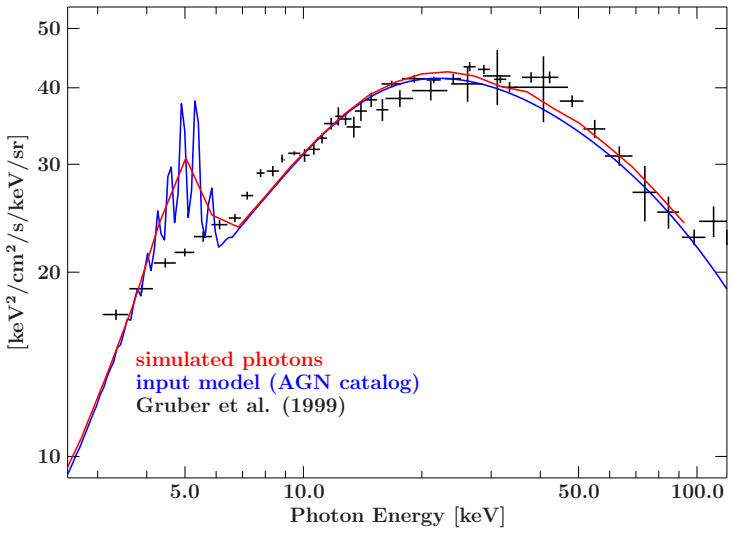

Figure 4.15: Comparison of the CXRB spectrum measured by Gruber et al. (1999) with *HEAO-1* and the model used for simulations. The blue graph represents the composite spectrum of the SIMPUT catalog containing the AGN, which has been generated with the software tools developed by Brand (2011), and the red graph displays the corresponding spectrum of the photon sample produced by SIXTE. The sharp line features below 6.4 keV originate from the Fe K-shell transition lines of AGN spectra with different redshifts. The spectra in the SIMPUT catalog are only available for a set of discrete redshift values with a quite rough step size.

ASM The ASM on the *RXTE* satellite has regularly monitored a particular set of sources (Levine et al., 1996). From these data a SIMPUT catalog containing 587 time-variable X-ray sources with their observed light curves has been compiled by C. Großberger (priv. comm.). Since the ASM only provides very rough spectral information based on three energy bands, the spectra of these sources in the SIMPUT catalog are represented by a representative model, which has been assembled for Cyg X-1 by V. Grinberg (priv. comm.). The justification for this approach is similar as for the RASS catalog, because the primary goal of the simulation of the eRASS does not require accurate spectroscopic data.

AGN As described in Sec. 1.3, the CXRB is assumed to originate from a large number of AGN, which have partly been resolved in deep surveys. Gilli et al. (2007) show that the observed CXRB spectrum can be composed of AGN spectra with a set of different spectral parameters.

Based on this approach, Brand (2011) has developed a Monte-Carlo simulation producing a random distribution of AGN with appropriate spectra down to a selected flux threshold. The positions of the AGN are uniformly distributed on the sky and the fluxes follow the $\log N$-$\log S$ distribution obtained from deep pointed observations. There are several catalogs available with all-sky distributions of AGN and different lower flux limits of 1×10^{-14}, 1×10^{-15}, 1×10^{-17}, and $1 \times 10^{-27}\,\mathrm{erg\,s^{-1}\,cm^{-2}}$ in the energy range 0.5–2 keV.

I have used these catalogs in the simulations of the eRASS on the one hand in order to extend RASS catalog to fainter fluxes, and on the other hand as a model for the CXRB[8]. As shown in Fig. 4.15, this model agrees quite well with the spectrum of the CXRB as measured by Gruber et al. (1999) with *HEAO-1*.

Galaxy Clusters Similar to the AGN catalog, Hölzl (2011) has compiled a SIMPUT catalog of randomly distributed galaxy clusters according to the cluster mass function given by Tinker et al. (2008). The corresponding X-ray luminosities are determined according to Vikhlinin et al. (2009a). Images of 64 galaxy clusters from the HIghest X-ray FLUx Galaxy Cluster Sample (HIFLUGCS, Reiprich & Böhringer, 2002) observed with *Chandra* (Hudson et al., 2010) are assigned to the entries in the SIMPUT catalog and scaled in size according to the respective

[8]The AGN catalogs have also been used in other simulations, such as the ones presented in Sec. 4.2.3, as a model for the CXRB.

redshifts. This cluster catalog is used as input for the simulation in order to represent the yet unknown sample of galaxy clusters to be detected with eROSITA.

GRXE The GRXE consists of diffuse X-ray emission aligned along the Galactic bulge and disk. Different models have been proposed for its origin (Revnivtsev et al., 2006; Ebisawa et al., 2008). As input data for simulations I have converted the *ROSAT* maps of the diffuse X-ray emission, which are provided by Snowden et al. (1995, 1997), into a SIMPUT catalog. However, these data comprise all diffuse emission observed with *ROSAT* in the low energy band 0.1–2 keV. It is difficult to disentangle the GRXE, e.g., from the CXRB in the available maps. This composition has to be taken into account, when using these data in combination with the AGN catalog, which also accounts for the CXRB.

In order to provide an alternative model of the GRXE that is clearly separated from the CXRB I have assembled a SIMPUT file with a simple geometric model of the emission region along the Galactic bulge and disk. According to the model used by Türler et al. (2010) the emission therein is described by two Lorentzians:

$$L_{\mathrm{X}} \sim \frac{\sigma_l}{l^2 + \sigma_l^2} \cdot \frac{\sigma_b}{b^2 + \sigma_b^2} \tag{4.6}$$

with l and b the Galactic longitude and latitude respectively, and $\sigma_l = 10.5\,\mathrm{deg}$ and $\sigma_b = 0.6\,\mathrm{deg}$. The spectrum assigned to this emission region is described by a power law with a photon index $\Gamma = 2.1$ (Revnivtsev et al., 2006).

Results

The simulation of the eRASS has been performed with the current attitude data provided by J. Robrade (priv. comm.). The corresponding exposure map is displayed in Fig. 4.16. For the all-sky image presented in Fig. 4.17 the following source catalogs have been used: the RASS, the ASM catalog, an artificial AGN catalog with a lower flux limit of $10^{-15}\,\mathrm{erg\,s^{-1}\,cm^{-2}}$, and the simple geometric model of the GRXE[9].

The simulated event files can be used, e.g., for verification tests of the NRTA software for eROSITA, which is developed at the Dr. Remeis Observatory Bamberg (Kreykenbohm et al., 2009). The task of the NRTA software is the monitoring of the instrument data directly after they become available on ground. It performs several sanity checks in order to assure the proper state and functionality of the instrument, and it searches for scientifically interesting transient phenomena in the observed data. The verification of the proper implementation of the NRTA is an ideal subject for simulated data. For instance, it is possible to insert an artificial transient source in the existing input catalogs and check, whether it is detected by the responsible algorithm.

I have included a software tool in SIXTE that converts the event files produced by the simulation into the binary data format foreseen for the raw data from the real eROSITA instrument[10]. The converted data can be directly used as input for the NRTA data processing pipeline. Although this pipeline is not fully operational yet, preliminary tests of the first stage with simulated data have been successful.

[9] For a detailed analysis an AGN catalog with a lower flux limit is required, as the detection limit of eROSITA lies below this threshold. However, for a simulation of an all-sky image as displayed in Fig. 4.17 the very faint sources can be neglected.

[10] As mentioned in Chapter 3, currently the data format of the TRoPIC is used, since the format for eROSITA has not been defined, yet.

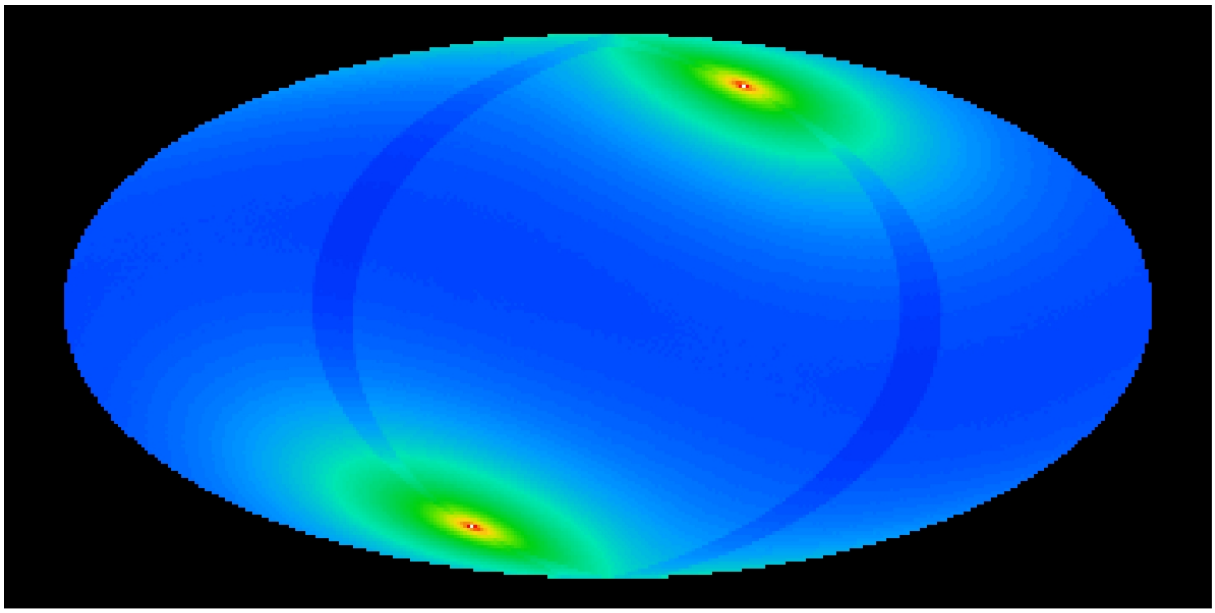

Figure 4.16: Exposure map for the full four-year interval of the eRASS in equatorial coordinates according to the attitude data provided by J. Robrade. The exposure times are vignetting corrected and the displayed map has a logarithmic color scale. The regions around the survey poles, which correspond to the ecliptic poles, have the deepest exposure and therefore the lowest sensitivity limit.

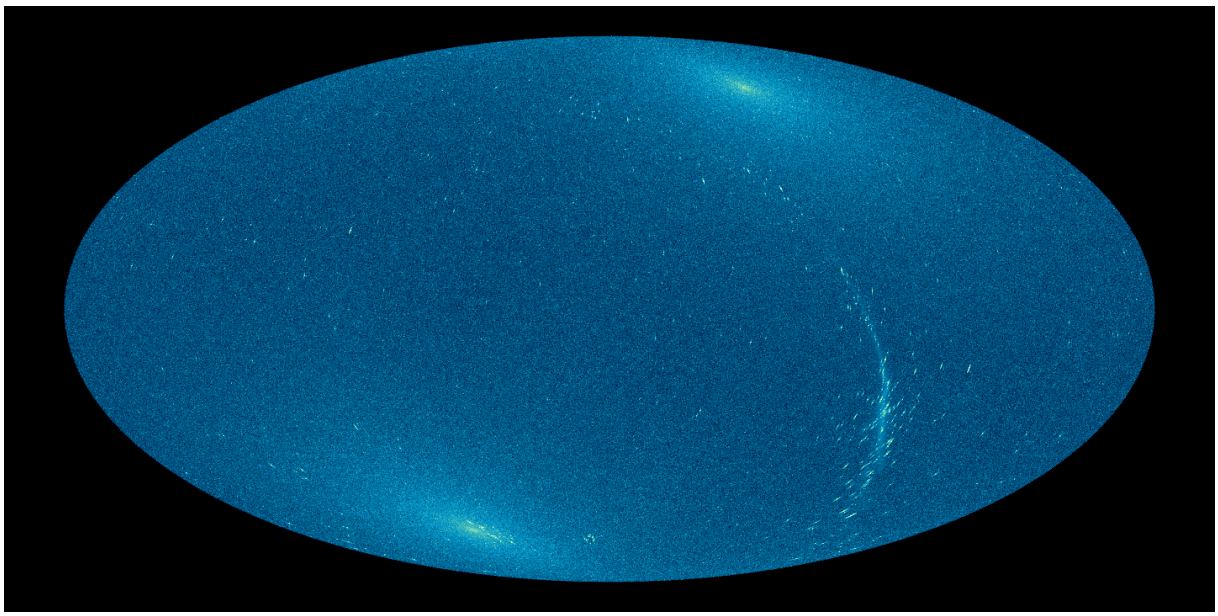

Figure 4.17: Image obtained from a simulation covering the full four-year period of the eRASS. The image is presented in equatorial coordinates with a logarithmic color scale. The regions around the survey poles have the deepest exposure. Therefore the integrated X-ray flux in these regions is very high. Another prominent region is the area around the Galactic Center in the lower right part of the image, which is populated with many bright sources and exhibits a significant contribution from the GRXE. The background radiation covering the whole sky originates mainly from the CXRB modeled by an AGN catalog with a very large number of individual point-like sources. Its appearance on the sky is homogeneous, as there is no spatial variation due to Galactic absorption included in the current versions of the AGN catalogs.

CHAPTER 5

IXO/ATHENA

5.1 Mission Profile

The currently most important X-ray telescopes are *XMM-Newton* (Jansen et al., 2001), *Chandra* (Weisskopf et al., 2000), and *Suzaku* (Mitsuda et al., 2007). The former two were launched in 1999, and the latter has been operating since 2005. Therefore the high energy astronomy community started to investigate different successor concepts. In Europe a proposal for the *XEUS* mission (Arnaud et al., 2008) was submitted to ESA as an L-class mission in the framework of the "Cosmic Vision 2015–2025" program (Bignami et al., 2005). In the USA the *Constellation-X* concept was proposed (Bookbinder et al., 2008) to NASA in the context of the "Astro2010 Decadal Survey".

In 2008 an international collaboration of scientists from Europe, the USA, and Japan, supported by ESA, NASA, and the Japan Aerospace Exploration Agency (JAXA) respectively, decided to join their efforts to develop an X-ray observatory offering unprecedented scientific capabilities. The concept of *IXO* (Bookbinder, 2010; Bookbinder et al., 2010; Barcons et al., 2011a) was assembled by this international collaboration in an assessment phase. However, the Astro2010 Decadal Survey (Blandford et al., 2011) made the statement that *IXO* would require significant technology developement and considered its schedule and cost budget as a possible risk. As the expected funding from NASA became unrealistic within the planned time frame, ESA decided to carry on the investigation of a re-designed mission with the name *ATHENA* based on a smaller budget fitting into the ESA cost frame. Although a key requirement for this new concept is the possibility to realize it without relying on support from outside of Europe, international contributions are still possible and welcome. Japanese and American scientists have already declared interest in participating in the development of the instruments for *ATHENA*.

With respect to *IXO* the *ATHENA* concept contains only two instruments instead of six and a decreased mirror area in order to avoid technological risks in the development of the telescope. Although some of the scientific goals of *IXO* had to be abandoned, *ATHENA* is still a very powerful observatory and is capable to perform many of the observations planned for *IXO* by compensating the smaller effective area with longer exposure times. Some particular fields such as the observation of galaxy clusters even profit from the slightly increased FOV of *ATHENA*.

In the context of my work I have performed several simulations as a contribution to the assessment of *IXO* and *ATHENA*. Although *ATHENA* will carry modified versions of only two of the six instruments foreseen for *IXO*, a reasonable amount of the experience gathered during the study of *IXO* is transferred to *ATHENA*. Therefore I also introduce *IXO* in this thesis, in addition to *ATHENA*. I give an overview of the concept of both missions and show some examples of my investigations.

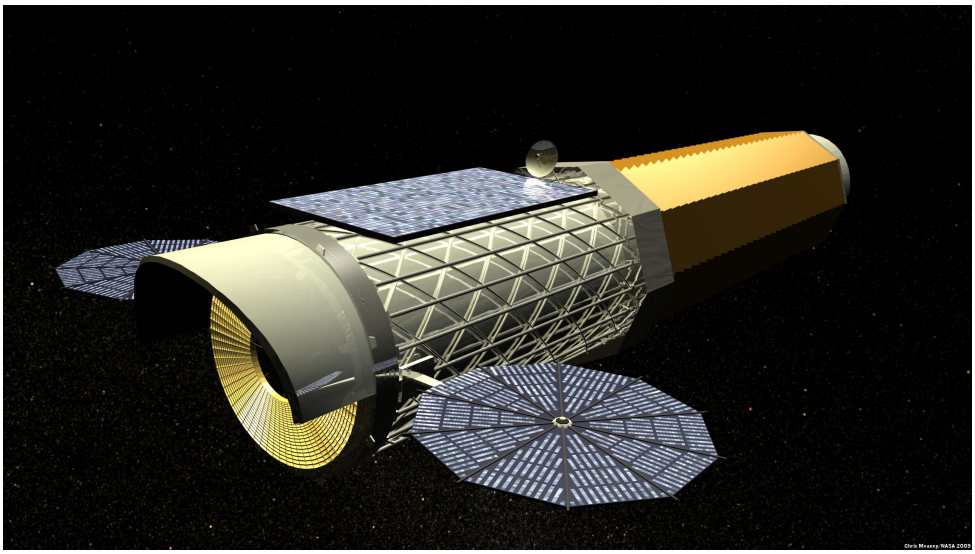

Figure 5.1: The *IXO* (`http://ixo.gsfc.nasa.gov/`). The mirror module shown on the front left side provides a large effective area of 3 m^2 at 1.25 keV. The Moveable Instrument Platform (MIP) with the focal plane instruments resides at the other end of the extendible optical bench on the rear right at a distance of 20 m behind the mirrors corresponding to the focal length.

5.1.1 *IXO* Configuration

This section provides a short summary of the *IXO* mission concept. A detailed overview is given by Bookbinder et al. (2010) and Barcons et al. (2011a).

IXO was planned for a launch around 2020–2022 with an Ariane-V rocket to a halo orbit (Farquhar, 1968; Howell, 1984) around the second Lagrange point L_2 of the Sun-Earth system (Fig. 4.2). Its design is based on a single telescope consisting either of SPO or a slumped glass mirror system with an effective area of at least 2.5 m^2 at 1.25 keV, a focal length of 20 m, and an angular resolution of 5 arcsec. A sketch of the spacecraft is displayed in Fig. 5.1. In order to achieve this long focal length, which is required for the large-area imaging of high energetic X-ray photons, an extendible optical bench is employed. It connects the mirror module with the Moveable Instrument Platform (MIP) containing five of the six instruments. The X-ray Grating Spectrometer (XGS) is constantly mounted in the optical path and used for all observations, whereas, depending on the respective science case, a particular one of the other instruments on the MIP is rotated into the focus of the telescope (Lechner et al., 2010b; Strüder et al., 2010; Barcons et al., 2011a).

In the following I give an overview of the individual instruments on *IXO*. For the WFI, the HTRS, and the XMS I have performed different investigations using the simulation software presented in this thesis. I will also shortly introduce the Hard X-ray Imager (HXI), the XGS, and the X-ray POLarimeter (XPOL), although the presented work does not contain any further analysis of these instruments. A detailed description of all instruments is given by Bookbinder et al. (2010) and Barcons et al. (2011a).

WFI

The WFI (Lechner et al., 2010b; Stefanescu et al., 2010; Strüder et al., 2010) is the main imaging device on *IXO* providing a wide FOV of 18 arcmin, good spectroscopic and adequate timing capabilities. Its detector consists of an array of 1024 × 1024 DePFET APSs with an edge length of 100 μm per pixel. The instrument covers the energy range 0.1–15 keV with a spectral resolution

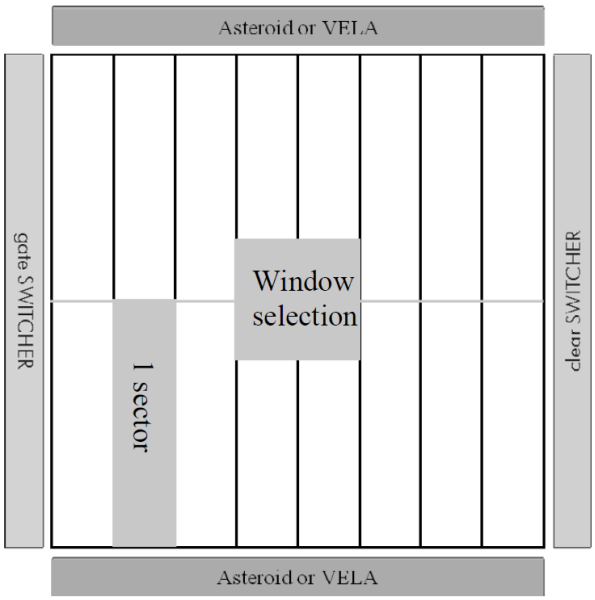

Figure 5.2: The WFI array of 1024 × 1024 DePFET pixels is divided into two hemispheres. Apart from the full-frame mode, it can be operated, e.g., in a window mode reading a subset of 16 × 16 pixels. During the assessment phase two possible ASICs (ASTEROID and VELA) have been investigated (Strüder et al., 2010).

of better than 130 eV at 6 keV (Barcons et al., 2011a).

The sensor is divided into two hemispheres, which are read out line-wise in a continuous mode with a speed of about 2.5–4 μs per line depending on the selected Application-Specific Integrated Circuit (ASIC). This translates to a time resolution of 1.28–2.05 ms for one detector frame. Apart from reading the whole 1024 × 1024 pixel array, it is also possible to operate the detector in a window mode on a 16 × 16 subset of the pixels in order to achieve a higher frame rate at the expense of the FOV, as indicated in Fig. 5.2. Additional operation modes are possible due to the random accessibility of the APSs.

HXI

The HXI is mounted directly behind the WFI and extends its energy range up to 40 keV with a resolution of better than 1 keV (Barcons et al., 2011a). The sensor of the instrument consists of two layers of double-sided Si strip detectors and a double-sided strip CdTe detector. It covers a FOV of 8 arcmin × 8 arcmin and has a spatial resolution of about 2.5 arcsec.

XMS

The Narrow Field Imager (NFI) or XMS on *IXO* consists of two arrays of TES microcalorimeters. The outer array covers a FOV of 5 arcmin × 5 arcmin corresponding to 52 × 52 pixels with an edge length of 600 μm. The central 20 × 20 pixels are replaced by an inner array of 40 × 40 smaller pixels with an edge length of 300 μm. The instrument covers the energy range 0.3–12 keV (Barcons et al., 2011a). The technology of TES microcalorimeters is described in Chapter 2. This instrument type provides non-dispersive imaging spectroscopy with an excellent energy resolution of 10 eV for the outer array and 2.5 eV for the inner array (den Herder et al., 2010).

However, the energy resolution of a TES microcalorimeter is strongly degraded if the time difference between subsequent photon impacts in a pixel is not long enough to sample the resulting current pulse with the required accuracy. Due to the large effective area and the relatively small PSF of *IXO*, this would prohibit observations of bright X-ray sources, as demonstrated by simulations in this work. Therefore Willingale (2009) proposed a Bright Source Defocusing Optic (BSDO) for the XMS. It consists of a Micro Channel Plate (MCP) distributing a part of the incident photons on a torus, which covers a large number of pixels around the central peak

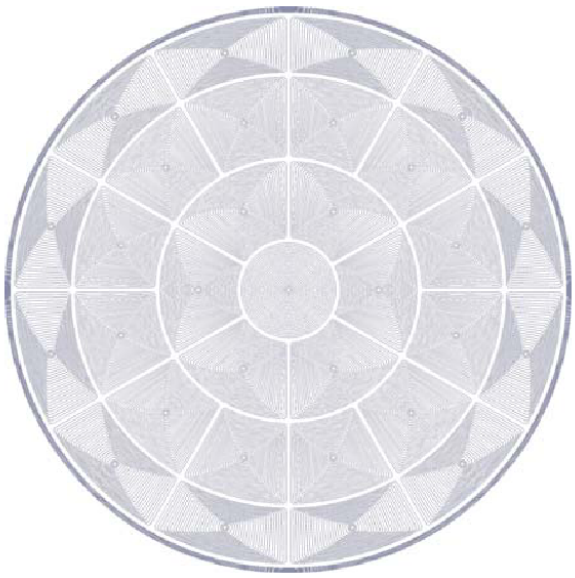

Figure 5.3: The HTRS array of 31 SDD pixels (Barcons et al., 2011a). The pixels have approximately equal area in order to minimize calibration issues due to different radiation damage over the lifetime of the instrument.

Table 5.1: Characteristic properties of the HTRS on *IXO* according to Barcons et al. (2011a).

detector type	31 SDD pixels
time resolution	$10\,\mu$s
energy resolution	150 eV at 6 keV
energy range	0.3–15 keV

of the PSF. The BSDO can be put into the photon beam for observations of bright sources in order to reduce the maximum photon rate per pixel.

HTRS

In contrast to the WFI and the XMS, the HTRS (Lechner et al., 2010a; Barret et al., 2010, 2011) is not an imaging instrument, but is designed for time-resolved spectroscopy of bright Galactic X-ray sources. Its detector consists of an array of 31 SDDs arranged in a circular shape, as shown in Fig. 5.3. It covers the energy range 0.3–15 keV (Barcons et al., 2011a) and has a spectral resolution of about 150 eV at 6 keV. The time resolution of the instrument is $10\,\mu$s. The characteristic properties of the HTRS are summarized in Table 5.1.

Due to the large collecting area of the *IXO* mirrors, the HTRS has to be able to cope with incident photon rates of up to 2×10^6 photons s^{-1}. The incident photon flux is quasi-homogeneously distributed among all 31 pixels in order to avoid a degradation of the energy resolution or the loss of data due to dead time or pile-up at these high count rates. This is achieved by placing the HTRS at a distance of 11.3 cm behind the focal plane (Schmid et al., 2011b). At this location the photon spot that would be observed from a point source with an instrument in the focal plane is smeared over the entire pixel array. As the HTRS is not an imaging instrument, this de-focusing has no major disadvantages. The occurrence of charge cloud splitting between adjacent pixels is prevented by an absorbing mask with a spoke width of $200\,\mu$m covering the edges of the SDD pixels (Barret et al., 2010). The resulting loss of $\leq 10\,\%$ of the incident photons is compensated by the advantage of avoiding calibration and data processing issues related to split events.

XGS

The XGS is a wavelength-dispersive spectrometer and consists of a set of gratings, which are mounted in the optical path between the mirrors and the MIP, and of several CCD cameras,

which measure the dispersed photon beam (Barcons et al., 2011a). Since the mounting of the gratings in the optical path is fixed and the CCD cameras are not located on the MIP, the XGS can be used in any observation in parallel to one of the other instruments on the MIP.

The XGS provides a spectral resolution of $E/\Delta E \geq 3000$ in the energy range 0.3–1.0 keV with an effective area of at least 1000 cm^2. For low energies the resolving power of the XGS therefore exceeds the capabilities of the XMS, whereas the latter has a better performance for higher photon energies. Due to its dispersion technique, the XGS is mainly suitable for observations of point-like sources.

XPOL

The XPOL is the only instrument on *IXO* enabling polarization measurements. It consists of a gas pixel detector with a moderate energy resolution of $\Delta E/E \approx 20\,\%$ in the energy range 2–10 keV (Barcons et al., 2011a). Its positional resolution is 5 arcsec. The instrument covers a FOV of 2.6 arcmin × 2.6 arcmin.

5.1.2 *ATHENA* Configuration

ATHENA is a powerful observatory for various kinds of investigations in the X-ray regime. The mission concept directly addresses three of the scientific objectives of ESA's "Cosmic Vision 2015–2025" program (Bignami et al., 2005), namely "Matter Under Extreme Conditions", "The Evolving Violent Universe", and "The Universe Taking Shape" (Barcons et al., 2011b). In addition to these items, *ATHENA* provides means to investigate several of the further questions highlighted in this program. With its high timing, spatial, and spectroscopic resolution exceeding any previous or current missions it will enable sophisticated observations in order to solve a large variety of issues in X-ray astronomy. Due to its unprecedented capabilities, it might also lead to the discovery of yet unknown phenomena.

The design of the two instruments on *ATHENA* has been adapted to meet the performance requirements imposed by the different scientific goals. Apart from the key questions of accretion physics, cosmic feedback, and large-scale structure, which are described in Chapter 1, *ATHENA* covers a wide field of different observational issues in the X-ray regime, ranging from charge exchange processes (Dennerl, 2010) in our solar system up to the large scale structure of galaxy clusters. The scientific objectives of *ATHENA* have also been covered by the *IXO* mission concept (Barcons et al., 2011a), however, some of the most ambitious goals of *IXO* had to be revised in order to be realizable within the reduced cost margin of *ATHENA*.

The setup of *ATHENA*, as presented in the following, represents the current status of the baseline configuration described by Barcons et al. (2011b). It might be different from the final mission implementation, for which even more ambitious goals are investigated. A sketch of the spacecraft is displayed in Fig. 5.4.

Similar to *IXO* for the *ATHENA* spacecraft a launch into a halo orbit around the L_2 of the Sun-Earth system in 2022 is foreseen. The spacecraft houses two independent SPO X-ray telescopes with equal effective area of 0.5 m^2 at 1.25 keV each (Bavdaz et al., 2011; Collon et al., 2011; Barcons et al., 2011b; Wille et al., 2011). The SPO technology provides a trade-off between mirror weight, effective area, and angular resolution. For a photon energy of 6 keV the mirrors still provide an effective area of 0.25 m^2 for each telescope. The angular resolution of the SPO is 10 arcsec in the baseline configuration, with a goal of 5 arcsec. Both instruments, the WFI and the XMS, are mounted in the focal plane at a distance of 12 m behind the mirrors of the telescopes. The design of the instruments has been adjusted from the *IXO* setup to the overall configuration of *ATHENA*.

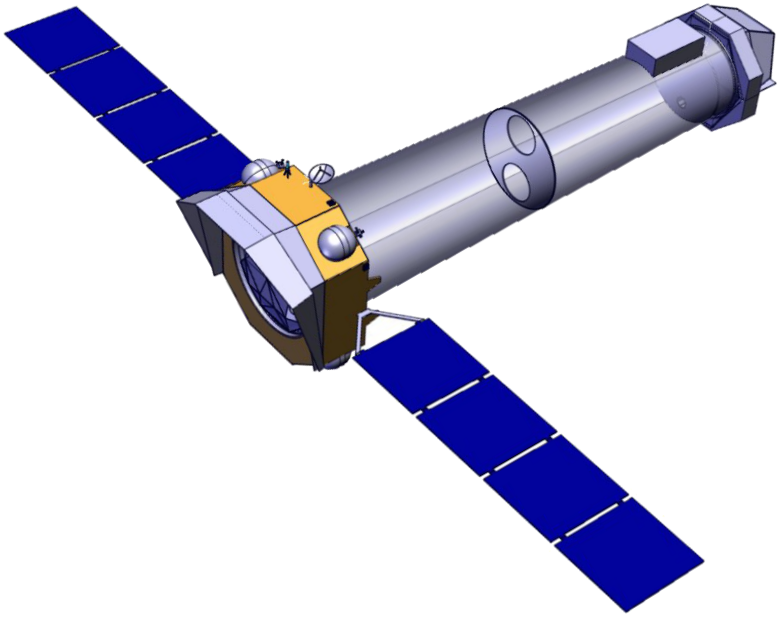

Figure 5.4: The *ATHENA* spacecraft (Bavdaz et al., 2011). On the left-hand side the service module and the mirror assembly with the two telescopes are displayed. The telescopes provide a total effective area of 1 m^2 at energies of 1.25 keV and an angular resolution of $\leq$ 10 arcsec. Both instruments, the WFI and the XMS, are mounted in the focal plane on the right-hand side of the figure. The focal length of 12 m is achieved with a fixed optical bench.

Table 5.2: Characteristic properties of the WFI on *ATHENA* according to Barcons et al. (2011b).

detector type	APS with 640 × 640 DePFET pixels
FOV	24 arcmin
pixel size	130 μm (2.2 arcsec)
time resolution	32 μs
energy resolution	150 eV at 6 keV
energy range	0.1–15 keV

WFI

The WFI on *ATHENA* is an X-ray camera based on APSs. It covers a large FOV of 24 arcmin and the energy range 0.1–15 keV with a nearly Fano-limited energy resolution of 150 eV at 6 keV (Barcons et al., 2011b). The instrument is ideal for wide-field observations with spatially and time-resolved spectroscopy.

Its detector consists of a matrix 640 × 640 DePFET pixels with an edge length of 130 μm each, corresponding to a plate scale of 2.2 arcsec pixel^{-1}. In contrast to, e.g., the EPIC-pn camera on *XMM-Newton*, the detector of the WFI is a monolithic device manufactured out of a single Si wafer, so there are no gaps in its large FOV. The detector is illuminated from the backside in order to gain radiation hardness and sensitivity to photons below 1 keV. The APS technology enables access to individual lines of the pixel matrix and therefore avoids calibration issues such as CTE corrections or OOT events (Sec. 2.3.1). Similar to the WFI in the *IXO* concept a 16 × 16 window readout mode is foreseen in addition to the full-frame mode in order to avoid problems with pile-up for observations of bright sources. In the full-frame mode the camera is operated with a time resolution of 1.28 ms. In the 16 × 16 window mode the time resolution is improved by a factor of 40 to 32 μs. The characteristic properties of the WFI are summarized in Table 5.2.

XMS

The XMS on *ATHENA* is an imaging instrument with a narrow FOV of 2 arcmin in diameter, but an excellent energy resolution of 3 eV for photons below 7 keV (Barcons et al., 2011b). It is designed in particular for spatially-resolved spectroscopy including accurate measurements of emission and absorption lines in the energy range of 0.3–12 keV. The detector consists of an array of 32 × 32 TES microcalorimeter pixels. Each pixel has a size of 250 μm × 250 μm translating

detector type	array of 32×32 TES microcalorimeter pixels
FOV	2 arcmin
pixel size	250 μm (2.2 arcsec)
energy resolution	3 eV below 7 keV
energy range	0.3–12 keV

Table 5.3: Characteristic properties of the XMS on *ATHENA* according to Barcons et al. (2011b).

to a plate scale of 4.3 arcsec pixel^{-1}. With these parameters the XMS will significantly exceed the capabilities of the cryogenic spectrometer on *Astro-H* (Mitsuda et al., 2010), which is the first satellite mission planned to include a calorimeter after the unsuccessful launch of *Astro-E* (Kunieda et al., 2001) and the failure of the XRS aboard *Suzaku* (Mitsuda et al., 2007).

In order to achieve the required operation temperature of 50 mK, an elaborate cooling chain is necessary. For the rejection of background events due to charged particles the instrument comprises an anti-coincidence detector. For the observation of bright sources it is essential to reduce the incident photon flux, e.g., by inserting a filter or a BSDO (Willingale, 2011a) in the optical path. Different concepts for that have been investigated based on simulations with SIXTE. The characteristic properties of the XMS are summarized in Table 5.3.

5.2 Simulations

Using the tools of the SIXTE framework I have performed different investigations of instruments on *IXO* and *ATHENA* as a contribution to the assessment studies of both mission concepts. During that phase the particular instrument configurations have been subject to various modifications. Though, in this context I only refer to the most recent setups.

In the following I present several investigations carried out for the WFI and the XMS, which are the two instruments that have been transferred from the *IXO* mission concept to *ATHENA*. Of course, some modifications of the instrument parameters had to be applied with respect to the *IXO* configuration. I also report on my simulations for the HTRS, which has been part of *IXO*, but is not foreseen for *ATHENA* any more. Nevertheless my work had a significant impact on the design of this instrument such that it is worth to be mentioned here.

5.2.1 WFI

The WFI is one of the two instruments that are part of the *IXO* as well as the *ATHENA* mission concept. Therefore some of the simulations presented in the following have also been carried out for the configuration corresponding to the parameters of *IXO*, although the displayed investigations refer to the study of *ATHENA*.

Image Simulations

One of the main advantages of *ATHENA* in comparison to current missions is a significant increase of the effective area and a corresponding reduction in the flux limit in deep surveys with the same amount of exposure time. In order to provide a realistic estimate of this gain in terms of sensitivity, I have simulated observations of the *Chandra* Deep Field–South (CDF-S) and of a region around the Galactic Center of the Milky Way with the WFI, assuming exposure times of 1 Ms and 500 ks respectively.

From both fields two typical sources have been selected. The corresponding spectra are shown, as they would be obtained with *Chandra* and with *ATHENA*. These simulations are part of the analysis in the "Yellow Book" that has been submitted to ESA as a documentation of the assessment study of *ATHENA* (Barcons et al., 2011b).

***Chandra* Deep Field–South** The CDF-S is a region with a Galactic latitude of about −54 deg. Therefore observations in this field are little affected by absorption due to the Galactic ISM ($N_{\rm H} \approx 8.8 \times 10^{19}\,{\rm cm}^{-2}$ according to Stark et al., 1992; Xue et al., 2011). The CDF-S is mostly populated by very faint sources, and it is an ideal target for deep surveys aiming at the detection of distant objects at high redshifts. The CDF-S has been subject to various observations with *Chandra* (Giacconi et al., 2002; Lehmer et al., 2005; Luo et al., 2008; Xue et al., 2011) and with *XMM-Newton* (Comastri et al., 2011). I have simulated a 1 Ms observation of this popular field with the WFI in order to illustrate the high sensitivity provided by the large effective area of the *ATHENA* telescope.

Setup In order to provide a realistic input for the simulation, I have compiled a SIMPUT catalog with various source types:

- For the central region around the position RA = 53.1 deg and Dec = −27.8 deg a comprehensive catalog of sources is provided by Xue et al. (2011). The data are obtained from various observations with *Chandra* adding up to a total exposure time of 4 Ms. I have converted the positions and the X-ray fluxes of the contained sources to the SIMPUT format such that they are usable for my simulations.
- The area covered by the catalog of Xue et al. (2011) is mainly limited by the FOV of *Chandra*. It corresponds to a smaller solid angle than the FOV of the WFI on *ATHENA* such that I had to add additional sources to the SIMPUT catalog in order to populate the full FOV of the WFI. These sources are taken from the catalog provided by Lehmer et al. (2005) for the extended CDF-S.
- In order to account for emission from faint extended sources, I have added a catalog of galaxy groups and clusters. The catalog is compiled from a recent observation of the CDF-S with *XMM-Newton* (A. Finoguenov, priv. comm.). The radial surface brightness profile of the galaxy clusters has been simulated according to a β-model (King, 1972):

$$S(r) \sim \left(1 + \left(\frac{r}{r_{\rm c}}\right)^2\right)^{-3\beta+0.5} \tag{5.1}$$

  with $\beta = 0.6$ according to Jones & Forman (1999) and a core radius $r_{\rm c} = 0.1\,r_{200}$.[1]
- In addition to the galaxy clusters, a map of unresolved diffuse emission from the mentioned *XMM-Newton* observation has been included in the simulation (A. Finoguenov, priv. comm.).

In order to provide a more realistic simulation input, it would have been necessary to replace the diffuse background emission by a large sample of faint AGN accounting for the CXRB (Sec. 4.2.4), since the sensitivity of *ATHENA* allows for the detection of fainter sources than those visible with *Chandra* or *XMM-Newton*. However, for the current analysis the presented data are sufficient. The faint AGN would not change the overall appearance of the output image significantly, but would only be detectable with appropriate source detection tools.

The spectra of the sources from the catalogs of Xue et al. (2011) and Lehmer et al. (2005) and the spectrum of the diffuse background radiation have been approximated by an absorbed power law model. The spectra of the galaxy groups and clusters are modeled with the `apec`[2] emission model (Smith et al., 2001). Although the assumption that the spectra of all the sources in the field can be identified with these common models is only a rough approximation, it is sufficient in order to convert the fluxes of the individual sources to proper count rates for the image simulation.

[1] The quantity r_{200} denotes the radius inside which the mean interior density is 200 times the critical density (Carlberg et al., 1997).

[2] `http://atomdb.org/`

For a closer analysis of the spectral capabilities of *ATHENA* in addition to its imaging properties I have selected two typical sources from the entire sample in the CDF-S. To these two sources I have applied more elaborate spectral models:

- As an example for an extremely faint source I have approximated the spectrum of a Compton-thick AGN at a redshift of $z = 3.7$ with an absorbed power law and a Gaussian Fe line. The source has a flux density of $4 \times 10^{-17}\,\mathrm{erg\,s^{-1}\,cm^{-2}}$ in the band 0.5–2 keV.
- As an example with multiple emission lines I have simulated a galaxy group at a redshift of $z = 1.6$. Its spectrum is defined by an `apec` model (Smith et al., 2001) with a temperature of 1 keV and chemical abundances $Z/Z_\odot = 0.3$ (parameters according to A. Finoguenov, priv. comm.). The source has a flux density of $2.3 \times 10^{-16}\,\mathrm{erg\,s^{-1}\,cm^{-2}}$ in the band 0.5–2 keV.

I have simulated the spectra of these two sources with `ISIS` both for the WFI on *ATHENA* and the ACIS-I on *Chandra*. Afterward I have fitted the corresponding models to the simulated data, in order to have an estimate of the reproducibility and therefore of the quality of the data. For that purpose I have binned the spectra to a comparable signal to noise ratio in order to allow a direct comparison of the spectroscopic capabilities of both instruments.

Results The image of a simulated 1 Ms observation of the CDF-S represented by the described SIMPUT source catalog is shown in Fig. 5.5. The simulated spectra of the two selected sources emphasize the difference between the *ATHENA* WFI and the *Chandra* ACIS-I in terms of sensitivity. *ATHENA* will allow the detection of much fainter sources and the modeling of spectra at much lower flux densities than with current missions. Although its angular resolution (10 arcsec in the presented simulation) is worse than that of *Chandra* (0.5 arcsec, Weisskopf et al., 2000, 2002), a deep observation such as the presented one is not limited by source confusion[3].

Galactic Center In contrast to the CDF-S, observations in the region around the Galactic Center at the position RA = 266.4 deg and Dec = −29.0 deg are strongly affected by absorption due to Galactic gas and dust ($N_\mathrm{H} \approx 6 \times 10^{22}\,\mathrm{cm^{-2}}$, according to Baganoff et al., 2003; Muno et al., 2009). Nevertheless this region is of high interest, since, apart from Sgr A*, the super-massive BH in the center of our galaxy, it contains several Low-Mass X-ray Binarys (LMXBs), High-Mass X-ray Binarys (HMXBs), and other X-ray sources (Sec. 1.3). I have simulated a 500 ks observation of the inner region around Sgr A* with the WFI on *ATHENA* in order to illustrate the spectroscopic capabilities of this instrument.

Setup The input for the simulation consists of three composite images from several observations with *Chandra* with a total exposure time of 2.25 Ms per image (Muno et al., 2009). The *Chandra* images contain data in the three energy bands 1–3, 3–5, and 5–8 keV. In the SIMPUT catalog assembled for the simulation with SIXTE the three images are modeled as extended X-ray sources with flat spectra for the respective energy bands. This approximation is sufficient to determine the proper photon rate for the image simulation.

For a spectroscopic analysis similar to the one for the CDF-S I have selected two typical sources out of the field:

- One of the most interesting sources in this region is probably the super-massive BH Sgr A* in the center of our galaxy itself. The X-ray emitting source associated to the position of the actual radio source Sgr A* is characterized by its frequent flares (Baganoff et al., 2003; Muno et al., 2004a; Marrone et al., 2008). For the simulation of its spectrum I have

[3]The detection limit of a deep observation with a particular instrument is mainly determined by the exposure time down to the regime of so-called source confusion. At some point the number density of faint sources (see log$N$-log$S$ relation in Sec. 1.3) becomes too high such that they cannot be resolved even with longer exposures due to the limited angular resolution of the telescope.

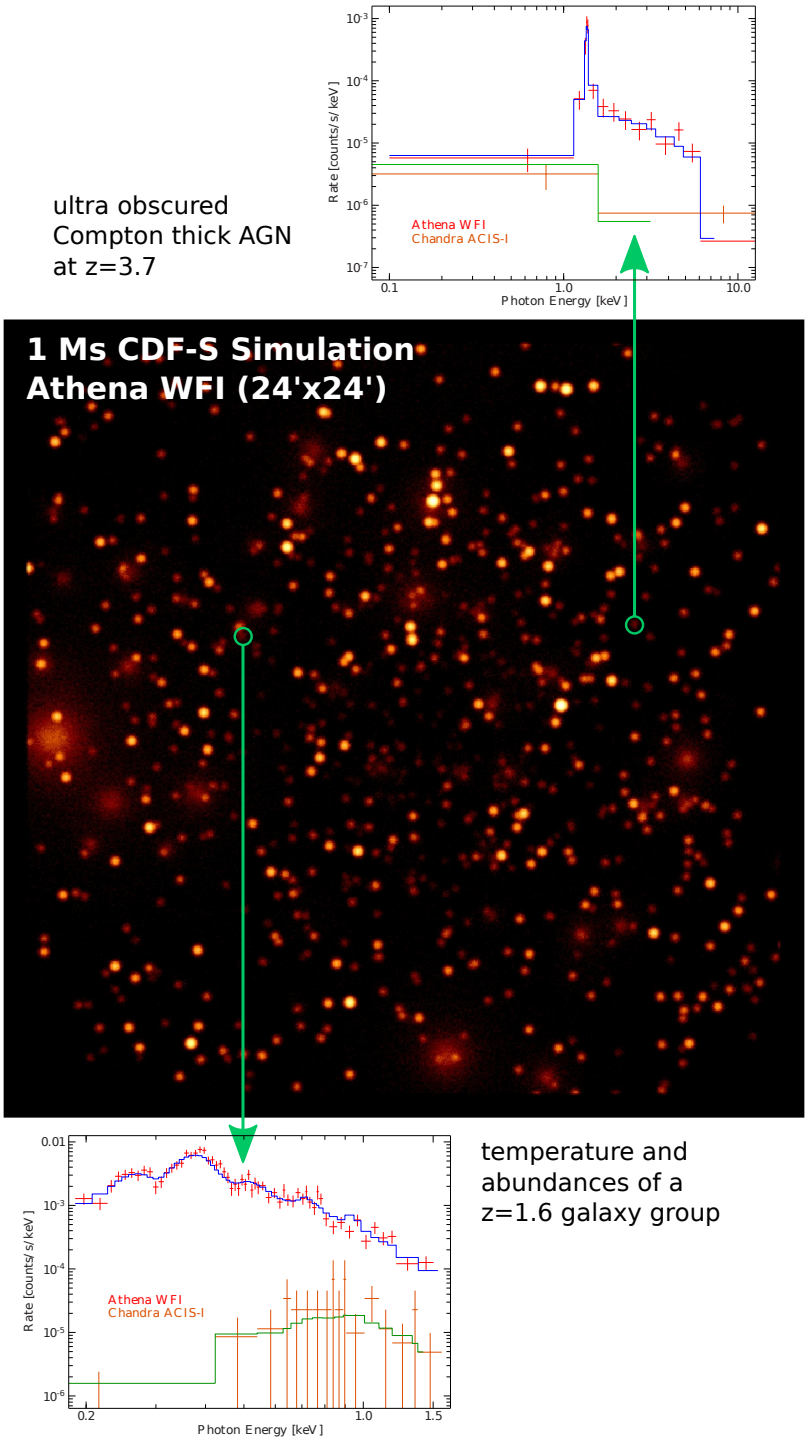

Figure 5.5: Image of a simulated 1 Ms observation of the CDF-S with the WFI on *ATHENA*. The color scale is logarithmic. Two typical faint sources have been selected in order to illustrate the gain in sensitivity provided by *ATHENA* with respect to *Chandra*. The spectra display the simulated data points with error bars as well as the fitted spectral models. In the spectrum of the obscured AGN the Fe line can be clearly resolved despite of its very faint flux density. For the ACIS-I on *Chandra* the observed counts (∼15 counts in the displayed spectral range) are not sufficient to unveil the spectral shape. With the WFI the temperature of the galaxy group as well as chemical abundances can be determined, whereas the sensitivity of the ACIS-I in the relevant energy range below 1 keV is not sufficient for spectroscopy.

assumed an absorbed power law model with various emission lines according to M. Nowak (priv. comm.). The corresponding flux density is $2 \times 10^{-13}\,\mathrm{erg\,s^{-1}\,cm^{-2}}$ in the energy band 2–8 keV.

- The second bright source in the simulated field is the LMXB GRS 1741.9-2853 (Muno et al., 2004b). For its spectrum I have assumed an absorbed power law model according to Degenaar & Wijnands (2010) for the outburst in 2009 with an artificial relativistically broadened Fe line according to the model provided by Dauser et al. (2010). The simulated flux density is $9 \times 10^{-11}\,\mathrm{erg\,s^{-1}\,cm^{-2}}$ in the energy band 2–10 keV.

The spectrum of Sgr A* has been simulated and fitted with `ISIS` for both instruments, the WFI on *ATHENA* as well as the ACIS-I on *Chandra*. The high flux of GRS 1741.9-2853 corresponds to $\sim$35 photons $\mathrm{s^{-1}}$ for the WFI and $\sim$3.5 photons $\mathrm{s^{-1}}$ for the ACIS-I. With an exposure time of 3.2 s per frame an observation of this source with the ACIS-I would be strongly affected by pile-up. The WFI, however, provides sufficient count rate capabilities to guarantee a negligible pile-up fraction.

In addition to Sgr A* and GRS 1741.9-2853, I have simulated observations of the diffuse emission in a 1 $\mathrm{arcmin^2}$ region close to Sgr A* with the WFI and the ACIS-I. The model for this simulation has been selected according to the parameters provided by Muno et al. (2004b). However, the spectra of Sgr A* and GRS 1741.9-2853 have been preferred for the composite Galactic Center image presented in the *ATHENA* Yellow Book (Barcons et al., 2011b).

Results The simulated image obtained from SIXTE for an exposure time of 500 ks is shown in Fig. 5.6. Due to the larger PSF of *ATHENA* with a HEW of 10 arcsec, the smearing of the sources is more evident than in the input *Chandra* images. However, the combination of the high spectral resolution of the WFI and the large effective area of *ATHENA* provides high quality spectra at much shorter exposure times than with *Chandra* and enables the discrimination of close-by emission lines.

The simulated spectrum of the diffuse emission close to Sgr A* for the WFI and the ACIS-I is shown in Fig. 5.7. In general, the quality of the spectral models obtained from fitting the simulated data with `ISIS` is much better for the WFI than for the ACIS-I.

Bright Source Performance

The *ATHENA* mission concept does not contain an instrument dedicated in particular to observations of bright Galactic sources such as the HTRS on *IXO*. This task is fulfilled by the WFI, which provides special operation modes with high time resolution and count rate capabilities. In the baseline configuration the detector is read out line-wise with one active line per hemisphere. The readout process starts in the center of the detector and proceeds towards the two opposite edges. This process is repeated continuously. For a single line an interval of 4 μs is required, i.e., the readout time for the full pixel array is

$$\frac{640}{2} \cdot 4\,\mu\mathrm{s} = 1.28\,\mathrm{ms} \tag{5.2}$$

This operation mode is denoted as full-frame mode. In order to provide a faster operation of the detector for observations of bright sources, a window mode is foreseen. In this mode only the inner 16 lines of the detector are repeatedly read out resulting in a frame time of only 32 μs. A sketch of the full-frame and the window mode is given in Fig. 5.8. In the window mode the FOV of the instrument is strongly limited. Therefore this mode is only recommendable for observations of bright point-like sources. In addition to the baseline configuration, it is considered to double the frame rate by using two active readout lines per hemisphere. However, this dual-line readout option gives rise to a higher power consumption.

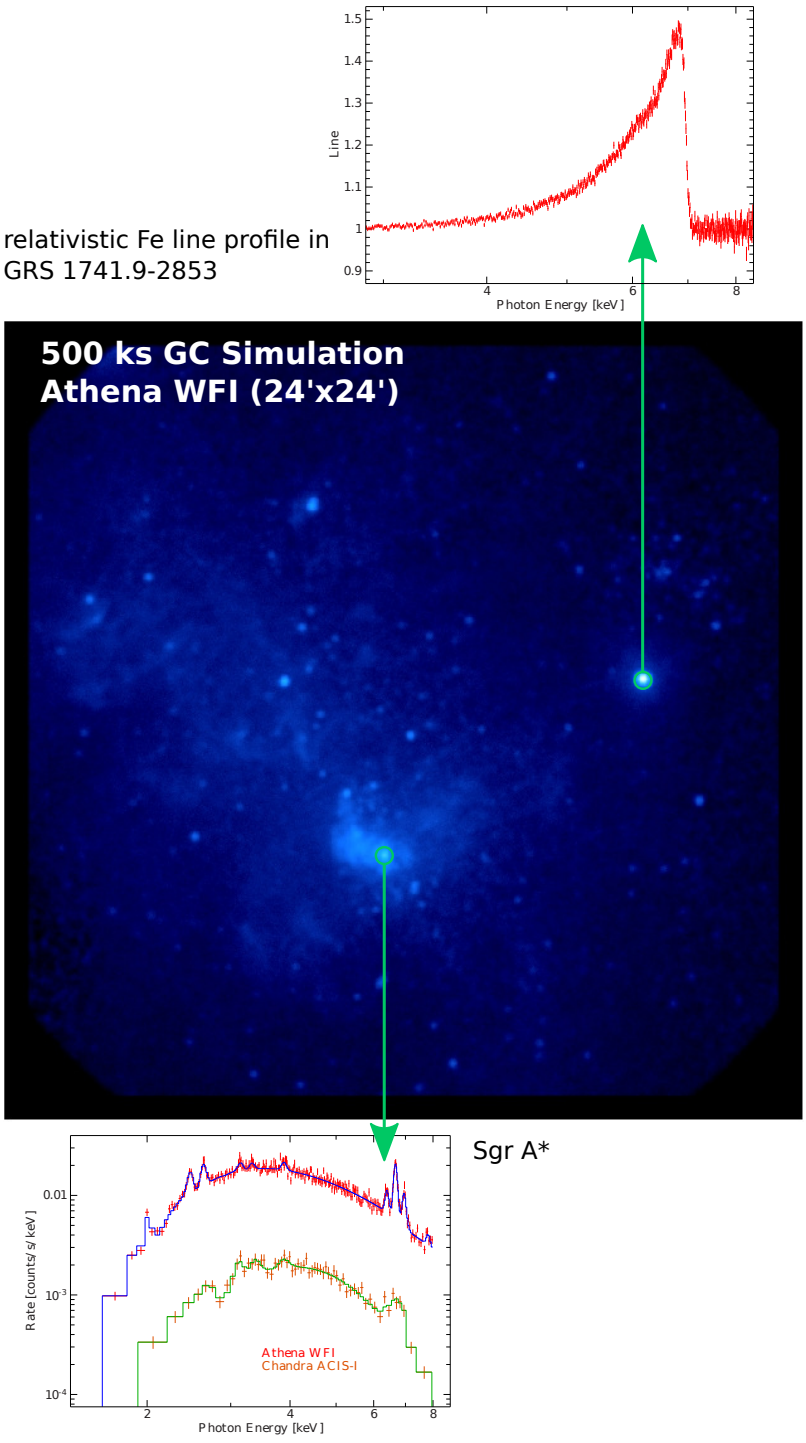

Figure 5.6: Image of a simulated 500 ks observation of the region around the Galactic Center with the WFI on *ATHENA*. The color scale is logarithmic. The spectrum of Sgr A* is shown on the bottom, illustrating the big advance of the spectroscopic capabilities of *ATHENA* in comparison to *Chandra*. The spectrum contains the simulated data points with error bars as well as the fitted model. The WFI provides a much higher throughput than the ACIS-I and enables the discrimination of individual emission lines. The spectrum on the top shows a simulated observation of a fake relativistically broadened Fe line added to the actual spectrum of the LMXB GRS 1741.9-2853. The high count rate capabilities of the WFI allow for an observation of this bright source, whereas data from the ACIS-I would be affected by pile-up problems ($\sim$11 counts frame^{-1}). With the data measured by the WFI the line profile can be accurately resolved.

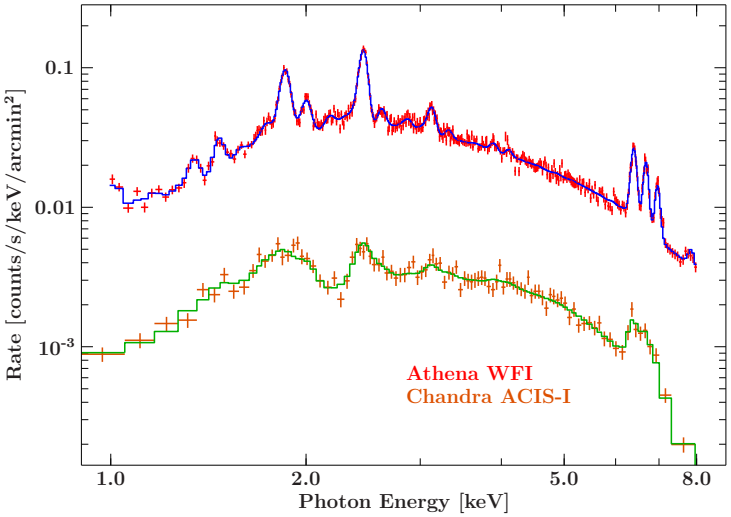

Figure 5.7: Simulated spectrum of the diffuse emission in a 1 arcmin^2 region close to the Galactic Center for the WFI and the ACIS-I. The data points have been re-binned to a comparable signal to noise ratio. Due to its about one order of magnitude higher throughput, the WFI in contrast to the ACIS-I enables the discrimination of individual emission lines in the fitted model.

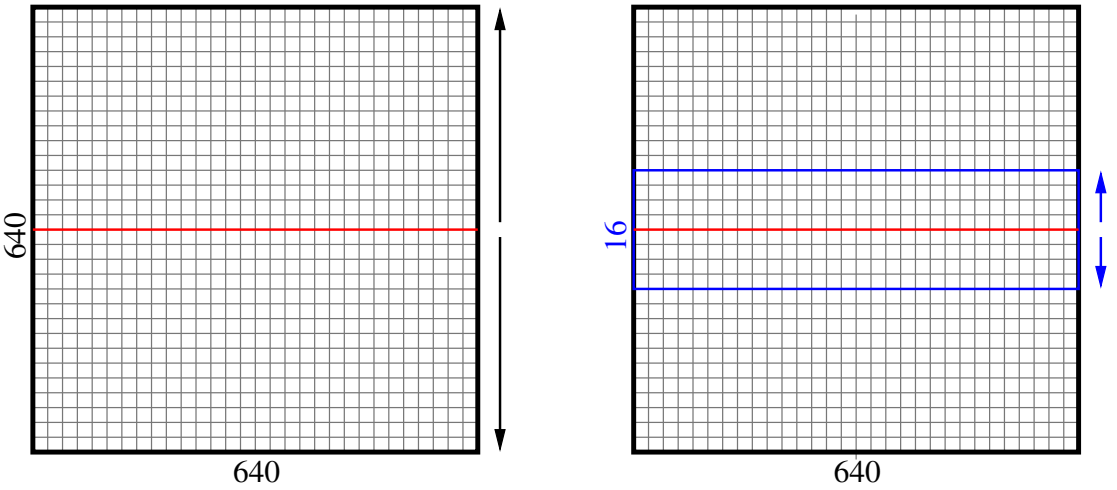

(a) In the full-frame mode all 640 lines are readout with two lines operated in parallel.

(b) In the window mode only the inner 16 lines are readout in order to provide a higher frame rate.

Figure 5.8: Readout modes of the baseline setup of the WFI on *ATHENA*. The displayed pattern does not represent the actual number of pixels, which is given by the number at the edge of the drawings.

In order to investigate the performance of the WFI in terms of pile-up, I have simulated observations of sources with Crab-like spectra and different brightness, as in Sec. 4.2.2 for eROSITA. The simulations presented here have been carried out for the WFI on *ATHENA* but are based on a previous analysis for the WFI on *IXO*. The overall setup has been adjusted to the configuration of *ATHENA*. This section only provides a short overview of the performed analysis, whereas detailed data are presented by Schmid & Wilms (2011a).

According to the instrument response for the *ATHENA* WFI, which is given in the file `ixo_wfi_default_owl_0.15_11.5_09052011.rsp`[4], and the spectral model defined by the parameters in Table 4.2, an observation of the Crab nebula corresponds to a photon rate of about 35 500 photons s^{-1}. The photons generated for the regarded sources are distributed among the pixels according to a 2-dimensional Gaussian, which I have used as an approximation of the PSF of the *ATHENA* telescope. I have assumed a HEW of 10 arcsec corresponding the mission

[4]The response matrix is available on the *ATHENA* web site: `http://www.mpe.mpg.de/athena/`.

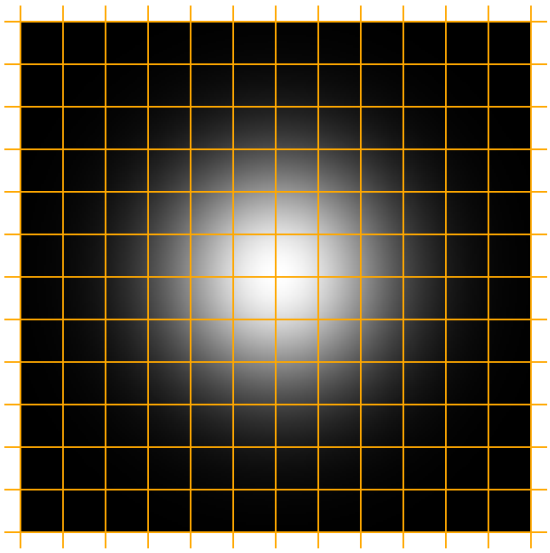

(a) The PSF centered on a corner between four pixels.

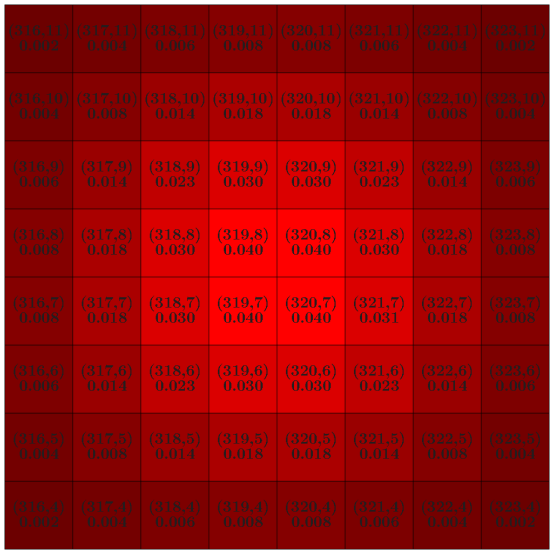

(b) Fraction of photons in the individual pixels. The upper two numbers in each pixel represent the pixel indices and the lower number denotes the fraction of incident photons.

Figure 5.9: *ATHENA* PSF on the inner part of the pixel array of the WFI. The displayed images correspond to a PSF with a HEW of 10 arcsec according to the mission requirements.

requirements. The photon distribution among the pixels is shown in Fig. 5.9.

Split events are produced according to the 2-dimensional Gaussian charge cloud model with $\sigma = 11\,\mu$m (Sec. 3.2.3). The signal arising from each photon impact is distributed among the affected pixels. The collected signals are subsequently read out according to one of the two presented detector operation modes and a pattern search is performed in order to identify all valid event patterns corresponding to the four basic types displayed in Fig. 2.19. Any other pattern types are discarded as invalid, since they cannot be created by a single photon impact. The simulations allow to identify events that are affected by pile-up by keeping track of individual photons. In contrast to a real observation it can therefore be determined, whether an event pattern originates from a single or from multiple photons.

In Fig. 5.10 the detector efficiency and the pile-up fraction are displayed as functions of the simulated photon rate. The data include all valid split patterns of singles, doubles, triples, and quadruples. The detector efficiency is defined as the ratio of the number of valid split patterns and the total number of simulated photons. This quantity is a measure for the throughput of the instrument, since only valid patterns are taken into account for the scientific analysis. Of course, valid pattern types can still be affected by pile-up (Sec. 2.3.2). The second quantity, the pile-up fraction therefore denotes the fraction of valid event patterns affected by energy or pattern pile-up. As indicated in Fig. 5.10, the pile-up fraction for observations of bright sources can be reduced by considering only single-pixel events and neglecting all other split pattern types (Ballet, 1999). However, this method also results in a reduced detector efficiency due to the lower number of usable events.

Apart from the baseline instrument configuration, I have analyzed various setups with different detector parameters, e.g., in terms of readout speed or pixel sizes. In order to obtain a relation between the pile-up and the time resolution of the detector, I have simulated different operation modes including the full-frame mode and several window modes with different window sizes. I have investigated the dual-line readout option as well as the mono-line setup. The resulting

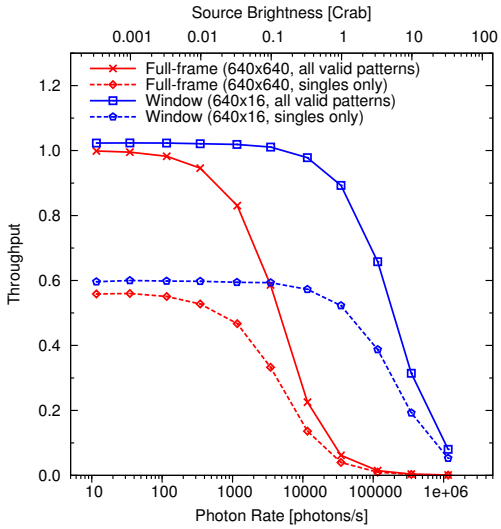

(a) Detector efficiency representing the number of valid split patterns and single pixel events respectively divided by the total number of simulated photons. The efficiency has a value slightly above 1 for low photon rates, which is an artifact in the simulation caused by split events between subsequent frames. Such inter-frame split events are possible because of the line-wise readout of the pixel array of the WFI. An explanation of a related effect giving rise to so-called misfit clusters is given by Lauf (2011).

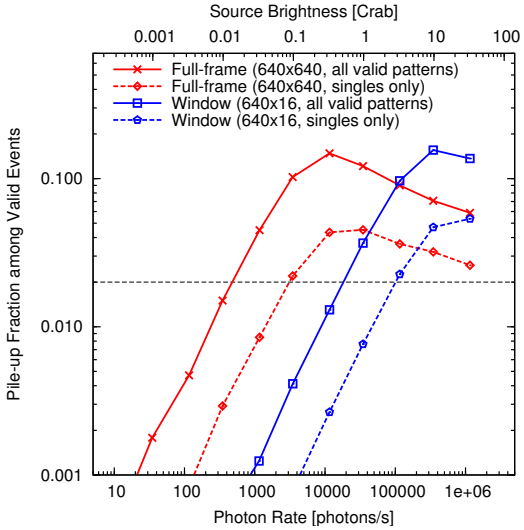

(b) Fraction of pile-up events among the valid split patterns and single pixel events respectively. The horizontal dashed line denotes a pile-up fraction of 2 %. As explained in Sec. 4.2.2, for very high count rates the pile-up fraction starts to decrease, since the core of the PSF only contains invalid patterns, which are discarded anyway, while the wings of the PSF are less affected by pile-up.

Figure 5.10: Simulated bright source performance of the WFI on *ATHENA* for the full-frame and window modes according to the baseline configuration. The bottom axis represents the simulated photon rate, the top axis gives the corresponding source brightness as a fraction of 1 Crab. If only single-pixel events are taken into account, the throughput of the instrument significantly decreases. However, the pile-up fraction among single-pixel events is much lower than for the combination of all valid pattern types, as expected by Ballet (1999).

relation between the detector readout speed and the threshold at which a pile-up limit of 2 % is reached are displayed in Fig. 5.11.

As already stated in Sec. 2.3.2, pile-up in an X-ray detector spoils the quality of the measured scientific data. Photon count statistics are affected if multiple photons are wrongly detected as a single-photon event. Also spectra can be distorted, since pile-up events produced by multiple photons are wrongly identified as single-photon events with a higher energy (Sec. 4.2.2). Due to these effects, a spectrum affected by pile-up has an excess of photons at higher energies, but the total number of counted photons is too low.

As in Chapter 4, I have simulated observations of sources with the same input spectrum defined by an absorbed power law with a photon index Γ of 2.1 and a hydrogen absorption column N_{H} of $0.4 \times 10^{22}\,\mathrm{cm}^{-2}$ but different brightness and therefore pile-up fraction with the WFI. From the simulated data I have produced spectra and fitted them again with an absorbed power law model. For low pile-up fractions the input parameters are recovered, whereas for higher pile-up fractions the values are significantly distorted according to the apparent excess of high energetic photons. The relation between the fitted parameters and the pile-up fraction in the simulated data is illustrated in Fig. 5.12. Spectra with higher pile-up fraction contain more high energetic photons and are therefore harder (corresponding to a lower photon index) than

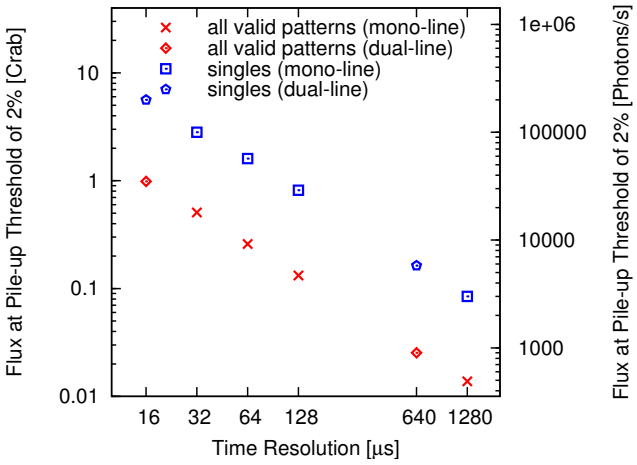

Figure 5.11: Relation between the flux for which the pile-up limit of 2 % is reached and the time resolution of different operation modes of the WFI on *ATHENA* as obtained from simulations with different readout modes. Data are shown for the mono-line option with one active readout line per hemisphere (corresponding to the baseline) and the dual-line option with two active lines per hemisphere.

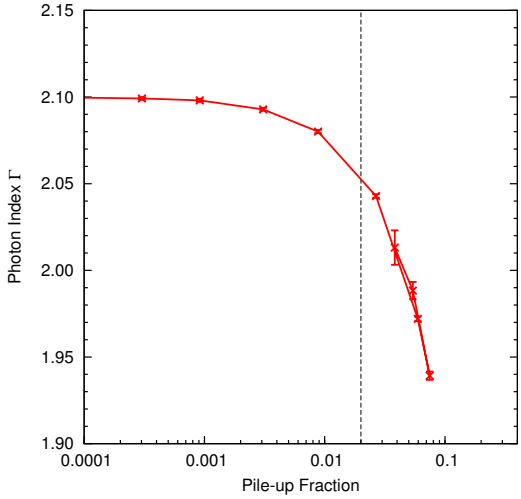

(a) Photon index of simulated spectra as a function of the pile-up fraction. The hydrogen absorption column has been frozen to its nominal value of $0.4 \times 10^{22}\,\mathrm{cm}^{-2}$ during the fit process. For higher pile-up fractions the simulated spectrum is significantly harder (lower photon index) than the input spectrum.

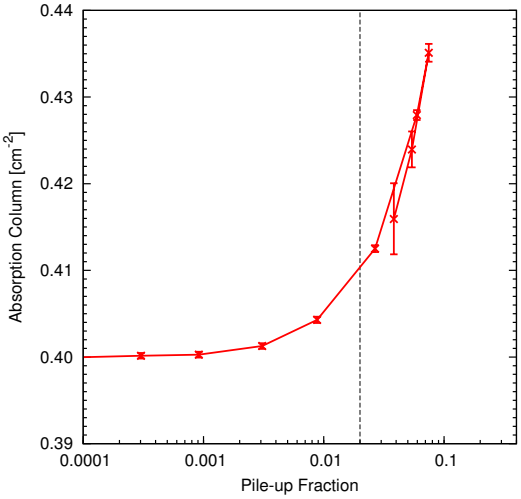

(b) Hydrogen absorption column of simulated spectra as a function of the pile-up fraction. The photon index has been frozen to its nominal value of 2.1 during the fit process. For higher pile-up fractions the simulated spectrum has a significantly lower contribution at low photon energies in comparison to the input spectrum, which is modeled by a higher absorption column.

Figure 5.12: Distortion of scientific data such as spectral parameters due to pile-up. The actual spectrum of the simulated X-ray source is defined as an absorbed power law model with a photon index Γ of 2.1 and a hydrogen absorption column N_H of $0.4 \times 10^{22}\,\mathrm{cm}^{-2}$. The figures display the parameters obtained from a fit with `ISIS` to simulated data with different pile-up fractions. For the analysis all valid split patterns have been taken into account. The vertical dashed line denotes a pile-up fraction of 2 %, which can be regarded as some kind of critical threshold.

the actual input spectrum of the observed source. Alternatively the observed distortion can be modeled by a higher absorption column, which reduces the photon flux a low energies. Similar to the simulations for eROSITA (Sec. 4.2.2), the data in Fig. 5.12 indicate that for a reasonable scientific analysis the pile-up fraction should be constrained to a level below 2 %. Above this threshold the derived spectral parameters might be significantly distorted.

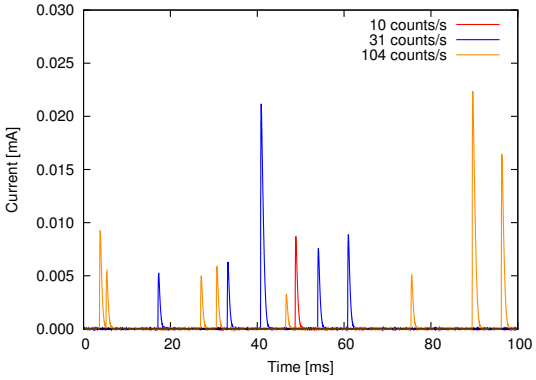

(a) For moderate count rates per pixel the amplitude and the shape of the pulses can be sampled with the required accuracy.

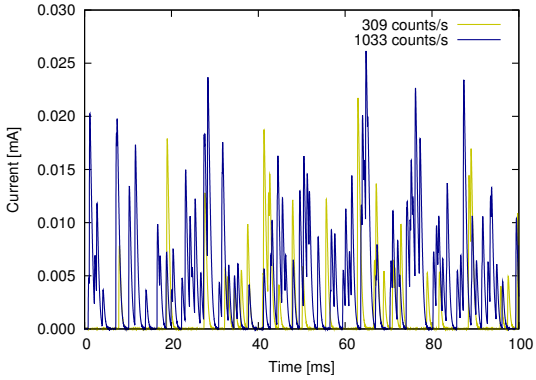

(b) For high count rates the individual pulses are overlapping and the energy resolution of the instrument is degraded.

Figure 5.13: Current pulses produced by absorbed photons in a single TES of the *ATHENA* XMS. I have calculated the pulse shapes with a program provided by S. Smith (priv. comm.).

5.2.2 XMS

As with the WFI, I have investigated the bright source performance of the XMS for both the *IXO* and the *ATHENA* assessment studies. In this section I present my analysis for the *ATHENA* configuration.

In order to determine the energy of a photon absorbed by one of the TES microcalorimeter pixels of the XMS, the amplitude and the shape of the resulting current pulse have to be determined with high precision. The readout electronics sample the current with a certain frequency in order to determine the pulse profile as a deviation from the baseline signal. If the average rate of photons in a single pixel is too high, the time difference between subsequent photons becomes too short for a sufficient number of sampling points such that the energy resolution of the TES is degraded. The plots in Fig. 5.13 display simulated current pulses produced by a sample of photons at different moderate and high count rates in order to illustrate the confusion between consecutive pulses.

In order to classify the energy resolution of a particular photon event, different event grades are introduced. The assignment of a grade to a particular event depends on the time difference between the photon impact and its preceding and successive events (SRE-PA, 2009; den Herder et al., 2010). The following three event grades can be identified:

- For a **high resolution** event no other photon may hit the same detector pixel during an interval starting 10τ before the event and lasting 40τ after the event.
- If a second photon hits the same pixel during the interval between 10τ after and 40τ after the regarded event, the event can be detected with **medium resolution**.
- If a second photon hits the same pixel during the interval between 10τ before and 10τ after the event, it can only be measured with **low resolution**.

A graphical illustration of the conditions for the different event grades is displayed in Fig. 5.14. The typical decay time corresponds to $\tau = 150\,\mu$s according to SRE-PA (2009). The fractional distribution of the individual event grades in a single pixel can be obtained as a function of the photon rate in this pixel. Assuming an exponential distribution of the time intervals between

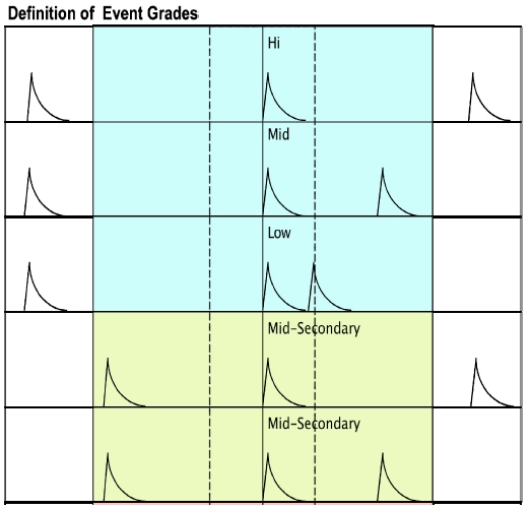

(a) Definition of different event grades for the *ATHENA* XMS. The colored regions denote a time interval of 40τ before and after the central photon event. The dashed lines represent the shorter interval of 10τ before and after the photon impact (den Herder et al., 2010).

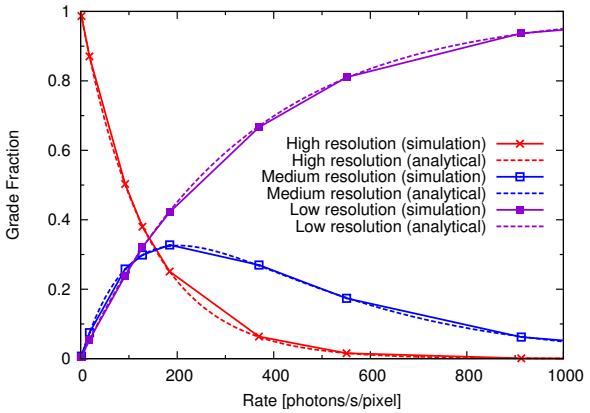

(b) Fraction of the different event grades in a single TES pixel as a function of the incident photon rate. The data are obtained from simulations as well as from an analytical model. They agree very well with the distribution presented by den Herder et al. (2010).

Figure 5.14: *ATHENA* XMS event grades.

subsequent photons, Poisson statistics yield

$$\begin{aligned} h(r) &= e^{-50\cdot\tau\cdot r} \\ m(r) &= e^{-20\cdot\tau\cdot r} - e^{-50\cdot\tau\cdot r} \\ l(r) &= 1 - e^{-20\cdot\tau\cdot r} \end{aligned} \tag{5.3}$$

where r denotes the photon rate per pixel, $h(r)$ the fraction of events with high energy resolution, $m(r)$ the fraction with medium energy resolution, and $l(r)$ the fraction with low energy resolution. This analytical model is very similar to the calculation of event loss due to dead time, as shown in Sec. 2.3.2.

In addition to the presented three grades, there is another class of events. Any number of multiple events in the same pixel that are separated by less than $20\,\mu$s are denoted to be affected by pile-up. They cannot be distinguished from each other because of the short time difference and are therefore wrongly detected as a single event with a higher photon energy corresponding to the sum of the energies of all involved photons.

In order to obtain an estimate of the spectroscopic capabilities of the XMS as a function of the incident photon rate, I have simulated observations of X-ray sources with different brightness. According to the instrument response, which is given in the file `ixo_xms_none_owl_0.15_11.5_09052011.rsp`[5], and the spectral model defined by the parameters in Table 4.2, an observation of the Crab nebula corresponds to a photon rate of about 32 000 photons s^{-1} incident on the XMS[6]. In the baseline configuration without any filter or other devices in the optical path the incident photons are distributed on the pixel array according to a 2-dimensional Gaussian, which I have assumed as a model for the PSF of the *ATHENA* telescope. Instead of the HEW of 10 arcsec corresponding to the requirements of the mission I

[5]The response matrix is available on the *ATHENA* web site: `http://www.mpe.mpg.de/athena/`.

[6]This number is lower than for the WFI, although both telescopes of *ATHENA* have the same effective area, because the XMS has a lower filling factor, i.e., there are small gaps between the individual TES pixels.

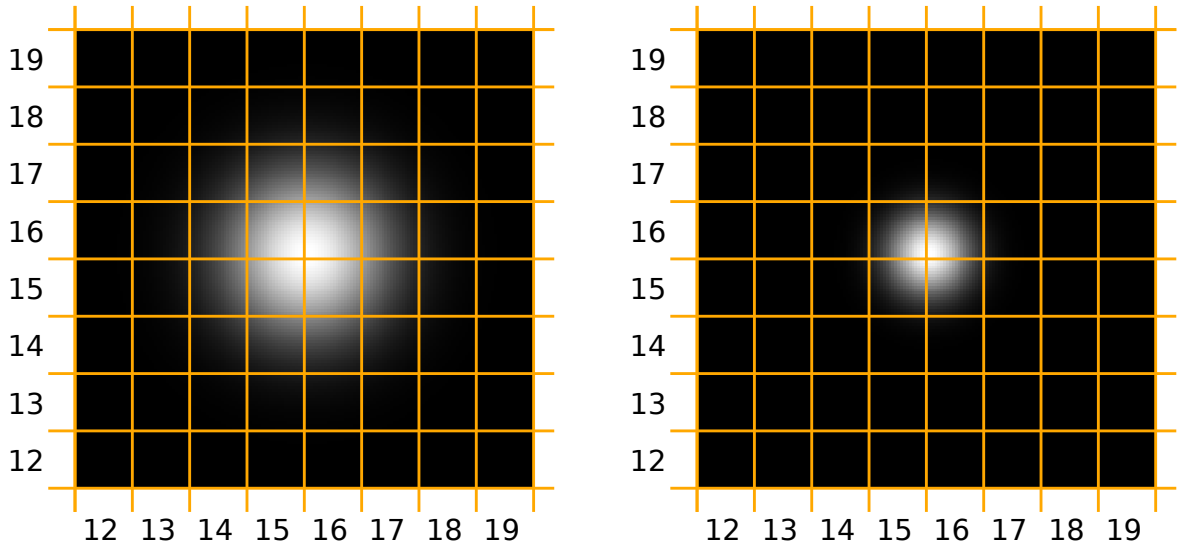

(a) PSF with 10 arcsec HEW (requirement). **(b)** PSF with 5 arcsec HEW (goal).

Figure 5.15: Gaussian PSF on the *ATHENA* XMS centered on the corner between the pixels (15, 15), (15, 16), (16, 15), and (16, 16).

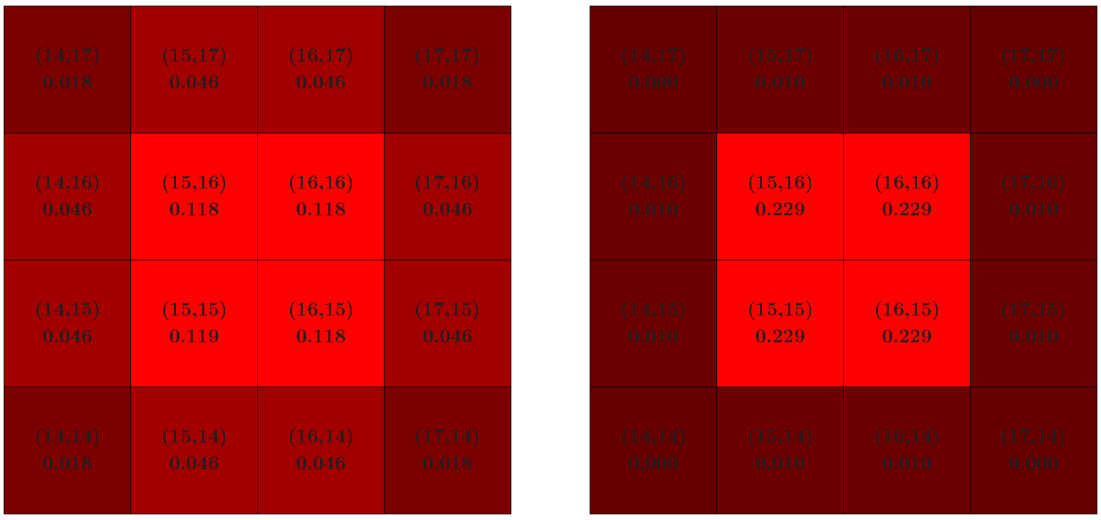

(a) PSF with 10 arcsec HEW (requirement). **(b)** PSF with 5 arcsec HEW (goal).

Figure 5.16: Photon distribution among the inner pixels of the *ATHENA* XMS array. The color scale reflects the fraction of incident photons in each pixel given by the bottom numbers. The numbers on the top represent the pixel indices.

have used the goal value of 5 arcsec for the presented data, in order to deal with the worst case scenario (in terms of pile-up). Although this narrower PSF is more advantageous for imaging purposes, it is also more challenging in terms of bright source performance. As the incident photons are distributed among a smaller number of pixels, the photon rate per pixel is higher than for a broader PSF. A comparison of the PSFs with 10 arcsec and with 5 arcsec HEW is displayed in Figs. 5.15 and 5.16. In the following I only refer to the 5 arcsec PSF displayed in Figs. 5.15b and 5.16b, although I have also investigated the other option (Schmid & Wilms, 2011b).

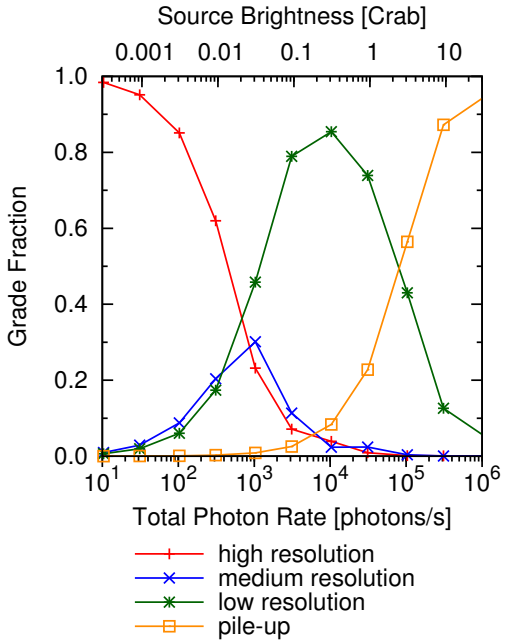

(a) Fractions of the different event grades.

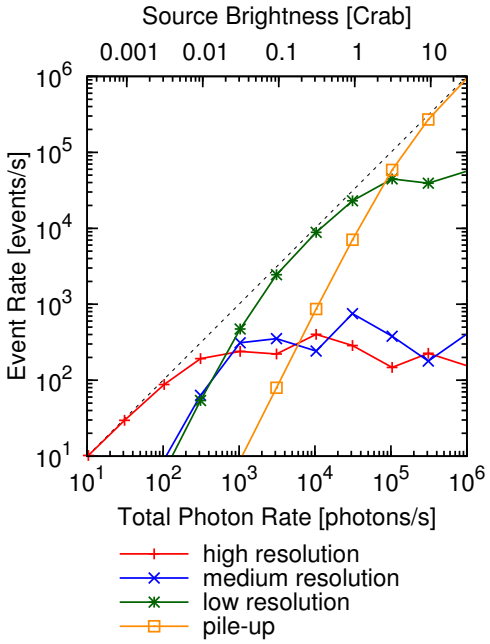

(b) Throughput of the different event grades. The dashed line denotes a throughput of 100 %.

Figure 5.17: Event grades of the *ATHENA* XMS without a filter as a function of the observed photon rate. The bottom axis denotes the total rate of photons incident on the XMS. The top axis displays the corresponding source brightness as a fraction of the Crab rate, which is defined as 32 000 photons s^{-1}.

In Fig. 5.17 the fractions of the individual event grades are displayed for observations with different incident photon fluxes. For observations of moderately bright sources above a few mCrab the fraction of events with high energy resolution is significantly decreasing. Therefore I have analyzed different techniques to preserve the measurement accuracy of the instrument in this count rate regime.

A common method used for CCDs such as the EPIC-pn camera in order to reduce the pile-up fraction in measured data is to neglect the events from the inner pixels of the detector, which are located in the core of the PSF. These pixels are exposed to the highest photon rates and are most strongly affected by pile-up. This method can also be applied to the XMS in order to avoid event degradation. For the particular alignment of the PSF that is shown in Fig. 5.15 the inner four pixels have been excised, as indicated in Fig. 5.18. The corresponding grade fractions are displayed in Fig. 5.19 and indicate that this procedure indeed allows for observations of sources that are about one order of magnitude brighter than with the standard observing mode. However, this method implies that about 91.6 % of the measured events are thrown away, which, of course, strongly reduces the throughput of the instrument.

An alternative method to reduce event degradation is the insertion of a flux-reducing filter in the optical path of the telescope. I have analyzed Be filters with different thickness, which reduce the effective area of the instrument, as shown in Fig. 5.20. The simulated performance is presented in Fig. 5.21 for a filter with a thickness of 500 μm. Data for other filters can be found in Schmid & Wilms (2011b).

Instead of simply reducing the total photon flux on the instrument, the BSDO proposed by Willingale (2011a) diffuses the incident photon beam. The corresponding spread among a wider range of TES pixels also results in a lower rate per individual pixel. I have performed simulations for the distribution displayed in Fig. 5.22. The results are shown in Fig. 5.23.

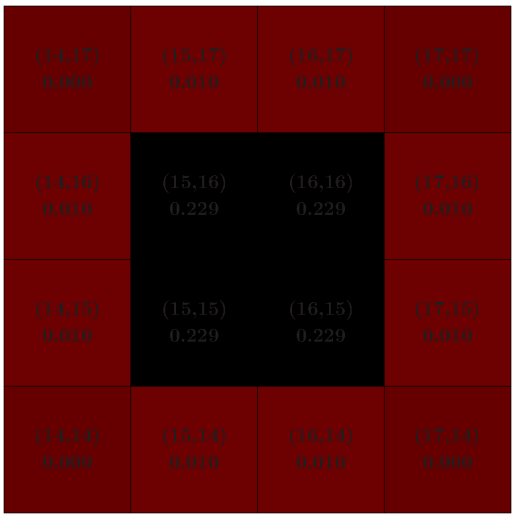

Figure 5.18: Photon distribution among the inner pixels of the *ATHENA* XMS array with an excised PSF core. The color scale reflects the fraction of incident photons in each pixel given by the bottom numbers. The numbers on the top represent the pixel indices.

In contrast to a Be filter, the overall loss of photons and therefore of effective area is less with the BSDO. The throughput of the BSDO is better at lower photon energies, whereas a Be filter is mainly transparent for high energetic photons (Fig. 5.20). The selection of an appropriate reduction method therefore depends on the particular scientific target. In any case, the diffusing BSDO is not suitable for observations of extended sources. The XMS on *ATHENA* will contain a filter wheel with a set of different filters and a BSDO, which can be rotated into the optical path for particular observations, depending on the respective astrophysical application. In comparison to the hardware-based reduction of the photon flux with a filter or a BSDO, the excising of highly illuminated pixels in the core of the PSF can usually be performed during the analysis after the observation and is therefore much more flexible.

5.2.3 HTRS

The HTRS is one of the instruments that have been designed for the *IXO* mission but are not part of the new *ATHENA* concept any more. Nevertheless, I present some of my contributions to the *IXO* instrument study.

Misalignment

In contrast to the WFI and the XMS, the HTRS is not an imaging instrument but primarily a spectrometer with high time resolution. It is mounted at a distance of 11.3 cm behind the focal plane of *IXO* (Barcons et al., 2011a). As a consequence the photons observed from a point-like source located on the optical axis of the telescope do not form a sharp spot on the detector surface, but an extended disk. Actually, the incident photons are quite homogeneously spread over the entire pixel array, reducing the count rate in each pixel and avoiding pile-up.

Due to this out-of-focus position, the standard PSF model for *IXO* with a HEW of 5 arcsec, which I have used for simulations of the WFI and the XMS, had to be modified for the HTRS, because it assumes an instrument location in the focal plane. For this purpose I have developed a particular Monte-Carlo simulation tool to calculate the distribution of incident photons on the detector surface of the HTRS (Schmid et al., 2011b). The algorithm is based on an idea by T. Oosterbroek (priv. comm.) for the original hexagonal pixel design of the HTRS (Oosterbroek, 2009) and has been extended by myself for the later selected circular pixel design. It provides the possibility of modifying the alignment of the HTRS with respect to its nominal position in order to study the impact of misalignment on the detector performance. The respective analysis is presented in (Schmid & Wilms, 2010a). The images in Figs. 5.24 and 5.25 display the

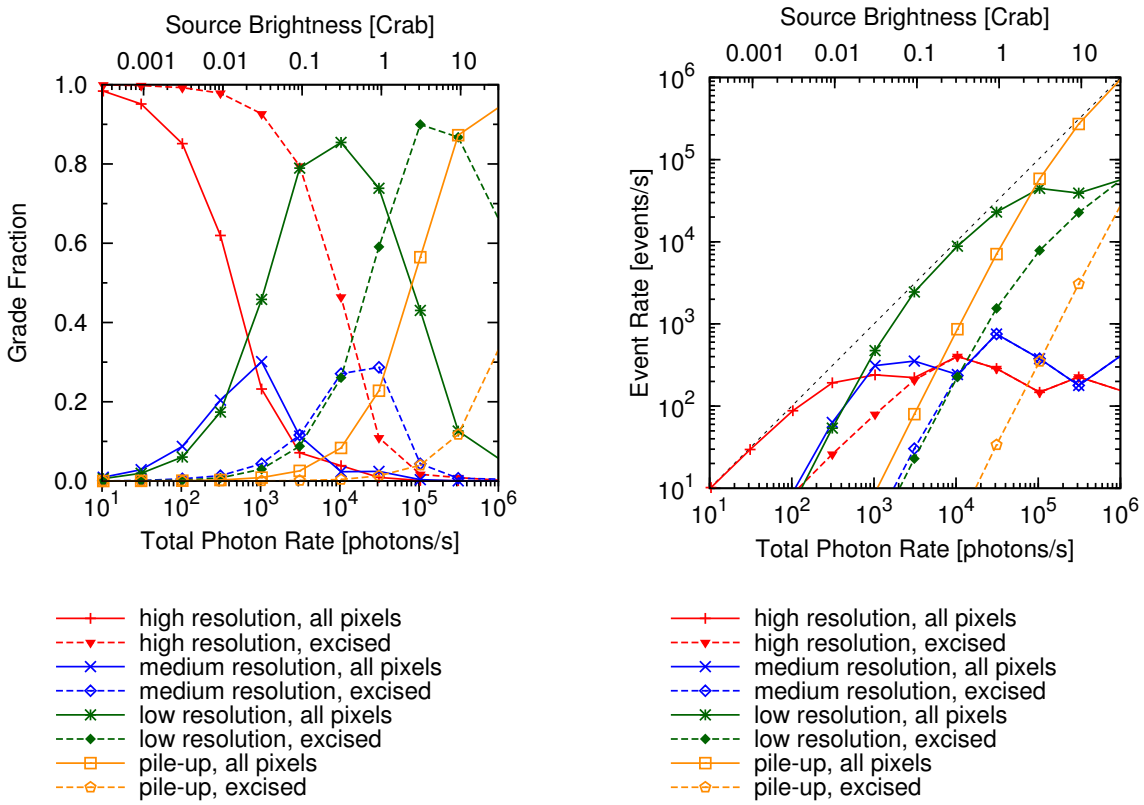

(a) Fractions of the different event grades.

(b) Throughput of the different event grades. The dashed line denotes a throughput of 100 %.

Figure 5.19: Event grades of the *ATHENA* XMS with an excised PSF core as a function of the observed photon rate. The bottom axis denotes the total rate of photons incident on the XMS. The top axis displays the corresponding source brightness as a fraction of the Crab rate according to the spectrum defined in Table 4.2. As a comparison the data for the operation mode including all pixels (Fig. 5.17) are also shown.

simulated distribution of incident photons for different photon energies and for different detector alignments.

Based on these data, the geometry of the pixel array has been adjusted in order to provide a quasi-homogeneous distribution of the incident photons among all 31 pixels and to guarantee that 99.9 % of the incident photons are located within the sensitive range of the detector. These conditions have to be fulfilled as long as the instrument alignment lies within the following margins imposed by the instrument requirements (Barret & HTRS System Team, 2010):

- horizontal position: 1 mm (circular)
- vertical position: ±1 mm
- detector plane: ±2 deg tilt

As the simulated data prove, both requirements can be fulfilled for an out-of-focus distance of 11.3 cm and for the pixel dimensions presented in Fig. 5.25. For this design the individual pixels have an equal area, which is convenient with regard to calibration issues[7]. The loss of photons due to the absorbing mask on top of the pixel edges for this configuration is ≤ 10 %.

In addition to a static misalignment due to an inaccurate mounting, the HTRS might be

[7]The degradation of the detector performance due to radiation damage during the lifetime of the mission scales with the area of the SDDs. If all pixels have equal areas, the relative deterioration between them is less challenging.

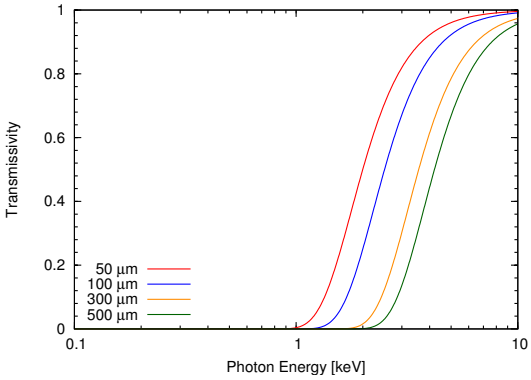

(a) Transmissivity of the filters.

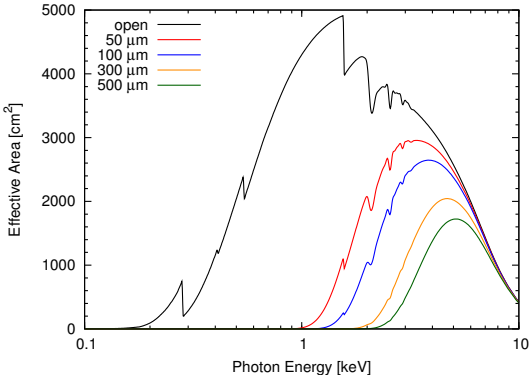

(b) Combined effective area of the telescope, filter, and detector.

Figure 5.20: The effect of Be filters with different thickness on the effective area of the *ATHENA* XMS.

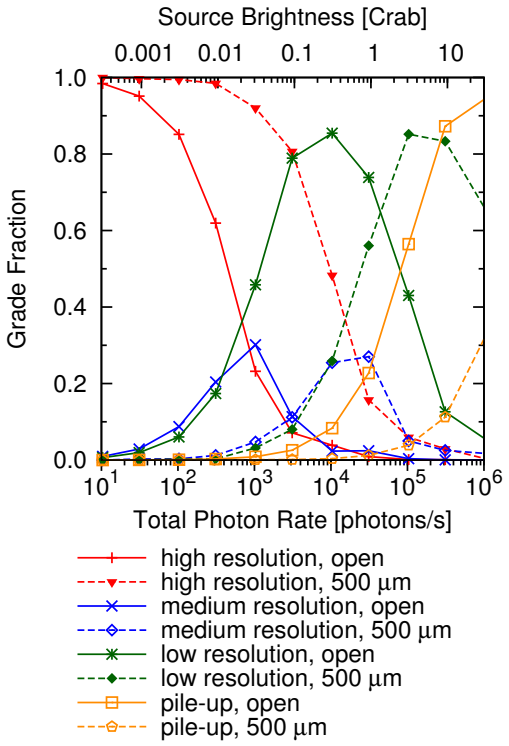

(a) Fractions of the different event grades.

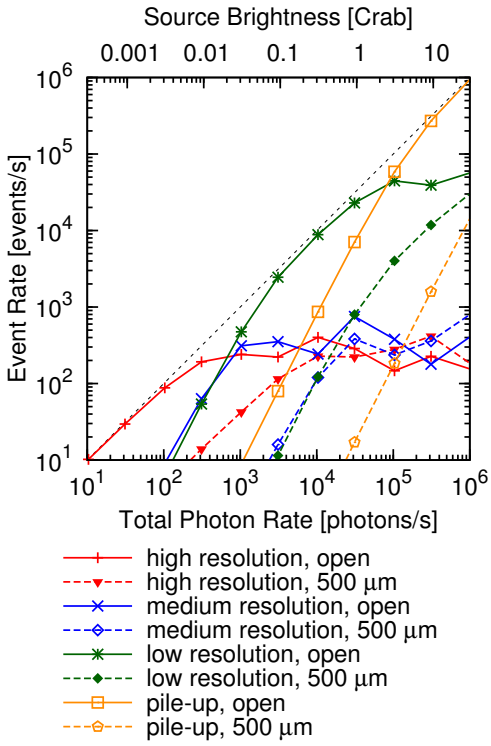

(b) Throughput of the different event grades. The dashed line denotes a throughput of 100 %.

Figure 5.21: Event grades of the *ATHENA* XMS with a 500 μm thick Be filter as a function of the observed photon rate. The bottom axis denotes the total rate of simulated photons. The top axis displays the corresponding source brightness as a fraction of the Crab rate according to the spectrum defined in Table 4.2. As a comparison the data for an open filter (Fig. 5.17) are also shown.

exposed to vibrations caused by other instruments on the MIP of *IXO*, in particular the cryogenic devices of the XMS. The count rate of the entire instrument or of individual pixels might be affected by these vibrations, because the absorption of photons by the mask covering the pixel edges depends on the relative position of the photon spot. I have analyzed this issue with simulations, assuming that the photon spot shown in Fig. 5.25 is oscillating relative to the pixel

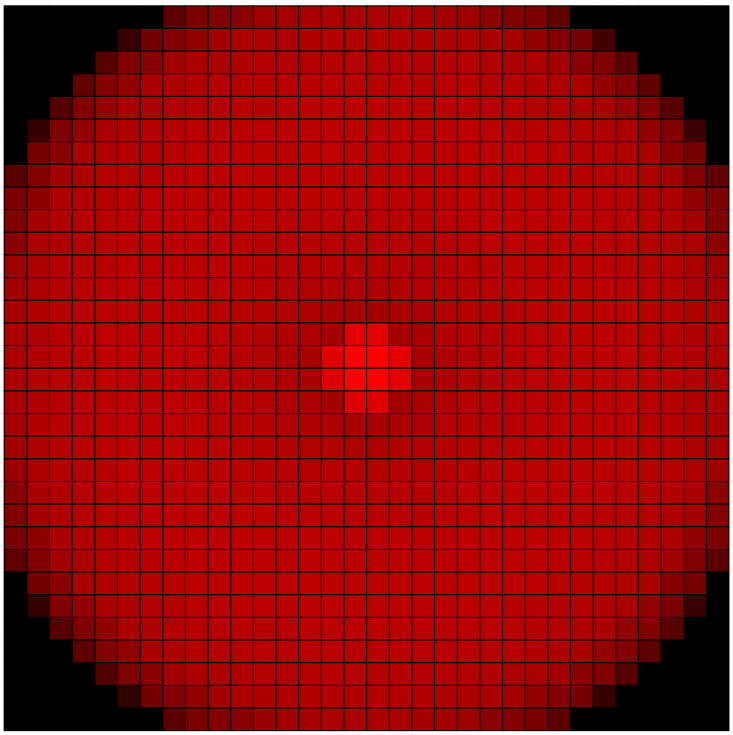

Figure 5.22: Distribution of the incident photons on the pixel array of the *ATHENA* XMS with the BSDO in the optical path (logarithmic color scale).

array. Pointing instabilities of the telescope with respect to the observed source would have a very similar effect.

The simulated count rates for a horizontal oscillation of the detector position with an amplitude of 100 μm and a frequency of 100 Hz during an illumination with monochromatic 1 keV photons are displayed in Fig. 5.26. The count rate variation is most significant for the outer ring of pixels, because the edge of the photon spot lies in this region. Therefore small horizontal shifts have a strong impact on the relative change of the count rate in these pixels, as indicated in Fig. 5.25. Though, the effect of the oscillation on the total count rate of the instrument is negligible.

It is important to keep in mind that the applied radially symmetric model of the mirror system is a rough simplification. In reality vibrations might have a stronger impact due to the particular modular structure of the SPO. Nevertheless, the presented approach provides a good estimate of the resulting phenomena, especially for the total instrument count rate.

Bright Source Performance

Although the HTRS is designed in particular for observations of bright Galactic sources, it might still suffer from pile-up and dead time effects due to the large effective area of the *IXO* mirrors and the corresponding high photon rates. Therefore an accurate investigation of the bright source performance of the instrument is very important, especially because it is intended for time-resolved spectroscopy and other timing analyses.

In the 31 SDD pixels of the HTRS the charges generated by incident photons are collected in the central anode. Each additional photon impact results in an increase of the collected charge and therefore the output voltage, which is sampled either by an analog (baseline) or a digital (optional) readout ASIC. Since the maximum input voltage range of the ASIC is of the order of 0.5–1 V, the pixel has to be cleared, when the voltage signal reaches the upper threshold (Lechner et al., 2010a). The information about photons incident during the reset interval with a length of about 500 ns is lost. Therefore this time interval is denoted as dead time. The fraction of

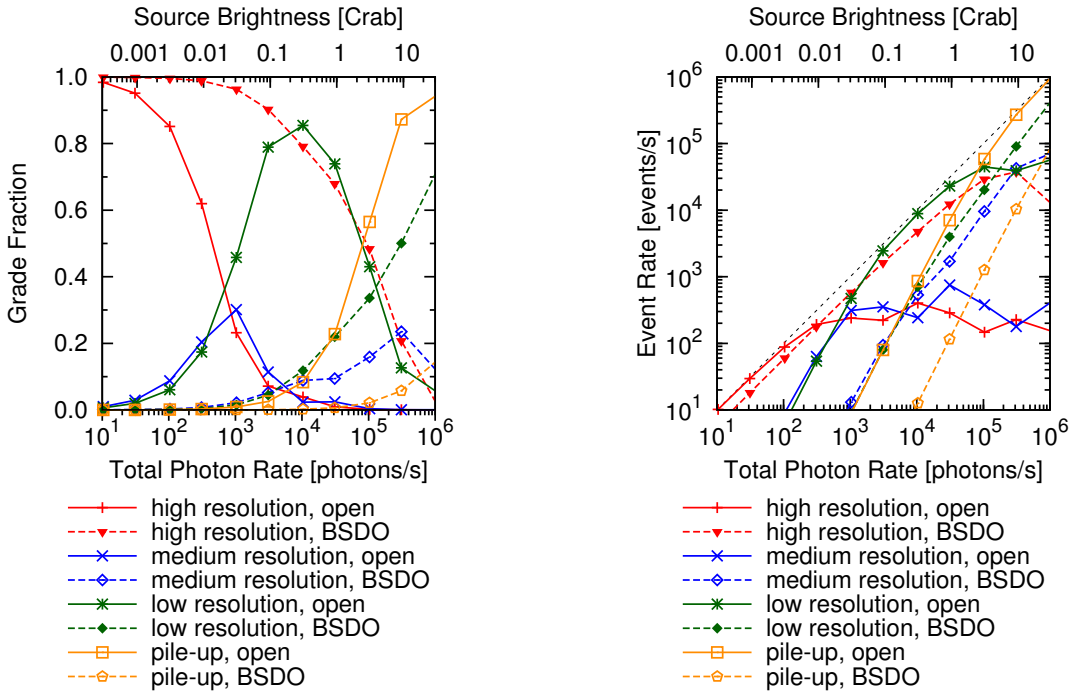

(a) Fractions of the different event grades.

(b) Throughput of the different event grades. The dashed line denotes a throughput of 100 %.

Figure 5.23: Event grades of the *ATHENA* XMS with the BSDO as a function of the observed photon rate. The top axis displays the corresponding source brightness as a fraction of the Crab rate according to the spectrum defined in Table 4.2. As a comparison the data without the BSDO (Fig. 5.17) are also shown.

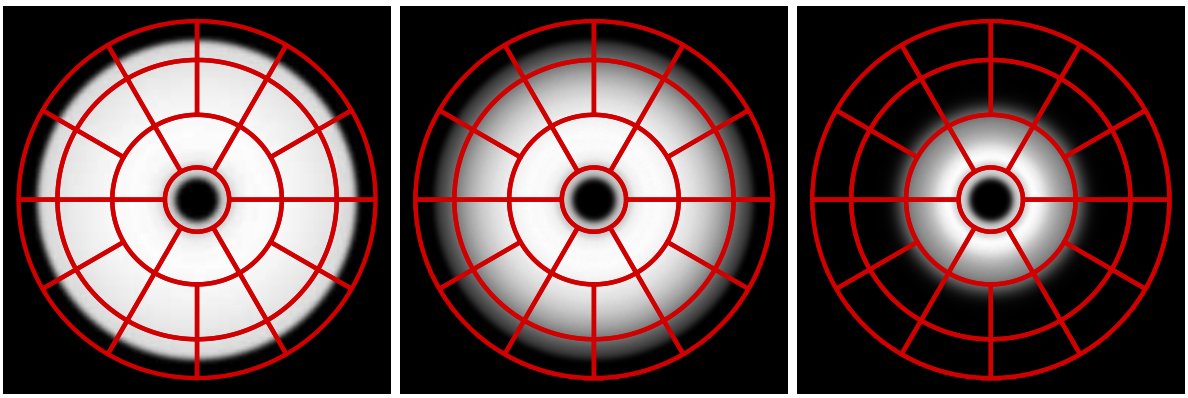

Figure 5.24: The size of the photon spot on the HTRS strongly depends on the energy of the incident photons due to the energy-dependent reflectivity of the outer mirror shells. The presented images display the distribution for 1, 2, and 6 keV photons.

dead time among the entire observing time depends on the rate of photons per pixel, i.e., on the source brightness, as shown in Fig. 5.27. For the regarded ASIC parameters the dead time for observations of X-ray sources up to 10 Crab is negligible ($< 0.1\,\%$). Dead time is therefore not further discussed in this context.

In the detector the energy of an incident photon is reconstructed by sampling the voltage step induced by the charge that is collected in the pixel. This sampling is performed either by an analog or a digital signal processing chain. For an accurate energy determination with the

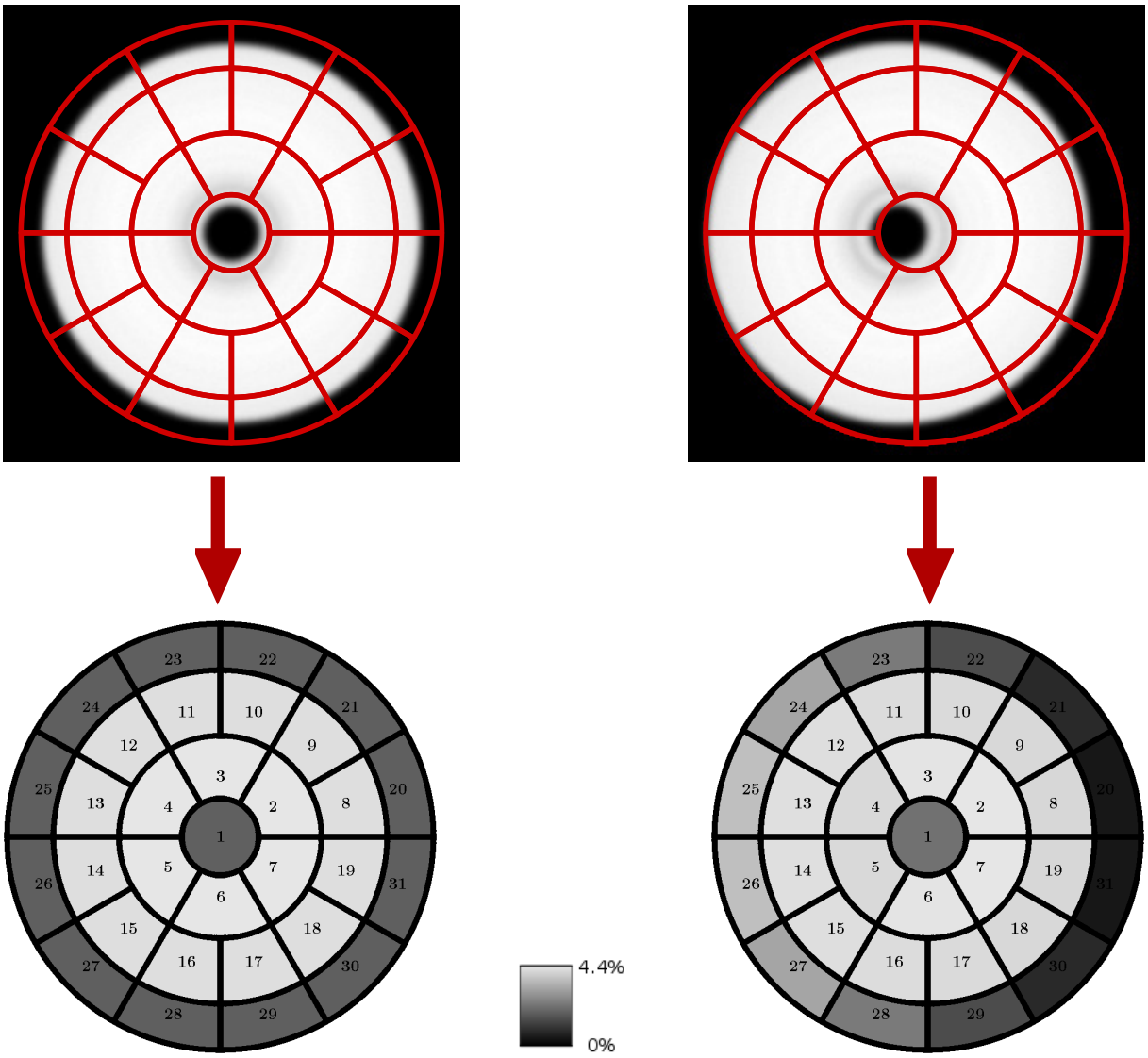

Figure 5.25: Distribution of 1 keV photons on the HTRS on *IXO* for nominal (left-hand) and worst case (right-hand) detector alignment. In the worst case setup the out-of-focus distance is increased by 1 mm, the horizontal position is shifted by 1 mm, and the detector plane is tilted by 2 deg with respect to the nominal alignment. The brightness scale of the images reflects the fraction of photons in each pixel, whereas the numbers denote the indices of the individual pixels. The radii in the presented geometry ($r_1 = 2.16\,\mathrm{mm}$, $r_2 = 5.70\,\mathrm{mm}$, $r_3 = 9.39\,\mathrm{mm}$, and $r_4 = 12.0\,\mathrm{mm}$) have been selected as a trade-off between calibration issues and a preferably quasi-homogeneous distribution of photons.

nominal resolution of the HTRS a particular time interval or a particular number of sampling points is required. This interval is of the order of 500–1250 ns, depending on the selected ASIC (Barret et al., 2010). If additional photons hit the pixel during this time, the shape of the voltage increase cannot be sampled with the required accuracy such that the energy resolution of the event is degraded.

Even worse is the case of pile-up, when the time interval between subsequent photons in the same pixel is too short to distinguish between the corresponding voltage steps. As a consequence multiple photons are wrongly identified as a single event with an energy corresponding to the sum of the contributing signals. The minimum time difference τ required to distinguish between two photons is 200 ns or 80 ns depending on the implemented readout electronics. A major fraction

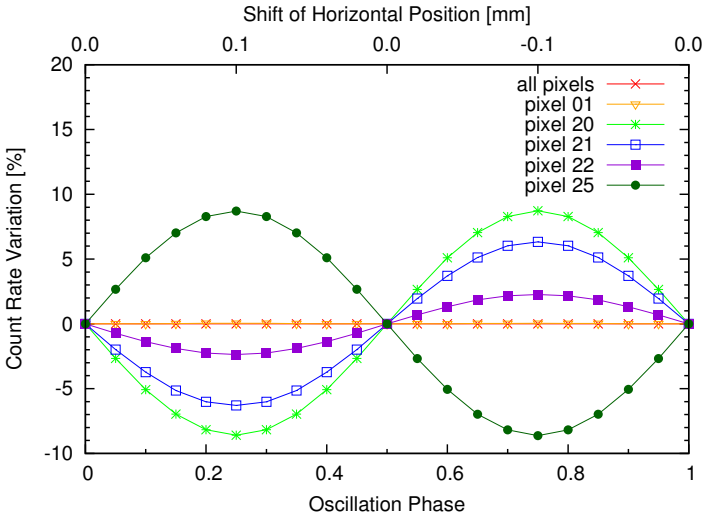

Figure 5.26: Variation of the count rate of the entire HTRS and of individual pixels due to oscillations of the horizontal detector position. Such oscillations can originate from vibrations of the MIP caused by other instruments or pointing instabilities of the telescope. As shown in the plot, the impact on the total count rate of the HTRS is negligible.

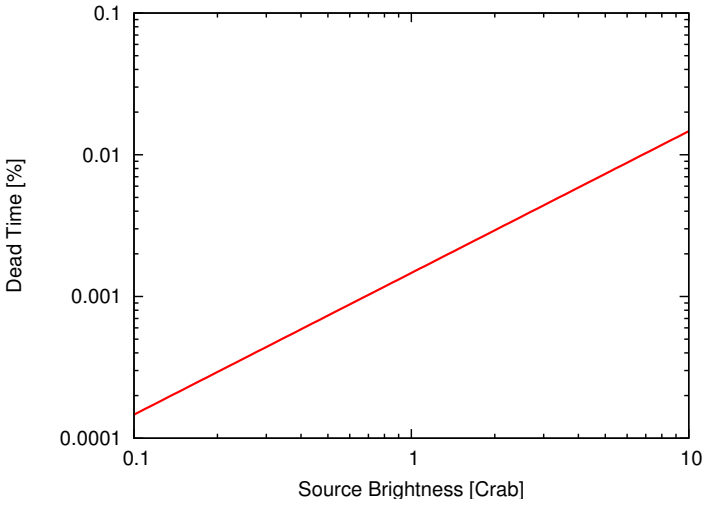

Figure 5.27: Estimated fraction of dead time for the HTRS due to clearing of the charge collected in the SDD pixels. The magnitude of the dead time depends on different parameters, such as the capacity of the SDD pixels and the input range of the readout ASIC. For the displayed setup assuming an analog readout option the dead time fraction is negligible even for observations of bright sources.

of such pile-up events can significantly distort the measured spectrum and count rate, similar as shown in Sec. 5.2.1.

The fraction of pile-up among the detected events can be estimated under the assumption of a homogeneous distribution of the incident photons among all 31 pixels. Taking into account that about 10 % of the incident photons are absorbed by the mask of the detector, the count rate due to the remaining photons in a single pixel can be obtained as

$$R' = \frac{R}{31} \cdot 0.9 \tag{5.4}$$

with the total rate of incident photons on the entire instrument R. According to Poisson statistics the probability that for a photon impact at time t_i there is at least one other photon in the same pixel within the interval $(t_i - \tau, t_i + \tau)$ is

$$P(k \geq 1) = 1 - \mathrm{e}^{-2\tau R'} \tag{5.5}$$

Therefore Eq. (5.5) constitutes an analytical estimate for the pile-up fraction among the measured events.

Apart from this analytical estimate, the pile-up fraction can also be determined by simulations regarding the time intervals between the detected events. In Fig. 5.28 the simulated and the analytical pile-up fraction are shown as functions of the source brightness. The presented data

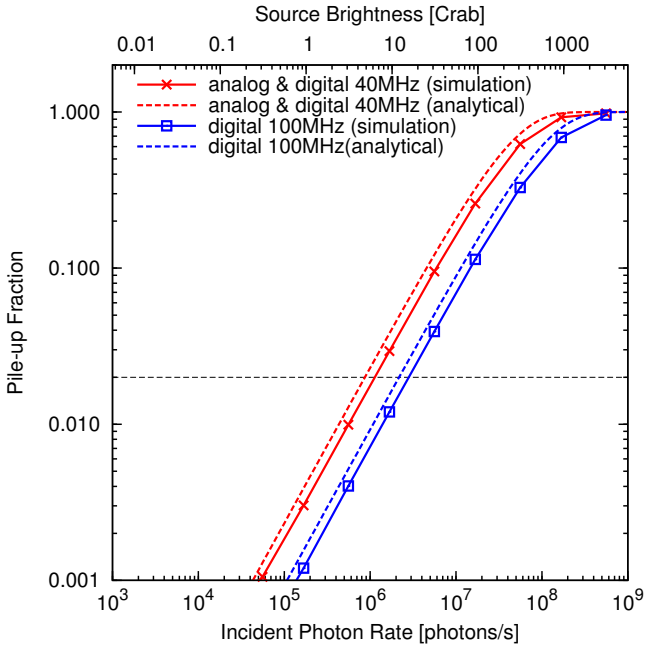

Figure 5.28: Pile-up fraction among the HTRS events obtained from simulated observations of sources with different brightness and from an analytical estimate. The minimum time required to distinguish between two subsequent photons in the same pixel is 200 ns for the analog (baseline) and the 40 MHz digital readout electronics and 80 ns for the 100 MHz digital concept. The straight lines with the data points represent the simulated data. The dotted lines indicate an analytical estimate according to Eq. (5.5) with the assumption that the incident photons are homogeneously distributed among all 31 pixels. The discrepancy between the simulated data and the theoretical estimate is caused by the fact that in the simulation the photons are not completely homogeneously distributed among all pixels. The horizontal dashed line indicates the pile-up threshold of 2 % imposed by the instrument requirements.

prove that the HTRS fulfills the imposed requirement of less than 2 % pile-up even at a source brightness of 1 Crab (Barcons et al., 2011a) for both the digital and analog readout electronics. Even for a brightness of 10 Crab, which can be reached in the outbursts of some flaring sources, the pile-up fraction is less than 10 %. The instrument therefore provides excellent count rate capabilities and enables time-resolved spectroscopy of bright Galactic X-ray sources.

In addition to the presented data, I have also investigated more sophisticated observational scenarios. For instance, if the observed X-ray source exhibits significant flux variations, the pile-up fraction might be different from the case of a constant photon rate (Knoll, 2010, Chapter 4)[8]. For the HTRS I have simulated an observation of the Crab pulsar with a maximum variation of the observed photon rate by a factor of ∼4. The resulting performance is slightly worse than the data presented in Fig. 5.28, but still fits the requirement of less than 2 % pile-up at 1 Crab very well.

[8] Assuming that a particular source with a periodic flux variation exhibits a photon rate r_1 during a fraction f_1 of the observation interval and a rate r_2 during the remaining time fraction f_2 ($f_1 + f_2 = 1$), the average pile-up fraction in general will be different from the pile-up fraction for the average rate:

$$p(r_1) \cdot \frac{f_1}{f_1 + f_2} + p(r_2) \cdot \frac{f_2}{f_1 + f_2} \neq p\left(r_1 \cdot \frac{f_1}{f_1 + f_2} + r_2 \cdot \frac{f_2}{f_1 + f_2}\right) \tag{5.6}$$

In this expression the non-linear function $p(r)$ resembles the pile-up fraction for a particular photon rate. For observations of bursting X-ray sources the left-hand side of Eq. (5.6) has to be taken into account.

CHAPTER 6

CONCLUSION

6.1 Outlook

In the following I provide a short overview of some applications of the SIXTE software package to other projects, which have not been presented in this thesis. These projects confirm the universal applicability of the developed simulation software.

6.1.1 MIRAX

The HXI of the Monitor e Imageador de RAios-X (MIRAX) experiment (Grindlay et al., 2011) is a wide-field coded mask instrument on the Brazilian *Lattes* satellite. It covers a FOV of 63 deg × 63 deg and the energy range 5–200 keV. One of its primary scientific objectives is the monitoring of BH and NS systems in the Galactic Bulge and Plane. The mission will be launched into a near-equatorial orbit with an inclination of 15 deg and an altitude of 650 km corresponding to a revolution time of 97 min. Based on these parameters I have calculated exposure maps for different instrument alignments in order to determine a convenient configuration with a suitable coverage of the region around the Galactic Center and the corresponding sensitivity limits for different regions of the sky. An example for a one-year exposure map is displayed in Fig. 6.1.

6.1.2 *XMM-Newton*

A possible application of the simulation software to an existing mission is the *XMM-Newton* telescope. The EPIC-pn camera (Strüder et al., 2001) is very similar to the pn-CCD implemented on eROSITA. It does not contain a framestore area such that OOT events play a more significant role, and, apart from the full-frame mode, it provides additional operation modes, such as the timing mode and the burst mode (Kendziorra et al., 1997, 1998, 1999; Kuster et al., 1999), which are suitable for observations of bright sources. All these modes can be described via the XML configuration of the generic detector model of SIXTE. An example for a detector image of an observation in timing mode is shown in Fig. 6.2.

Although the EPIC-pn camera is a well calibrated instrument, simulations can still provide a better understanding of several instrumental effects, such as optical and X-ray loading (Kendziorra et al., 1999), or the impact of pile-up for the different operational modes. In particular for derived modes such as the modified timing mode (Kendziorra et al., 2004) further investigations based on simulated data can help to understand particular features observed in measurements. However, for such an analysis a very detailed configuration of the detector model is required based on calibration data in order to obtain physically correct results. This issue is beyond the scope of this thesis and will be part of future investigations.

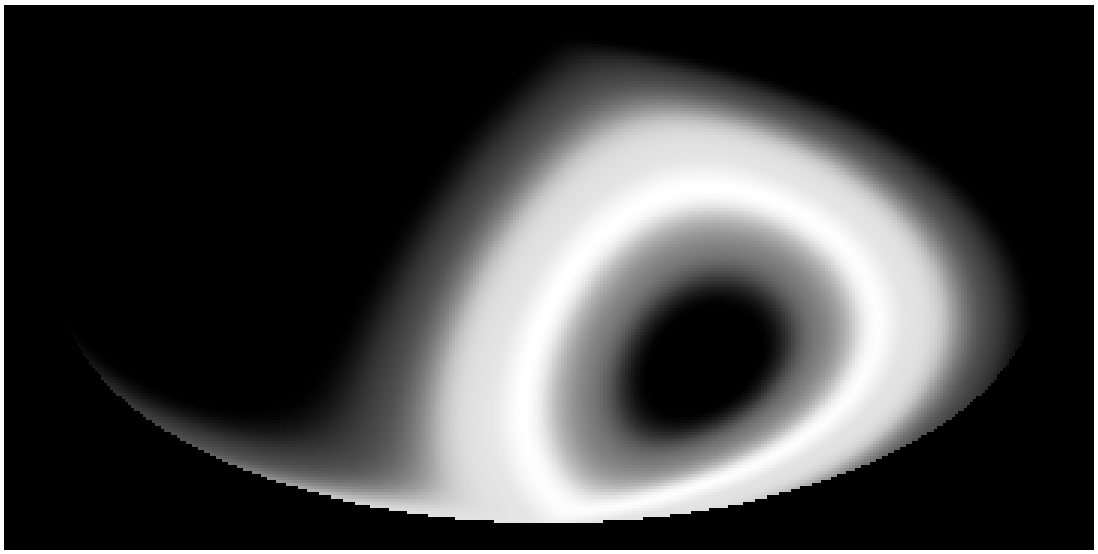

Figure 6.1: Exposure map for the MIRAX HXI after one year of mission duration in Galactic coordinates and Hammer-Aitoff projection. Due to the particular orbit of the satellite, the telescope performs a scan over the Galactic Center, which corresponds to the center of the image, for about 20 min every 97 min. Therefore it allows quasi-continuous monitoring of bright Galactic sources located in this region.

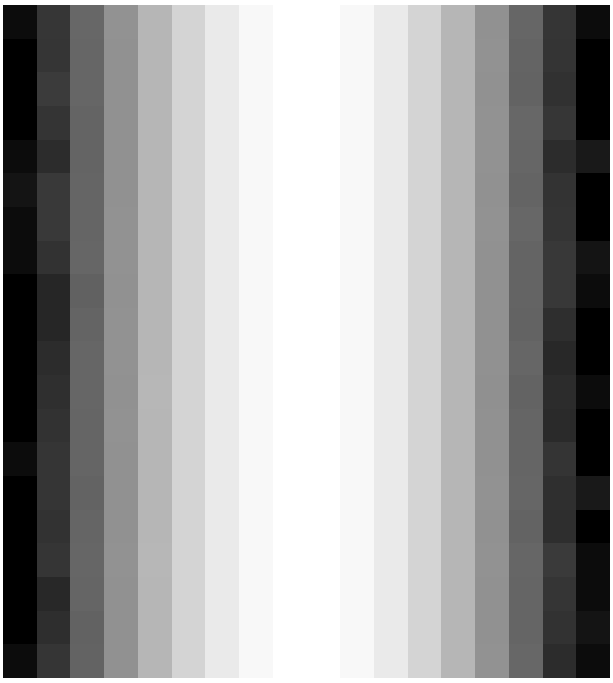

Figure 6.2: Detector image of the EPIC-pn camera on *XMM-Newton* operated in timing mode. Due to the continuous shifting of the charges in the detector pixels, the spatial information in vertical direction is lost. The charges of each 10 adjacent pixels in vertical direction are summed to one macro pixel. In horizontal direction the displayed intensity distribution resembles the PSF. The image has a logarithmic brightness scale.

6.1.3 *GRAVITAS*

The *General Relativistic Astrophysics VIa Timing And Spectroscopy* (*GRAVITAS*) concept (Nandra et al., 2010) was submitted to ESA as a proposal for an M-class mission in the framework of the Cosmic Vision 2015–2025 program (Bignami et al., 2005). However, it has not been selected by the responsible committee for an assessment phase such that the study of the mission concept is currently frozen. According to its costs, *GRAVITAS* would have been located in the intermediate range between small missions, such as eROSITA, and large missions, such as *IXO* or *ATHENA*. The technical concept consists of seven independent Wolter type I telescopes,

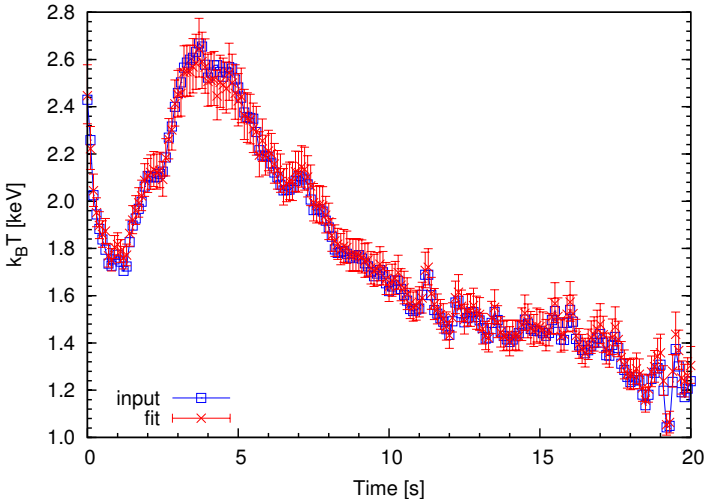

Figure 6.3: Temperature evolution of the (type I) X-ray burst KS 1731–26. The blue curve represents the input data according to (Galloway et al., 2008), whereas the red curve displays the parameters obtained by fitting the simulated spectra with an absorbed black body spectrum. The time resolution is 0.1 s.

each with its own detector, similar to eROSITA. In contrast to eROSITA, the optical system of *GRAVITAS* provides a large effective area at relatively high photon energies, namely 1.5 m^2 at 6.4 keV. The proposed HIgh Framerate Imager (HIFI) detector is an APS based on the DePFET technology similar to the WFI on *IXO*/*ATHENA*. The main scientific objectives of *GRAVITAS* are accretion physics and general relativistic effects around super-massive BHs and in the environment of Galactic BH and NS binaries.

A key driver for the design of the HIFI detector has been the capability to provide a high throughput of photons required for the intended observations. Therefore I have performed a similar analysis of the bright source performance of the instrument as for the WFI on *IXO*/*ATHENA* (Sec. 5.2.1). I have investigated the throughput and the pile-up among the detected events for different pixel sizes, readout speeds, and PSF parameters. For the justification of the imposed requirements in terms of the maximum pile-up fraction I have studied the quality of fitted spectral parameters for different pile-up fractions. Some of the simulated data corresponding to the instrument configuration selected for the proposal to ESA are presented in Schmid & Wilms (2010b).

For instance, in order to study the scientific capabilities of the HIFI in the high count rate regime, I have simulated an observation of the thermonuclear (type I) X-ray burst KS 1731–26 according to Galloway et al. (2008), similar to the analysis presented by Martin (2009) for the HTRS on *IXO*. The burst has been modeled by a time evolution of the simulated absorbed black body spectrum resembling the observed temperature evolution, as presented by Galloway et al. (2008). The instrument model of the HIFI has been operated in 16×16 window mode, corresponding to a time resolution of 16 μs. The maximum count rate during the burst is $\sim$48 000 counts s^{-1}. The spectra obtained from the simulated data have been fitted again with an absorbed black body spectrum in order to recover the input temperature. As shown in Fig. 6.3, pile-up effects did not have a significant impact on the determination of the temperature.

6.1.4 *LOFT*

Like *GRAVITAS* the *Large Observatory For x-ray Timing* (*LOFT*, Feroci et al., 2010, 2011) has been a proposal for an M-class mission in the framework of the Cosmic Vision 2015–2025 program (Bignami et al., 2005). In contrast to *GRAVITAS*, it has been selected for an assessment phase by ESA. *LOFT* is designed for observations of bright Galactic sources such as BH and NS binaries in the energy range 2–50 keV. It consists of two instruments. The Large Area Detector (LAD) provides a large effective area of 10 m^2, a high time resolution of 10 μs, and an adequate energy

resolution of ∼260 eV at 6 keV. The Wide Field Monitor (WFM) provides a large FOV in order to monitor time-variable X-ray sources.

The LAD is a collimating instrument with a FOV of several tens of arcmin designed for pointed observations of bright sources with a high throughput of X-ray photons. It therefore enables time-resolved spectroscopy and the detection of high-frequency QPOs for a detailed study of the accretion physics in the direct vicinity of BHs and NSs. The WFM consists of several coded mask cameras. Similar to the ASM on *RXTE* it will continuously monitor a major fraction of the sky. The monitoring is performed in parallel to the pointed observations with the LAD. The WFM will detect transient phenomena such as flares and provides triggers for quick follow-up observations with other instruments such as the LAD. Both instruments contain Si-based semiconductor detectors.

During the assessment phase elaborate simulation models are developed for both instruments, the LAD and the WFM. Therefore I am extending the existing framework for imaging telescopes provided by SIXTE to collimating instruments. I have implemented a new charge cloud model for the SDDs according to Campana et al. (2011). Part of this work has already been completed such that first simulations are possible, but the implementation of detailed detector-specific properties is still on-going. In order to provide a quick and easy access to simulations, I am developing a web-interface in cooperation with several colleagues at the Dr. Remeis-Sternwarte, which enables scientists from other institutes to simulate observations of typical sources. These investigations are in particular important for the current assessment phase of the *LOFT* mission.

6.1.5 Solid State Physics

Apart from X-ray astronomy, the simulation framework provided by SIXTE can also be applied to different fields of physics. For instance, Prof. Dr. Pietsch and his group at the University of Siegen investigate the crystal structure of different materials exposed to synchrotron radiation by measurements of the refraction pattern of the Laue spots with a detector, which is similar to the EPIC-pn camera (Strüder et al., 2001) on *XMM-Newton*. Therefore the instrumental effects of this camera, such as OOT events or pile-up, can be analyzed using the generic detector model of SIXTE adjusted to the particular instrument configuration.

This study is being performed by Tahir Kalim in the course of his diploma thesis in the group of Prof. Dr. Pietsch. Due to the high intensity of the synchrotron beam, the measurements are strongly affected by pile-up, which is much higher than for typical observations in X-ray astronomy. A simulated spectrum is displayed in Fig. 6.4. This application of SIXTE to solid state physics provides evidence for the universal applicability of the implemented detector models.

6.2 Summary

The assembly of X-ray telescopes is based on a variety of different technologies, especially in terms of detector types and operation modes. A detailed understanding of the instrumental features is required both for the development of new X-ray telescopes and for the analysis and interpretation of data measured with existing instruments. This knowledge can partly be obtained from sophisticated calibration measurements. However, such experiments with hardware are limited by different constraints and are not completely flexible, since the production of detector prototypes is very challenging. Therefore the analysis of instrument-related features has to be complemented by simulated data.

Apart from the investigation of instrumental effects, the data obtained from simulations are also ideal to test the scientific analysis software for new X-ray missions, which is usually developed parallel to the hardware components. In order to provide a comprehensive verification

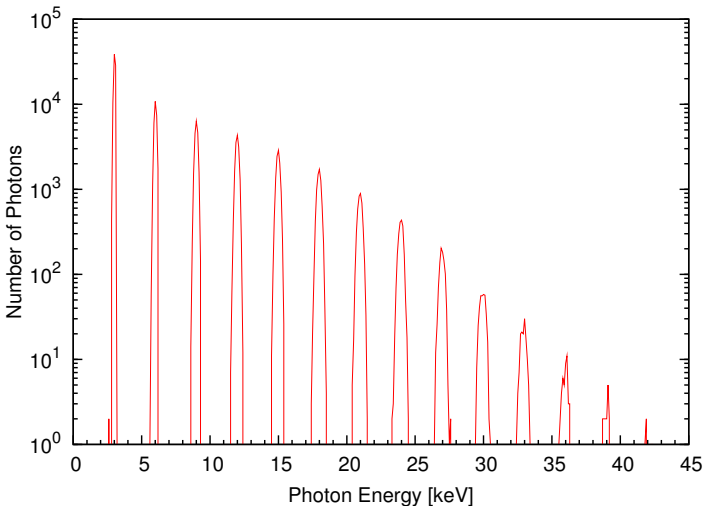

Figure 6.4: Simulated spectrum for a particular Laue spot. The energy of the fundamental line is 3 keV. Due to strong pile-up, various higher orders with integer multiples of the fundamental energy are visible.

of the analysis software at the launch of a mission, it is indispensable to rely of various test scenarios enabled by simulations of the telescope.

Both goals imply high demands on the quality of the numerical models implemented in the simulation software. However, a fully realistic approach such as a ray-tracing simulation is often impossible due to limited computational power. The development of a simulation software for an X-ray instrument usually has to deal with a trade-off between numerical efficiency and physical accuracy. With the software package presented in this thesis I have designed a universal tool for simulations of various X-ray telescopes, which can be easily adjusted to different instrument configurations and to different demands. Based on the included calibration data it can provide different levels of physical accuracy. The modular concept of the software package and the generic detector model, which is set up via an XML configuration file, are the key items of this flexible approach.

As demonstrated by the examples in Chapters 4 and 5 and in Sec. 6.1, the generic detector model can cover many of the instrument technologies used in current and next-generation X-ray missions. For more complicated detector designs, such as the HTRS on *IXO*, the detector model can be replaced by a particular implementation for this detector type fitting in the surrounding simulation framework, as it was done for the analysis in Sec. 5.2.3.

The presented examples indicate the wide range of applications of the simulation software. Depending on the accuracy of the input and configuration data the simulations are suitable to investigate instrumental effects, such as the average survey PSF of eROSITA, the alignment requirements of the HTRS on *IXO*, or the bright source performance for various detector types. The simulations can be used to verify the gain in terms of observational capabilities for future instruments in comparison to existing ones, as for the WFI on *ATHENA* and the ACIS-I on *Chandra*. It is also possible to generate realistic event data for measurements such as survey observations of fields populated with galaxy clusters and AGN with eROSITA. Some examples of additional applications to other projects demonstrate the universal capabilities of the simulation software. All in all it constitutes a powerful tool for various investigations on X-ray telescopes.

BIBLIOGRAPHY

Aird, J., Nandra, K., Laird, E. S., et al. 2010, Monthly Notices of the Royal Astronomical Society, 401, 2531

Alig, R. C., Bloom, S., & Struck, C. W. 1980, Physical Review B, 22, 5565

Allison, J., Amako, K., Apostolakis, J., et al. 2006, IEEE Transactions on Nuclear Science, 53, 270

Amelio, G. F., Tompsett, M. F., & Smith, G. E. 1970, Bell Syst. Tech. J., 49, 593

Antonucci, R., 1993, Annual Review of Astronomy and Astrophysics, 31, 473

Arnaud, K., 2008, HEAdas Developer's Guide (v. 1.1), HEASARC, Greenbelt, USA

Arnaud, K. A., 1996, in Astronomical Data Analysis Software and Systems V, ed. G. H. Jacoby & J. Barnes, Vol. 101, Astronomical Society of the Pacific Conference Series, 17

Arnaud, K. A., & Smith, R. K. 2011, in Handbook of X-Ray Astronomy, ed. K. Arnaud, R. Smith, A. Siemiginowska, Cambridge Observing Handbooks for Research Astronomers, (Cambridge: Cambridge University Press), 39

Arnaud, M., Barcons, X., Barret, D., et al. 2008, Experimental Astronomy, 24

Aschenbach, B., 1981, Space Science Reviews, 29, 443

Aschenbach, B., 1985, Reports on Progress in Physics, 48, 579

Aschenbach, B., 2009, Experimental Astronomy, 26, 95

Baganoff, F. K., Maeda, Y., Morris, M., et al. 2003, Astrophysical Journal, 591, 891

Ballet, J., 1999, Astronomy and Astrophysics Supplement Series, 135, 371

Balucinska-Church, M., & McCammon, D. 1992, Astrophysical Journal, 400, 699

Bandler, S. R., Bailey, C. N., Bookbinder, J. A., et al. 2010, in Space Telescopes and Instrumentation 2010: Ultraviolet to Gamma Ray, ed. M. Arnaud, S. S. Murray, T. Takahashi, Vol. 7732, Proc. of SPIE, 38

Barcons, X., Bregman, J., Ohashi, T., et al. 2011a, IXO Assessment Study Report, Technical report, (Paris: ESA)

Barcons, X., Lumb, D. H., Nandra, K., et al. 2011b, Athena Assessment Study Report, Technical report, (Paris: ESA)

Bardeen, J. M., 1970, Nature, 226, 64

Bardeen, J. M., Press, W. H., & Teukolsky, S. A. 1972, Astrophysical Journal, 178, 347

Barret, D., Belloni, T., Bhattacharyya, S., et al. 2008, in Space Telescopes and Instrumentation 2008: Ultraviolet to Gamma Ray, ed. M. J. L. Turner, K. A. Flanagan, Vol. 7011, Proc. of SPIE, 0E

Barret, D., & HTRS System Team 2010, HTRS / Platform Interface Requirement Document, Technical report, (Toulouse: CESR)

Barret, D., Medale, J.-L., Rohde, M., Skinner, G. K., & Strüder, L. 2004, in High-Energy Detectors in Astronomy, ed. H. A. D., Vol. 5501, Proc. of SPIE, 23

Barret, D., Olive, J.-F., & Miller, M. C. 2006, Monthly Notices of the Royal Astronomical Society, 370, 1140

Barret, D., Ravera, L., Amoros, C., et al. 2011, in Fast X-ray timing and spectroscopy at ex-

treme count rates, ed. D. Barret, M. Mendez, S. Paltani, Vol. HTRS 2011, Proc. of Science, 003

Barret, D., Ravera, L., Bodin, P., et al. 2010, in Space Telescopes and Instrumentation 2010: Ultraviolet to Gamma Ray, ed. M. Arnaud, S. S. Murray, T. Takahashi, Vol. 7732, Proc. of SPIE, 1M

Bavdaz, M., Rando, N., Wille, E., et al. 2011, in Optics for EUV, X-Ray, and Gamma-Ray Astronomy V, ed. S. L. O'Dell, G. Pareschi, Vol. 8147, Proc. of SPIE, 0C

Beijersbergen, M., Kraft, S., Bavdaz, M., et al. 2004a, in Design and Microfabrication of Novel X-Ray Optics II, ed. Snigirev, A. A. and Mancini, D. C., Vol. 5539, Proc. of SPIE, 104

Beijersbergen, M., Kraft, S., Gunther, R., et al. 2004b, in UV and Gamma-Ray Space Telescope Systems, ed. G. Hasinger & M. J. L. Turner, Vol. 5488, Proc. of SPIE, 868

Bentley, J. L., 1975, Commun. ACM, 18, 509

Berry, R., & Burnell, J. 2005, The handbook of astronomical image processing, (Richmond, VA: Willmann-Bell)

Berti, E., & Volonteri, M. 2008, Astrophysical Journal, 684, 822

Bignami, G., Cargill, P., Schutz, B., & Turon, C. 2005, Cosmic Vision, Technical report, (Paris: ESA)

Blandford, R. D., Haynes, M. P., Huchra, J. P., et al. 2011, New Worlds, New Horizons in Astronomy and Astrophysics, (Washington, D.C.: The National Academies Press)

Böhringer, H., 2011, in American Institute of Physics Conference Series, ed. F. A. Aharonian, W. Hofmann, & F. M. Rieger, Vol. 1381, American Institute of Physics Conference Series, 137

Bondi, H., 1952, Monthly Notices of the Royal Astronomical Society, 112, 195

Bondi, H., & Hoyle, F. 1944, Monthly Notices of the Royal Astronomical Society, 104, 273

Bookbinder, J., 2010, in Space Telescopes and Instrumentation 2010: Ultraviolet to Gamma Ray, ed. M. Arnaud, S. S. Murray, T. Takahashi, Vol. 7732, Proc. of SPIE, 1B

Bookbinder, J., Barret, D., Bautz, M., et al. 2010, The International X-ray Observatory - RFI, Technical report, (Cambridge: Smithsonian Astrophysical Observatory)

Bookbinder, J., Smith, R., Hornschemeier, A., et al. 2008, in Space Telescopes and Instrumentation 2008: Ultraviolet to Gamma Ray, ed. M. J. L. Turner, K. A. Flanagan, Vol. 7011, Proc. of SPIE, 02

Borgani, S., & Guzzo, L. 2001, Nature, 409, 39

Borgani, S., Murante, G., Springel, V., et al. 2004, Monthly Notices of the Royal Astronomical Society, 348, 1078

Box, G. E. P., & Muller, M. E. 1958, Annals of Mathematical Statistics, 29, 2, 610

Boyle, W. S., & Smith, G. E. 1970, Bell Syst. Tech. J., 49, 587

Bradt, H. V., Rothschild, R. E., & Swank, J. H. 1993, Astronomy and Astrophysics Supplement Series, 97, 355

Brand, T., 2011, Simulation of AGNs for eROSITA, bachelor thesis

Brandt, W. N., & Hasinger, G. 2005, Annual Review of Astronomy & Astrophysics, 43, 827

Burwitz, V., Friedrich, P., Bräuninger, H., et al. 2011, in Optics for EUV, X-Ray, and Gamma-Ray Astronomy V, ed. S. L. O'Dell, G. Pareschi, Vol. 8147, Proc. of SPIE, 08

Böhringer, H., 2008, in The Universe in X-Rays, ed. J. E. Trümper, G. Hasinger, Astronomy and Astrophysics Library, (Berlin, Heidelberg: Springer), 395

Cackett, E. M., Miller, J. M., Ballantyne, D. R., et al. 2010, Astrophysical Journal, 720, 205

Cackett, E. M., Miller, J. M., Bhattacharyya, S., et al. 2008, Astrophysical Journal, 674, 415

Calabretta, M. R., & Greisen, E. W. 2002, Astronomy and Astrophysics, 395, 1077

Cameron, R. A., Bautz, M. W., Brissenden, R. J., et al. 2004, in UV and Gamma-Ray Space Telescope Systems, ed. G. Hasinger, M. Turner, Vol. 5488, Proc. of SPIE, 572

Campana, R., Zampa, G., Feroci, M., et al. 2011, Nuclear Instruments and Methods in Physics Research A, 633, 22

Cappelluti, N., Brusa, M., Hasinger, G., et al. 2009, Astronomy and Astrophysics, 497, 635

Cappelluti, N., Hasinger, G., Brusa, M., et al.

2007, Astrophysical Journal Supplement Series, 172, 341

Cappelluti, N., Predehl, P., Böhringer, H., et al. 2011, Memorie della Societa Astronomica Italiana Supplementi, 17, 159

Carlberg, R. G., Yee, H. K. C., & Ellingson, E. 1997, Astrophysical Journal, 478, 462

Carter, B., 1971, Physical Review Letters, 26, 331

Carter, J. A., & Read, A. M. 2007, Astronomy and Astrophysics, 464, 1155

Castelli, C., Wells, A., McCarthy, K., & Holland, A. 1991, Nuclear Instruments and Methods in Physics Research A, 310, 240

Chang, P., Bildsten, L., & Wasserman, I. 2005, Astrophysical Journal, 629, 998

Citterio, O., Bonelli, G., Conti, G., Mattaini, E., & Santambrogio, E. 1988, Applied Optics, 27, 1470

Collon, M. J., Günther, R., Ackermann, M., et al. 2008, in Space Telescopes and Instrumentation 2008: Ultraviolet to Gamma Ray, ed. M. J. L. Turner, K. A. Flanagan, Vol. 7011, Proc. of SPIE, 1E

Collon, M. J., Günther, R., Ackermann, M., et al. 2009, in Optics for EUV, X-Ray, and Gamma-Ray Astronomy IV, ed. S. L. O'Dell, G. Pareschi, Vol. 7437, Proc. of SPIE, 1A

Collon, M. J., Günther, R., Ackermann, M., et al. 2011, in Optics for EUV, X-Ray, and Gamma-Ray Astronomy V, ed. S. L. O'Dell, G. Pareschi, Vol. 8147, Proc. of SPIE, 0D

Collon, M. J., Günther, R., Ackermann, M., et al. 2010, in Space Telescopes and Instrumentation 2010: Ultraviolet to Gamma Ray, ed. M. Arnaud, S. S. Murray, T. Takahashi, Vol. 7732, Proc. of SPIE, 1F

Collon, M. J., Günther, R., Kraft, S., et al. 2007, in Optics for EUV, X-Ray, and Gamma-Ray Astronomy III, ed. S. L. O'Dell, G. Pareschi, Vol. 6688, Proc. of SPIE, 13

Collon, M. J., Kraft, S., Günther, R., et al. 2006a, in Space Telescopes and Instrumentation II: Ultraviolet to Gamma Ray, ed. M. J. L. Turner, G. Hasinger, Vol. 6266, Proc. of SPIE, 1T

Collon, M. J., Kraft, S., Günther, R., et al. 2006b, in Space Telescopes and Instrumentation II: Ultraviolet to Gamma Ray, ed. M. J. L. Turner, G. Hasinger, Vol. 6266, Proc. of SPIE, 18

Comastri, A., & Brusa, M. 2008, Astronomische Nachrichten, 329, 122

Comastri, A., Ranalli, P., Iwasawa, K., et al. 2011, Astronomy and Astrophysics, 526, L9

Compton, A. H., 1923, Physical Review, 21, 483

Cotton, W. D., Tody, D., & Pence, W. D. 1995, Astronomy and Astrophysics Supplement Series, 113, 159

Dauser, T., Wilms, J., Reynolds, C. S., & Brenneman, L. W. 2010, Monthly Notices of the Royal Astronomical Society, 409, 1534

Davis, J. E., 2001a, The Astrophysical Journal, 562, 575

Davis, J. E., 2001b, The Astrophysical Journal, 548, 1010

de Korte, P. A. J., van Baar, J. J., Baars, N. H. R., et al. 2004, in High-Energy Detectors in Astronomy, ed. A. D. Holland, Vol. 5501, Proc. of SPIE, 167

de Marco, B., Iwasawa, K., Cappi, M., et al. 2009, Astronomy and Astrophysics, 507, 159

Deák, I., 1990, Random Number Generators and Simulation, Mathematical Methods of Operations Research 4, (Budapest: Akadémiai Kiadó) (transl. of Véletlenszám generátorok és alkalmazásuk, Budapest: Akadémiai Kiadó, 1990)

Degenaar, N., & Wijnands, R. 2010, Astronomy and Astrophysics, 524, A69

den Herder, J. W., Brinkman, A. C., Kahn, S. M., et al. 2001, Astronomy and Astrophysics, 365, L7

den Herder, J. W., Kelley, R. L., Mitsuda, K., et al. 2010, in Space Telescopes and Instrumentation 2010: Ultraviolet to Gamma Ray, ed. M. Arnaud, S. S. Murray, T. Takahashi, Vol. 7732, Proc. of SPIE, 1H

Dennerl, K., 2010, Space Science Reviews, 157, 57

Dicke, R. H., Peebles, P. J. E., Roll, P. G., & Wilkinson, D. T. 1965, Astrophysical Journal, 142, 414

Duro, R., Dauser, T., Wilms, J., et al. 2011, Astronomy and Astrophysics, 533, L3+

Ebisawa, K., Yamauchi, S., Tanaka, Y., et al. 2008, Publications of the Astronomical Soci-

ety of Japan, 60, 223

Edgar, R. J., 2011, in Handbook of X-Ray Astronomy, ed. K. Arnaud, R. Smith, A. Siemiginowska, Cambridge Observing Handbooks for Research Astronomers, (Cambridge: Cambridge University Press), 23

Enss, C., 2001, Journal of Low Temperature Physics, 124, 353, 10.1023/A:1017502724149

Fabian, A. C., Rees, M. J., Stella, L., & White, N. E. 1989, Monthly Notices of the Royal Astronomical Society, 238, 729

Fabian, A. C., Sanders, J. S., Allen, S. W., et al. 2011, Monthly Notices of the Royal Astronomical Society, 418, 2154

Fabian, A. C., Sanders, J. S., Allen, S. W., et al. 2003, Monthly Notices of the Royal Astronomical Society, 344, L43

Fabian, A. C., Zoghbi, A., Ross, R. R., et al. 2009, Nature, 459, 540

Fano, U., 1947, Physical Review, 72, 26

Farquhar, R. W., 1968, Ph.D. thesis, Stanford University

Farrell, S. A., Webb, N. A., Barret, D., Godet, O., & Rodrigues, J. M. 2009, Nature, 460, 73

Fenimore, E. E., & Cannon, T. M. 1978, Applied Optics, 17, 337

Feroci, M., Stella, L., Vacchi, A., et al. 2010, in Space Telescopes and Instrumentation 2010: Ultraviolet to Gamma Ray, ed. M. Arnaud, S. S. Murray, T. Takahashi, Vol. 7732, Proc. of SPIE, 1V

Feroci, M., Stella, L., van der Klis, M., et al. 2011, Experimental Astronomy, 100

Ferrando, P., Arnaud, M., Briel, U., et al. 2009, in American Institute of Physics Conference Series, ed. J. Rodriguez & P. Ferrando, Vol. 1126, American Institute of Physics Conference Series, 3

Ferrando, P., Arnaud, M., Briel, U., et al. 2006, in Space Telescopes and Instrumentation II: Ultraviolet to Gamma Ray, ed. M. J. L. Turner, G. Hasinger, Vol. 6266, Proc. of SPIE, 0F

Foster, A. R., Smith, R. K., Brickhouse, N. S., Kallman, T. R., & Witthoeft, M. C. 2010, Space Science Reviews, 157, 135

Frank, J., 1978, Monthly Notices of the Royal Astronomical Society, 184, 87

Frank, J., King, A., & Raine, D. 1992, Accretion Power in Astrophysics, (Cambridge, New York: Cambridge University Press)

Fraser, G. W., Abbey, A. F., Holland, A., et al. 1994, Nuclear Instruments and Methods in Physics Research A, 350, 368

Friedman, H., Lichtman, S. W., & Byram, E. T. 1951, Physical Review, 83, 1025

Friedman, J. H., Bentley, J. L., & Finkel, R. A. 1977, ACM Trans. Math. Softw., 3, 209

Friedrich, P., 2008, in The Universe in X-Rays, ed. J. E. Trümper, G. Hasinger, Astronomy and Astrophysics Library, (Berlin, Heidelberg: Springer), 41

Friedrich, P., 2011, eROSITA X-Ray Optics, Talk on the First eROSITA International Conference in Garmisch-Partenkirchen, Germany, October 2011

Friedrich, P., Aschenbach, B., Braeuninger, H., et al. 2005a, in Optics for EUV, X-Ray, and Gamma-Ray Astronomy II, ed. Citterio, O. and O'Dell, S. L., Vol. 5900, Proc. of SPIE, 258

Friedrich, P., Aschenbach, B., Braig, C., et al. 2006, in Space Telescopes and Instrumentation II: Ultraviolet to Gamma Ray, ed. M. J. L. Turner, G. Hasinger, Vol. 6266, Proc. of SPIE, 1G

Friedrich, P., Bräuninger, H., Budau, B., et al. 2008, in Space Telescopes and Instrumentation 2008: Ultraviolet to Gamma Ray, ed. M. J. L. Turner, K. A. Flanagan, Vol. 7011, Proc. of SPIE, 2T

Friedrich, P., Predehl, P., Hasinger, G., et al. 2004, in UV and Gamma-Ray Space Telescope Systems, ed. Hasinger, G. and Turner, M. J. L., Vol. 5488, Proc. of SPIE, 837

Friedrich, P., Predehl, P., Meidinger, N., et al. 2005b, in Optics for EUV, X-Ray, and Gamma-Ray Astronomy II, ed. Citterio, O. and O'Dell, S. L., Vol. 5900, Proc. of SPIE, 172

Fürmetz, M., Predehl, P., Eder, J., & Tiedemann, L. 2010, in Space Telescopes and Instrumentation 2010: Ultraviolet to Gamma Ray, ed. M. Arnaud, S. S. Murray, T. Takahashi, Vol. 7732, Proc. of SPIE, 3K

Galeazzi, M., 2004, Nuclear Instruments and Methods in Physics Research A, 520, 320

Galeazzi, M., 2006, in Low Temperature Physics, ed. Takano, Y. and Hershfield, S. P. and Hill, S. O. and Hirschfeld, P. J. and Goldman, A. M., Vol. 850, American Institute of Physics Conference Series, 1599

Galeazzi, M., 2011, IEEE Transactions on Applied Superconductivity, 21, 267

Galloway, D. K., Muno, M. P., Hartman, J. M., Psaltis, D., & Chakrabarty, D. 2008, Astrophysical Journal Supplement Series, 179, 360

Gatti, E., & Rehak, P. 1984, Nuclear Instruments and Methods in Physics Research, 225, 608

Geant4 Collaboration, 2003, Nuclear Instruments and Methods in Physics Research A, 506, 250

George, I. M., & Angelini, L. 1995, Specification of Physical Units within OGIP FITS files, OGIP/93-001, NASA/GSFC, Greenbelt, USA

George, I. M., Arnaud, K. A., Ruamsuwan, B. P. L., & Corcoran, M. F. 1998, The Calibration Requirements for Spectral Analysis, HEASARC, Greenbelt, USA

George, I. M., Arnaud, K. A., Ruamsuwan, B. P. L., & Corcoran, M. F. 2007, The Calibration Requirements for Spectral Analysis, HEASARC, Greenbelt, USA

George, I. M., & Yusaf, R. 1994, The OGIP Format for 'Vignetting' Functions, CAL/GEN/92-021, HEASARC, Greenbelt, USA

George, I. M., & Yusaf, R. 1995, The OGIP Format for 2-D (Image) Point Spread Function Datasets, CAL/GEN/92-027, HEASARC, Greenbelt, USA

George, I. M., & Zellar, R. S. 1995, The OGIP Format for effective area files, CAL/GEN/92-019, HEASARC, Greenbelt, USA

Giacconi, R., 2009, Experimental Astronomy, 25, 143

Giacconi, R., Bechtold, J., Branduardi, G., et al. 1979a, Astrophysical Journal Letters, 234, L1

Giacconi, R., Branduardi, G., Briel, U., et al. 1979b, Astrophysical Journal, 230, 540

Giacconi, R., Gursky, H., Paolini, F. R., & Rossi, B. B. 1962, Physical Review Letters, 9, 439

Giacconi, R., Kellogg, E., Gorenstein, P., Gursky, H., & Tananbaum, H. 1971, Astrophysical Journal Letters, 165, L27

Giacconi, R., Zirm, A., Wang, J., et al. 2002, Astrophysical Journal Supplement Series, 139, 369

Gilli, R., Comastri, A., & Hasinger, G. 2007, Astronomy and Astrophysics, 463, 79

Gondoin, P., van Katwijk, K., Aschenbach, B. R., et al. 1994, in Space Optics 1994: Earth Observation and Astronomy, ed. Cerutti-Maori, M. G. and Roussel, P., Vol. 2209, Proc. of SPIE, 438

Górski, K. M., Hivon, E., Banday, A. J., et al. 2005, Astrophysical Journal, 622, 759

Gould, H., Tobochnik, J., & Christian, W. 2006, An introduction to computer simulation methods: Applications to Physical Systems (third edition), (San Francisco: Addison-Wesley)

Grant, C. E., 2011, in Handbook of X-Ray Astronomy, ed. K. Arnaud, R. Smith, A. Siemiginowska, Cambridge Observing Handbooks for Research Astronomers, (Cambridge: Cambridge University Press), 39

Greisen, E. W., & Calabretta, M. R. 2002, Astronomy and Astrophysics, 395, 1061

Griffiths, R., Petre, R., Hasinger, G., et al. 2004, in UV and Gamma-Ray Space Telescope Systems, ed. Hasinger, G. and Turner, M. J. L., Vol. 5488, Proc. of SPIE, 209

Grindlay, J., Allen, B., Angelini, L., et al. 2011, The Hard X-ray Imager for MIRAX, Technical report, (Washington: NASA)

Gruber, D. E., Matteson, J. L., Peterson, L. E., & Jung, G. V. 1999, Astrophysical Journal, 520, 124

Hanisch, R. J., Farris, A., Greisen, E. W., et al. 2001, Astronomy and Astrophysics, 376, 359

Hanke, M., 2011, Ph.D. thesis, Dr. Karl Remeis-Sternwarte, Astronomisches Institut der Universität Erlangen-Nürnberg, Sternwartstr. 7, 96049 Bamberg, Germany

Harrison, F. A., Boggs, S., Christensen, F., et al. 2010, in Space Telescopes and Instrumentation 2010: Ultraviolet to Gamma Ray, ed. M. Arnaud, S. S. Murray, T. Takahashi, Vol. 7732, Proc. of SPIE, 0S

Hasinger, G., Altieri, B., Arnaud, M., et al. 2001, Astronomy and Astrophysics, 365, L45

Hoare, C. A. R., 1962, The Computer Journal, 5, 10

Hölzl, J., 2011, Observing Galaxy Clusters with eROSITA: Simulations, diploma thesis

Hopkinson, G. R., 1992, IEEE Transactions on Nuclear Science, 39, 2018

Houck, J. C., 2002, in High Resolution X-ray Spectroscopy with XMM-Newton and Chandra, ed. G. Branduardi-Raymont

Houck, J. C., & Denicola, L. A. 2000, in Astronomical Data Analysis Software and Systems IX, ed. N. Manset, C. Veillet, & D. Crabtree, Vol. 216, Astronomical Society of the Pacific Conference Series, 591

Howell, K. C., 1984, Celestial Mechanics, 32, 53

Hoyle, F., & Lyttleton, R. A. 1939, Proc. of the Cambridge Philosophical Society, 35, 405

Hudson, D. S., Mittal, R., Reiprich, T. H., et al. 2010, Astronomy and Astrophysics, 513, A37

Irwin, K. D., 1995, Applied Physics Letters, 66, 1998

Irwin, K. D., 2002, Physica C Superconductivity, 368, 203

Irwin, K. D., Audley, M. D., Beall, J. A., et al. 2004, Nuclear Instruments and Methods in Physics Research A, 520, 544

Irwin, K. D., Hilton, G. C., Wollman, D. A., & Martinis, J. M. 1996, Applied Physics Letters, 69, 1945

Irwin, K. D., Hilton, G. C., Wollman, D. A., & Martinis, J. M. 1998, Journal of Applied Physics, 83, 3978

Iwasawa, K., Miniutti, G., & Fabian, A. C. 2004, Monthly Notices of the Royal Astronomical Society, 355, 1073

Janesick, J. R., 2007, Photon Transfer DN $\rightarrow$ λ, (Bellingham: SPIE)

Jansen, F., Lumb, D., Altieri, B., et al. 2001, Astronomy and Astrophysics, 365, L1

Jones, C., & Forman, W. 1999, Astrophysical Journal, 511, 65

Kelley, R. L., Mitsuda, K., Allen, C. A., et al. 2007, Publications of the Astronomical Society of Japan, 59, 77

Kemmer, J., & Lutz, G. 1987, Nuclear Instruments and Methods in Physics Research A, 253, 365

Kemmer, J., Lutz, G., Prechtel, U., et al. 1990, Nuclear Instruments and Methods in Physics Research A, 288, 92

Kendziorra, E., 2008, in The Universe in X-Rays, ed. J. E. Trümper, G. Hasinger, Astronomy and Astrophysics Library, (Berlin, Heidelberg: Springer), 15

Kendziorra, E., Bihler, E., Colli, M., et al. 1998, in EUV, X-Ray, and Gamma-Ray Instrumentation for Astronomy IX, ed. Siegmund, O. H. W. and Gummin, M. A., Vol. 3445, Proc. of SPIE, 50

Kendziorra, E., Bihler, E., Grubmiller, W., et al. 1997, in EUV, X-Ray, and Gamma-Ray Instrumentation for Astronomy VIII, ed. Siegmund, O. H. and Gummin, M. A., Vol. 3114, Proc. of SPIE, 155

Kendziorra, E., Colli, M., Kuster, M., et al. 1999, in EUV, X-Ray, and Gamma-Ray Instrumentation for Astronomy X, ed. Siegmund, O. H. W. and Flanagan, K. A., Vol. 3765, Proc. of SPIE, 204

Kendziorra, E., Wilms, J., Haberl, F., et al. 2004, in UV and Gamma-Ray Space Telescope Systems, ed. Hasinger, G. and Turner, M. J. L., Vol. 5488, Proc. of SPIE, 613

Kilbourne, C. A., Bandler, S. R., Brown, A.-D., et al. 2007, in UV, X-Ray, and Gamma-Ray Space Instrumentation for Astronomy XV, ed. O. H. W. Siegmund, Vol. 6686, Proc. of SPIE, 06

Kilbourne, C. A., Doriese, W. B., Bandler, S. R., et al. 2008, in Space Telescopes and Instrumentation 2008: Ultraviolet to Gamma Ray, ed. M. J. L. Turner, K. A. Flanagan, Vol. 7011, Proc. of SPIE, 04

Kimmel, N., Hartmann, R., Holl, P., et al. 2006a, in High Energy, Optical, and Infrared Detectors for Astronomy II, ed. D. A. Dorn, A. D. Holland, Vol. 6276, Proc. of SPIE, 0D

Kimmel, N., Hartmann, R., Holl, P., Meidinger, N., & Strüder, L. 2006b, Nuclear Instruments and Methods in Physics Research A, 568, 134

Kimmel, N., Hiraga, J. S., Hartmann, R., Meidinger, N., & Strüder, L. 2006c, Nuclear In-

struments and Methods in Physics Research A, 568, 128
King, I., 1962, Astronomical Journal, 67, 471
King, I. R., 1972, Astrophysical Journal Letters, 174, L123
Kirkpatrick, P., & Baez, A. V. 1948, Journal of the Optical Society of America (1917-1983), 38, 766
Kirsch, M. G., Briel, U. G., Burrows, D., et al. 2005, in UV, X-Ray, and Gamma-Ray Space Instrumentation for Astronomy XIV, ed. Siegmund, O. H. W., Vol. 5898, Proc. of SPIE, 22
Kirsch, M. G. F., Schönherr, G., Kendziorra, E., et al. 2006, Astronomy and Astrophysics, 453, 173
Klein, R. W., & Roberts, S. D. 1984, SIMULATION, 43, 193
Knoll, G. F., 2010, Radiation detection and measurement
Koyama, K., Tsunemi, H., Dotani, T., et al. 2007, Publications of the Astronomical Society of Japan, 59, 23
Kraft, R. P., Burrows, D. N., Garmire, G. P., et al. 1995, Nuclear Instruments and Methods in Physics Research A, 361, 372
Kreykenbohm, I., Schmid, C., Wilms, J., Brunner, H., & Lamer, G. 2009, in Astronomical Data Analysis Software and Systems XVIII, ed. Bohlender, D. A. and Durand, D. and Dowler, P., Vol. 411, Astronomical Society of the Pacific Conference Series, 285
Kunieda, H., Ishida, M., Endo, T., et al. 2001, Applied Optics, 40, 553
Kuntz, K. D., 2011, in Handbook of X-Ray Astronomy, ed. K. Arnaud, R. Smith, A. Siemiginowska, Cambridge Observing Handbooks for Research Astronomers, (Cambridge: Cambridge University Press), 146
Kuster, M., Benlloch, S., Kendziorra, E., & Briel, U. G. 1999, in EUV, X-Ray, and Gamma-Ray Instrumentation for Astronomy X, ed. Siegmund, O. H. and Flanagan, K. A., Vol. 3765, Proc. of SPIE, 673
Laor, A., 1991, Astrophysical Journal, 376, 90
Lattimer, J. M., & Prakash, M. 2001, Astrophysical Journal, 550, 426
Lattimer, J. M., & Prakash, M. 2007, Physics Reports, 442, 109
Lauf, T., 2011, Ph.D. thesis, Technische Universität München
Lechner, P., Amoros, C., Barret, D., et al. 2010a, in High Energy, Optical, and Infrared Detectors for Astronomy IV, ed. A. D. Holland, D. A. Dorn, Vol. 7742, Proc. of SPIE, 0W
Lechner, P., Andricek, L., Briel, U., et al. 2008, in High Energy, Optical, and Infrared Detectors for Astronomy III, ed. D. A. Dorn, A. D. Holland, Vol. 7021, Proc. of SPIE, 10
Lechner, P., Aschauer, F., Bombelli, L., et al. 2010b, in High Energy, Optical, and Infrared Detectors for Astronomy IV, ed. A. D. Holland, D. A. Dorn, Vol. 7742, Proc. of SPIE, 0T
Lechner, P., Fiorini, C., Hartmann, R., et al. 2001, Nuclear Instruments and Methods in Physics Research A, 458, 281
Lechner, P., Hartmann, R., Holl, P., et al. 2003, Nuclear Instruments and Methods in Physics Research A, 509, 302
Lehmer, B. D., Brandt, W. N., Alexander, D. M., et al. 2005, Astrophysical Journal Supplement Series, 161, 21
Levine, A. M., Bradt, H., Cui, W., et al. 1996, Astrophysical Journal Letters, 469, L33
Li, J., Kastner, J. H., Prigozhin, G. Y., & Schulz, N. S. 2003, Astrophysical Journal, 590, 586
Li, J., Kastner, J. H., Prigozhin, G. Y., et al. 2004, Astrophysical Journal, 610, 1204
Liu, Q. Z., van Paradijs, J., & van den Heuvel, E. P. J. 2006, Astronomy and Astrophysics, 455, 1165
Liu, Q. Z., van Paradijs, J., & van den Heuvel, E. P. J. 2007, Astronomy and Astrophysics, 469, 807
Lumb, D. H., Berthiaume, G. D., Burrows, D. N., Garmire, G. P., & Nousek, J. A. 1991, Experimental Astronomy, 2, 179
Lumb, D. H., Warwick, R. S., Page, M., & De Luca, A. 2002, Astronomy and Astrophysics, 389, 93
Luo, B., Bauer, F. E., Brandt, W. N., et al. 2008, Astrophysical Journal Supplement Series, 179, 19
Lutz, G., 1999, Semiconductor radiation detectors: device physics, (Berlin, Heidelberg:

Springer)
Lutz, G., 2005, Nuclear Instruments and Methods in Physics Research A, 549, 103
Lutz, G., Andricek, L., Eckardt, R., et al. 2007, Nuclear Instruments and Methods in Physics Research A, 572, 311
Markevitch, M., & Vikhlinin, A. 2007, Physics Reports, 443, 1
Marrone, D. P., Baganoff, F. K., Morris, M. R., et al. 2008, Astrophysical Journal, 682, 373
Marshall, F. E., Boldt, E. A., Holt, S. S., et al. 1980, Astrophysical Journal, 235, 4
Martin, M., 2009, Dissertation, Eberhard-Karls-Universität Tübingen, Tübingen
Meidinger, N., Andritschke, R., Ebermayer, S., et al. 2009, in UV, X-Ray, and Gamma-Ray Space Instrumentation for Astronomy XVI, Vol. 7435, Proc. of SPIE, 02
Meidinger, N., Andritschke, R., Ebermayer, S., et al. 2010, Nuclear Instruments and Methods in Physics Research A, 624, 321
Meidinger, N., Andritschke, R., Elbs, J., et al. 2011, in UV, X-Ray, and Gamma-Ray Space Instrumentation for Astronomy XVII, ed. L. Tsakalakos, Vol. 8145, Proc. of SPIE, 02
Meidinger, N., Andritschke, R., Elbs, J., et al. 2008, in Space Telescopes and Instrumentation 2008: Ultraviolet to Gamma Ray, ed. M. J. L. Turner, K. A. Flanagan, Vol. 7011, Proc. of SPIE, 0J
Meidinger, N., Andritschke, R., Hälker, O., et al. 2006, in High Energy, Optical, and Infrared Detectors for Astronomy II, Vol. 6276, Proc. of SPIE, 18
Meidinger, N., Andritschke, R., Hälker, O., et al. 2007, in UV, X-Ray, and Gamma-Ray Space Instrumentation for Astronomy XV, ed. O. H. W. Siegmund, Vol. 6686, Proc. of SPIE, 0H
Merloni, A., Predehl, P., Becker, W., et al. 2011, eROSITA White Book: Technical description, Scientific goals and outlook, Technical report, (Garching: MPE)
Meschede, D., 2002, Gerthsen Physik, (Berlin, Heidelberg: Springer)
Mewe, R., Lemen, J. R., & van den Oord, G. H. J. 1986, Astronomy and Astrophysics Supplement Series, 65, 511
Miller, M. C., Lamb, F. K., & Psaltis, D. 1998, Astrophysical Journal, 508, 791
Mitsuda, K., Bautz, M., Inoue, H., et al. 2007, Publications of the Astronomical Society of Japan, 59, 1
Mitsuda, K., Kelley, R. L., Boyce, K. R., et al. 2010, in Space Telescopes and Instrumentation 2010: Ultraviolet to Gamma Ray, ed. M. Arnaud, S. S. Murray, T. Takahashi, Vol. 7732, Proc. of SPIE, 11
Miyamoto, S., Kitamoto, S., Iga, S., Negoro, H., & Terada, K. 1992, Astrophysical Journal Letters, 391, L21
Moore, M., 1991, Ph.D. thesis, University of Cambridge
Moseley, S. H., Mather, J. C., & McCammon, D. 1984, Journal of Applied Physics, 56, 1257
Müller, J., 1973, Nuclear Instruments and Methods, 112, 47
Muno, M. P., Arabadjis, J. S., Baganoff, F. K., et al. 2004a, Astrophysical Journal, 613, 1179
Muno, M. P., Baganoff, F. K., Bautz, M. W., et al. 2004b, Astrophysical Journal, 613, 326
Muno, M. P., Bauer, F. E., Baganoff, F. K., et al. 2009, Astrophysical Journal Supplement Series, 181, 110
Mühlegger, M., 2010, Dissertation, Technische Universität München, München
Nandra, K., Barret, D., Fabian, A., et al. 2010, GRAVITAS General Relativistic Astrophysics VIa Timing And Spectroscopy, Technical report, (Paris: ESA)
Nandra, K., O'Neill, P. M., George, I. M., & Reeves, J. N. 2007, Monthly Notices of the Royal Astronomical Society, 382, 194
Nandra, K., Pounds, K. A., Stewart, G. C., Fabian, A. C., & Rees, M. J. 1989, Monthly Notices of the Royal Astronomical Society, 236, 39P
Nartallo, R., Evans, H., Daly, E., et al. 2000, Radiation Environment Induced Degradation on Chandra and Implications for XMM, Technical report, (Paris: ESA)
Ness, J.-U., Ehle, M., Breitfellner, M., et al. 2010, XMM-Newton Users Handbook (Issue 2.8.1)
Nowak, M. A., Hanke, M., Trowbridge, S. N., et al. 2011, Astrophysical Journal, 728, 13

Oosterbroek, T., 2009, HTRS: sizing and positioning for IXO CDF design, Technical report, (Paris: ESA)

Paerels, F., 2010, Space Science Reviews, 157, 15

Pavlinsky, M., Akimov, V., Levin, V., et al. 2011, in Optics for EUV, X-Ray, and Gamma-Ray Astronomy V, ed. S. L. O'Dell, G. Pareschi, Vol. 8147, Proc. of SPIE, 06

Pavlinsky, M., Arefiev, V., Churazov, E., et al. 2007, in Optics for EUV, X-Ray, and Gamma-Ray Astronomy III, ed. S. L. O'Dell, G. Pareschi, Vol. 6688, Proc. of SPIE, 0L

Pavlinsky, M., Hasinger, G., Parmar, A., et al. 2006, in Space Telescopes and Instrumentation II: Ultraviolet to Gamma Ray, ed. M. J. L. Turner, G. Hasinger, Vol. 6266, Proc. of SPIE, 0O

Pavlinsky, M., Sunyaev, R., Churazov, E., et al. 2008, in Space Telescopes and Instrumentation 2008: Ultraviolet to Gamma Ray, ed. M. J. L. Turner, K. A. Flanagan, Vol. 7011, Proc. of SPIE, 0H

Pavlinsky, M., Sunyaev, R., Churazov, E., et al. 2009, in Optics for EUV, X-Ray, and Gamma-Ray Astronomy IV, ed. S. L. O'Dell, G. Pareschi, Vol. 7437, Proc. of SPIE, 08

Pence, W., 1999, in Astronomical Data Analysis Software and Systems VIII, ed. D. M. Mehringer, R. L. Plante, & D. A. Roberts, Vol. 172, Astronomical Society of the Pacific Conference Series, 487

Pence, W. D., Chiappetti, L., Page, C. G., Shaw, R. A., & Stobie, E. 2010, Astronomy and Astrophysics, 524, A42

Perotti, F., & Fiorini, C. 1999, Nuclear Instruments and Methods in Physics Research A, 423, 356

Pfeffermann, E., 2008a, in The Universe in X-Rays, ed. J. E. Trümper, G. Hasinger, Astronomy and Astrophysics Library, (Berlin, Heidelberg: Springer), 21

Pfeffermann, E., 2008b, in The Universe in X-Rays, ed. J. E. Trümper, G. Hasinger, Astronomy and Astrophysics Library, (Berlin, Heidelberg: Springer), 5

Piraino, S., Santangelo, A., & Kaaret, P. 2000, Astronomy and Astrophysics, 360, L35

Planck, M., 1901, Annalen der Physik, 309, 553

Pommé, S., 1999, Nuclear Instruments and Methods in Physics Research A, 432, 456

Pommé, S., Denecke, B., & Alzetta, J.-P. 1999, Nuclear Instruments and Methods in Physics Research A, 426, 564

Ponz, J. D., Thompson, R. W., & Munoz, J. R. 1994, Astronomy and Astrophysics Supplement Series, 105, 53

Popp, M., 2000, Ph.D. thesis, Ludwig-Maximilians-Universität München

Porter, F. S., Brown, G. V., Boyce, K. R., et al. 2004, Review of Scientific Instruments, 75, 3772

Porter, F. S., Kelley, R. L., & Kilbourne, C. A. 2006, Nuclear Instruments and Methods in Physics Research A, 559, 436

Pottschmidt, K., 2002, Ph.D. thesis, Eberhard-Karls-Universität Tübingen

Pratt, G. W., Croston, J. H., Arnaud, M., & Böhringer, H. 2009, Astronomy and Astrophysics, 498, 361

Predehl, P., 1999, in EUV, X-Ray, and Gamma-Ray Instrumentation for Astronomy X, ed. Siegmund, O. H. and Flanagan, K. A., Vol. 3765, Proc. of SPIE, 172

Predehl, P., Andritschke, R., Becker, W., et al. 2011, in UV, X-Ray, and Gamma-Ray Space Instrumentation for Astronomy XVII, ed. L. Tsakalakos, Vol. 8145, Proc. of SPIE, 0D

Predehl, P., Andritschke, R., Böhringer, H., et al. 2010a, in Space Telescopes and Instrumentation 2010: Ultraviolet to Gamma Ray, ed. M. Arnaud, S. S. Murray, T. Takahashi, Vol. 7732, Proc. of SPIE, 0U

Predehl, P., Andritschke, R., Bornemann, W., et al. 2007, in UV, X-Ray, and Gamma-Ray Space Instrumentation for Astronomy XV, ed. O. H. W. Siegmund, Vol. 6686, Proc. of SPIE, 17

Predehl, P., Böhringer, H., Brunner, H., et al. 2010b, AIP Conf. Proc., 1248, 543

Predehl, P., Friedrich, P., & Hasinger, G. 2003, in X-Ray and Gamma-Ray Telescopes and Instruments for Astronomy, ed. Trümper,J. E. and Tananbaum, H. D., Vol. 4851, Proc. of SPIE, 314

Predehl, P., Hasinger, G., Böhringer, H., et al. 2006, in Space Telescopes and Instrumen-

tation II: Ultraviolet to Gamma Ray, ed. M. J. L. Turner, G. Hasinger, Vol. 6266, Proc. of SPIE, 0P

Preparata, F. P., & Shamos, M. I. 1985, Computational geometry. an introduction

Pringle, J. E., & Rees, M. J. 1972, Astronomy and Astrophysics, 21, 1

Pringle, J. E., Rees, M. J., & Pacholczyk, A. G. 1973, Astronomy and Astrophysics, 29, 179

Raymond, J. C., & Smith, B. W. 1977, Astrophysical Journal Supplement Series, 35, 419

Read, A. M., & Ponman, T. J. 2003, Astronomy and Astrophysics, 409, 395

Rees, M. J., Begelman, M. C., Blandford, R. D., & Phinney, E. S. 1982, Nature, 295, 17

Reiprich, T. H., & Böhringer, H. 2002, Astrophysical Journal, 567, 716

Revnivtsev, M., Sazonov, S., Gilfanov, M., Churazov, E., & Sunyaev, R. 2006, Astronomy and Astrophysics, 452, 169

Roncarelli, M., Moscardini, L., Tozzi, P., et al. 2006, Monthly Notices of the Royal Astronomical Society, 368, 74

Rosswog, S., & Bruggen, M. 2007, Introduction to High-Energy Astrophysics, (Cambridge: Cambridge University Press)

Salpeter, E. E., 1964, Astrophysical Journal, 140, 796

Schmid, C., 2008, Simulation of the imaging and detection properties of the eROSITA experiment on Spectrum-X-Gamma, diploma thesis

Schmid, C., Martin, M., Wilms, J., et al. 2010, AIP Conf. Proc., 1248, 591

Schmid, C., Smith, R., & Wilms, J. 2011a, SIMPUT – A File Format for Simulation Input, Technical report, (Cambridge: HEASARC)

Schmid, C., & Wilms, J. 2010a, Effects of misalignment on the HTRS, Technical report, (Bamberg: ECAP)

Schmid, C., & Wilms, J. 2010b, GRAVITAS Bright Source Performance, Technical report, (Bamberg: ECAP)

Schmid, C., & Wilms, J. 2011a, Bright Source Performance of the Athena WFI, Technical report, (Bamberg: ECAP)

Schmid, C., & Wilms, J. 2011b, Bright Source Performance of the Athena XMS, Technical report, (Bamberg: ECAP)

Schmid, C., Wilms, J., Oosterbroek, T., et al. 2011b, in Fast X-ray timing and spectroscopy at extreme count rates, ed. D. Barret, M. Mendez, S. Paltani, Vol. HTRS 2011, Proc. of Science, 070

Schönherr, G., Wilms, J., Kretschmar, P., et al. 2007, Astronomy and Astrophysics, 472, 353

Schwartz, D., 2011, in Handbook of X-Ray Astronomy, ed. K. Arnaud, R. Smith, A. Siemiginowska, Cambridge Observing Handbooks for Research Astronomers, (Cambridge: Cambridge University Press), 6

Schwarzschild, K., 1916, Abh. Konigl. Preuss. Akad. Wissenschaften, Berlin, 189–196

Serlemitsos, P. J., & Soong, Y. 1996, Astrophysics and Space Science, 239, 177

Serlemitsos, P. J., Soong, Y., Chan, K.-W., et al. 2007, Publications of the Astronomical Society of Japan, 59, 9

Short, A. D., Keay, A., & Turner, M. J. 1998, in EUV, X-Ray, and Gamma-Ray Instrumentation for Astronomy IX, ed. Siegmund, O. H. and Gummin, M. A., Vol. 3445, Proc. of SPIE, 13

Silverman, J. D., Green, P. J., Barkhouse, W. A., et al. 2008, Astrophysical Journal, 679, 118

Smith, R. K., Brickhouse, N. S., Liedahl, D. A., & Raymond, J. C. 2001, Astrophysical Journal Letters, 556, L91

Smith, S. J., Bandler, S. R., Brekosky, R. P., et al. 2008, in Space Telescopes and Instrumentation 2008: Ultraviolet to Gamma Ray, ed. M. J. L. Turner, K. A. Flanagan, Vol. 7011, Proc. of SPIE, 26

Snowden, S. L., Egger, R., Freyberg, M. J., et al. 1997, Astrophysical Journal, 485, 125

Snowden, S. L., Freyberg, M. J., Plucinsky, P. P., et al. 1995, Astrophysical Journal, 454, 643

Soltau, H., Holl, P., Kemmer, J., et al. 1996, Nuclear Instruments and Methods in Physics Research A, 377, 340

SRE-PA, 2009, IXO Payload Definition Document, Technical report, (Paris: ESA)

Stahle, C. K., McCammon, D., & Irwin, K. D.

1999, Physics Today, 52, 32
Stark, A. A., Gammie, C. F., Wilson, R. W., et al. 1992, Astrophysical Journal Supplement Series, 79, 77
Staubert, R., & Trümper, J. 2008, in The Universe in X-Rays, ed. J. E. Trümper, G. Hasinger, Astronomy and Astrophysics Library, (Berlin, Heidelberg: Springer), 3
Stefanescu, A., Bautz, M. W., Burrows, D. N., et al. 2010, Nuclear Instruments and Methods in Physics Research A, 624, 533
Stelzer, B., Flaccomio, E., Montmerle, T., et al. 2005, Astrophysical Journal Supplement Series, 160, 557
Strüder, L., Aschauer, F., Bautz, M., et al. 2010, in Space Telescopes and Instrumentation 2010: Ultraviolet to Gamma Ray, ed. M. Arnaud, S. S. Murray, T. Takahashi, Vol. 7732, Proc. of SPIE, 1I
Strüder, L., Briel, U., Dennerl, K., et al. 2001, Astronomy and Astrophysics, 365, L18
Strüder, L., Holl, P., Lutz, G., & Kemmer, J. 1987, Nuclear Instruments and Methods in Physics Research A, 253, 386
Strüder, L., & Meidinger, N. 2008, in The Universe in X-Rays, ed. J. E. Trümper, G. Hasinger, Astronomy and Astrophysics Library, (Berlin, Heidelberg: Springer), 51
Strüder, L., Meidinger, N., Pfeffermann, E., et al. 2000, in X-Ray Optics, Instruments, and Missions III, ed. Trümper, J. E. and Aschenbach, B., Vol. 4012, Proc. of SPIE, 342
Takahashi, T., Mitsuda, K., Kelley, R., et al. 2010, in Space Telescopes and Instrumentation 2010: Ultraviolet to Gamma Ray, ed. M. Arnaud, S. S. Murray, T. Takahashi, Vol. 7732, Proc. of SPIE
Takahashi, T., Nakazawa, K., Watanabe, S., et al. 2005, Nuclear Instruments and Methods in Physics Research A, 541, 332
Tawa, N., Hayashida, K., Nagai, M., et al. 2008, Publications of the Astronomical Society of Japan, 60, 11
Tenzer, C., Warth, G., Kendziorra, E., & Santangelo, A. 2010, in High Energy, Optical, and Infrared Detectors for Astronomy IV, Vol. 7742, Proc. of SPIE, 0Y
Thorne, K. S., 1974, Astrophysical Journal, 191, 507
Timmer, J., & König, M. 1995, Astronomy and Astrophysics, 300, 707
Tinker, J., Kravtsov, A. V., Klypin, A., et al. 2008, Astrophysical Journal, 688, 709
Toor, A., & Seward, F. D. 1974, Astronomical Journal, 79, 995
Treis, J., Fischer, P., Halker, O., et al. 2005a, IEEE Transactions on Nuclear Science, 52, 1083
Treis, J., Fischer, P., Hälker, O., et al. 2005b, in UV, X-Ray, and Gamma-Ray Space Instrumentation for Astronomy XIV, ed. Siegmund, O. H. W., Vol. 5898, Proc. of SPIE, 256
Trümper, J., 1982, Advances in Space Research, 2, 241
Trümper, J., 1992, Royal Astronomical Society, Quarterly Journal, 33, 165
Tsunemi, H., Hayashida, K., Tsuru, T. G., et al. 2010, in Space Telescopes and Instrumentation 2010: Ultraviolet to Gamma Ray, ed. M. Arnaud, S. S. Murray, T. Takahashi, Vol. 7732, Proc. of SPIE, 10
Türler, M., Chernyakova, M., Courvoisier, T. J.-L., et al. 2010, Astronomy and Astrophysics, 512, A49
Turner, M. J. L., Abbey, A., Arnaud, M., et al. 2001, Astronomy and Astrophysics, 365, L27
Ueda, Y., Akiyama, M., Ohta, K., & Miyaji, T. 2003, Astrophysical Journal, 598, 886
Urry, C. M., & Padovani, P. 1995, Publications of the Astronomical Society of the Pacific, 107, 803
Vernani, D., Borghi, G., Calegari, G., et al. 2011, in Optics for EUV, X-Ray, and Gamma-Ray Astronomy V, ed. S. L. O'Dell, G. Pareschi, Vol. 8147, Proc. of SPIE, 07
Vikhlinin, A., Burenin, R. A., Ebeling, H., et al. 2009a, Astrophysical Journal, 692, 1033
Vikhlinin, A., Kravtsov, A. V., Burenin, R. A., et al. 2009b, Astrophysical Journal, 692, 1060
Voges, W., Aschenbach, B., Boller, T., et al. 1999, Astronomy and Astrophysics, 349, 389
Voges, W., Aschenbach, B., Boller, T., et al. 2000a, IAU Circ., 7432, 1
Voges, W., Aschenbach, B., Boller, T., et al. 2000b, VizieR Online Data Catalog, 9029, 0

Weisskopf, M. C., Brinkman, B., Canizares, C., et al. 2002, Publications of the Astronomical Society of the Pacific, 114, 1

Weisskopf, M. C., Tananbaum, H. D., Van Speybroeck, L. P., & O'Dell, S. L. 2000, in X-Ray Optics, Instruments, and Missions III, ed. J. E. Trümper, B. Aschenbach, Vol. 4012, Proc. of SPIE, 2

Wells, D. C., Greisen, E. W., & Harten, R. H. 1981, Astronomy and Astrophysics Supplement Series, 44, 363

Wien, W., 1894, Annalen der Physik, 288, 132

Wikus, P., Adams, J. S., Baker, R., et al. 2010, in Space Telescopes and Instrumentation 2010: Ultraviolet to Gamma Ray, ed. M. Arnaud, S. S. Murray, T. Takahashi, Vol. 7732, Proc. of SPIE

Wille, E., Wallace, K., & Bavdaz, M. 2011, in Optics for EUV, X-Ray, and Gamma-Ray Astronomy V, ed. S. L. O'Dell, G. Pareschi, Vol. 8147, Proc. of SPIE, 0E

Wille, M., 2011, Detector Performance of eROSITA, diploma thesis

Willingale, R., 2009, in Bulletin of the American Astronomical Society, Vol. 41, Bulletin of the American Astronomical Society, 358

Willingale, R., 2011a, Bright Source Defocusing Optic for Athena XMS, Technical report, (Leicester: University of Leicester)

Willingale, R., 2011b, International X-ray Observatory – The Path to Mirror Readiness, Talk on the IXO Science Meeting in Rome, Italy, March 2011

Willingale, R., & Spaan, F. H. P. 2010, in Space Telescopes and Instrumentation 2010: Ultraviolet to Gamma Ray, ed. M. Arnaud, S. S. Murray, T. Takahashi, Proc. of SPIE, 41

Wilms, J., 2006, Nature, 444, 699

Wilms, J., 2008, Chinese Journal of Astronomy and Astrophysics Supplement, 8, 281

Wilms, J., Allen, A., & McCray, R. 2000, Astrophysical Journal, 542, 914

Winkler, C., Courvoisier, T. J.-L., Di Cocco, G., et al. 2003, Astronomy and Astrophysics, 411, L1

Winkler, C., Diehl, R., Ubertini, P., & Wilms, J. 2011, Space Science Reviews, 161, 149

Wolter, H., 1952a, Annalen der Physik, 10, 94

Wolter, H., 1952b, Annalen der Physik, 10, 286

Worsley, M. A., Fabian, A. C., Bauer, F. E., et al. 2005, Monthly Notices of the Royal Astronomical Society, 357, 1281

Xue, Y. Q., Luo, B., Brandt, W. N., et al. 2011, Astrophysical Journal Supplement Series, 195, 10

Zhang, J., Cui, W., Juda, M., et al. 1998, Physical Review B, 57, 4472

Zhang, W., Jahoda, K., Swank, J. H., Morgan, E. H., & Giles, A. B. 1995, Astrophysical Journal, 449, 930

Zhang, W. W., Content, D. A., Lehan, J. P., et al. 2005, in Optics for EUV, X-Ray, and Gamma-Ray Astronomy II, ed. O. Citterio, S. L. O'Dell, Vol. 5900, Proc. of SPIE, 247

APPENDIX **A**

USING SIXTE

A.1 Software Package

The SIXTE software package for simulations of astronomical X-ray telescopes described in this thesis is publicly available[1]. In addition to the functional description in Chapter 3, a practical overview with an instruction for the usage of the software is given in the following.

A.1.1 Installation

The SIXTE software has been developed on a Linux computer and can be installed and operated on a similar system. Its source code is maintained with the `git`[2] version control system and is publicly available.

Required Packages The installation of the SIXTE software requires the following packages:

- libexpat1-dev
- libgsl0-dev
- HEAsoft[3]

SIMPUT Library Before installing the SIXTE software package you have to download and install the SIMPUT library. In order to obtain the source code from its public `git` repository, please use the following command:

```
git clone http://www.sternwarte.uni-erlangen.de/git.public/simput.git/
```

You can compile and install the SIMPUT library with the following commands:

```
cd simput
autoreconf --install
./configure --prefix=$HOME
make
make install
```

The optional argument

```
--prefix=\$HOME
```

[1] Although the software is developed with great care, no warranty is given for proper functionality. Errors and bugs can be reported to the developer without any guarantee of support.

[2] `http://git-scm.com/`

[3] `http://heasarc.nasa.gov/docs/software/ftools/`

means that the installation will be done in your user-specific home directory, i.e., the library is installed in `$HOME/lib` and the header files in `$HOME/include`.

SIXTE The SIXTE source code repository can be cloned using the following command:

```
git clone http://www.sternwarte.uni-erlangen.de/git.public/sixt/
```

The local clone of the repository can be updated to recent changes by running the command git pull in the project directory. Of course, this latter step is not required directly after cloning the repository, but only in order to keep it up-to-date afterward.

Compiling and installing the code is analogous to the steps required for the SIMPUT library, except that in addition the folder has to be specified, where the PIL parameter files are stored.

```
cd sixt
autoreconf --install
./configure --prefix=$HOME PFILESDIR=$HOME/pfiles
make
make install
```

These steps are also described in the file `INSTALL.txt`, which is contained in the project directory.

The source code documentation tool `doxygen` is used to obtain a comprehensive documentation of the program code in HTML or LaTeX format, based on code-internal comments for the individual data structures and functions. The documentation can be generated by the following command, which creates a sub-directory `doc/` within the project directory:

```
doxygen doxygen.config
```

A.1.2 Simulation Run

After installation a simulation can be run from the shell with the command

```
runsixt
```

and the following parameters:

- `Simput`: Source catalog containing the definition of the X-ray sources to be observed according to the SIMPUT format (Appendix B).
- `Prefix`: Prefix for the output files (photon, impact, event, and pattern list).
- `Mission`: Mission name (e.g., 'SRG' or 'ATHENA').
- `Instrument`: Instrument name (e.g., 'eROSITA').
- `Mode`: Instrument mode (e.g., 'FULLFRAME').
- `RA`: Right Ascension of telescope pointing direction (deg).
- `Dec`: Declination of telescope pointing direction (deg).
- `Exposure`: Simulated exposure time (s)

In addition the following optional parameters can be specified:

- `XMLFile`: Name of XML file with instrument definition. Overwrites the settings for `Mission`, `Instrument`, and `Mode`.
- `Attitude`: File with the time dependent attitude information of the telescope pointing direction.
- `PhotonList`: Name of the output file containing the photon list. Is used in combination with the specified `Prefix`.
- `ImpactList`: Name of the output file containing the impact list. Is used in combination with the specified `Prefix`.

- `EventList`: Name of the output file containing the event list. Is used in combination with the specified `Prefix`.
- `PatternList`: Name of the output file containing the pattern list. Is used in combination with the specified `Prefix`.
- `MJDREF`: Reference Modified Julian Date.
- `TIMEZERO`: Time offset with respect to `MJDREF`.
- `Seed`: Seed for random number generator.
- `chatter`: Verbosity level for program output.
- `history`: Flag whether program parameters are stored in the header of FITS output files.
- `clobber`: Overwrite existing output files.

The following program call would, e.g., initiate a simulation of a pointed observation of a region around RA = 30.5 deg, Dec = −18.3 deg with the eROSITA telescope on *SRG* and an exposure time of 10 ks. The observed sources are defined in the file `sources.fits`.

```
runsixt Prefix=sim_ \
 Mission=SRG Instrument=eROSITA Mode=none RA=30.5 Dec=-18.3 \
 PhotonList=photons.fits ImpactList=impacts.fits \
 EventList=events.fits PatternList=pattern.fits \
 Simput=sources.fits Exposure=10000.
```

The output of the simulation program are a photon list, an impact list, an event list, and a pattern list stored in the current working directory. These data products are described in detail in Chapter 3. They can be further processed with the auxiliary tools, which are also explained in Chapter 3.

A.2 Instrument Setup

The setup of the instrument mock-up for the simulation is defined in an XML file with a particular format. This section provides an overview of the relevant XML tags and explains a sample detector definition file for one eROSITA camera.

A.2.1 XML Tags

This section provides an overview of the XML tags used to define a particular detector configuration.

`<telescope name="...">...</telescope>`
Encapsulates the definition of a particular telescope.

`<fov diameter="..."/>`
Diameter of the FOV of the instrument in [deg].

`<focallength value="..."/>`
Focal length of the telescope in [m].

`<vignetting filename="..."/>`
File containing the vignetting function of the telescope (George & Yusaf, 1994).

`<psf filename="..."/>`
File containing the 2-dimensional PSF of the telescope (George & Yusaf, 1995).

`<detector>...</detector>`
Encapsulates the detector definition.

`<dimensions xwidth="..." ywidth="..."/>`
Number of pixels in x- and y-direction.

`<pixelborder x="..." y="..."/>`
Border of each pixel in [m].

`<wcs xrpix="..." yrpix="..." xrval="..." yrval="..." xdelt="..." ydelt="..."/>`
Definition of the detector coordinate system according to the WCS keywords introduced by Greisen & Calabretta (2002) and Calabretta & Greisen (2002).

`<cte value="..."/>`
CTE of each line shift in a CCD device.

`<arf filename="..."/>`
File containing the detector ARF (George et al., 1998, 2007), which includes the effective area of the telescope, the quantum efficiency of the detector, the transmission of possible filters, etc.

`<rmf filename="..."/>`
File containing the detector redistribution matrix, the RMF (George et al., 1998, 2007).

`<split type="..." par1="..." par2="..."/>`
Model for the charge cloud splitting between adjacent pixels. Currently available are a Gaussian (`GAUSS`) and an exponential model (`EXPONENTIAL`) developed for eROSITA by K. Dennerl (priv. comm.). For the exponential model only the first parameter (`par1`) is relevant.

`<threshold_readout_lo_keV value="..."/>`
Lower detector readout threshold in [keV].

`<threshold_readout_up_keV value="..."/>`
Upper detector readout threshold in [keV].

`<threshold_event_lo_keV value="..."/>`
Lower threshold for an event detection in [keV].

`<threshold_split_lo_fraction value="..."/>`
Lower threshold for a split partner as a fraction of the total signal of the pattern.

`<erobackground filename="..."/>`
File containing data about the detector background produced, e.g., by cosmic ray photons. Currently such data are only available for eROSITA.

`<readout mode="...">...</readout>`
Either a time-triggered (`TIME`) or a event-triggered (`EVENT`) mode are available. For the time-triggered mode the definition of the readout sequence is defined by the encapsulated XML tags.

`<wait time="..."/>`
Defines a period of inactivity in [s]. During that time the detector is exposed to incident radiation.

`<readoutline lineindex="..." readoutindex="..."/>`
Read out a particular line of the detector pixel array and assign the selected line number, which might be different from the actual line index (this is required, e.g., for CCD detectors, where lines are shifted).

`<lineshift/>`
Shift the collected charges in a CCD by one line towards the readout anodes.

`<newframe/>`
Defines the start of a new detector frame.

`<loop start="..." end="..." increment="..." variable="...">...</loop>`
Repeats the contained XML tags, while the loop variable is increased from its starting to its end value by the specified increment.

Additional XML tags can be easily introduced if required for different instrument configurations.

A.2.2 Example

The example XML code below displays the definition of one of the seven eROSITA telescopes and the corresponding detector.

```
<?xml version="1.0"?>
<instrument>

<telescope name="eROSITA">
  <fov diameter="1.02"/>
  <focallength value="1.6"/>
  <vignetting filename="erosita.vignetting.fits"/>
  <psf filename="erosita.psf.7.5mum.fits"/>
</telescope>

<detector>
  <dimensions xwidth="384" ywidth="384"/>
  <pixelborder x="0." y="0."/>
  <wcs xrpix="192.5" yrpix="192.5" xrval="0." yrval="0."
       xdelt="75.e-6" ydelt="75.e-6"/>
  <cte value="1"/>
  <arf filename="erosita_iv_1telonaxis_ff.arf"/>
  <rmf filename="erosita_iv_1telonaxis_ff.rmf"/>
  <split type="exponential" par1="0.355"/>
  <threshold_readout_lo_keV value="0."/>
  <threshold_readout_up_keV value="12."/>
  <threshold_event_lo_keV value="150.e-3"/>
  <threshold_split_lo_fraction value="0.01"/>
  <erobackground filename="eROSITA_hitlist_reduced_1308_81s.fits"/>

  <readout mode="time">
    <wait time="0.05"/>

    <loop start="0" end="383" increment="1" variable="$i">
      <readoutline lineindex="0" readoutindex="$i"/>
      <lineshift/>
      <wait time="0.3e-6"/>
    </loop>

    <newframe/>
  </readout>
```

```
</detector>
</instrument>
```

The telescope has a FOV of 1.02 deg and a focal length of 1.6 m. The PSF and vignetting are described in two separate files including several data sets for different energies and off-axis angles.

The detector consists of 384×384 pixels with an area of $75\,\mu\text{m} \times 75\,\mu\text{m}$ each. The applied coordinate system is centered on the detector. Its origin coincides with the intersection of the optical axis of the telescope with the detector plane. The pixels have no borders. The presented detector model does not include a particular framestore area. Instead the collected charges in the sensitive part of the pixel array are read out with the same speed as the transfer time to the framestore area. This approach is, of course, only possible in the simulation and avoids the necessity of a framestore region.

The combined effective area of the instrument taking into account the effective area of the telescope and the quantum efficiency of the detector is stored in the specified ARF. The energy resolution and related effects such as an escape peak are described by the RMF. For the simulation a CTE of 100 % is assumed. Charge cloud splitting between neighboring pixels is simulated according to the model developed by K. Dennerl (priv. comm.). The data in the specified file are used to produce random events accounting for the detector background.

The lower threshold for the readout of the detector is set to 0 keV, and the upper threshold to 12 keV. The pattern analysis algorithm selects only events with a signal of more than 150 eV as main events. Split partners are searched with a threshold of 1 % of the total signal of the main event in its direct neighborhood.

The readout mode of the detector is characterized by an exposure time of 50 ms followed by 384 subsequents readouts and line shifts, as typical for a CCD. As previously mentioned, the model for the framestore area is replaced by a fast line readout, which is equivalent to the time required to transfer the detector image into the framestore area. In the presented configuration a single line shift lasts $0.3\,\mu$s, i.e., the readout of the whole array takes about $115\,\mu$s corresponding approximately to the transfer time from the imaging to the framestore area (Chapter 4).

With this XML description the essential parameters of the instrument mock-up of a single eROSITA telescope and detector sub-system are defined. Additional XML definition files for various instruments can be found in the SIXTE software package.

APPENDIX **B**

SIMPUT FILE FORMAT

In the following the SIMPUT format definition is presented, which I have developed in cooperation with R. Smith and J. Wilms (Schmid et al., 2011a). It has been adopted as an official document by the HEASARC and can also be found on the web site of the Smithsonian Astrophysical Observatory (SAO) of the Harvard University[1].

[1] `http://hea-www.harvard.edu/HEASARC`

SIMPUT
A File Format for Simulation Input

Christian Schmid[1] (christian.schmid@sternwarte.uni-erlangen.de),
Randall Smith[2] (rsmith@cfa.harvard.edu),
Jörn Wilms[1] (joern.wilms@sternwarte.uni-erlangen.de)

[1]ECAP, Sternwartstr. 7, 96049 Bamberg, Germany
[2]SAO, 60 Garden St., Cambridge, MA 02138, USA

Version: 2011 Dec 16
(HDUVERS = 1.0.0)

SUMMARY

We present a standard format for source input files to be used in simulations of astronomical observations. Each source file contains a catalog with one or multiple sources, which are described by specific properties such as position, brightness, energy spectrum, as well as optional characteristics such as time variability, polarization, and spatial extent.
This file format defines a common basis to exchange data between different software packages and scientific groups. It was developed in particular for the simulation of X-ray telescopes, but can also be used in different wavelength domains.

LOG OF SIGNIFICANT CHANGES

Release **D**ate	**S**ections Changed	**B**rief Notes
2011 Dec 16		Initial version

1 Introduction

In X-ray astronomy, simulations of existing and future telescopes are used both to estimate the scientific capabilities provided by an instrument and to understand particular phenomena in measured data. Therefore there are a growing number of different simulation tools for particular issues, each implementing its own particular format for simulation input data.

X-ray point sources may be modeled using coordinates given either on the command line or in a separate file. For extended sources there are also various approaches parameterizing the observable shape or specifying an input image. The range of possible input formats extends even further when additional parameters such as the spectral shape or brightness variability have to be considered.

Due to the large number of existing input formats it is difficult to use data generated for one particular simulation within another software package. We address this issue by introducing a common input data format for simulations of astronomical X-ray telescopes based on the Flexible Image Transport System (FITS) file format defined by Hanisch et al. (2001) and Pence et al. (2010). The format enables modeling of all relevant source properties starting with source positions, spatial shapes for extended sources, energy spectra, polarization of the emitted radiation, as well as time-variable features such as brightness, spectral, and spatial variations. It can be regarded as an interface between different simulations and different scientific groups, for example the users of a simulation and a Magnetohydrodynamic (MHD) modeler providing the input data. The use of this format simplifies the conversion processes needed to prepare for a simulation and provides a clear and flexible way to describe all relevant features to model X-ray sources.

Although the file format has been developed in particular for simulations of X-ray telescopes, it can also be used in different wavelength domains of astronomy by adjusting the required units. The usage of physical units within this format is based on the specification defined by George & Angelini (1995) and Pence et al. (2010).

2 File Format

A SIMPUT FITS file contains several different types of extensions with the formats described in this section. The main file must contain one source catalog extension defining the individual sources. Of course, the catalog can also consist of a single source. Additional data such as spectra, light curves, or images can be stored in separate extensions in the same file or in separate FITS files. An example for the basic structure of a SIMPUT file is shown in Fig. 1.

The file format can describe point-like and spatially extended sources with either constant or time-variable brightness. The spectral shape, spatial extension, or polarization of the emitted photons might also be time-dependent. The emitted radiation can have a particular polarization. By combining different features of the presented format, one can describe nearly all astronomical sources. For instance a spatially extended source, which has different emission regions with particular spectra, can be described as the superposition of several separate source images with appropriate spectra. In addition each of these spectra can have different polarization.

In the following part of this section the format of the individual extension types is defined. The proposed order of columns in binary tables is not mandatory, but can be modified. Additional columns are allowed. Undefined string entries in a table are denoted by the FITS NULL value.

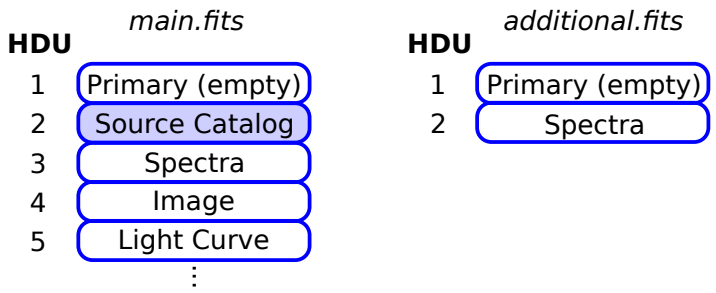

Figure 1: A SIMPUT file ('main.fits') contains one source catalog extension with the basic description of one or multiple sources. Additional data such as spectra, light curves, and images can be stored in separate HDUs or even in separate FITS files ('additional.fits'). The individual entries in the source catalog refer to the required extensions.

2.1 Source Catalog Extension

Description The main extension in a SIMPUT FITS file is a source catalog providing the basic properties of individual sources. It defines source characteristics such as the position and brightness. Additional information about the source spectrum, light curve, and spatial extension may be stored in separate FITS file HDUs. The entries in the catalog contain links to the corresponding extensions using the extended filename syntax (Pence, 1999).

In order to be used as simulation input, a SIMPUT FITS file must contain exactly one source catalog extension, even if it describes only a single source. The name of this extension is **SRC_CAT**.

Extension Header The following keywords are mandatory:

- `HDUCLASS` - contains the string `HEASARC`
- `HDUCLAS1` - contains the string `SIMPUT`
- `HDUCLAS2` - contains the string `SRC_CAT`
- `HDUVERS = '1.0.0'` - giving the version of the format
- `EXTNAME` - contains the string `SRC_CAT`
- `RADESYS` - reference coordinate system, e.g. `FK5`
- `EQUINOX` - reference coordinate system, e.g. `2000.0`

The usage of the RADESYS and EQUINOX keywords is described by Calabretta & Greisen (2002) and Pence et al. (2010).

Data Format The data within the extension are organized as a BINTABLE with the following columns:

1. *ID*, an **integer** value containing a unique identifier for each entry.
   The FITS column name is **SRC_ID**.
   (unitless).
   This column is required.

2. *Name*, a **string** containing the name of the source (need not be unique, as a single source might be modeled by several entries).
   The FITS column name is **SRC_NAME**.

(unitless).
This column is optional.

3. α, a **floating point** value containing the right ascension of the source.
The FITS column name is **RA**.
The recommended units are decimal deg.
This column is required.

4. δ, a **floating point** value containing the declination of the source.
The FITS column name is **DEC**.
The recommended units are decimal deg.
This column is required.

5. ρ, a **floating point** value containing the rotation angle (measured in the direction N-E-S-W) around the reference point for extended sources and of the polarization vector for polarized sources respectively (see notes below). This quantity is only defined for extended or polarized sources.
The FITS column name is **IMGROTA**.
The recommended units are deg.
This column is optional.

6. *Image Scale*, a **floating point** value containing the inverse linear scaling factor for extended sources (see notes below). This quantity is only defined for extended sources.
The FITS column name is **IMGSCAL**.
(unitless).
This column is optional.

7. $E_{\rm min}$, a **floating point** value specifying the lower value of the reference energy band.
The FITS column name is **E_MIN**.
The recommended units are keV.
This column is required.

8. $E_{\rm max}$, a **floating point** value specifying the upper value of the reference energy band.
The FITS column name is **E_MAX**.
The recommended units are keV.
This column is required.

9. *Flux Density*, a **floating point** value containing the source flux density in the specified reference energy band.
The FITS column name is **FLUX**.
The recommended units are $\mathrm{erg\,s^{-1}\,cm^{-2}}$.
This column is required.

10. *Spectrum*, a **string** containing a reference to a FITS file HDU describing the energy spectrum of the source. The reference is given via the extended filename syntax (see notes below). If source spectra are defined in the light curve extension (see Sec. 2.4.1) this field must be NULL.
The FITS column name is **SPECTRUM**.
(unitless).
This column is required.

11. *Image*, a **string** containing a reference to a FITS file HDU with an image of the source. The reference is given via the extended filename syntax (see notes below). For a point source or if several source images are defined in the light curve extension (see Sec. 2.4.1), this field must be NULL.
The FITS column name is **IMAGE**.
(unitless).
This column is optional.

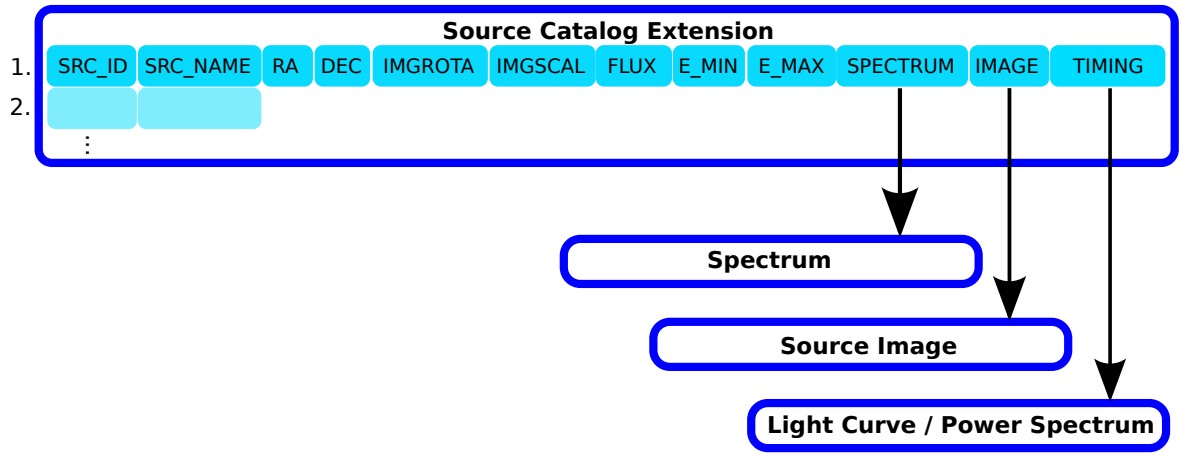

Figure 2: Layout of the source catalog extension. Apart from basic source properties such as the position or energy flux density each source must refer to a spectrum extension. The specification of a light curve or PSD and a source image is optional. If the spectrum or the spatial shape of a source is time-dependent, the corresponding fields in the source catalog must be NULL. In that case the light curve must contain links to the respective spectra or images.

12. *Timing*, a **string** containing a reference to a FITS file HDU defining the time-dependence of the source brightness. As described in Sec. 2.4 this can be either a light curve or a Power Spectral Density (PSD). The reference is given via the extended filename syntax (see notes below). For a constant source this field must be NULL.
    The FITS column name is **TIMING**.
    (unitless).
    This column is optional.

The basic scheme of the source catalog extension is displayed in Fig. 2.

Points to note & Conventions

- The reference energy band defined in the E_MIN and E_MAX columns must be covered by the assigned source spectrum.
- Links to additional FITS file HDUs containing spectra, light curves, or images are given according to the extended filename syntax (Pence, 1999) by the name of the corresponding file, the extension name (EXTNAME), extension version (EXTVER), and required additional selectors such as the table row containing a particular spectrum or the corresponding name, in case the spectrum table contains a NAME column. For instance the spectrum in row number 4 within the HDU with `EXTNAME = SPECTRUM` and the `EXTVER = 3` stored in the file `data.fits` is identified by the reference `data.fits[SPECTRUM,3][#row==4]`.

  If the spectrum table contains the optional column NAME (see Sec. 2.2.1), the particular spectrum, which has the value `'powerlaw2.1'` in its NAME field, is identified with the reference `data.fits[SPECTRUM,3][NAME=='powerlaw2.1']`. The latter syntax is more flexible in terms of the table structure, since spectra can be rearranged without taking care of their row numbers.

  References to data residing within the current file are given without the filename, in order to avoid inconsistency problems, when the file is renamed: `[SPECTRUM,3][#row==4]`

- In order to model a time-variable source, multiple energy spectra or images might be required to describe the temporal evolution of the system. In that case the source must refer to a light curve containing a SPECTRUM or IMAGE column with links to the corresponding FITS file HDUs (see Sec. 2.4.1), and the SPECTRUM or IMAGE fields in the source catalog must be NULL.
- A single extended source with different energy spectra for different emission regions can be described by multiple entries in the source catalog with different images and spectra. The superposition of all entries in the simulation results in the complete image of the extended source.
- Different source entries in the catalog can refer to the same spectrum, light curve, or source image. It is possible to apply individual scales to spectra or images through the FLUX, IMGSCAL, and IMGROTA columns in order to match the respective sources. For instance, the flux density given for a particular entry in the catalog determines the absolute flux for this source, providing the possibility to use the same spectral shape for multiple sources with different brightness.

  In a similar way extended sources, which are either characterized by a source image or by a photon list, can be rotated and scaled in size using the columns IMGROTA and IMGSCAL. The rotation is performed around the reference point of the source image or photon list in N-E-S-W direction. The angular extent γ of the image or photon list is scaled as follows in order to obtain the simulated source extent γ':

$$\gamma' = \frac{1}{\mathrm{IMGSCAL}} \cdot \gamma \tag{1}$$

  The rotation angle is also applied to the polarization direction defined in a spectrum.

2.2 Spectrum Extension

In SIMPUT files there are three different basic ways to describe the energy spectrum of a source. Each entry in the catalog must refer to at least one such spectrum extension. Several sources with different brightness can refer to the same spectrum, which is scaled according to the particular energy flux density of the respective entries in the catalog.

A time-variable source can also have multiple spectra specified in the assigned light curve extension (see Sec. 2.4.1). The spectra valid for the different points of time or phases during the simulated time interval are stored separately in different rows of a spectrum extension or even in different HDUs. In order to have a continuous spectral variation, the simulation software might, e.g., apply a linear interpolation for the time intervals in between two specified spectra.

Each spectrum extension can contain information about the polarization of the emitted radiation by specifying the following optional keywords:

- `STOKES1` - Stokes parameter
- `STOKES2` - Stokes parameter
- `STOKES3` - Stokes parameter
- `RADESYS` - reference coordinate system, e.g. `FK5`
- `EQUINOX` - reference coordinate system, e.g. `2000.0`

The keywords STOKES1, STOKES2, and STOKES3 define the 2nd, 3rd, and 4th component of the normalized Stokes vector (Stokes, 1852) specifying the polarization of the emitted radiation. The information about the absolute intensity of the measured radiation is neglected, such that the first component of the normalized Stokes vector (STOKES0) has always a value of 1, and therefore does not have to be specified explicitly. The absolute intensity is given by the particular source brightness. The keywords RADESYS and EQUINOX define the coordinate system the polarization direction refers to.

In order to be able to reuse the same spectrum for different source entries in the catalog, the polarization direction can be modified by the IMGROTA value in the catalog. For each individual source the polarization direction is rotated by this angle in N-E-S-W direction.

2.2.1 Mission-Independent Spectrum

This is the preferred format for the description of a source spectrum, because it is mission-independent and physically accurate at the same time. It can therefore be used for simulations of different telescopes covered by the specified energy range.

Description The spectrum extension describes one or multiple energy spectra in a mission- (and therefore effective area-) independent way giving the photon flux density distribution in a particular energy range. In order to determine the observed photon spectrum for a specific telescope, it has to be multiplied with the corresponding effective area (George & Zellar, 1995) or Ancillary Response File (ARF) (George et al., 1998, 2007) respectively.

Similar to Pulse Height Amplitude (PHA) II files (Arnaud et al., 2009; George & Arnaud, 2004) multiple spectra can be stored in a single binary table HDU. Each single spectrum is stored in a single row using vector columns. The spectra in the table can be either identified by their row number or by a unique name defined in the corresponding optional column.

Extension Header The following keywords are mandatory:

- `HDUCLASS` - should contain the string `HEASARC`
- `HDUCLAS1` - should contain the string `SIMPUT`
- `HDUCLAS2` - should contain the string `SPECTRUM`
- `HDUVERS = '1.0.0'` - giving the version of the format

If applicable the following optional keyword can be used to specify the spectral model and parameters the spectrum has been generated from:

- `MODEL` - filename refering to the spectral model and parameters

Data Format The data within the extension are organized as a BINTABLE with the following columns:

1. *Name*, a fixed-length **string** containing a unique case-sensitive designator for each individual spectrum.
   The FITS column name is **NAME**.
   (unitless).
   This column is optional.
2. *Energy*, a **floating point** fixed or variable length array containing the grid of photon energy values.
   The FITS column name is **ENERGY**.
   The recommended units are keV.
   This column is required.

3. *Photon Flux Density Distribution*, a **floating point** fixed or variable length array containing the photon flux densities at the respective energies. The number of entries in the array must be the same as the number of entries in the array contained in the ENERGY column.
   The FITS column name is **FLUX**.
   The recommended units are photon $\mathrm{s}^{-1}\,\mathrm{cm}^{-2}\,\mathrm{keV}^{-1}$.
   This column is required.

Points to note & Conventions

- The energy flux density can be easily obtained by multiplying the photon flux density with the corresponding photon energy.
- Each array in the ENERGY column should have ascending order.
- In order to refer to a particular spectrum in the table via the extended filename syntax, the filename and the HDU have to be specified in combination with either the respective row number or the unique name of the spectrum, in case the NAME column is present.
- It is important that the NAME column, if present, has a fixed and not a variable length, since with variable length strings a selection like `NAME=='...'` via the extended filename syntax is not supported by the cfitsio library.

2.2.2 PHA File

The source spectrum can also be modeled by a standard PHA file (Arnaud et al., 2009; George & Arnaud, 2004) either of type I or type II. The latter may contain multiple spectra within a single HDU table.

Points to note & Conventions

- PHA files contain the convolution of the source spectrum with a mission-dependent detector response matrix. Since the convolution with the response matrix is a non-invertible process, the original spectrum cannot be uniquely reconstructed from these data. This has to be taken into account when using PHA files to describe source spectra for input to a simulation.

  The specification of a PHA spectrum might be useful, if an existing observation of a source with a particular telescope must be simulated for a different telescope and the energy resolution of the telescope the PHA file was made for is comparable or better than the resolution of the telescope in the simulation. The approximate unfolding can be done, e.g., with the procedure described by Nowak et al. (2005).

  The mission-independent spectral format (Sec. 2.2.1) is preferred in terms of simulation input data.
- Using PHA II files multiple spectra can be stored in a single HDU, each occupying one row in the binary table. The entries in the source catalog can refer to the individual spectra via the extended filename syntax specifying the respective row number.
- In order to be able to determine the photon energies corresponding to the channels used in the PHA file, an appropriate detector response file containing an EBOUNDS extension has to be specified via the RESPFILE header keyword in the PHA file.

2.2.3 Photon List

Description The energy spectrum of an X-ray source can also be described by specifying a sample of photons distributed according to the respective spectrum. This approach can be useful if the photon sample is obtained, e.g., from a complicated MHD simulation.

Extension Header The following keywords are mandatory:

- `HDUCLASS` - contains the string `HEASARC`
- `HDUCLAS1` - contains the string `SIMPUT`
- `HDUCLAS2` - contains the string `PHOTONS`
- `HDUVERS = '1.0.0'` - giving the version of the format
- `RADESYS` - reference coordinate system, e.g. `FK5`
- `EQUINOX` - reference coordinate system, e.g. `2000.0`
- `REFRA` - right ascension of reference point in deg
- `REFDEC` - declination of reference point deg

The usage of the RADESYS and EQUINOX keywords is described by Calabretta & Greisen (2002) and Pence et al. (2010).

In addition a photon list with information about the arrival time of the photons must contain the following time definition keywords, even if the energy spectrum is not time-dependent:

- `MJDREF` - MJD for reference time
- `TSTART` - start time
- `TSTOP` - stop time
- `TIMEZERO` - zero time
- `TIMESYS` - the system used to define the time
- `TIMEUNIT` - unit for TSTART, TSTOP, TIMEZERO. The recommended units are s.
- `CLOCKCOR` - if time is corrected to UT

The usage of the time definition keywords is described by Angelini et al. (1994).

Data Format The data within the extension are organized as a BINTABLE with the following columns:

1. *Time*, a **floating point** value containing the arrival time of the photon (relative to the offset given by the header keyword TIMEZERO).
   The FITS column name is **TIME**.
   The units are defined by the header keyword TIMEUNIT.
   This column is optional.
2. α, a **floating point** value containing the right ascension of the origin of the photon.
   The FITS column name is **RA**.
   The recommended units are deg.
   This column is required.
3. δ, a **floating point** value containing the declination of the origin of the photon.
   The FITS column name is **DEC**.
   The recommended units are deg.
   This column is required.

4. *Energy*, a **floating point** value containing the energy of the photon.
   The FITS column name is **ENERGY**.
   The recommended units are keV.
   This column is required.

5. *Polarization Angle*, a **floating point** value containing the polarization angle of the photon.
   The FITS column name is **POLANG**.
   The recommended units are deg.
   This column is optional.

Points to note & Conventions

- The main advantage of photon lists is that event lists obtained from observations can be easily converted to this format and therefore be used as input for simulations of different telescopes.
- A photon list is capable of describing the energy spectrum of a source, the spacial distribution of the emitted photons, and also time-dependent phenomena in case the optional TIME column is used. For time-independent photon lists the simulation software can randomly select entries. In that case no sorting of the list is required. For time-dependent photon lists it is up to the simulation to apply an appropriate algorithm to select photons without destroying the time-dependent features.
- The number of photons in the list should be sufficiently large for the statistical purpose of the simulation. Depending on the applied algorithm not every photon in the list will be used in a simulation, but only some of them will be selected by a randomization process. The number of actually required photons depends on the particular source flux density, the effective area of the selected telescope and the length of the simulated time interval. If N is the number of photons in the list with an energy in the reference range and T is the simulated time interval, the photon rate required for the simulation of a particular source should be at least by a factor of 5 smaller than N/T in order to guarantee a sufficiently large number of photons. The simulation software has to make sure that this criterion is fulfilled.
- In order to be able to reuse the same photon list extension for different entries in the source catalog, the direction of each photon in the simulation is obtained from its right ascension and declination value with respect to the reference point defined by the REFRA and REFDEC keywords and its position in the source catalog. For each catalog entry the refence point is translated to match the position in the source catalog, and the angular distances of the individual photons with respect to the reference point are scaled by a factor 1/IMGSCAL. In addition the photon positions are rotated around the reference point in N-E-S-W direction according to the angle given in the IMGROTA column.
- Each photon in the list can have a polarization defined by the optional POLANG column. The angle is determined with respect to the north pole of the reference coordinate system via the eastern direction. For the special case of a photon coming directly from one of the poles the angle is measured with respect to the meridian corresponding to RA=0. In order to be able to reuse the same photon list for different sources, the polarization angle can be adjusted by the IMGROTA value in the source catalog. This value, which can be different for each source, is added to the IMGROTA angle in order to obtain the polarization direction.

  The specification of an explicit polarization angle overrides the polarization characteristics defined by the header keywords STOKES1, STOKES2, and STOKES3.

2.3 Image Extension

Description Extended sources are described by an image obtained from an observation or from a simulation. The image represents the spatial distribution of the flux density. The coordinates of the image are given via World Coordinate System (WCS) keywords.

If the spatial shape of a source is time-dependent, this can be described by several images valid for particular points of time or phases in case of a periodic system. The relation between the time or phase of the system and the corresponding images is defined in the light curve extension (see Sec. 2.4.1).

Extension Header The following keywords are mandatory:

- `HDUCLASS` - should contain the string `HEASARC`
- `HDUCLAS1` - should contain the string `SIMPUT`
- `HDUCLAS2` - should contain the string `IMAGE`
- `HDUVERS = '1.0.0'` - giving the version of the format

The image coordinates are defined by an appropriate set of WCS header keywords, as described by Greisen & Calabretta (2002), Calabretta & Greisen (2002) and Pence et al. (2010). For instance one can use the following keywords:

- `CTYPE1` - WCS axis type
- `CTYPE2` - WCS axis type
- `CUNIT1` - units of CRVAL1 and CDELT1
- `CUNIT2` - units of CRVAL2 and CDELT2
- `CRPIX1` - reference point in pixels
- `CRPIX2` - reference point in pixels
- `CRVAL1` - coordinate value at reference point
- `CRVAL2` - coordinate value at reference point
- `CDELT1` - coordinate increment at reference point
- `CDELT2` - coordinate increment at reference point
- `RADESYS` - reference coordinate system, e.g. `FK5`
- `EQUINOX` - reference coordinate system, e.g. `2000.0`

In addition the following optional header keyword can be used to specify the normalization of the flux represented by the source image:

- `FLUXSCAL` - scaling factor (see below)

If FLUXSCAL is not given as a header keyword, it is calculated by summing up all pixel values.

Data Format The source image is a FITS image representing the spatial flux distribution. The absolute value of the flux density for a particular pixel $F(\text{pixel})$ is obtained from the reference flux density in the source catalog F_{catalog}, the pixel value $f(\text{pixel})$, and the value of FLUXSCAL via the following relation:

$$F(\text{pixel}) = \frac{f(\text{pixel})}{\text{FLUXSCAL}} \cdot F_{\text{catalog}} \tag{2}$$

In order to be able to reuse the same image for multiple sources in a catalog, the absolute position of the image in the sky defined by the WCS header keywords, is neglected. Instead of that, the reference

Light Curve

PHASE	FLUX	SPECTRUM
0.1	0.82	spectra.fits[SPECTRUM,1][#row==1]
0.2	1.15	spectra.fits[SPECTRUM,1][#row==2]
⋮	⋮	⋮

Figure 3: The light curve shown in this figure represents a periodic system with a spectral evolution during the transition between the different phases of the oscillation. The spectrum corresponding to each phase is given in a table column, such that the specification of a spectrum for this particular source in the source catalog table is not applicable. In the same way different source images can be assigned to particular phases or points of time in the light curve using the optional IMAGE column.

point given by the CRPIX1 and CRPIX2 header keywords is translated to match the position of the individual source specified by the corresponding RA and DEC values in the source catalog. In addition to this translation the image can be rotated and linearly scaled using the optional columns IMGROTA and IMGSCAL in the source catalog. The rotation angle around the reference point is defined in the direction N-E-S-W. The linear scale of 1/IMGSCAL is applied to the angular extent of the image.

Points to note & Conventions

- A spatially extended source with different emission regions characterized by particular spectra can be modeled by a superposition of several images in combination with the spectra describing the particular emission features of the corresponding regions. An example of that is shown in Sec. 3.2.

2.4 Time Variability Extension

Brightness variability of a source can be modeled either by an explicit light curve or by a PSD, which can be used to simulate a light curve.

2.4.1 Light Curve

Description The time-dependence of the flux density of a source can be explicitly described by a light curve. If the variability is periodic, one can also specify the phase of the oscillation instead of the time in the light curve.

A light curve can be used to model, e.g., the pulse profile of the Crab pulsar, or to implement time-dependent source spectra and images. If a source is oscillating between a hard and a soft spectrum, it can be described by a light curve specifying the brightness variation during the different phases of this oscillation and giving references to the corresponding spectra (see Fig. 3 and Sec. 3.2).

Extension Header The following keywords are mandatory:

- `HDUCLASS` - should contain the string `HEASARC`
- `HDUCLAS1` - should contain the string `SIMPUT`
- `HDUCLAS2` - should contain the string `LIGHTCUR`

- `HDUVERS = '1.0.0'` - giving the version of the format
- `MJDREF` - MJD for reference time
- `TSTART` - start time
- `TSTOP` - stop time
- `TIMEZERO` - zero time
- `TIMESYS` - the system used to define the time
- `TIMEUNIT` - unit for `TSTART, TSTOP, TIMEZERO`. The recommended units are s.
- `CLOCKCOR` - if time is corrected to UT
- `PERIODIC` - flag whether the light curve is periodic (`1`) or not (`0`)

The usage of the time definition keywords is described by Angelini et al. (1994).

If the light curve describes a periodic system, the following additional keywords are required:

- `PHASE0` - phase of periodic oscillation at TIMEZERO (recommended value between 0 and 1)
- `PERIOD` - duration of one oscillation period (units given by TIMEUNIT)

In addition the following optional header keyword can be used to specify the normalization of the flux represented by the light curve:

- `FLUXSCAL` - scaling factor (see below)

If FLUXSCAL is not given as a header keyword, it is assumed to be unity.

Data Format The data within the extension are organized as a BINTABLE with the following columns:

1. *Time*, an **floating point** value containing the time (relative to the offset given by the header keyword TIMEZERO). If this column exists, the table must not contain a PHASE column.
   The FITS column name is **TIME**.
   The units are defined by the header keyword TIMEUNIT.
   This column is optional (either TIME or PHASE column must exist).

2. *Phase*, a **floating point** value containing the phase in a periodic system. If this column exists, the table must not contain a TIME column.
   The FITS column name is **PHASE**.
   (unitless, value in the interval from 0 to 1).
   This column is optional (either TIME or PHASE column must exist).

3. *Relative Flux*, a **floating point** value containing the relative source flux density with respect to the reference value given in the source catalog.
   The FITS column name is **FLUX**.
   (unitless).
   This column is required.

4. *Spectrum*, a **string** containing a reference to the FITS file HDU describing the energy spectrum of the source valid for this particular point of time or phase respectively. The reference is given via the extended filename syntax (see Sec. 2.1). Entries in this column might be NULL (see notes below).
   The FITS column name is **SPECTRUM**.
   (unitless).
   This column is optional.

5. *Image*, a **string** containing a reference to the FITS file HDU with an image of the source valid for this particular point of time or phase respectively. The reference is given via the extended filename syntax (see Sec. 2.1). Entries in this column might be NULL (see notes below).
   The FITS column name is **IMAGE**.
   (unitless).
   This column is optional.

The table must contain either a TIME or PHASE column.

The absolute energy flux density $F(t)$ for a particular time t is obtained from the reference flux density in the source catalog $F_{\rm catalog}$, the light curve value $l(t)$, and the value of FLUXSCAL via the following relation:

$$F(t) = \frac{l(t)}{\rm FLUXSCAL} \cdot F_{\rm catalog} \tag{3}$$

Points to note & Conventions

- The TIME and PHASE column are mutually exclusive. A light curve extension may contain only one of them. For periodic systems the PHASE column should be used instead of the TIME column.
- The TIME and PHASE columns should have ascending order.
- A complex time-variable system with time lags or independent variability in different energy bands can be modeled by a superposition of multiple entries in the source catalog, each having its own spectrum and light curve.
- The SPECTRUM and IMAGE columns are only used for sources with time-dependent spectrum or spatial extent. Otherwise the spectrum and image for a particular source should be defined in the source catalog (see Sec. 2.1).
- If the light curve has a very high resolution, references to the spectra or images might not be given for all time bins. Some entries in these columns might be NULL. In that case the simulation must interpolate between the given spectra or images.
- It is up to the simulation software to make sure that the required time interval is covered by the light curve. Otherwise the source can, e.g., be either considered to be in an off-state or a warning for the user can be produced.

2.4.2 Power Spectral Density

Description Instead of giving an explicit light curve the time-variability of a source can be described by a PSD, which can be converted to a light curve in the simulation itself, e.g. by using the algorithm presented by Timmer & König (1995). In contrast to a light curve a PSD can be used to describe statistically-independent brightness variations such as noise for different sources with only one data set.

Extension Header The following keywords are mandatory:

- `HDUCLASS` - should contain the string `HEASARC`
- `HDUCLAS1` - should contain the string `SIMPUT`

- `HDUCLAS2` - should contain the string `POWSPEC`
- `HDUVERS = '1.0.0'` - giving the version of the format

Data Format The data within the extension are organized as a BINTABLE with the following columns:

1. *Frequency*, a **floating point** value containing the frequency.
   The FITS column name is **FREQUENC**.
   The units are Hz.
   This column is required.
2. *Power*, a **floating point** value containing the power spectral density of the flux variation with a normalization according to Miyamoto et al. (1992). Details are given in the notes below.
   The FITS column name is **POWER**.
   The units are rms Hz^{-1}.
   This column is required.

Points to note & Conventions

- The FREQUENC column should have ascending order from low to high frequencies. The frequencies must define an equally-spaced grid from $f_{\min} = 1/T$ to $f_{\max} = 1/(2\Delta t)$ with Δt the resolution of the generated light curve and $T = N\Delta t$ its total length. The individual frequencies can therefore be calculated as $f_i = \frac{i}{N\Delta t}$ for $1 \leq i \leq N/2$.
- The PSD can be converted into a light curve using, e.g., the algorithm presented by Timmer & König (1995). The resulting light curve represents the relative flux variation of the reference flux given in the source catalog (cp. Sec. 2.4.1). Therefore the average of the generated light curve must be 1.
- The PSD has a normalization according to the one introduced by Miyamoto et al. (1992), which is defined for light curves containing the measured count rates. Since the light curve generated from the PSD represents the relative variation of the reference flux and is therefore unitless, the normalization factor of the PSD is adapted to $A = 2(\Delta t)^2/T = 2\Delta T/N$. With this normalization the integral of the PSD over a certain frequency range represents the square of the root mean square (rms) caused by the variations in this range. The integral over all frequencies gives the total rms squared:

$$\int_0^\infty \mathrm{PSD}(f)df = \mathrm{rms}^2 \tag{4}$$

3 Examples

In order to illustrate the structure of the SIMPUT file format, this section lists two examples. One of them describes a simple system of two single X-ray point sources with constant brightness each having its own spectrum. The other one describes an extended X-ray source with different polarized emission regions and a point source oscillating between two states.

3.1 Simple Example

The following example describes a simple system of two single point-like X-ray sources. Both sources have a constant brightness and each of them has its own spectrum. All data are combined in one FITS file 'simple.fits' with three HDUs (one empty primary, one source catalog, and one spectrum extension containing both spectra).

3.1.1 simple.fits

The primary HDU is empty and therefore neglected here.

HDU 2 This HDU contains the source catalog.

```
XTENSION= 'BINTABLE'           / binary table extension
BITPIX  =                    8 / 8-bit bytes
NAXIS   =                    2 / 2-dimensional binary table
NAXIS1  =                   61 / width of table in bytes
NAXIS2  =                    2 / number of rows in table
PCOUNT  =                    0 / size of special data area
GCOUNT  =                    1 / one data group (required keyword)
TFIELDS =                   10 / number of fields in each row
TTYPE1  = 'SRC_ID  '           / label for field   1
TFORM1  = 'J       '           / data format of field: 4-byte INTEGER
TTYPE2  = 'SRC_NAME'           / label for field   2
TFORM2  = '8A      '           / data format of field: ASCII Character
TTYPE3  = 'RA      '           / label for field   3
TFORM3  = 'E       '           / data format of field: 4-byte REAL
TTYPE4  = 'DEC     '           / label for field   4
TFORM4  = 'E       '           / data format of field: 4-byte REAL
TTYPE5  = 'E_MIN   '           / label for field   5
TFORM5  = 'E       '           / data format of field: 4-byte REAL
TTYPE6  = 'E_MAX   '           / label for field   6
TFORM6  = 'E       '           / data format of field: 4-byte REAL
TTYPE7  = 'FLUX    '           / label for field   7
TFORM7  = 'E       '           / data format of field: 4-byte REAL
TTYPE8  = 'SPECTRUM'           / label for field   8
TFORM8  = '21A     '           / data format of field: ASCII Character
TTYPE9  = 'IMAGE   '           / label for field   9
TFORM9  = '4A      '           / data format of field: ASCII Character
TTYPE10 = 'TIMING  '           / label for field  10
TFORM10 = '4A      '           / data format of field: ASCII Character
EXTNAME = 'SRC_CAT '           / name of this binary table extension
HDUCLASS= 'HEASARC '
HDUCLAS1= 'SIMPUT  '
HDUCLAS2= 'SRC_CAT '
HDUVERS = '1.0.0   '
RADECSYS= 'FK5     '
EQUINOX =                2000.
```

```
TUNIT3  = 'deg     '
TUNIT4  = 'deg     '
TUNIT5  = 'keV     '
TUNIT6  = 'keV     '
TUNIT7  = 'erg/s/cm**2'
END

        SRC_ID      SRC_NAME RA              DEC             E_MIN
                             deg             deg             keV
      1           1 SIMPLE-1   2.3469999E+01  -8.1199999E+00   1.0000000E+00
      2           2 SIMPLE-2   2.3920000E+01  -7.8800001E+00   5.0000000E-01

        E_MAX           FLUX            SPECTRUM               IMAGE TIMING
        keV             erg/s/cm**2
      1   1.0000000E+01   5.3299999E-12 [SPECTRUM,1][#row==1] NULL  NULL
      2   1.2000000E+01   2.1799999E-11 [SPECTRUM,1][#row==2] NULL  NULL
```

HDU 3 This HDU contains the spectra of both sources in the catalog. The spectrum of the first source is stored in the first row, the spectrum of the second source in the second row. The spectra do not have explicit names. In the source catalog they are therefore identified by their row numbers.

```
XTENSION= 'BINTABLE'           / binary table extension
BITPIX  =                    8 / 8-bit bytes
NAXIS   =                    2 / 2-dimensional binary table
NAXIS1  =                 1592 / width of table in bytes
NAXIS2  =                    2 / number of rows in table
PCOUNT  =                    0 / size of special data area
GCOUNT  =                    1 / one data group (required keyword)
TFIELDS =                    2 / number of fields in each row
TTYPE1  = 'ENERGY  '           / label for field   1
TFORM1  = '199E    '           / data format of field: 4-byte REAL
TTYPE2  = 'FLUX    '           / label for field   2
TFORM2  = '199E    '           / data format of field: 4-byte REAL
EXTNAME = 'SPECTRUM'           / name of this binary table extension
HDUCLASS= 'HEASARC '
HDUCLAS1= 'SIMPUT  '
HDUCLAS2= 'SPECTRUM'
HDUVERS = '1.0.0   '
EXTVER  =                    1
TUNIT1  = 'keV     '
TUNIT2  = 'photon/s/cm**2/keV'
END

        ENERGY          FLUX
        keV             photon/s/cm**2/keV
      1   1.5000001E-01   2.4728054E-31
          2.5000000E-01   6.2420354E-06
          3.5000002E-01   9.5439591E-02
          4.4999999E-01   1.7395179E+00
          5.5000001E-01   3.5762501E+00
```

```
...
    2   1.5000001E-01   1.3464495E+00
        2.5000000E-01   6.6499883E-01
        3.5000002E-01   4.2314768E-01
        4.4999999E-01   2.8910592E-01
        5.5000001E-01   2.2885039E-01
...
```

3.2 Elaborate Example

The following example file contains an extended X-ray source with two different polarized emission regions described by two separate images, and a point source oscillating between two states, one with a hard spectrum and low intensity and one with a soft spectrum and high intensity.

In the source catalog the extended source is split up in two separate entries, each with a specific spectrum and image of the particular emission regions. The periodic point source consists of a single entry in the catalog referring to a periodic light curve and two spectra for the different states. The source catalog and the light curve of the second source are stored in the file 'elaborate.fits', the spectra and images in the separate file 'data.fits'.

3.2.1 elaborate.fits

The primary HDU is empty and therefore neglected here.

HDU 2 This HDU contains the source catalog.

```
XTENSION= 'BINTABLE'           / binary table extension
BITPIX  =                    8 / 8-bit bytes
NAXIS   =                    2 / 2-dimensional binary table
NAXIS1  =                   93 / width of table in bytes
NAXIS2  =                    3 / number of rows in table
PCOUNT  =                    0 / size of special data area
GCOUNT  =                    1 / one data group (required keyword)
TFIELDS =                   12 / number of fields in each row
TTYPE1  = 'SRC_ID  '           / label for field   1
TFORM1  = 'J       '           / data format of field: 4-byte INTEGER
TTYPE2  = 'SRC_NAME'           / label for field   2
TFORM2  = '10A     '           / data format of field: ASCII Character
TTYPE3  = 'RA      '           / label for field   3
TFORM3  = 'E       '           / data format of field: 4-byte REAL
TTYPE4  = 'DEC     '           / label for field   4
TFORM4  = 'E       '           / data format of field: 4-byte REAL
TTYPE5  = 'IMGROTA '           / label for field   5
TFORM5  = 'E       '           / data format of field: 4-byte REAL
TTYPE6  = 'IMGSCAL '           / label for field   6
TFORM6  = 'E       '           / data format of field: 4-byte REAL
TTYPE7  = 'E_MIN   '           / label for field   7
```

```
TFORM7  = 'E       '           / data format of field: 4-byte REAL
TTYPE8  = 'E_MAX   '           / label for field   8
TFORM8  = 'E       '           / data format of field: 4-byte REAL
TTYPE9  = 'FLUX    '           / label for field   9
TFORM9  = 'E       '           / data format of field: 4-byte REAL
TTYPE10 = 'SPECTRUM'           / label for field  10
TFORM10 = '21A     '           / data format of field: ASCII Character
TTYPE11 = 'IMAGE   '           / label for field  11
TFORM11 = '18A     '           / data format of field: ASCII Character
TTYPE12 = 'TIMING  '           / label for field  12
TFORM12 = '12A     '           / data format of field: ASCII Character
EXTNAME = 'SRC_CAT '           / name of this binary table extension
HDUCLASS= 'HEASARC '
HDUCLAS1= 'SIMPUT  '
HDUCLAS2= 'SRC_CAT '
HDUVERS = '1.0.0   '
RADECSYS= 'FK5     '
EQUINOX =                 2000.
TUNIT3  = 'deg     '
TUNIT4  = 'deg     '
TUNIT5  = 'deg     '
TUNIT7  = 'keV     '
TUNIT8  = 'keV     '
TUNIT9  = 'erg/s/cm**2'
END
```

	SRC_ID	SRC_NAME	RA	DEC	IMGROTA
			deg	deg	deg
1	1	EXTENDED-1	-1.0500000E+01	-3.0999999E+00	3.0000000E+01
2	2	EXTENDED-2	-1.0500000E+01	-3.0999999E+00	3.0000000E+01
3	3	PERIODIC	-9.6999998E+00	-4.1999998E+00	0.0000000E+00

	IMGSCAL	E_MIN	E_MAX	FLUX
		keV	keV	erg/s/cm**2
1	8.9999998E-01	5.0000000E-01	1.0000000E+01	7.6999998E-14
2	8.9999998E-01	5.0000000E-01	1.0000000E+01	9.9999998E-14
3	0.0000000E+00	1.0000000E-01	1.5000000E+01	5.6999998E-11

	SPECTRUM	IMAGE	TIMING
1	data.fits[SPECTRUM,1]	data.fits[IMAGE,1]	NULL
2	data.fits[SPECTRUM,2]	data.fits[IMAGE,2]	NULL
3	NULL	NULL	[LIGHTCUR,1]

HDU 3 This HDU contains the light curve of the periodic source.

```
XTENSION= 'BINTABLE'           / binary table extension
BITPIX  =                    8 / 8-bit bytes
NAXIS   =                    2 / 2-dimensional binary table
NAXIS1  =                   43 / width of table in bytes
```

```
NAXIS2  =                   10 / number of rows in table
PCOUNT  =                    0 / size of special data area
GCOUNT  =                    1 / one data group (required keyword)
TFIELDS =                    3 / number of fields in each row
TTYPE1  = 'PHASE   '           / label for field   1
TFORM1  = 'E       '           / data format of field: 4-byte REAL
TTYPE2  = 'FLUX    '           / label for field   2
TFORM2  = 'E       '           / data format of field: 4-byte REAL
TTYPE3  = 'SPECTRUM'           / label for field   3
TFORM3  = '35A     '           / data format of field: ASCII Character
EXTNAME = 'LIGHTCUR'           / name of this binary table extension
HDUCLASS= 'HEASARC '
HDUCLAS1= 'SIMPUT  '
HDUCLAS2= 'LIGHTCUR'
HDUVERS = '1.0.0   '
EXTVER  =                    1
MJDREF  =                48043.
TSTART  =                    0.
TSTOP   =                    0.
TIMEZERO=                    0.
TIMESYS = 'MJD     '
TIMEUNIT= 's       '
CLOCKCOR= 'YES     '
PERIODIC=                    1
PHASE0  =                 0.31
PERIOD  =               283680.
FLUXSCAL=                    1.
END
```

	PHASE	FLUX	SPECTRUM
1	0.0000000E+00	1.4700000E+00	data.fits[SPECTRUM,3][NAME=='hard']
2	1.0000000E-01	1.3802379E+00	NULL
3	2.0000000E-01	1.1452379E+00	NULL
4	3.0000001E-01	8.5476196E-01	NULL
5	4.0000001E-01	6.1976200E-01	NULL
6	5.0000000E-01	5.2999997E-01	data.fits[SPECTRUM,3][NAME=='soft']
7	6.0000002E-01	6.1976206E-01	NULL
8	6.9999999E-01	8.5476196E-01	NULL
9	8.0000001E-01	1.1452380E+00	NULL
10	8.9999998E-01	1.3802379E+00	NULL

3.2.2 data.fits

HDU 1 This HDU contains one of the two emission region images of the first source.

```
SIMPLE  =                    T / file does conform to FITS standard
BITPIX  =                  -32 / number of bits per data pixel
NAXIS   =                    2 / number of data axes
NAXIS1  =                    3 / length of data axis 1
```

```
NAXIS2  =                    3 / length of data axis 2
EXTEND  =                    T / FITS dataset may contain extensions
COMMENT   FITS (Flexible Image Transport System) format is defined in 'Astronomy
COMMENT   and Astrophysics', volume 376, page 359; bibcode: 2001A&A...376..359H
EXTNAME = 'IMAGE   '
HDUCLASS= 'HEASARC '
HDUCLAS1= 'SIMPUT  '
HDUCLAS2= 'IMAGE   '
HDUVERS = '1.0.0   '
EXTVER  =                    1
CTYPE1  = 'RA---CAR'
CTYPE2  = 'DEC--CAR'
CUNIT1  = 'deg     '
CUNIT2  = 'deg     '
CRPIX1  =                   2.
CRPIX2  =                   2.
CRVAL1  =                   0.
CRVAL2  =                   0.
CDELT1  =                 0.25
CDELT2  =                 0.25
RADECSYS= 'FK5     '
EQUINOX =                2000.
FLUXSCAL=                 0.8
END
```

HDU 2 This HDU contains the other emission region image of the first source.

```
XTENSION= 'IMAGE   '           / IMAGE extension
BITPIX  =                  -64 / number of bits per data pixel
NAXIS   =                    2 / number of data axes
NAXIS1  =                    3 / length of data axis 1
NAXIS2  =                    3 / length of data axis 2
PCOUNT  =                    0 / required keyword; must = 0
GCOUNT  =                    1 / required keyword; must = 1
EXTNAME = 'IMAGE   '
HDUCLASS= 'HEASARC '
HDUCLAS1= 'SIMPUT  '
HDUCLAS2= 'IMAGE   '
HDUVERS = '1.0.0   '
EXTVER  =                    2
CTYPE1  = 'RA---CAR'
CTYPE2  = 'DEC--CAR'
CUNIT1  = 'deg     '
CUNIT2  = 'deg     '
CRPIX1  =                   2.
CRPIX2  =                   2.
CRVAL1  =                   0.
CRVAL2  =                   0.
CDELT1  =                 0.25
CDELT2  =                 0.25
```

```
RADECSYS= 'FK5     '
EQUINOX =                2000.
FLUXSCAL=                 0.18
END
```

HDU 3 This HDU contains the emission spectrum of the first source corresponding to the first image in HDU 1.

```
XTENSION= 'BINTABLE'           / binary table extension
BITPIX  =                    8 / 8-bit bytes
NAXIS   =                    2 / 2-dimensional binary table
NAXIS1  =                 4003 / width of table in bytes
NAXIS2  =                    1 / number of rows in table
PCOUNT  =                    0 / size of special data area
GCOUNT  =                    1 / one data group (required keyword)
TFIELDS =                    3 / number of fields in each row
TTYPE1  = 'NAME    '           / label for field   1
TFORM1  = '11A     '           / data format of field: ASCII Character
TTYPE2  = 'ENERGY  '           / label for field   2
TFORM2  = '499E    '           / data format of field: 4-byte REAL
TTYPE3  = 'FLUX    '           / label for field   3
TFORM3  = '499E    '           / data format of field: 4-byte REAL
EXTNAME = 'SPECTRUM'           / name of this binary table extension
HDUCLASS= 'HEASARC '
HDUCLAS1= 'SIMPUT  '
HDUCLAS2= 'SPECTRUM'
HDUVERS = '1.0.0   '
EXTVER  =                    1
TUNIT2  = 'keV     '
TUNIT3  = 'photon/s/cm**2/keV'
STOKES1 =                   0.
STOKES2 =                   1.
STOKES3 =                   0.
RADECSYS= 'FK5     '
EQUINOX =                2000.
END
```

```
        NAME        ENERGY          FLUX
                    keV             photon/s/cm**2/keV
      1 cutoffpl1.6   1.1993988E-01   3.0327507E+01
                      1.5981963E-01   1.8991982E+01
                      1.9969940E-01   1.3242880E+01
                      2.3957916E-01   9.8731565E+00
                      2.7945894E-01   7.7058897E+00
      ...
```

HDU 4 This HDU contains the emission spectrum of the first source corresponding to the second image in HDU 2. This emission spectrum has a different shape and polarization than the spectrum in HDU 3.

```
XTENSION= 'BINTABLE'           / binary table extension
BITPIX  =                    8 / 8-bit bytes
NAXIS   =                    2 / 2-dimensional binary table
NAXIS1  =                 4003 / width of table in bytes
NAXIS2  =                    1 / number of rows in table
PCOUNT  =                    0 / size of special data area
GCOUNT  =                    1 / one data group (required keyword)
TFIELDS =                    3 / number of fields in each row
TTYPE1  = 'NAME    '           / label for field   1
TFORM1  = '11A     '           / data format of field: ASCII Character
TTYPE2  = 'ENERGY  '           / label for field   2
TFORM2  = '499E    '           / data format of field: 4-byte REAL
TTYPE3  = 'FLUX    '           / label for field   3
TFORM3  = '499E    '           / data format of field: 4-byte REAL
EXTNAME = 'SPECTRUM'           / name of this binary table extension
HDUCLASS= 'HEASARC '
HDUCLAS1= 'SIMPUT  '
HDUCLAS2= 'SPECTRUM'
HDUVERS = '1.0.0   '
EXTVER  =                    2
TUNIT2  = 'keV     '
TUNIT3  = 'photon/s/cm**2/keV'
STOKES1 =                   -1.
STOKES2 =                    0.
STOKES3 =                    0.
RADECSYS= 'FK5     '
EQUINOX =                2000.
END

        NAME         ENERGY          FLUX
                     keV             photon/s/cm**2/keV
      1 cutoffpl2.0   1.1993988E-01   3.5723953E+01
                      1.5981963E-01   1.9869173E+01
                      1.9969940E-01   1.2651364E+01
                      2.3957916E-01   8.7613888E+00
                      2.7945894E-01   6.4260769E+00
      ...
```

HDU 5 This HDU contains the two spectra assigned to the periodic point source. The soft spectrum in row 1 corresponds to phase 0.0 of the oscillation, the hard spectrum in row 2 corresponds to phase 0.5. The spectra have explanatory names, which are used to identify them.

```
XTENSION= 'BINTABLE'           / binary table extension
BITPIX  =                    8 / 8-bit bytes
NAXIS   =                    2 / 2-dimensional binary table
NAXIS1  =                 7996 / width of table in bytes
NAXIS2  =                    2 / number of rows in table
PCOUNT  =                    0 / size of special data area
GCOUNT  =                    1 / one data group (required keyword)
TFIELDS =                    3 / number of fields in each row
```

```
TTYPE1  = 'NAME    '           / label for field   1
TFORM1  = '4A      '           / data format of field: ASCII Character
TTYPE2  = 'ENERGY  '           / label for field   2
TFORM2  = '999E    '           / data format of field: 4-byte REAL
TTYPE3  = 'FLUX    '           / label for field   3
TFORM3  = '999E    '           / data format of field: 4-byte REAL
EXTNAME = 'SPECTRUM'           / name of this binary table extension
HDUCLASS= 'HEASARC '
HDUCLAS1= 'SIMPUT  '
HDUCLAS2= 'SPECTRUM'
HDUVERS = '1.0.0   '
EXTVER  =                    3
TUNIT2  = 'keV     '
TUNIT3  = 'photon/s/cm**2/keV'
END

        NAME ENERGY          FLUX
             keV             photon/s/cm**2/keV
      1 soft   1.0995996E-01   0.0000000E+00
               1.2987988E-01   0.0000000E+00
               1.4979979E-01   2.9488223E-31
               1.6971973E-01   2.9728314E-21
               1.8963963E-01   6.3448235E-15
       ...
      2 hard   1.0995996E-01   0.0000000E+00
               1.2987988E-01   0.0000000E+00
               1.4979979E-01   4.2622720E-32
               1.6971973E-01   4.6921411E-22
               1.8963963E-01   1.0827691E-15
       ...
```

4 Summary

The presented format provides a common standard to define elaborate models of astronomical sources as input for simulation programs. It comprises approaches to specify simplistic point-like sources up to detailed descriptions of time-variable spatially extended systems with polarized emission. Although it has been developed in the context of X-ray astronomy, it provides sufficient flexibility to be suitable for other wavelengths.

References

Angelini L., Pence W., Tennant A.F., 1994, The Porposed Timing FITS File Format for High Energy Astrophysics Data, OGIP/93-003, HEASARC, Greenbelt, USA

Arnaud K.A., George I.M., Tennant A.F., 2009, The OGIP Spectral File Format, OGIP/92-007, HEASARC, Greenbelt, USA

Calabretta M.R., Greisen E.W., 2002, Astronomy and Astrophysics 395, 1077

George I.M., Angelini L., 1995, Specification of Physical Units within OGIP FITS files, OGIP/93-001, NASA/GSFC, Greenbelt, USA

George I.M., Arnaud K.A., 2004, The OGIP Spectral File Format Addendum: Changes log, OGIP/92-007a, HEASARC, Greenbelt, USA

George I.M., Arnaud K.A., Ruamsuwan B.P.L., Corcoran M.F., 1998, The Calibration Requirements for Spectral Analysis, HEASARC, Greenbelt, USA

George I.M., Arnaud K.A., Ruamsuwan B.P.L., Corcoran M.F., 2007, The Calibration Requirements for Spectral Analysis, HEASARC, Greenbelt, USA

George I.M., Zellar R.S., 1995, The OGIP Format for effective area files, CAL/GEN/92-019, HEASARC, Greenbelt, USA

Greisen E.W., Calabretta M.R., 2002, Astronomy and Astrophysics 395, 1061

Hanisch R.J., Farris A., Greisen E.W., et al., 2001, Astronomy and Astrophysics 376, 359

Miyamoto S., Kitamoto S., Iga S., et al., 1992, Astrophysical Journal Letters 391, L21

Nowak M.A., Wilms J., Heinz S., et al., 2005, Astrophysical Journal 626, 1006

Pence W., 1999, In: D. M. Mehringer, R. L. Plante, & D. A. Roberts (ed.) Astronomical Data Analysis Software and Systems VIII, Vol. 172. Astronomical Society of the Pacific Conference Series, p. 487

Pence W.D., Chiappetti L., Page C.G., et al., 2010, Astronomy and Astrophysics 524, A42

Stokes G.C., 1852, Trans. Cambridge Philos. Soc. 9, 399

Timmer J., König M., 1995, Astronomy and Astrophysics 300, 707

A List of Acronyms

ARF Ancillary Response File

FITS Flexible Image Transport System

HDU Header and Data Unit

MHD Magnetohydrodynamic

PHA Pulse Height Amplitude

PSD Power Spectral Density

rms root mean square

WCS World Coordinate System

ACKNOWLEDGMENTS

First of all I would like to thank my advisor Jörn Wilms for his continuous and helpful support. Although it was sometimes difficult to get an audience in his office due to his crowded schedule, I could always rely on him spending a significant part of his precious time in case of any serious trouble. I especially want to acknowledge his willingness to solve any administrative issues and to write proposals in order to ensure the necessary funding for our projects.

I also would like to thank all my colleagues from the X-ray group at the Dr. Remeis-Sternwarte Bamberg for their versatile support. The working atmosphere in this group was extremely friendly. Questions with any concern have never been rejected, but openly discussed and finally solved with joined forces. In particular I want to thank my colleagues Moritz Böck, Thomas Dauser, Felix Fürst, and Manfred Hanke for their support concerning any questions related to `ISIS` or issues with fitting spectral data. Without the input of Thorsten Brand, Victoria Grinberg, Christoph Großberger, Johannes Hölzl, Ingo Kreykenbohm, and Michael Wille it would have been impossible to perform many of the simulations for eROSITA and *LOFT*. Big parts of my work strongly relied on the power of the computer cluster in the observatory such that many of the simulations would not have been possible without the support from our administrators Thomas Dauser, Manfred Hanke, Ingo Kreykenbohm, and Fritz-Walter Schwarm. When I encountered any problems, some of these guys usually reacted on very short terms and tried to solve the problem. I thank Michael Wille, Felix Fürst, and Ingo Kreykenbohm for reviewing this thesis and providing me with helpful comments. Amongst my office mates I am especially grateful to Laura Bárragan for her patient willingness to improve my knowledge of the Spanish language. I want to thank all my colleagues in the top floor of the observatory for the friendly and productive atmosphere in our offices.

Since any satellite projects are developed in major collaborations, I had to rely on lots of input from many colleagues working at different institutes. I will try to mention all of them, and I hope that those whom I forget, will not be too angry with me. Starting with the colleagues in Tübingen, it was always a pleasure to me to meet Chris Tenzer on various meetings and conferences. He provided the data, on which the detector background model for eROSITA in SIXTE is based. I would like to thank Michael Martin and Benjamin Mück for many fruitful discussions about simulation software during our numerous meetings in Bamberg and in Tübingen. At MPE I would like to thank Martin Mühlegger for our conversations about simulations for eROSITA. In particular the simulated observations of the light cones populated with galaxy clusters would have been impossible without his help and the support by Hermann Brunner and Fabrizia Guglielmetti. I am grateful to Peter Friedrich for providing me with the simulated data for the eROSITA PSF model, to Konrad Dennerl for explanations of his charge split model, and to Frank Haberl for producing special response matrices for eROSITA containing only the quantum efficiency of the detector. Maria Fürmetz and Jan Robrade (Hamburg Observatory) supplied me

with the attitude data for the eRASS, which has been a key ingredient for my simulations. Kirpal Nandra initiated the simulation of the CDF-S with the WFI on *ATHENA*, which is presented in this thesis, and Alexis Finoguenov provided me with some of the necessary input data. I want to thank for Peter Predehl and all the guys at MPE for the friendly atmosphere throughout our cooperation and their support in any situation.

Proceeding with international collaborations, I really enjoyed the hospitality of Didier Barret during my frequent stays at the Centre d'Etude Spatiale des Rayonnements (CESR) in Toulouse and the collaboration with him in terms of *IXO* and *ATHENA*. I would like to thank Damien Rambaud for the discussions about the dead time of the HTRS and Jan-Willem den Herder for his suggestions concerning the simulations of the XMS. Stephen Smith and Richard Kelley provided me with useful information about microcalorimeters. I would like to thank Michael Nowak for his support with any concerns related to the *Chandra* X-ray observatory and him and his wife Nirah for their hospitality during my visits at the Massachusetts Institute of Technology (MIT). Similarly Randall Smith deserves my thankfulness for his hospitality at the Center for Astrophysics (CfA) of the Harvard university, the fruitful discussions in his office about various issues related to simulations, and the close cooperation regarding the SIMPUT file format. I thank Keith Arnaud and William Pence for reviewing the SIMPUT format document. During my various visits to the USA I have very much enjoyed the sightseeing tours with Katja Pottschmidt, Ivica Mišcovičová, and Jörn Wilms over the weekends.

I would also like to thank my colleagues from the group of optical astronomers at the Dr. Remeis-Sternwarte. Although there has not been much overlap of our work due to the different wavelength regimes, I enjoyed the pleasant atmosphere, which was enforced by events such as barbecues in the garden of the observatory.

I acknowledge the financial support of my work by the German Bundesministerium für Wirtschaft und Technologie (BMWi) under DLR grant number 50 QR 0903.

Last but not least I would like to thank my family for their continuous support of my career. Based their financial and moral support I could always fully concentrate on my studies and my work.